

# **An Analysis of the Oscillation of Atmospheric Neutrinos**

by

Shimpei Tobayama

B.Sc., Keio University, 2010

A THESIS SUBMITTED IN PARTIAL FULFILLMENT OF  
THE REQUIREMENTS FOR THE DEGREE OF  
DOCTOR OF PHILOSOPHY

in

The Faculty of Graduate and Postdoctoral Studies  
(Physics)

THE UNIVERSITY OF BRITISH COLUMBIA

(Vancouver)

December 2016

© Shimpei Tobayama 2016

# Abstract

This thesis presents an analysis of the oscillation of atmospheric neutrinos observed in Super-Kamiokande, a large underground water Cherenkov detector in Japan. The observed atmospheric neutrino events are reconstructed and selected using a newly developed maximum likelihood event reconstruction algorithm, and a Markov chain Monte Carlo technique is employed to present the results on neutrino oscillation parameters as marginalized Bayesian posterior probabilities.

The result of analyzing the SK-IV data of 2520 days exposure shows a preference for normal mass hierarchy with the posterior probability of 85.9%, and the mode and the 68% credible interval of each oscillation parameter's marginalized 1D posterior probability distribution for normal hierarchy are  $\sin^2 \theta_{23} = 0.606^{+0.044}_{-0.118}$  and  $\Delta m_{32}^2 = 2.13^{+0.17}_{-0.38} \times 10^{-3} \text{ eV}^2$ .

# Preface

This thesis is ultimately based on the work by the past and present members of the Super-Kamiokande(SK) and T2K collaborations, which are both large international collaborations comprising hundreds of members. My specific contributions are below.

For the Photosensor Test Facility described in Section 3.7, I performed the early-stage designing of the magnetic field compensation system using finite element analysis, and also designed, constructed and tested the waterproof optical head unit in collaboration with Philip Lu and Chapman Lim at TRIUMF.

For the atmospheric neutrino simulation in Chapter 4, using the latest simulation softwares developed by the SK and T2K collaborations, I produced the atmospheric neutrino MC dataset for the SK collaboration and performed extensive validation, making detailed comparisons to the old simulation to understand its behaviour. This MC dataset was used for the atmospheric neutrino analysis presented in Chapter 8.

I developed the SK event reconstruction algorithm described in Chapter 6 in collaboration with the T2K collaborators in Canada and US. The base software framework was developed by myself and Michael Wilking (formerly at TRIUMF, now at Stony Brook U.), who also developed and optimized the  $\pi^0$  reconstruction in Section 6.9. The time window algorithm described in Section 6.6.2 was developed by Patrick de Perio (formerly at U. Toronto, now at Columbia U.) and Andrew Missert at CU Boulder.

The T2K  $\nu_e$  appearance analysis described in Chapter 7 has been published by the T2K collaboration as: K. Abe *et al.*, “Observation of Electron Neutrino Appearance in a Muon Neutrino Beam”, Phys. Rev. Lett., 112:061802, 2014. I performed the validation studies for the far detector (SK) data in addition to my involvement in the development of the new  $\pi^0$  rejection method using the event reconstruction mentioned above.

The SK atmospheric neutrino oscillation analysis presented in Chapter 8 was performed largely by myself. I studied event selection methods using the new event reconstruction mentioned above. Systematic uncertainties on flux and cross section described in Section 8.2 are mostly inherited from the

## *Preface*

---

existing atmospheric neutrino analysis framework at SK, while I introduced new methods to propagate FSI uncertainties as described in Section 8.2.3. Uncertainties on detector response and reconstruction was evaluated by the collaborators in the SK energy scale working group which I was part of, and main contributions were made by Miao Jiang at Kyoto U. and Yusuke Suda at U. Tokyo. Based on the basic Markov chain Monte Carlo (MCMC) analysis software developed in T2K, I developed an analysis framework to perform Bayesian oscillation analysis of atmospheric neutrinos using MCMC and performed sensitivity studies and the final data analysis. This is the first atmospheric neutrino analysis at SK which uses MCMC.

# Table of Contents

<b>Abstract</b> . . . . .	ii
<b>Preface</b> . . . . .	iii
<b>Table of Contents</b> . . . . .	v
<b>List of Tables</b> . . . . .	ix
<b>List of Figures</b> . . . . .	x
<b>Acknowledgements</b> . . . . .	xvi
<b>1 Introduction</b> . . . . .	1
1.1 The Standard Model and Neutrinos . . . . .	1
1.2 Neutrino Oscillations . . . . .	3
1.2.1 Neutrino Mass and Mixing . . . . .	3
1.2.2 Neutrino Oscillations in Vacuum . . . . .	4
1.2.3 CP Violation in Neutrino Oscillations . . . . .	6
1.2.4 Neutrino Oscillations in Matter . . . . .	6
1.3 Experimental Status . . . . .	9
1.3.1 Solar and Reactor Neutrinos . . . . .	9
1.3.2 Atmospheric and Accelerator Neutrinos . . . . .	11
1.3.3 Measurement of $\theta_{13}$ . . . . .	14
1.4 Unresolved Issues . . . . .	15
1.5 Probing the Unknowns with Atmospheric Neutrinos . . . . .	16
1.6 Thesis Overview . . . . .	19
<b>2 Super-Kamiokande</b> . . . . .	20
2.1 Detector Overview . . . . .	20
2.2 A Water Cherenkov Detector . . . . .	22
2.3 Detector Phases and SK-IV . . . . .	23
2.4 Inner Detector . . . . .	24

---

*Table of Contents*

---

2.5	Outer Detector . . . . .	25
2.6	Water and Air Purification . . . . .	26
2.7	Data Acquisition . . . . .	26
<b>3</b>	<b>Detector Calibration . . . . .</b>	<b>28</b>
3.1	Relative PMT Gain Calibration . . . . .	28
3.2	Absolute PMT Gain Calibration . . . . .	29
3.3	PMT Quantum Efficiency . . . . .	30
3.4	Relative Timing Calibration . . . . .	31
3.5	Water Property Measurement . . . . .	33
3.6	PMT and Black Sheet Reflectivity . . . . .	37
3.7	Photosensor Test Facility . . . . .	38
<b>4</b>	<b>Atmospheric Neutrino Simulation . . . . .</b>	<b>43</b>
4.1	Atmospheric Neutrino Flux . . . . .	43
4.2	Neutrino Interaction . . . . .	45
4.2.1	Elastic and Quasi-Elastic Scattering . . . . .	46
4.2.2	Meson Exchange Current . . . . .	47
4.2.3	Single Meson Production . . . . .	48
4.2.4	Deep Inelastic Scattering . . . . .	48
4.2.5	Final State Interaction . . . . .	49
4.3	Detector Simulation . . . . .	50
<b>5</b>	<b>Data Reduction . . . . .</b>	<b>52</b>
5.1	First and Second Reduction . . . . .	52
5.2	Third Reduction . . . . .	53
5.3	Fourth Reduction . . . . .	54
5.4	Fifth Reduction . . . . .	54
5.5	Final FC Selection . . . . .	55
<b>6</b>	<b>Event Reconstruction . . . . .</b>	<b>56</b>
6.1	Likelihood Function . . . . .	56
6.2	Predicted Charge . . . . .	57
6.2.1	Predicted Charge from Direct Light . . . . .	57
6.2.2	Cherenkov Emission Profile . . . . .	58
6.2.3	Solid Angle Factor . . . . .	60
6.2.4	Light Transmission Factor . . . . .	61
6.2.5	PMT Angular Acceptance . . . . .	61
6.2.6	Predicted Charge from Indirect Light . . . . .	61
6.2.7	Parabolic Approximation . . . . .	64

---

*Table of Contents*

---

6.3	Unhit Probability and Charge Likelihood . . . . .	66
6.4	Time Likelihood . . . . .	67
6.4.1	Direct Light Time Likelihood . . . . .	67
6.4.2	Indirect Light Time Likelihood . . . . .	69
6.4.3	Merging Direct and Indirect Light Time Likelihoods .	69
6.5	Vertex Pre-fit . . . . .	74
6.6	Subevent Algorithm . . . . .	75
6.6.1	Peak Finder . . . . .	75
6.6.2	Defining Time Windows and Final Subevents . . . .	77
6.6.3	Performance of the Subevent Algorithm . . . . .	78
6.7	Single-Ring Fit . . . . .	78
6.7.1	Single-Ring Electron & Muon Fit . . . . .	79
6.7.2	Performance of the Single-Ring e & $\mu$ Fitter . . . .	79
6.7.3	$e/\mu$ Particle Identification . . . . .	80
6.7.4	In-Gate Decay Electron Fit . . . . .	85
6.8	Upstream-Track $\pi^+$ Fit . . . . .	87
6.8.1	$\mu/\pi^+$ Identification . . . . .	88
6.9	$\pi^0$ Fit . . . . .	90
6.9.1	$e/\pi^0$ Identification . . . . .	91
6.10	Multi-Ring Fit . . . . .	92
6.10.1	Initial Multi-Ring Fit . . . . .	92
6.10.2	Sequential Multi-Ring Fit . . . . .	95
6.10.3	Performance of the Multi-Ring Fitter . . . . .	96
6.11	fiTQun in SK-I to III . . . . .	102
<b>7</b>	<b>First Application of fiTQun: T2K <math>\nu_e</math> Appearance . . . . .</b>	<b>105</b>
7.1	T2K Experiment . . . . .	105
7.2	$\nu_e$ Appearance Analysis . . . . .	108
7.3	$\nu_e$ Event Selection . . . . .	110
7.4	Results . . . . .	112
<b>8</b>	<b>Atmospheric Neutrino Oscillation Analysis . . . . .</b>	<b>116</b>
8.1	Event Selection and Binning . . . . .	116
8.1.1	Selection Criteria . . . . .	117
8.1.2	$\nu/\bar{\nu}$ Separation for Single-Ring Events . . . . .	118
8.1.3	Multi-Ring $\nu_e/\bar{\nu}_e$ Selection . . . . .	119
8.1.4	Sample Statistics and Purities . . . . .	123
8.1.5	Binning . . . . .	123
8.1.6	Observing the Oscillation Effects . . . . .	127
8.2	Systematic Uncertainties . . . . .	132

## Table of Contents

---

8.2.1	Atmospheric Neutrino Flux . . . . .	132
8.2.2	Neutrino Interaction . . . . .	134
8.2.3	Final State Interaction . . . . .	135
8.2.4	Detector Response and Reconstruction . . . . .	137
8.3	Event Rate Prediction . . . . .	139
8.3.1	Oscillation Weighting . . . . .	139
8.3.2	Propagating Variations of Systematics . . . . .	140
8.4	Bayesian Analysis using Markov Chain Monte Carlo . . . . .	142
8.4.1	Likelihood Function . . . . .	143
8.4.2	Bayesian Posterior Probability . . . . .	143
8.4.3	Marginalization and Parameter Estimation . . . . .	144
8.4.4	Markov Chain Monte Carlo . . . . .	145
8.5	Sensitivity Studies . . . . .	147
8.6	Data Analysis Results . . . . .	154
8.6.1	Posterior Distributions . . . . .	155
8.6.2	Zenith Angle Distributions . . . . .	160
8.6.3	Goodness of Fit . . . . .	162
8.6.4	Result Comparison to Other Experiments . . . . .	162
<b>9</b>	<b>Conclusions and Outlook . . . . .</b>	<b>168</b>
<b>Bibliography . . . . .</b>		<b>171</b>

## Appendices

<b>A</b>	<b>List of Systematic Parameters . . . . .</b>	<b>180</b>
<b>B</b>	<b>Atmospheric Neutrino Selection Improvement by fitQun</b>	<b>182</b>

# List of Tables

1.1	Fermions in the Standard Model . . . . .	1
2.1	Definition of the event triggers . . . . .	27
6.1	Decay electron detection efficiencies for stopping cosmic-ray muons for data and MC . . . . .	78
7.1	Assumed values for the oscillation parameters . . . . .	111
7.2	Expected numbers of signal and background events passing each selection stage . . . . .	112
8.1	Interaction mode breakdown and the total event rates for each event sample . . . . .	126
8.2	Default values for the oscillation parameters which are used for event rate calculation . . . . .	128
8.3	True oscillation parameters for the Asimov dataset production	147
8.4	Priors for the oscillation parameters . . . . .	148
8.5	The 1D posterior mode and the 68% HPD credible intervals .	155
8.6	Posterior probabilities for the mass hierarchy and the $\theta_{23}$ octant	160
8.7	Oscillation parameters which are used to calculate the event rate predictions shown in Figures 8.26 to 8.28. . . . .	162
9.1	Expected posterior probabilities for favouring the correct mass hierarchy for different SK exposure . . . . .	169
A.1	List of systematic parameters. Continues to Table A.2. . . . .	180
A.2	List of systematic parameters. Continues from Table A.1. . .	181
B.1	Interaction mode breakdown and the total MC event rates for each event sample categorized by the APFIT-based selection	183

# List of Figures

1.1	Examples of weak interaction processes involving neutrinos . . . . .	3
1.2	Coherent scattering of neutrinos in matter . . . . .	6
1.3	${}^8\text{B}$ solar neutrino flux measured by SNO through different channels . . . . .	10
1.4	Zenith angle distributions observed at Super-Kamiokande . . . . .	13
1.5	The ordering of the neutrino mass . . . . .	16
1.6	The oscillation probability $P(\nu_\mu \rightarrow \nu_e)$ and the ratio of oscillated to unoscillated $\nu_e$ flux for atmospheric neutrinos reaching the Super-Kamiokande detector . . . . .	17
2.1	A sketch of the Super-Kamiokande detector . . . . .	21
2.2	The supporting structure and the PMTs . . . . .	21
2.3	A schematic drawing of Cherenkov radiation . . . . .	22
2.4	An event display of a single electron event . . . . .	23
2.5	A schematic drawing of the Hamamatsu 20-inch PMT . . . . .	24
2.6	Quantum efficiency of the photocathode as a function of wavelength . . . . .	25
3.1	The observed charge distribution for single p.e. hits obtained from the nickel source calibration data . . . . .	30
3.2	A schematic view of the timing calibration system . . . . .	31
3.3	The TQ distribution for an ID PMT . . . . .	32
3.4	The timing distribution of ID PMTs at a charge bin $\sim 1$ p.e. .	33
3.5	A schematic view of the laser injector system for measuring the water property and the reflectivity of the PMTs . . . . .	34
3.6	The TOF-subtracted hit time distributions for the laser injector data taken at 405 nm . . . . .	35
3.7	Light absorption and scattering coefficients as a function of wavelength . . . . .	36
3.8	Time variation of the light absorption and scattering coefficients measured at various wavelengths . . . . .	37

*List of Figures*

---

3.9	A schematic view of the apparatus for black sheet reflectivity measurement . . . . .	38
3.10	A schematic drawing of the PTF and the external view of the PTF magnetic field compensation system . . . . .	39
3.11	A SK PMT submerged in the tank filled with water . . . . .	40
3.12	The interior of the water-tight optical head box . . . . .	41
3.13	Local variations of the gain of a SK PMT . . . . .	42
4.1	Zenith angle distributions of the atmospheric neutrino flux at Super-K averaged over the azimuth . . . . .	44
4.2	The direction-averaged atmospheric neutrino flux at Super-K as a function of energy . . . . .	45
4.3	$\nu_\mu$ and $\bar{\nu}_\mu$ CC cross sections per nucleon divided by neutrino energy, plotted as a function of energy . . . . .	47
4.4	$\pi^+ - {}^{12}\text{C}$ scattering cross sections . . . . .	50
4.5	Low momentum $\pi^+$ absorption cross sections compared between experimental data and the variations of the NEUT pion cascade model . . . . .	51
6.1	Schematic diagram describing the variables relevant to predicted charge calculation . . . . .	58
6.2	Cherenkov emission profile $g(p, s, \cos \theta)$ for electrons . . . . .	59
6.3	Cherenkov emission profile $g(p, s, \cos \theta)$ for muons . . . . .	60
6.4	Angular acceptance of the PMT . . . . .	62
6.5	A schematic diagram describing the variables relevant to the scattering table . . . . .	63
6.6	The photon acceptance factor $J(s)$ overlaid with an approximating parabola . . . . .	65
6.7	The unhit probability $P(\text{unhit} \mu)$ with and without the correction for the PMT threshold effect . . . . .	66
6.8	The normalized charge likelihood $f_q(q \mu)$ . . . . .	68
6.9	The direct light residual time likelihood $f_t^{\text{dir}}(t^{\text{res}})$ for 300 MeV/c electrons . . . . .	70
6.10	The direct light residual time likelihood $f_t^{\text{dir}}(t^{\text{res}})$ for 2000 MeV/c electrons . . . . .	71
6.11	The direct light residual time likelihood $f_t^{\text{dir}}(t^{\text{res}})$ for 450 MeV/c muons . . . . .	72
6.12	The direct light residual time likelihood $f_t^{\text{dir}}(t^{\text{res}})$ for 2000 MeV/c muons . . . . .	73

---

*List of Figures*

---

6.13	Distribution of the scanned goodness $G(\mathbf{x}, t)$ as a function of time $t$ . . . . .	76
6.14	Single-ring electron and muon vertex resolution for FC true-fiducial CCQE events in atmospheric neutrino MC, compared between APFIT and fitQun . . . . .	81
6.15	Single-ring electron and muon vertex resolution plotted as a function of true momentum, for FC true-fiducial CCQE events in atmospheric neutrino MC, compared between APFIT and fitQun . . . . .	81
6.16	Single-ring electron and muon direction resolution for FC true-fiducial CCQE events in atmospheric neutrino MC, compared between APFIT and fitQun . . . . .	82
6.17	Single-ring electron and muon direction resolution plotted as a function of true momentum, for FC true-fiducial CCQE events in atmospheric neutrino MC, compared between APFIT and fitQun . . . . .	82
6.18	Single-ring electron and muon momentum resolution plotted as a function of true momentum, for FC true-fiducial CCQE events in atmospheric neutrino MC, compared between APFIT and fitQun . . . . .	83
6.19	Event displays of simulated single electron and muon events . . . . .	83
6.20	Likelihood separation of single-ring electron and muon events in the FC true-fiducial CCQE event sample in the atmospheric neutrino MC . . . . .	84
6.21	Misidentification rate of single-ring electron and muon events in the FC true-fiducial CCQE event sample in the atmospheric neutrino MC, plotted as a function of true momentum	84
6.22	Event displays of an MC event which has an in-gate decay electron . . . . .	86
6.23	Charge distribution for hits that are associated with each in-gate subevent, for the same event which was shown in Figure 6.22 . . . . .	86
6.24	A schematic diagram of a charged pion which undergoes a hadronic scattering on a nucleus and the rings it produces, and an event display of a simulated single $\pi^+$ event . . . . .	87
6.25	A schematic diagram describing how an upstream-track hypothesis is constructed in fitQun . . . . .	88
6.26	Likelihood separation of $\nu_\mu$ CCQE and NC $\pi^+$ events . . . . .	89
6.27	A schematic diagram showing how the $\pi^0$ hypothesis is constructed . . . . .	90

*List of Figures*

---

6.28 CC single electron and NC single $\pi^0$ events in the FC true-fiducial atmospheric neutrino MC sample, separated using the $\pi^0$ fit variables . . . . .	91
6.29 Misidentification rate for the $\pi^0$ rejection cut Equation 6.28, for the CC single electron and NC single $\pi^0$ events in the FC true-fiducial atmospheric neutrino MC sample, plotted as a function of the true particle momentum . . . . .	92
6.30 A tree diagram showing how the tree of the multi-ring hypotheses evolve as the number of rings is increased . . . . .	93
6.31 Distribution of the square root of the log likelihood ratio between the best-fit single-ring electron hypothesis and the 2R hypothesis assuming electron as the first ring, for FC sub-GeV atmospheric neutrino MC events with no decay electrons detected . . . . .	94
6.32 Reconstructed event categories of $\nu_e$ CC events with no visible pions in final state in the FC atmospheric neutrino MC for fiTQun and APFIT . . . . .	97
6.33 Reconstructed event categories of NC events with a single $\pi^0$ and no visible $\pi^\pm$ in final state in the FC atmospheric neutrino MC for fiTQun and APFIT . . . . .	97
6.34 Reconstructed event categories of $\nu_e$ CC events with a single $\pi^0$ and no visible $\pi^\pm$ in final state in the FC atmospheric neutrino MC for fiTQun and APFIT . . . . .	98
6.35 Reconstructed event categories of $\nu_\mu$ CC events with no visible pions in final state in the FC atmospheric neutrino MC for fiTQun and APFIT . . . . .	99
6.36 Reconstructed event categories of $\nu_\mu$ CC events with a single $\pi^0$ and no visible $\pi^\pm$ in final state in the FC atmospheric neutrino MC for fiTQun and APFIT . . . . .	99
6.37 Reconstructed invariant mass calculated using the 2nd and the 3rd rings for events reconstructed as 3e ring by fiTQun and APFIT in the FC atmospheric neutrino MC . . . . .	100
6.38 Reconstructed invariant mass calculated using the 2nd and the 3rd rings for events reconstructed as 1 $\mu$ + 2e ring by fiTQun and APFIT in the FC atmospheric neutrino MC . . . . .	101
6.39 Distributions of the log likelihood ratio between the fiTQun single-ring electron and muon fits for the FC sub-GeV single-ring atmospheric neutrino events in each SK phase . . . . .	103
6.40 Time variation of the light attenuation length in water . . . . .	104

*List of Figures*

---

7.1	Schematic drawing of the T2K beam production site . . . . .	105
7.2	T2K $\nu_\mu$ beam spectrum at different off-axis angles and the $\nu_\mu$ survival probability at SK . . . . .	106
7.3	A schematic drawing of ND280 . . . . .	107
7.4	Predicted T2K neutrino flux at SK . . . . .	108
7.5	$\pi^0$ rejection cut which was used in the previous $\nu_e$ appearance analysis . . . . .	113
7.6	2D distribution of the fitQun $\pi^0$ cut variables after the $E_\nu^{\text{rec}} < 1250\text{MeV}$ cut, for the dataset shown in Table 7.2 . . . . .	114
7.7	The best-fit (for normal hierarchy) $p_e - \theta_e$ distribution plotted with the observed data . . . . .	115
8.1	Distribution of the variables which are used for the Multi-GeV Multi-ring E-like(MME) likelihood selection . . . . .	121
8.2	Distribution of the sum of $\ln(L_{\text{sig}}/L_{\text{bkg}})$ for all four MME selection variables . . . . .	122
8.3	Distribution of the variables which are used for the multi-ring $\nu_e/\bar{\nu}_e$ likelihood separation . . . . .	124
8.4	Distribution of the sum of $\ln(L_{\nu_e}/L_{\bar{\nu}_e})$ for all three $\nu_e/\bar{\nu}_e$ separation variables . . . . .	125
8.5	Binning for each event sample . . . . .	127
8.6	The effect of $\sin^2 \theta_{23}$ variations on the distributions of the cosine of the zenith angle for sub-GeV samples . . . . .	129
8.7	The effect of $\sin^2 \theta_{23}$ variations on the distributions of the cosine of the zenith angle for Multi-GeV samples . . . . .	129
8.8	The effect of $\delta_{\text{CP}}$ variations on the distributions of the cosine of the zenith angle for Sub-GeV samples . . . . .	130
8.9	The effect of the mass hierarchy on the distributions of the cosine of the zenith angle for Multi-GeV e-like samples . . . . .	131
8.10	Uncertainty on the flux normalization as a function of energy	132
8.11	The fractional error matrix $\text{sgn}(V_{ij}) \times \sqrt{ V_{ij} }$ for the sub-GeV samples . . . . .	136
8.12	The fractional error matrix $\text{sgn}(V_{ij}) \times \sqrt{ V_{ij} }$ for the multi-GeV samples . . . . .	137
8.13	Reconstructed vertex Z position of stopping cosmic-ray muons entering from the top of the detector . . . . .	138
8.14	The response coefficient $f_i^j$ for the $M_A^{\text{QE}}$ systematic for the $\nu_e$ CC events in each bin in the sub-GeV one-ring e-like 0decay sample . . . . .	142

*List of Figures*

---

8.15	$\Delta m_{32}^2$ and $-\ln P(\vec{o}, \vec{f} D)$ , the negative-log of the posterior probability, plotted against the number of steps taken in each chain . . . . .	149
8.16	The marginalized 2D posterior distribution for $\Delta m_{32}^2$ and $\sin^2 \theta_{23}$ given the Asimov dataset . . . . .	150
8.17	The 2D marginalized posterior distributions for $\sin^2 \theta_{23}$ and $\delta_{\text{CP}}$ given the Asimov dataset . . . . .	152
8.18	The marginalized 1D posterior distributions for $\sin^2 \theta_{23}$ , $ \Delta m_{32}^2 $ and $\delta_{\text{CP}}$ . . . . .	153
8.19	The mean and the $\sigma$ of the marginalized 1D posterior for each systematic parameter in the case of assuming normal hierarchy, for the Asimov dataset . . . . .	154
8.20	The marginalized 2D posterior distribution for $\Delta m_{32}^2$ and $\sin^2 \theta_{23}$ given the SK-IV FC data . . . . .	156
8.21	The marginalized 2D posterior distributions for $ \Delta m_{32}^2 $ and $\sin^2 \theta_{23}$ for the cases of assuming normal and inverted hierarchy	157
8.22	The marginalized 2D posterior distributions for $\sin^2 \theta_{23}$ and $\delta_{\text{CP}}$ for the cases of assuming normal and inverted hierarchy .	158
8.23	The marginalized 1D posterior distributions for $\sin^2 \theta_{23}$ , $ \Delta m_{32}^2 $ and $\delta_{\text{CP}}$ for the cases of assuming normal and inverted hierarchy	159
8.24	The marginalized 1D posterior distributions for $\sin^2 \theta_{23}$ and $\delta_{\text{CP}}$ after marginalizing over the mass hierarchy . . . . .	160
8.25	The mean and the $\sigma$ of the marginalized 1D posterior for each systematic parameter in the cases of assuming normal and inverted hierarchy . . . . .	161
8.26	Distributions of the cosine of the zenith angle for the sub-GeV event samples . . . . .	163
8.27	Distributions of the cosine of the zenith angle for the multi-GeV e-like event samples . . . . .	164
8.28	Distributions of the cosine of the zenith angle for the multi-GeV $\mu$ -like and other event samples . . . . .	165
8.29	Distribution of the log likelihood ratio between the observed data and fake data which is used for the goodness of fit test .	166
8.30	90% credible and confidence regions for $\Delta m_{32}^2$ and $\sin^2 \theta_{23}$ for the results from various experiments . . . . .	167
B.1	90% HPD credible regions for $\Delta m_{32}^2$ and $\sin^2 \theta_{23}$ compared between the cases of using APFIT or fITQun for event selection, on Asimov datasets . . . . .	184

# Acknowledgements

First and foremost, I thank my supervisor, Hiro Tanaka, for all of his support. His generosity and patience for letting me pursue my interests and the guidance throughout were essential for completing the long PhD journey.

I also thank Akira Konaka, for stimulating my interests in Super-K and atmospheric neutrinos through a number of inspiring discussions. Many thanks to Mike Wilking, without whom the most important part of my work, fiTQun, would have never happened. Working with Patrick de Perio was always fun, and I thank him for showing me what it is to be a successful graduate student and also for broadening my horizons in many aspects.

I am grateful to the members of the SKanada group: Sophie Berkman, John Martin, Corina Nantais and Roman Tacik, and the US collaborators including Andy Missant, Eric Zimmerman and Cris Vilela, for all the progress made over the years in fiTQun and various other new efforts at Super-K.

I also thank Scott Oser, whose deep insights in statistics helped me form the basis of my knowledge in statistics. I thank all the past and present members of the T2K-Canada group: not only was it a great pleasure working with this extraordinary group of talent, the collaboration “meatings” we had in Tokai were the highlights of my life as a graduate student.

It was a great privilege working with the collaborators on the Super-K experiment. Special thanks to the SK E-scale team: Shunichi Mine, Yusuke Suda and Miao Jiang, without whose help I would have not been able to finish my analysis in such a timely manner. I also thank Roger Wendell for helping me figure out the various details in atmospheric neutrino analysis, and Richard Calland for the great help on MCMC.

I'd like to offer my special thanks to Tomonobu Tomura and my friends in Kamioka for making the life in Kamioka such a wonderful experience.

I am grateful to Haruka Haruno, Minami Kaido, Kirara Amanogawa and Towa Akagi who, during the most difficult times, gave me hope and enlightened the path to complete my PhD: a long dream since childhood.

Finally, I'd like to sincerely thank my parents, grandparents, sister and my entire family. I am where I am only because of their continuous support and encouragement. I say to them all: *hontou-ni arigato-gozaimasu!*

# Chapter 1

## Introduction

Neutrino physics has achieved remarkable progress in the past two decades. Once thought to be massless, neutrinos are now confirmed to have nonzero mass by the discovery of neutrino oscillations which necessitates the revision of the established theory of the Standard Model of particle physics. Despite the recent progress, many of the properties of neutrinos still remain unknown, and improving our knowledge of neutrinos leads the path toward the fundamental theories governing the universe.

### 1.1 The Standard Model and Neutrinos

The Standard Model of particle physics includes six quarks and six leptons as shown in Table 1.1, which are all spin 1/2 Dirac fermions and each fermion has a corresponding antiparticle which has opposite charge.

	Charge	1st generation	2nd generation	3rd generation
quarks	+2/3	up	charm	top
	-1/3	down	strange	bottom
leptons	-1	electron	muon	tau
	0	electron neutrino	muon neutrino	tau neutrino

Table 1.1: Fermions in the Standard Model.

There are three generations of quarks and each generation has two types of quarks, one with the electric charge of +2/3 and the other with -1/3. Similar to quarks there are three generations of leptons, and each generation has a charged lepton with -1 electric charge and a neutrino which is electrically neutral. The six quarks and the three charged leptons are massive, and the mass gets larger as the generation increases, for instance, a charm quark is heavier than an up quark, and a muon is heavier than an electron. Neutrinos are assumed to be massless in the Standard Model, and until the discovery of neutrino oscillations which is explained in the following section, experimental results were consistent with zero neutrino mass.

### 1.1. The Standard Model and Neutrinos

---

There are three fundamental interactions in the Standard Model which are the strong, the electromagnetic and the weak interactions, and they are mediated by gauge bosons which are spin 1 particles. The strong interaction is mediated by gluons which are massless, and they only interact with quarks and other gluons but not with leptons. The electromagnetic interaction is mediated by photons which are also massless, and they interact with all electrically charged particles; i.e. all fermions except for neutrinos interact electromagnetically. Finally, weak interactions occur to all fermions and are mediated by the weak bosons:  $W^\pm$  which have  $\pm 1$  electric charge and  $Z^0$  which is neutral. Unlike the other gauge bosons the weak bosons are massive.

The above interactions in the Standard Model are fundamentally defined by local gauge symmetries which also require the gauge bosons to be massless, and the strong interaction is described by a  $SU(3)$  symmetry in the interactions between the quark and the gluon fields. The electromagnetic and the weak interactions arise from the fundamental electroweak interaction which is described by a  $SU(2) \times U(1)$  symmetry. The corresponding gauge fields interact with the Higgs field which spontaneously breaks the symmetry and results in the massive weak bosons mediating the weak interaction and the massless photons mediating the electromagnetic interaction. The symmetry breaking caused by the Higgs field also gives rise to the mass of the quarks and the charged leptons, and introduces a massive spin 0 Higgs boson.

As stated earlier, neutrinos interact by the weak interaction only and are insusceptible to the electromagnetic or the strong interactions, and thus they rarely interact with matter. The three generations, which are also called the flavours of neutrinos are labeled as  $\nu_e$ ,  $\nu_\mu$  and  $\nu_\tau$ , and each of them respectively couples via the charged current(CC) weak interaction mediated by the  $W^\pm$  boson to the charged lepton of the corresponding flavour: electron, muon and tau. A CC interaction involves a neutrino and a charged lepton of the same flavour only, or rather, neutrino flavours are defined by the flavour of the charged lepton with which each neutrino partners via the CC interaction. The CC interaction is responsible for various weak decay processes involving neutrinos such as the muon decay illustrated on the left of Figure 1.1. The interaction mediated by the  $Z^0$  boson as on the right of Figure 1.1 is called the neutral current(NC) weak interaction, and neutrinos do not change their type by NC interactions.

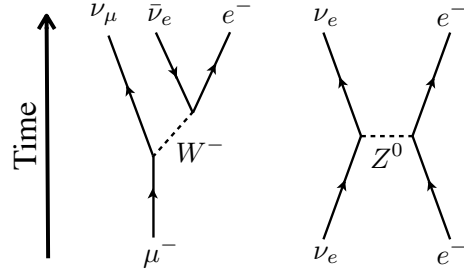


Figure 1.1: Examples of weak interaction processes involving neutrinos. The left diagram is the decay of a muon into an electron and neutrinos via the charged current interaction, and the right diagram is a neutral current electron-neutrino scattering.

## 1.2 Neutrino Oscillations

The neutrino mass is experimentally known to be small. The observation that neutrinos are produced with definite helicity[1] suggests that neutrinos are massless, and the results of any direct mass measurements to date by precision kinematic measurement of various weak decay processes are consistent with zero mass[2]. However, the discovery of neutrino oscillations has proven that neutrino mass is, in fact, not zero, which contradicts the assumption made in the Standard Model. This section describes the basic theories behind neutrino oscillations.

### 1.2.1 Neutrino Mass and Mixing

Suppose now that neutrinos do have nonzero mass, and consider free neutrinos propagating in vacuum. Since there are three neutrino flavours there are three orthogonal states  $|\nu_\alpha\rangle$  ( $\alpha = e, \mu, \tau$ ) which are the eigenstates of the weak interaction. One can also define the mass eigenstates  $|\nu_i\rangle$  ( $i = 1, 2, 3$ ) which are the eigenstates of the free particle Hamiltonian with the possibly different mass eigenvalues  $m_i$  ( $i = 1, 2, 3$ ), and since each of them form a complete basis the two bases are related by a unitary matrix  $U$ :

$$|\nu_\alpha\rangle = \sum_i^3 U_{\alpha i}^* |\nu_i\rangle. \quad (1.1)$$

A general  $N \times N$  unitary matrix has  $N^2$  real free parameters,  $N(N - 1)/2$  of which can be considered as rotation angles as in the case for a real orthogonal matrix of the same size, and the remaining  $N(N + 1)/2$

## 1.2. Neutrino Oscillations

---

real parameters can be attributed to complex phases. Therefore, the  $3 \times 3$  unitary matrix  $U$  can be characterized by 3 rotation(mixing) angles and 6 complex phases. However, assuming that neutrinos are standard Dirac fermions, one can freely define the phase of each of the flavour and the mass eigenstates without changing any physical consequences, and 5 of the phase parameters can be therefore factored out from the mixing matrix as they are physically not meaningful. Thus, the fundamental matrix  $U$  which describes the mixing of the flavour eigenstates and the mass eigenstates has three mixing angles and a single complex phase. The matrix is analogous to the Cabibbo-Kobayashi-Maskawa(CKM) matrix[3] which describes the quark mixing in weak interactions, and it is known as the Pontecorvo-Maki-Nakagawa-Sakata(PMNS) matrix[4][5] which is usually parameterized as:

$$U = \begin{pmatrix} 1 & 0 & 0 \\ 0 & \cos \theta_{23} & \sin \theta_{23} \\ 0 & -\sin \theta_{23} & \cos \theta_{23} \end{pmatrix} \begin{pmatrix} \cos \theta_{13} & 0 & \sin \theta_{13} e^{-i\delta_{CP}} \\ 0 & 1 & 0 \\ -\sin \theta_{13} e^{i\delta_{CP}} & 0 & \cos \theta_{13} \end{pmatrix} \times \begin{pmatrix} \cos \theta_{12} & \sin \theta_{12} & 0 \\ -\sin \theta_{12} & \cos \theta_{12} & 0 \\ 0 & 0 & 1 \end{pmatrix}, \quad (1.2)$$

where  $\theta_{12}$ ,  $\theta_{13}$  and  $\theta_{23}$  are the mixing angles and  $\delta_{CP}$  is the complex phase. Two extra complex phases  $\alpha_1$  and  $\alpha_2$ , known as the Majorana phases, need to be introduced in the mixing matrix as  $U \rightarrow U \times \text{diag}(1, e^{i\alpha_1}, e^{i\alpha_2})$  if neutrinos are Majorana fermions as opposed to Dirac fermions, i.e. if a neutrino is its own antiparticle. In such case, one can no longer freely choose the phase of the mass eigenstates and the corresponding degrees of freedom must remain in the unitary matrix.

### 1.2.2 Neutrino Oscillations in Vacuum

Consider now the time evolution of a flavour eigenstate in Equation 1.1 as it propagates in vacuum. The transition amplitude between the flavour eigenstates  $\nu_\alpha$  and  $\nu_\beta$  after time  $t$  is ( $c, \hbar = 1$  in the following discussions):

$$\langle \nu_\beta | e^{-i\hat{H}t} | \nu_\alpha \rangle = \sum_i^3 e^{-iE_i t} U_{\beta i} U_{\alpha i}^*, \quad (1.3)$$

where  $\hat{H}$  is the free particle Hamiltonian and  $E_i \equiv \sqrt{\mathbf{p}^2 + m_i^2}$  is the energy eigenvalue of the free particle with momentum  $\mathbf{p}$ . It can be seen from the equation that the transition amplitude between different flavour eigenstates

## 1.2. Neutrino Oscillations

---

can be nonzero as the time elapses, and the transition probability from the state  $\nu_\alpha$  to  $\nu_\beta$  is:

$$P(\nu_\alpha \rightarrow \nu_\beta)(t) = |\langle \nu_\beta | e^{-i\hat{H}t} | \nu_\alpha \rangle|^2 = \sum_{i,j}^3 U_{\alpha i}^* U_{\beta i} U_{\alpha j} U_{\beta j}^* e^{-i(E_i - E_j)t}. \quad (1.4)$$

Note that the Majorana phases  $\alpha_1$  and  $\alpha_2$  mentioned in the previous section do not affect the transition probability at all, as the phases cancel when the matrix elements are multiplied by their complex conjugates. Thus,  $\theta_{12}$ ,  $\theta_{13}$ ,  $\theta_{23}$  and  $\delta_{CP}$  are the only parameters in the mixing matrix which affect the transition probability, regardless of whether neutrinos are Dirac or Majorana fermions.

In the ultra-relativistic limit of  $\mathbf{p}^2 \gg m_i^2$ ,

$$E_i - E_j = \sqrt{\mathbf{p}^2 + m_j^2} - \sqrt{\mathbf{p}^2 + m_i^2} \approx \frac{\Delta m_{ij}^2}{2E}, \quad (1.5)$$

where  $E \approx |\mathbf{p}|$  is the characteristic energy and

$$\Delta m_{ij}^2 \equiv m_i^2 - m_j^2. \quad (1.6)$$

Using Equation 1.5 and also replacing the time  $t$  with the distance  $L$  the neutrino traveled, Equation 1.4 now reads:

$$P(\nu_\alpha \rightarrow \nu_\beta) = \sum_{i,j}^3 U_{\alpha i}^* U_{\beta i} U_{\alpha j} U_{\beta j}^* \exp\left(-i \frac{\Delta m_{ij}^2 L}{2E}\right), \quad (1.7)$$

and the unitarity condition of  $U$  further leads the equation to:

$$\begin{aligned} P(\nu_\alpha \rightarrow \nu_\beta) = \delta_{\alpha\beta} & - 4 \sum_{i>j} \operatorname{Re} [U_{\alpha i}^* U_{\beta i} U_{\alpha j} U_{\beta j}^*] \sin^2 \left( \frac{\Delta m_{ij}^2 L}{4E} \right) \\ & + 2 \sum_{i>j} \operatorname{Im} [U_{\alpha i}^* U_{\beta i} U_{\alpha j} U_{\beta j}^*] \sin \left( \frac{\Delta m_{ij}^2 L}{2E} \right). \end{aligned} \quad (1.8)$$

From this equation it can be seen that neutrinos can change its flavour as it travels in space, and since the transition probability varies periodically according to the phase  $\propto L/E$  the phenomenon is referred to as the neutrino oscillation. In order for the oscillation to happen, the following two conditions are required, one of which is that the mixing matrix  $U \neq I$ , i.e. the flavour and the mass eigenstates are not identical. The other condition is that  $\Delta m_{ij}^2 \neq 0$ , i.e., at least one of three mass eigenvalues has to be different from the others. Thus, an observation of neutrino oscillations is an evidence of nonzero neutrino mass.

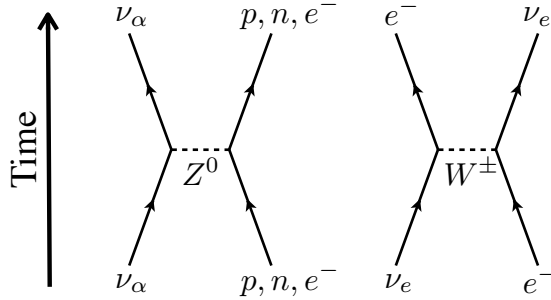


Figure 1.2: Coherent scattering of neutrinos in matter. The left diagram is a NC scattering which involves all neutrinos, and the right diagram is a CC scattering which involves electron neutrinos only. Note that such scattering also occurs for antineutrinos, while in such case the CC scattering is described by an ‘‘annihilation-creation-type’’ diagram, i.e., the right diagram rotated by 90 degrees.

### 1.2.3 CP Violation in Neutrino Oscillations

For antineutrinos, mixing as in Equation 1.1 is described by the complex conjugate of the mixing matrix:

$$|\bar{\nu}_\alpha\rangle = \sum_i^3 U_{\alpha i} |\bar{\nu}_i\rangle, \quad (1.9)$$

and since the mixing matrix is different between neutrinos and antineutrinos if  $\delta_{CP}$  is neither 0 nor  $\pi$ ,  $\delta_{CP}$  is referred to as the CP violating phase. In such case, it immediately follows that the sign of the third term in Equation 1.8 flips for antineutrinos, which suggests that the oscillation probability will be different between neutrinos and antineutrinos. Thus, CP violation in the lepton sector can be probed through neutrino oscillation measurements.

### 1.2.4 Neutrino Oscillations in Matter

When neutrinos propagate in matter, the interactions between the neutrinos and the matter change the oscillation behaviour. The phenomenon, which was first introduced by Wolfenstein[6] and subsequently elaborated by Mikheev and Smirnov[7], is known as the matter effect or the MSW effect of neutrino oscillations.

When neutrinos propagate in matter, all three flavours of neutrinos undergo neutral current coherent scattering with protons, neutrons and electrons as shown on the left of Figure 1.2. Such interaction introduces an

## 1.2. Neutrino Oscillations

---

effective potential  $V_{NC}$  which simply shifts the energy levels of all types of neutrinos by a same amount. Since ordinary matter contains electrons but not muons or taus, for electron neutrinos only the coherent charged current scattering as on the right of Figure 1.2 also occurs in addition to the NC scattering, and the process introduces an additional potential  $V_{CC}$  which only affects electron neutrinos:

$$V_{CC} = \pm \sqrt{2} G_F N_e. \quad (1.10)$$

In the equation,  $G_F$  is the Fermi coupling constant,  $N_e$  is the number density of electrons in the matter and the positive and the negative signs are for neutrinos and antineutrinos respectively.

In order to see the effect on the oscillations, for simplicity, consider now a case of two flavour oscillations between two flavour eigenstates  $\nu_e$  and  $\nu_x$ , where  $\nu_x$  is a non-electron state which is insusceptible to  $V_{CC}$  and can be considered as some combination of  $\nu_\mu$  and  $\nu_\tau$ . The flavor states are related to the mass eigenstates  $\nu_i$  with energies  $E_i$  by a mixing matrix  $U$ :

$$\begin{pmatrix} \nu_e \\ \nu_x \end{pmatrix} = U \begin{pmatrix} \nu_1 \\ \nu_2 \end{pmatrix} \equiv \begin{pmatrix} \cos \theta & \sin \theta \\ -\sin \theta & \cos \theta \end{pmatrix} \begin{pmatrix} \nu_1 \\ \nu_2 \end{pmatrix}. \quad (1.11)$$

Let  $H \equiv \text{diag}(E_1, E_2) \equiv H_0 + H_1$  be the free particle Hamiltonian in the mass basis where  $H_0 \equiv (E_1 + E_2)/2 \times \text{diag}(1, 1)$  and

$$H_1 \equiv \frac{E_2 - E_1}{2} \times \text{diag}(-1, 1) = \frac{\Delta m^2}{4E} \times \text{diag}(-1, 1), \quad (1.12)$$

where Equation 1.5 was used and  $\Delta m^2 \equiv m_2^2 - m_1^2$ . Since adding a term proportional to the unit matrix to the Hamiltonian merely adds a common phase to all neutrino types and does not affect oscillations,  $H_0$  can be ignored, and the vacuum Schrödinger equation in the flavour basis becomes:

$$\begin{aligned} i \frac{d}{dt} \begin{pmatrix} \nu_e \\ \nu_x \end{pmatrix} &= U H_1 U^\text{T} \begin{pmatrix} \nu_e \\ \nu_x \end{pmatrix} \\ &= \frac{\Delta m^2}{4E} \begin{pmatrix} -\cos 2\theta & \sin 2\theta \\ \sin 2\theta & \cos 2\theta \end{pmatrix} \begin{pmatrix} \nu_e \\ \nu_x \end{pmatrix}, \end{aligned} \quad (1.13)$$

which describes the oscillation of flavour states in vacuum. Solving the equation, the transition probability is:

$$P(\nu_e \rightarrow \nu_x) = \sin^2 2\theta \sin^2 \frac{\Delta m^2 L}{4E}, \quad (1.14)$$

## 1.2. Neutrino Oscillations

---

where the substitution  $t \rightarrow L$  was done as before.

Consider now the oscillations in matter, in which case the Hamiltonian has an additional potential term due to matter. The potential is diagonal in the flavour basis in the form  $\text{diag}(V_{\text{CC}} + V_{\text{NC}}, V_{\text{NC}})$ , and shifting the matrix by a multiple of unit matrix the Schrödinger equation in matter becomes:

$$i \frac{d}{dt} \begin{pmatrix} \nu_e \\ \nu_x \end{pmatrix} = \frac{\Delta m^2}{4E} \begin{pmatrix} -\cos 2\theta + x & \sin 2\theta \\ \sin 2\theta & \cos 2\theta - x \end{pmatrix} \begin{pmatrix} \nu_e \\ \nu_x \end{pmatrix}, \quad (1.15)$$

where

$$x \equiv \frac{2EV_{\text{CC}}}{\Delta m^2}. \quad (1.16)$$

One can then define the effective mixing angle  $\theta_M$  and the mass splitting  $\Delta m_M^2$  such that:

$$\sin 2\theta_M \equiv \frac{\sin 2\theta}{\sqrt{\sin^2 2\theta + (\cos 2\theta - x)^2}}, \quad (1.17)$$

$$\Delta m_M^2 \equiv \Delta m^2 \sqrt{\sin^2 2\theta + (\cos 2\theta - x)^2}, \quad (1.18)$$

and Equation 1.15 now becomes:

$$i \frac{d}{dt} \begin{pmatrix} \nu_e \\ \nu_x \end{pmatrix} = \frac{\Delta m_M^2}{4E} \begin{pmatrix} -\cos 2\theta_M & \sin 2\theta_M \\ \sin 2\theta_M & \cos 2\theta_M \end{pmatrix} \begin{pmatrix} \nu_e \\ \nu_x \end{pmatrix}. \quad (1.19)$$

This is of the same form as Equation 1.13 but the original mixing angle and the mass splitting  $\theta$  and  $\Delta m^2$  are now replaced by the effective values in matter  $\theta_M$  and  $\Delta m_M^2$ . This is the matter effect, and the oscillation amplitude and the frequency are changed from the case in vacuum due to the CC interaction with matter shifting the energy levels.

A dramatic consequence follows when:

$$x = \cos 2\theta. \quad (1.20)$$

In such case,  $\sin 2\theta_M = 1$ , and the mixing becomes maximal regardless of the original value of the mixing angle  $\theta$ . Such effect is known as the MSW resonance, and it occurs when the energy level splitting in matter  $\Delta m_M^2$  becomes minimal. Note that the resonance is sensitive to the sign of  $\Delta m^2$  as well as whether it is a neutrino ( $V_{\text{CC}} > 0$ ) or an antineutrino ( $V_{\text{CC}} < 0$ ): if  $\Delta m^2 > 0$  the resonance only happens for neutrinos, whereas if  $\Delta m^2 < 0$  it only happens for antineutrinos.

## 1.3 Experimental Status

Through the observation of neutrinos from various sources, neutrino oscillation is now an established fact, and the majority of the oscillation parameters have been measured. This section summarizes the different neutrino oscillation experiments which have been performed to date.

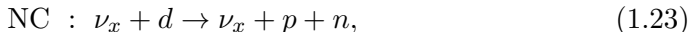
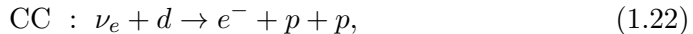
### 1.3.1 Solar and Reactor Neutrinos

The sun produces electron neutrinos through various nuclear fusion and  $\beta$ -decay processes at its interior, with their energy generally ranging in a few to ten MeV. The first measurement of solar neutrinos was made by the Homestake experiment in 1968[8], which detected the neutrinos by counting the decays of the radioisotope of argon produced in a chlorine tank via the reaction:



The observed neutrino flux was  $\sim 1/3$  of the prediction from the standard solar model(SSM)[9], and this was the first observed indication of neutrino flavour transitions in history. Several experiments which followed also observed a significant deficit of the solar neutrino flux compared to the SSM prediction. However, the effect which was eventually known as the solar neutrino problem remained unresolved for more than 30 years since its initial observation.

The first conclusive measurement to resolve the problem was made by the SNO experiment, which was capable of measuring both the electron neutrino flux and the total neutrino flux from the sun using heavy water[10][11]. In SNO, neutrinos can be detected by the CC and NC interactions on deuterium and also by elastic scattering (ES) on electron as the following:



$\nu_x$  above represents any of the three neutrino flavours, and while the NC interaction on deuterium occurs equally for all neutrino flavours, only  $\nu_e$  undergoes the CC interaction, and the experiment is thus capable of measuring the total flux and the  $\nu_e$  flux separately through the two channels. For the elastic scattering on electron, the channel is sensitive to all neutrino flavours via NC interactions, however, since  $\nu_e$  can also undergo CC interactions with electron the cross section of this process for  $\nu_e$  is larger by a

### 1.3. Experimental Status

---

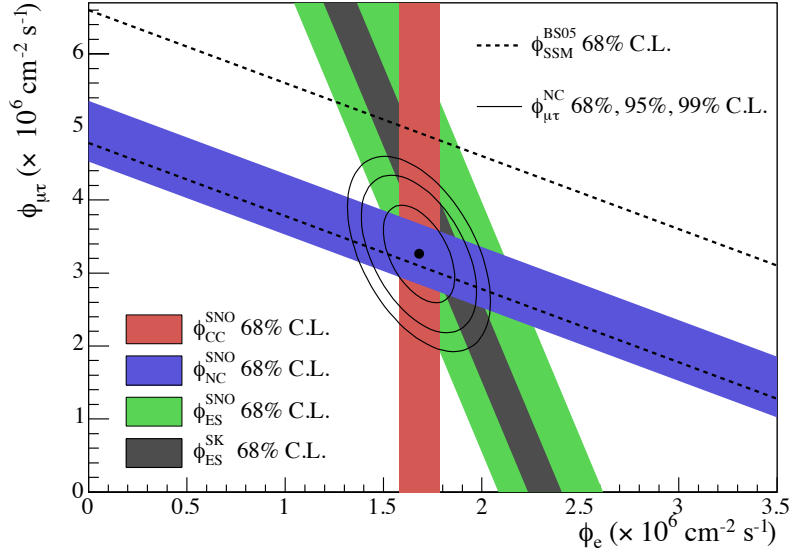


Figure 1.3:  ${}^8\text{B}$  solar neutrino flux measured by SNO through different channels. The horizontal axis is the  $\nu_e$  flux and the vertical axis is the sum of the  $\nu_\mu$  and  $\nu_\tau$  flux. 68% allowed regions from the CC, NC and ES measurements are shown as the red, blue and green bands respectively, and the ES measurement result from Super-Kamiokande is shown as a gray band. The dashed lines represents the SSM prediction of the total neutrino flux. The point and the contours represent the best estimate and the allowed regions at 68, 95 and 99% confidence levels by combining the CC and NC results. Figure taken from [12].

factor of  $\sim 6$  compared to  $\nu_{\mu,\tau}$  (“ES” refers to all elastic scattering on electron via CC and NC interactions). As shown in Figure 1.3, the result of the experiment showed a clear deficit of the  $\nu_e$  flux by a factor of  $\sim 1/3$  relative to the total flux which agreed with the SSM prediction, which is a decisive evidence for the flavour transition of solar neutrinos. Combining the SNO results with another solar neutrino measurement by Super-Kamiokande[13] as well as the reactor neutrino measurement by KamLAND[14], it is now confirmed that the flavour transition of the solar neutrinos occurs via the mechanism known as the large mixing angle(LMA) MSW solution[6][7].

According to the LMA-MSW solution, due to the high matter density at the core of the sun, the matter effect described in Section 1.2.4 significantly changes the energy levels of the neutrinos such that at energies  $\sim 10$  MeV the second mass eigenstate  $\nu_2$  becomes nearly equal to the  $\nu_e$  state, i.e.,

### 1.3. Experimental Status

---

neutrinos at that energy are produced in a nearly pure  $\nu_2$  state at the core. As the neutrinos propagate through the sun and exit to space, the matter density gradually decreases such that the neutrino state changes adiabatically, keeping the neutrinos produced at the core in a nearly-pure  $\nu_2$  state until they exit the sun while the flavour composition of the neutrino state changes according to the change in the matter density. The neutrinos then propagate until they get detected on earth spending most of the time in vacuum, during which the neutrino flavours do not oscillate as it is already in a mass eigenstate. An observer on earth then projects the mass-state neutrinos onto flavour states, and the flavour change  $\nu_e \rightarrow \nu_x$  of solar neutrinos is thus observed. The observation of the solar neutrino flavour transition measures the parameters  $\theta_{12}$  and  $\Delta m_{21}^2$ .

Another method to measure  $\theta_{12}$  and  $\Delta m_{21}^2$  is to study the “disappearance” of  $\bar{\nu}_e$ ’s coming from nuclear reactors, by measuring the deficit in the  $\bar{\nu}_e$  flux due to the transition  $\bar{\nu}_e \rightarrow \bar{\nu}_x$  in a  $\mathcal{O}(100 \text{ km})$  path in the air, which is effectively a vacuum. The KamLAND experiment[14] measured a significant deficit of the  $\bar{\nu}_e$  flux from the various nuclear reactors in Japan compared to the expectations assuming no oscillations, measuring the oscillation parameters precisely and thus contributing to resolving the solar neutrino problem.

From the global analysis of various solar and reactor neutrino data, the current known values for  $\theta_{12}$  and  $\Delta m_{21}^2$  are[15]:

$$\sin^2 \theta_{12} = 0.304^{+0.014}_{-0.013}, \quad (1.25)$$

$$\Delta m_{21}^2 = 7.53 \pm 0.18 \times 10^{-5} \text{ eV}^2. \quad (1.26)$$

#### 1.3.2 Atmospheric and Accelerator Neutrinos

Atmospheric neutrinos are produced by the cosmic ray particles impinging on earth’s atmosphere. Primary cosmic ray particles are mostly protons and helium nuclei, and when they interact with the nuclei in the atmosphere, they produce hadronic showers which consist mostly of pions as well as some kaons. Neutrinos are produced when the produced hadrons decay, for example, through the decays of charged pions and the subsequent decays of muons:

$$\pi^+ \rightarrow \mu^+ + \nu_\mu \rightarrow \nu_\mu + e^+ + \bar{\nu}_\mu + \nu_e, \quad (1.27)$$

$$\pi^- \rightarrow \mu^- + \bar{\nu}_\mu \rightarrow \bar{\nu}_\mu + e^- + \nu_\mu + \bar{\nu}_e. \quad (1.28)$$

Thus, the atmospheric neutrino flux contains neutrinos and antineutrinos of both electron and muon type with the flavour ratio  $(\nu_\mu + \bar{\nu}_\mu)/(\nu_e + \bar{\nu}_e) \sim 2$ ,

### 1.3. Experimental Status

---

while the ratio increases at higher energy since  $\mu^\pm$  have a higher chance to reach the ground without decay. Since the cosmic ray flux is close to isotropic the neutrinos come from all directions, and while the ones produced in the atmosphere right above a detector and coming downward only travel for  $\sim 10$  km before reaching the detector, the ones produced on the other side of the earth coming upward travel  $> 10,000$  km across the earth. The path length of atmospheric neutrinos therefore ranges between  $10 - 10^4$  km depending on the zenith angle of neutrino's direction, and together with energies ranging from  $10^{-1}$  to  $10^3$  GeV, atmospheric neutrinos cover a wide range of  $L/E$  to which the oscillation phase depends on, making them a perfect source for studying neutrino oscillations.

In the late 1980's and early 1990's, experiments using large underground water Cherenkov detectors such as Kamiokande[16][17] and IMB-3[18][19] observed a large deficit in the flavour ratio  $(\nu_\mu + \bar{\nu}_\mu)/(\nu_e + \bar{\nu}_e)$ : the measured ratio was nearly half of what was expected. The results suggested neutrino oscillations of a different kind from that involving solar neutrinos.

In 1998, Super-Kamiokande[20] reported a large deficit in the upward-going  $\nu_\mu$  events compared to the expectations assuming no oscillations while the downward-going  $\nu_\mu$ 's as well as  $\nu_e$ 's from all directions were rather consistent with expectations, as shown in Figure 1.4. This is a strong evidence for  $\nu_\mu$  oscillating to  $\nu_\tau$  or to unknown sterile states, and the data was, in fact, consistent with a two flavour  $\nu_\mu \rightarrow \nu_\tau$  mixing described by:

$$P(\nu_\mu \rightarrow \nu_\tau) = \sin^2 2\theta \sin^2 \frac{\Delta m^2 L}{4E}, \quad (1.29)$$

with a maximal mixing of  $\sin^2 2\theta = 1$  ( $\theta = 45^\circ$ ) and  $|\Delta m^2| \approx \mathcal{O}(10^{-3} \text{ eV}^2)$ .

The oscillation effect observed in atmospheric neutrinos were then confirmed by experiments using artificial neutrinos produced from accelerators. In such experiments, a high energy proton beam is collided with a target producing hadronic showers which subsequently produce an intense  $\nu_\mu$  beam, and the neutrinos are then observed at a large far detector located at  $\mathcal{O}(100 \text{ km})$  distance. Unlike atmospheric neutrinos, accelerator neutrino beams are very pure in  $\nu_\mu$ 's with small contaminations from  $\nu_e$ 's or antineutrinos, and the neutrino energy is tuned  $\sim 1$  GeV such that the  $\nu_\mu$  disappearance effect  $\nu_\mu \rightarrow \nu_x$  becomes maximal at the far detector based on the  $\Delta m^2$  observed at Super-Kamiokande. K2K[21] and MINOS[22] are the first of such long-baseline accelerator neutrino experiments, and they both observed significant deficit in the observed  $\nu_\mu$  events as well as distortions in the  $\nu_\mu$  energy spectrum, producing results consistent with the atmospheric neutrino observation at Super-Kamiokande.

### 1.3. Experimental Status

---

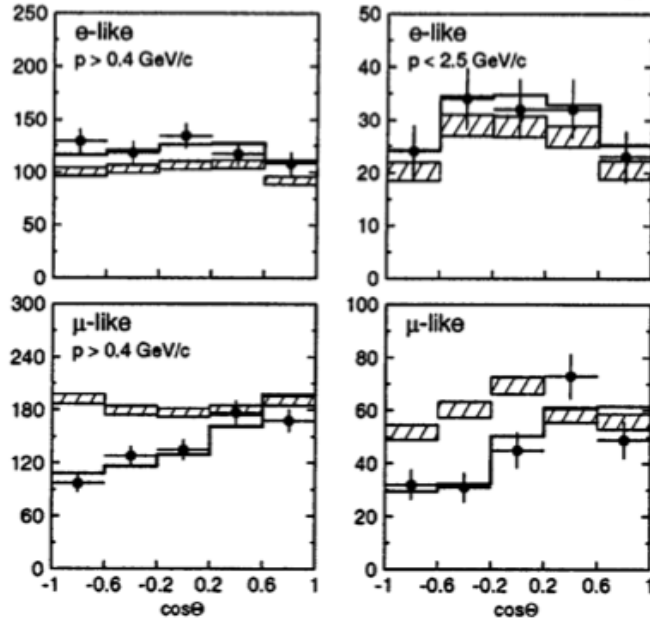


Figure 1.4: Zenith angle distributions for electron-like (top) and muon-like (bottom) events in sub-GeV (left) and multi-GeV (right), observed at Super-Kamiokande.  $\cos\theta < 0$  and  $\cos\theta > 0$  represent upward- and downward-going events respectively. The hatched bands show the expectations assuming no oscillations, while the black lines are the best-fit to data assuming  $\nu_\mu \rightarrow \nu_\tau$  oscillations. Figure taken from [20].

There are many ongoing experiments which are currently measuring the parameters  $\theta_{23}$  and  $\Delta m_{32}^2$ , which govern  $\nu_\mu \rightarrow \nu_\tau$  oscillations, with increasing precision, and their results are in general still consistent with the maximal mixing of  $\theta_{23} = 45^\circ$ , and  $|\Delta m_{32}^2|$  is measured to be  $\sim 2.5 \times 10^{-3} \text{ eV}^2$  with  $\sim 5\%$  uncertainty[15]. The latest results from the long-baseline experiment T2K[23] is (assuming  $\Delta m_{32}^2 > 0$ ):

$$\sin^2 \theta_{23} = 0.532^{+0.046}_{-0.068}, \quad (1.30)$$

$$|\Delta m_{32}^2| = 2.545^{+0.081}_{-0.084} \times 10^{-3} \text{ eV}^2. \quad (1.31)$$

Latest results on  $\theta_{23}$  and  $\Delta m_{32}^2$  from the atmospheric and accelerator neutrino experiments are discussed again in Section 8.6.4.

Note that oscillation experiments are often insensitive to the sign of  $\Delta m_{32}^2$  as can be seen from the expressions for oscillation probabilities Equa-

### 1.3. Experimental Status

---

tions 1.8 and 1.29, and although the absolute value of  $\Delta m_{32}^2$  has been measured rather precisely, its sign is still not determined. This is not the case for  $\Delta m_{21}^2$ , since the matter effect observed in solar neutrinos are only possible if  $\Delta m_{21}^2 > 0$  as discussed in Section 1.2.4. Similarly, one way to determine the sign of  $\Delta m_{32}^2$  is to observe the oscillations driven by  $\Delta m_{32}^2$  for neutrinos which travel through significant amount of matter, which will be discussed more in Section 1.5.

#### 1.3.3 Measurement of $\theta_{13}$

The mixing angle  $\theta_{13}$  was considered to be small, as the solar and atmospheric neutrino results were able to be explained assuming it is zero. The first attempt to directly measure  $\theta_{13}$  was made by CHOOZ, by observing the  $\bar{\nu}_e$  disappearance  $\bar{\nu}_e \rightarrow \bar{\nu}_x$  from a nuclear reactor at  $\sim 1$  km, which is much shorter than KamLAND. At such distance and the  $\bar{\nu}_e$  energy of  $\sim 3$  MeV, rather than the oscillation driven by the “solar” oscillation parameters  $\theta_{12}$  and  $\Delta m_{21}^2$ , the oscillation driven by  $\theta_{13}$  and  $\Delta m_{31}^2$ :

$$P(\bar{\nu}_e \rightarrow \bar{\nu}_e) \approx 1 - \sin^2 2\theta_{13} \sin^2 \frac{\Delta m_{31}^2 L}{4E}, \quad (1.32)$$

becomes dominant, and  $\theta_{13}$  can be measured by such short-baseline reactor antineutrino experiments. The result showed no evidence for nonzero  $\theta_{13}$ , giving an upper limit of  $\sin^2 2\theta_{13} < 0.15$  at 90% confidence level[24].

In 2012, new generations of short-baseline reactor experiments Double Chooz[25], Daya Bay[26] and RENO[27] separately reported that  $\sin^2 2\theta_{13} \approx 0.1$  by observing clear deficit in the reactor  $\bar{\nu}_e$  flux, where Daya Bay and RENO excluded  $\theta_{13} = 0$  at  $5.2\sigma$  and  $4.9\sigma$  respectively.

$\theta_{13}$  can also be measured via the appearance of  $\nu_e$  in a pure accelerator  $\nu_\mu$  beam, whose probability is expressed to the leading order as:

$$P(\nu_\mu \rightarrow \nu_e) \approx \sin^2 2\theta_{13} \sin^2 \theta_{23} \sin^2 \frac{\Delta m_{31}^2 L}{4E}. \quad (1.33)$$

As in the equation, the leading term in the appearance probability is proportional to  $\sin^2 2\theta_{13}$  and  $\nu_e$  appearance is thus greatly suppressed if  $\theta_{13} = 0$ . In 2011, T2K reported the first indication of  $\nu_e$  appearance excluding  $\theta_{13} = 0$  at  $2.5\sigma$  significance[28], and the updated result in 2013 showed the first decisive evidence for  $\nu_e$  appearance at  $7.3\sigma$ [29].

The current best measurements for  $\theta_{13}$  come from the short-baseline reactor experiments, and the averaged values from them are[15]:

$$\sin^2 2\theta_{13} = 8.5 \pm 0.5 \times 10^{-2}. \quad (1.34)$$

## 1.4 Unresolved Issues

Although many of the parameters involved in neutrino oscillations have been measured, there are still important open questions which need to be answered in order to fully understand the nature of neutrinos.

First of all, it is not known whether  $\theta_{23}$  mixing is exactly maximal ( $45^\circ$ ), and if not, whether the angle is larger or smaller than  $45^\circ$ . This is known as the  $\theta_{23}$  octant, and the cases  $\theta_{23} < 45^\circ$  and  $\theta_{23} > 45^\circ$  are referred to as the first and the second octant respectively.  $\nu_\mu$  disappearance is the primary oscillation mode which is sensitive to  $\theta_{23}$ , however, since the oscillation probability has a parameter dependence of the form  $\sin^2 2\theta_{23}$ , this mode alone cannot determine the octant. Therefore, one needs to look at other subdominant oscillation effects such as the ones involving  $\nu_e$  in order to resolve the octant, for instance, the  $\nu_\mu \rightarrow \nu_e$  oscillation whose leading term depends on  $\sin^2 \theta_{23}$  as in Equation 1.33.

While the squared mass differences between the neutrino mass states have been measured rather precisely, the sign of  $\Delta m_{32}^2$ (or  $\Delta m_{31}^2$ ) is still yet to be determined. As illustrated in Figure 1.5, the case  $\Delta m_{32}^2 > 0$  is referred to as normal hierarchy(NH) in which case the mass eigenstate  $m_3$  has the largest mass, whereas  $\Delta m_{32}^2 < 0$  is called inverted hierarchy(IH) in which case  $m_3$  has the smallest mass. The absolute mass is also unknown since oscillation experiments can only measure the mass differences. From cosmological measurements, the sum of the mass of the three neutrinos are measured to be less than 0.3 eV[2], and combining the knowledge of the mass hierarchy from oscillation experiments we may be able to fully reveal the mass structure of the neutrinos in near future. Furthermore, the origin of the neutrino mass and the reason for its smallness compared to other particles is still not known. Some of the appealing theories which can explain this assume that neutrinos are Majorana fermions, i.e. a neutrino is its own antiparticle, which is a fundamentally new type of particles which have never been observed. The next generation of neutrino-less double beta decay experiments can determine whether or not neutrinos are Majorana fermions in case the mass hierarchy is inverted, but not necessarily if it is normal hierarchy[30]. Therefore, information regarding the mass hierarchy provides valuable input in order to unveil the fundamental nature of the massive neutrinos. Knowledge of the mass hierarchy also resolves the degeneracies in the oscillation probabilities such that the sensitivity of various ongoing and future neutrino oscillation experiments to  $\delta_{CP}$  can be significantly improved.

Finally, and probably most importantly, it is still an open question whether CP is violated for leptons, i.e., whether  $\delta_{CP}$  is nonzero. Some lead-

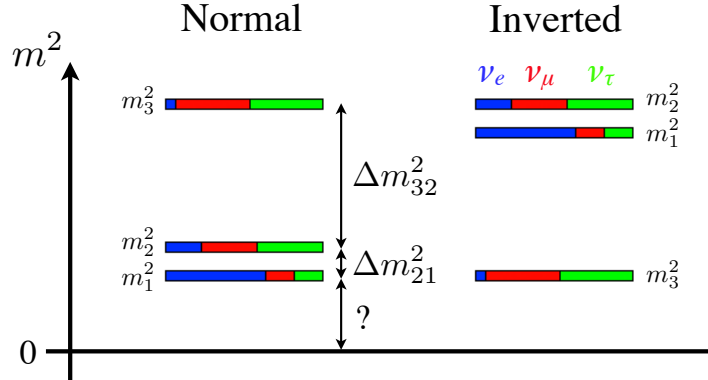


Figure 1.5: The ordering of the neutrino mass. For normal hierarchy  $m_3$  is the heaviest state and  $\Delta m_{32}^2 > 0$ , whereas for inverted hierarchy  $m_3$  is the lightest and  $\Delta m_{32}^2 < 0$ . The absolute mass is also still unknown and only the relative mass differences have been measured.

ing theories suggest that CP violation in the lepton sector can produce the matter-antimatter asymmetry which is essential to the formation of the current matter-dominated universe[31]. Although the observable CP violation in the currently known leptons itself may not necessarily be directly related to such process[32][33], it is nonetheless of fundamental interest whether CP violation can be observed in neutrino oscillations.

## 1.5 Probing the Unknowns with Atmospheric Neutrinos

The primary oscillation effect which is seen in atmospheric neutrinos is the  $\nu_\mu$  disappearance, and from the probability  $P(\nu_\mu \rightarrow \nu_\mu)$  one can measure  $\sin^2 2\theta_{23}$  and  $|\Delta m_{32}^2|$ . However, due to the wide range of energies and the long path length in matter, atmospheric neutrinos provide other information on the oscillation parameters through various sub-leading oscillation effects, allowing us to probe the remaining unknown properties of neutrinos.

As mentioned in Section 1.3.2, the path length of atmospheric neutrinos varies as a function of the zenith angle of neutrinos' direction. Since neutrino oscillation is characterized by the oscillation phase proportional to  $L/E$ , oscillation effects for atmospheric neutrinos manifest in the two-dimensional distributions of zenith angle versus energy. Figure 1.6 shows the oscillation probability  $P(\nu_\mu \rightarrow \nu_e)$  and the ratio of oscillated to unoscillated  $\nu_e$  flux

### 1.5. Probing the Unknowns with Atmospheric Neutrinos

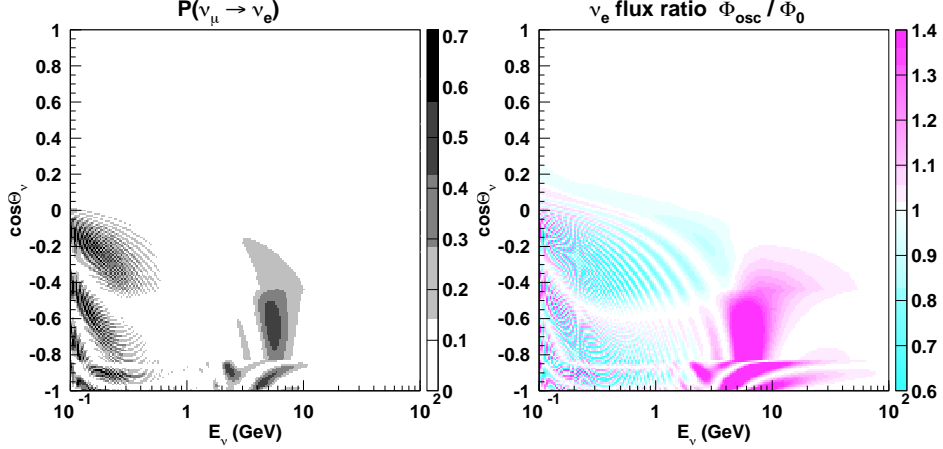


Figure 1.6: The oscillation probability  $P(\nu_\mu \rightarrow \nu_e)$ (left) and the ratio of oscillated to unoscillated  $\nu_e$  flux(right) for atmospheric neutrinos reaching the Super-Kamiokande detector. The horizontal axes are the neutrino energy and the vertical axes are the cosine of the zenith angle of neutrino direction where  $\cos \theta = 1$  is downward-going and  $\cos \theta = -1$  is upward-going. Oscillation probabilities are calculated by assuming the following oscillation parameters:  $(\Delta m_{21}^2, \Delta m_{32}^2, \sin^2 \theta_{12}, \sin^2 \theta_{23}, \sin^2 \theta_{13}, \delta_{CP}) = (7.7 \times 10^{-5} \text{ eV}^2, +2.1 \times 10^{-3} \text{ eV}^2, 0.3, 0.5, 0.04, 0^\circ)$ . Taken from [36].

for atmospheric neutrinos reaching the Super-Kamiokande detector. The oscillation probabilities are calculated by fully considering the three-flavour oscillation effects in matter, using the methods by Barger *et al.*[34] and assuming the radial density structure of the earth described in [35]. In the figure, discontinuities can be seen at  $\cos \theta \approx -0.45$  and  $\cos \theta \approx -0.84$  which correspond to the upper and the lower mantle boundary and the lower mantle and the outer core boundary respectively, which is due to the discrete change in the matter density causing the matter induced oscillation probabilities to change discretely. Some of the prominent oscillation effects are described in the following.

The enhancement of the  $\nu_\mu \rightarrow \nu_e$  oscillation probability seen in 2 – 10 GeV upward going region is due to the MSW resonance effect which happens while the neutrinos traverse the earth’s core. Following a discussion similar to Section 1.2.4, when  $\Delta m_{32}^2 \gg \Delta m_{21}^2$ , the transition probability in constant density matter is approximated as[37]:

$$P(\nu_\mu \rightarrow \nu_e) \approx \sin^2 2\theta_{13,M} \sin^2 \theta_{23} \sin^2 \frac{\Delta m_{32,M}^2 L}{4E}, \quad (1.35)$$

where the effective mixing angle and mass splitting in matter are:

$$\sin 2\theta_{13,M} = \frac{\sin 2\theta_{13}}{\sqrt{\sin^2 2\theta_{13} + (\cos 2\theta_{13} - x_{32})^2}}, \quad (1.36)$$

$$\Delta m_{32,M}^2 = \Delta m_{32}^2 \sqrt{\sin^2 2\theta_{13} + (\cos 2\theta_{13} - x_{32})^2}, \quad (1.37)$$

while

$$x_{32} \equiv \frac{2EV_{CC}}{\Delta m_{32}^2}, \quad (1.38)$$

and  $V_{CC} = \pm\sqrt{2}G_F N_e$  as before. MSW resonance happens when the resonance condition

$$x_{32} = \cos 2\theta_{13} \quad (1.39)$$

is satisfied, and  $\nu_e$  appearance due to  $\theta_{13}$  becomes maximal despite the small value of the actual  $\theta_{13}$  parameter. Since the sign of  $V_{CC}$  flips between neutrinos and antineutrinos, the enhancement happens for neutrinos only if  $\Delta m_{32}^2 > 0$  and for antineutrinos only if  $\Delta m_{32}^2 < 0$ . Thus, mass hierarchy can be probed by observing the excess in multi-GeV upward-going  $\nu_e$  and  $\bar{\nu}_e$  flux. Furthermore, since the appearance probability Equation 1.35 is proportional to  $\sin^2 \theta_{23}$  and not  $\sin^2 2\theta_{23}$ , this oscillation effect also provides sensitivity to the  $\theta_{23}$  octant.

The oscillation patterns seen below 1 GeV on the left plot are the oscillations driven by  $\theta_{12}$  and  $\Delta m_{21}^2$  which are relevant for solar neutrino oscillations. Assuming  $\theta_{13} = 0$  and constant matter density, the oscillation probabilities in such region are given as[38]:

$$P(\nu_e \rightarrow \nu_e) = 1 - P_{ex}, \quad (1.40)$$

$$P(\nu_e \rightarrow \nu_\mu) = P(\nu_\mu \rightarrow \nu_e) = P_{ex} \cos^2 \theta_{23}, \quad (1.41)$$

where

$$P_{ex} = \sin^2 2\theta_{12,M} \sin^2 \frac{\Delta m_{21,M}^2 L}{4E}. \quad (1.42)$$

$\sin 2\theta_{12,M}$  and  $\Delta m_{21,M}^2$  are expressed simply by replacing the mixing angle and mass splitting in Equation 1.36 and Equation 1.37 by  $\theta_{12}$  and  $\Delta m_{21}^2$ . Consider now the effect of this oscillation on the net observed  $\nu_e$  flux. Letting

$$r \equiv \Phi_\mu^0 / \Phi_e^0 \quad (1.43)$$

## 1.6. Thesis Overview

---

be the ratio of  $\nu_\mu$  and  $\nu_e$  flux before oscillation, the fractional difference in the observed  $\nu_e$  flux due to oscillation, considering the contributions from both  $\nu_e$  and  $\nu_\mu$  produced in the atmosphere, is expressed as:

$$\frac{\Phi_e}{\Phi_e^0} - 1 = P_{ex} \left( r \cos^2 \theta_{23} - 1 \right). \quad (1.44)$$

As mentioned previously, for low energy atmospheric neutrinos the flux flavour ratio  $r$  is roughly 2, and the terms in the parenthesis cancel when  $\cos^2 \theta_{23} = 0.5$ , i.e. when  $\theta_{23}$  mixing is maximal. When  $\theta_{23} < 45^\circ$  an excess of sub-GeV  $\nu_e$  flux is observed, while if  $\theta_{23} > 45^\circ$  a deficit will be seen instead, and this oscillation effect therefore provides sensitivity to the  $\theta_{23}$  octant.

When the  $\Delta m_{21}^2$  driven oscillations depending on  $\theta_{13}$  is also considered, i.e. when not taking the approximation  $\theta_{13} = 0$  in the discussion above, the interference between the  $\theta_{13}$ -dependent oscillations and the oscillations described by Equation 1.41 introduces a dependence of oscillation probabilities on  $\delta_{CP}$ . The interference gives an overall  $\sim 3\%$  effect on the observed total  $\nu_e$  flux in sub-GeV depending on the value of  $\delta_{CP}$ [39], and although this is not particularly a large effect this provides sensitivity to  $\delta_{CP}$ .

The oscillation effects discussed here will be revisited in Section 8.1.6.

## 1.6 Thesis Overview

In this thesis, atmospheric neutrino data observed at the Super-Kamiokande detector is analyzed in order to measure the neutrino oscillation parameters, namely,  $\sin^2 \theta_{23}$ ,  $\Delta m_{32}^2$  including its sign and  $\delta_{CP}$ , to which atmospheric neutrino data has sensitivity. Chapter 2 describes of the Super-Kamiokande detector, and its calibration methods are summarized in Chapter 3. Chapter 4 describes the atmospheric neutrino simulation which is used in conjunction with the observed data in the oscillation analysis. Chapter 5 gives an overview of the data reduction process to select atmospheric neutrinos from the data acquired at Super-Kamiokande. Chapter 6 details the maximum likelihood event reconstruction algorithm “fiTQun” which was recently developed for Super-Kamiokande, which provides input information to the oscillation analysis. As an example of the application of fiTQun, Chapter 7 summarizes the T2K  $\nu_e$  appearance analysis which was the first physics analysis in which fiTQun was used. Chapter 8 details the methods for the atmospheric neutrino oscillation analysis and presents the results of analyzing Super-Kamiokande data. The conclusions and the future outlook of the analysis are summarized in Chapter 9.

## Chapter 2

# Super-Kamiokande

Super-Kamiokande(Super-K, SK) is a large underground water Cherenkov detector located in the Kamioka mine in Mt. Ikenoyama, Gifu Prefecture, Japan. The detector consists of a water tank holding 50 kt of ultra-pure water, and the photomultiplier tubes (PMTs) lining the tank interior detect the Cherenkov radiation which is produced by charged particles which propagate in the water. The primary purposes of the detector are nucleon decay searches and the detection of neutrinos from various sources: solar neutrinos, astrophysical neutrinos such as the ones from supernovae, atmospheric neutrinos and accelerator neutrinos in long-baseline neutrino oscillation experiments such as K2K and T2K.

### 2.1 Detector Overview

Figure 2.1 shows the sketch of the detector and the surrounding experimental area. The water tank is a vertical cylinder of 41.4 m in height and 39.3 m in diameter holding 50 kt of ultra-pure water in total, and the volume is optically separated into two concentric cylinders: the inner detector(ID) which is the main detector region holding 32 kt of water with 36.2 m in height and 33.8 m in diameter, and the outer detector(OD) which is a cylindrical shell volume surrounding the ID with its thickness being 2.05 m on the top and the bottom and 2.2 m on the side. The OD serves as a veto detector for cosmic ray backgrounds entering from outside of the detector as well as a passive shield against other entering backgrounds such as neutrons and gamma rays produced in the surrounding rock. The two detector regions are separated by a 55 cm wide stainless steel supporting structure covered with opaque materials as shown in Figure 2.2, and the inner side of the supporting structure is mounted with 11,129 20-inch PMTs facing inward viewing the ID volume, while the outer side is mounted with 1,885 8-inch PMTs facing outward viewing the OD. Since the PMTs are sensitive to magnetic fields, 26 Helmholtz coils line the wall of the tank and reduce the geomagnetic field to  $\sim 50$  mG.

The detector has a  $\sim 1000$  m overburden of rock which has a shielding

## 2.1. Detector Overview

---

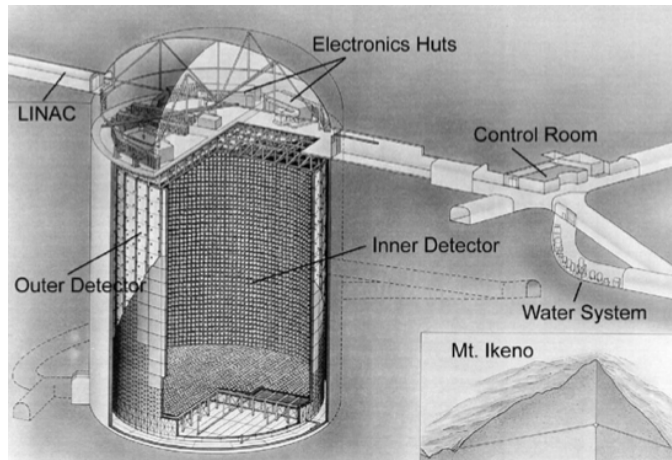


Figure 2.1: A sketch of the Super-Kamiokande detector. Taken from [40].

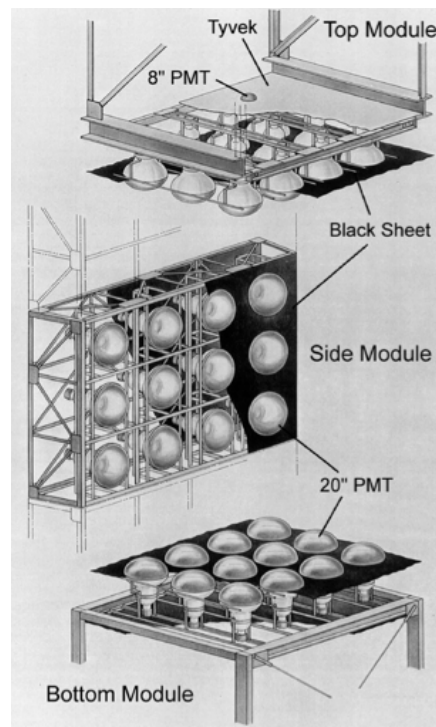


Figure 2.2: The supporting structure and the PMTs. Taken from [40].

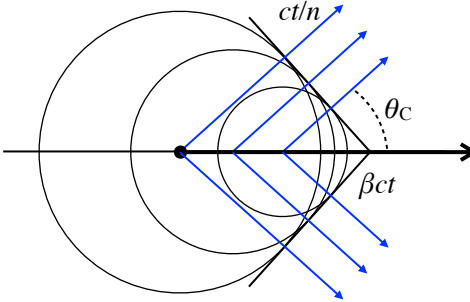


Figure 2.3: A schematic drawing of Cherenkov radiation.

effect against cosmic rays equivalent to 2700 m of water. The rate of cosmic rays reaching the detector is reduced to  $\sim 3$  Hz which is low enough that various nucleon decay and neutrino studies can be performed without concerns about cosmic ray muon backgrounds.

## 2.2 A Water Cherenkov Detector

Cherenkov radiation is an electrodynamic phenomenon which is analogous to the sonic boom produced by an object travelling faster than the speed of sound. When a charged particle travels in a dielectric medium with refractive index  $n$  at velocity  $v=\beta c$  which exceeds the phase velocity  $c/n$  of light in the medium, the local disturbances to the dielectric caused by the moving charge radiate electromagnetic waves which form an electromagnetic shock wave as schematically shown in Figure 2.3. This is the Cherenkov light, and the light is emitted as a cone with its opening angle  $\theta_C$  relative to the particle's direction satisfying:

$$\cos \theta_C = \frac{1}{n\beta}. \quad (2.1)$$

Since  $n \approx 1.34$  in water at the typical visible light wavelength the detector is sensitive to, for a particle traveling at  $\beta=1$  Cherenkov light is therefore emitted at the angle  $\theta_C \approx 42^\circ$ . The number of emitted photons per wavelength per unit travel distance of the particle is given as:

$$\frac{d^2N}{dx d\lambda} = \frac{2\pi\alpha}{\lambda^2} \left(1 - \frac{1}{n^2\beta^2}\right), \quad (2.2)$$

where  $\lambda$  is the wavelength and  $\alpha$  is the fine-structure constant.

### 2.3. Detector Phases and SK-IV

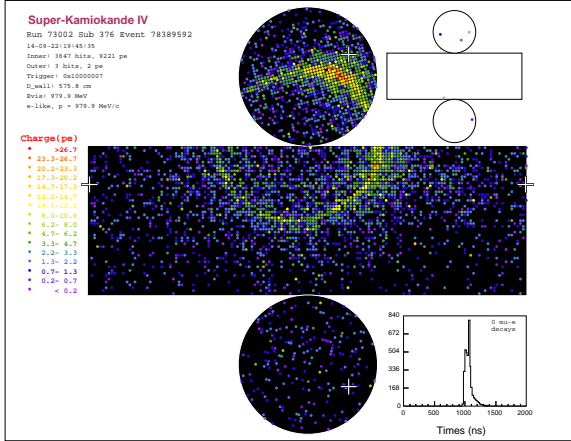


Figure 2.4: An event display of a single electron event in the atmospheric neutrino data, where the unrolled view of the ID is shown in the figure. Each dot represents a PMT which detected Cherenkov photons, and the colour scale indicates the integrated charge which corresponds to the number of photons detected at each PMT.

Since  $\beta>1/n$  is required in order for a particle to emit Cherenkov radiation, the momentum threshold at which this occurs for various particle types assuming  $n=1.34$  are roughly: 0.57 MeV/c for an electron, 118 MeV/c for a muon, 156 MeV/c for a  $\pi^+$  and 1052 MeV/c for a proton.

In Super-Kamiokande, neutrinos are detected when they interact with the water and produce charged particles above the Cherenkov threshold, and the cone of light emitted by a charged particle is observed as a ring by the PMTs on the detector wall as shown in Figure 2.4. For each event the time of the first photon arrival as well as the integrated charge at each PMT is recorded, and from that information the type and the kinematics of the particles are inferred as described in Chapter 6.

## 2.3 Detector Phases and SK-IV

Since Super-K started its operation in 1996, there have been four distinct detector phases. The initial phase, referred to as SK-I, started in April 1996 and continued until the detector was shut down for a scheduled maintenance in July 2001. On November 12, 2001 when the detector was being refilled with water after the completion of the maintenance, one of the PMTs at the bottom imploded, causing a shock wave which destroyed more than half

## 2.4. Inner Detector

---

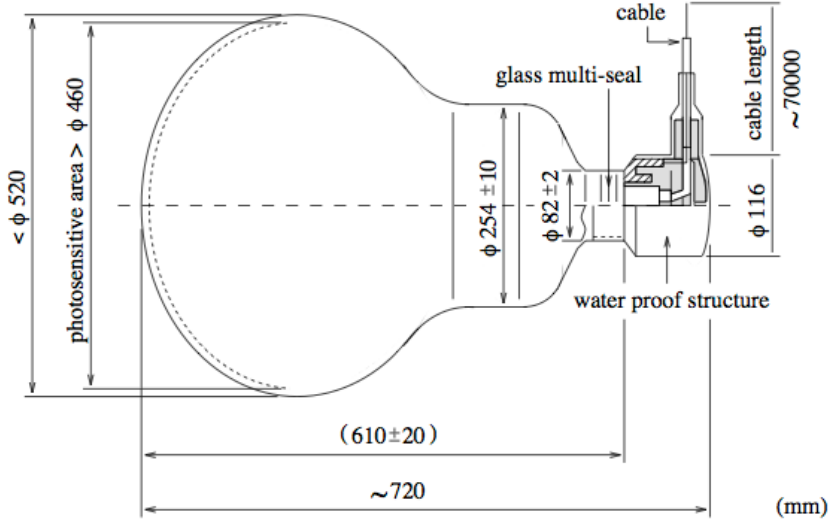


Figure 2.5: A schematic drawing of the Hamamatsu 20-inch PMT used for the ID. Taken from [40].

of the PMTs in the detector. After the accident the detector was operated temporarily by redistributing the surviving PMTs evenly, while each ID PMT was enclosed in a cover made of acrylic and fibre-reinforced plastic(FRP) in order to prevent another implosion accident. The second phase of the detector, SK-II, ran in such configuration with less than half of the original photo-coverage between October 2002 and October 2005. The detector was then brought back to its original full capacity after installing additional PMTs, and the SK-III phase started in July 2006. Finally, in September 2008 the detector underwent a brief shut down in order to upgrade the electronics, and the SK-IV phase continues since then until the present day.

This thesis focuses on analyzing the data from SK-IV only, and the configurations of the detector in this phase are described in the following.

## 2.4 Inner Detector

Figure 2.5 shows a schematic drawing of the Hamamatsu 20-inch PMT which is used in the ID. 11,129 of the PMTs are evenly placed on the wall of the ID on a 70 cm square grid realizing 40% coverage of the ID surface area by the photocathodes, and Cherenkov photons produced by the particles in the

## 2.5. Outer Detector

---

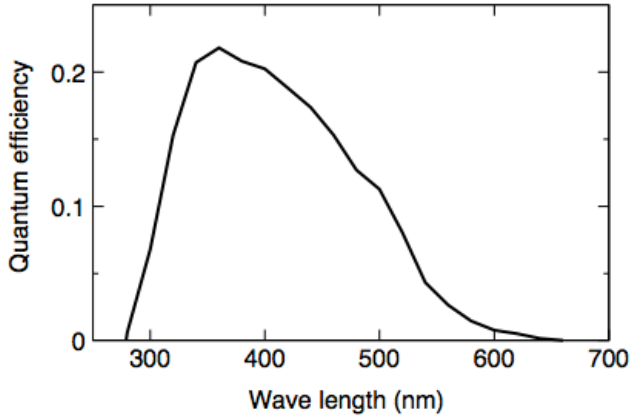


Figure 2.6: Quantum efficiency of the photocathode as a function of wavelength. Taken from [40].

ID are detected with high efficiency and resolution. The photocathodes are composed of a bialkali (Sb-K-Cs) material which has quantum efficiency as shown in Figure 2.6 with a peak efficiency being around 22% at 360 nm wavelength. The 11-stage dynode in the PMT has a gain of  $10^7$  when supplied with high voltage ranging in 1700-2000V, and the collection efficiency of the first dynode is over 70%. The transit time spread for a single photoelectron signal is 2.2 ns.

In order to protect the detector against PMT implosions as happened in 2001, each ID PMT is enclosed in a FRP housing with an acrylic window covering the photocathode area so that the shock wave does not occur even if one of the PMTs imploded. The spaces on the ID wall between the PMTs are covered with opaque black sheets made of polyethylene terephthalate ensuring the ID and the OD are optically well separated.

## 2.5 Outer Detector

The outer detector consists of evenly-spaced 1,885 8-inch PMTs facing outward to the OD water. Unlike the ID, the spaces between the PMTs are covered with a reflective material Tyvek which has  $\sim 90\%$  reflectivity at 400 nm in order to increase the photon collection efficiency in the OD. To further enhance the light collection, each PMT is also surrounded by a 60 cm square wavelength-shifting plates which absorbs the ultra-violet Cherenkov photons and reemits blue-green visible light to which the PMTs are sensitive.

## 2.6. Water and Air Purification

---

Although the timing resolution of the OD PMTs slightly degrade from 13 ns to 15 ns due to the reemission process, the wavelength shifter increases the light collection efficiency in the OD by 60% which is more important than the timing resolution considering the role of the OD as a veto detector for entering backgrounds. In order to better distinguish between entering, exiting and through-going particle events, the barrel region of the OD is optically separated from the top and the bottom regions by Tyvek.

## 2.6 Water and Air Purification

As Cherenkov light needs to travel tens of metres in the detector water before reaching the PMTs to be detected, maintaining high transparency of the water is crucial for this experiment. The water which is originally taken from the spring water in the mine undergoes multiple filtering, sterilizing and degassing processes in order to remove particle, bacterial and radioactive contaminants from the water. The water is continuously purified and circulated at a rate of  $\sim 50$  t/hr, and its temperature is kept at  $\sim 13$  °C with temporal variations within 0.01 °C using a heat exchanger in order to suppress bacterial growth as well as stabilizing the detector response.

As the rock in the mine has high radon content, the air in the mine is naturally rather high in radioactivity. In order to reduce the radon level in the air especially so that it does not contaminate the detector water, filtered Rn-free air is continuously supplied from outside of the mine into the experimental area, keeping the area at positive pressure. Furthermore, the rock surrounding the experimental hall is entirely coated with a polyurethane material in order to prevent the radon in the rock from being released into the air.

## 2.7 Data Acquisition

When a photon hits the photocathode of a PMT and produces a photoelectron(p.e.), the signal is amplified by the dynodes in the PMT and produces a pulse current signal. In SK-IV, such analog signal from a PMT is first fed into a charge-to-time convertor(QTC) which was specially designed for Super-K[41]. When the input signal from a PMT exceeds a discriminator threshold(we will call this a “hit” for brevity), the QTC starts integrating the charge from the signal over the following 400 ns, and then outputs a rectangular pulse signal whose rising edge representing the time the input analog signal crossed the threshold and the width of the pulse representing

## 2.7. Data Acquisition

---

the integrated charge. The output rectangular signal from the QTC is then digitized by a time-to-digital convertor(TDC), and the digitized charge and time, which represent the number of the detected p.e.'s and the production time of the first p.e. at the PMT respectively, are then sent for further processing and are eventually used in physics analyses. The QTC demonstrates an overall dynamic range of 0.2-2500 pC which corresponds to a maximum signal of  $\sim$ 1000 p.e., and the non-linearity of charge is measured to be below 1% across the entire dynamic range. Such high dynamic range and linearity enables precise analyses of neutrinos events across a wide range of energy.

Since it is not feasible to store the information of every single hit in the detector, an event trigger is issued when the number of PMTs that are simultaneously hit exceeds a certain threshold, and only the hits that are accompanied by a trigger are saved. Event triggering in SK-IV is done entirely by software using the digitized hit time information from the detector, and depending on the purpose there are five different types of event triggers which are summarized in Table 2.1. A triggering computer continuously monitors the observed data and calculates the variable  $N_{200}$  which represents the number of hits in a sliding 200 ns time window at a given time. When  $N_{200}$  exceeds the defined threshold of a trigger, the trigger is issued and the charge and time information for the hits which are contained in the entire event time window around the trigger is recorded. For the OD trigger  $N_{200}$  is calculated using the hits in the OD PMTs only, while for the other triggers hits in the ID are used. The thresholds for the SLE and SHE triggers were lowered in May 2015 and September 2011 respectively. The events accompanying the high-energy(HE) trigger are used in this atmospheric neutrino analysis.

Trigger Type	$N_{200}$ Threshold	Event Time Window ( $\mu\text{s}$ )
SLE	34 $\rightarrow$ 31	[−0.5, +1.0]
LE	47	[−5, +35]
HE	50	[−5, +35]
SHE	70 $\rightarrow$ 58	[−5, +35]
OD	22 (in OD)	[−5, +35]

Table 2.1: Definition of the event triggers. The triggers based on ID hits are: Super Low Energy(SLE), Low Energy(LE), High Energy(HE) and Special High Energy(SHE) triggers. The OD trigger is based on OD hits.

# Chapter 3

# Detector Calibration

This chapter describes the procedures for calibrating the Super-Kamiokande detector. The calibration results are used for producing the detector simulation which is described in Section 4.3 as well as for analyzing the observed data. Further details on the calibration methods can be found in [42].

As mentioned in Chapter 2, what Super-K records as data is ultimately the charge and the time information from the PMTs through the electronics, and their charge and time response therefore needs to be calibrated precisely. The dominant factors which characterize the charge response are the quantum efficiency and the gain of the PMTs, and as the characteristics of each PMT have non-negligible variations, such properties need to be calibrated on an individual PMT basis. The time response also has significant variations between different PMT channels. In addition to the response of the PMTs and the electronics, the optical properties of water and other components in the detector also need to be measured in order to precisely model the Cherenkov photon propagation in the detector simulation.

## 3.1 Relative PMT Gain Calibration

The supply high voltage for the PMTs are set individually for each PMT so that the charge response for a given light intensity is approximately the same across all PMTs. In order to measure and correct for the remaining individual variations in the PMT gain, the following measurement is done.

The measurement uses the same apparatus as the timing calibration which is described in detail in Section 3.4. As schematically shown in Figure 3.2, pulsed laser light is injected isotropically at a fixed position near the centre of the ID, and the hits and the charge at the ID PMTs are then measured repeatedly by flashing the laser at two different intensities.

One set of measurements is performed by flashing the laser at high intensity  $I_H$  such that every PMT detects several photons at a time. In such case, the average measured charge  $Q(i)$  at the  $i$ -th PMT is proportional to the intensity  $I_H$  of the injected light as well as the individual gain of the

### 3.2. Absolute PMT Gain Calibration

---

PMT  $G(i)$ :

$$Q(i) \propto I_H \times a(i) \times \epsilon(i) \times G(i). \quad (3.1)$$

In this equation, the measured charge is also proportional to the light acceptance  $a(i)$ , which depends on the PMT's geometrical configuration within the detector, and the quantum efficiency  $\epsilon(i)$  of the PMT.

Another set of measurements is made by flashing the laser at very low intensity  $I_L$  so that only a few PMTs get hit at a time. At such low intensity a PMT detects at most one photon at a time, and the average number of hits  $N(i)$  at each PMT, which is equivalent to the hit probability, is proportional to the intensity of the injected light but is almost independent of the PMT gain due to the low hit discriminator threshold:

$$N(i) \propto I_L \times a(i) \times \epsilon(i). \quad (3.2)$$

Since the position of the light source is unchanged and the only difference between the two sets of measurements is the intensity of the injected light, by taking the ratio  $Q(i)/N(i)$  the factors which vary between individual PMTs cancel except for the gain  $G(i)$ , and the relative individual variation of the PMT gain is thus obtained from the measured ratio:

$$G(i) \propto Q(i)/N(i). \quad (3.3)$$

According to the measurement, the variation of the gain across all PMTs has a standard deviation of 5.9%, and the individual relative gain factor obtained above is used to correct the observed charge at each PMT to effectively make the charge response of the PMTs uniform across the entire detector when the data is analyzed.

## 3.2 Absolute PMT Gain Calibration

The absolute gain, which relates the measured charge to the number of detected p.e.'s at a PMT, is obtained by a calibration measurement using a “nickel source”: a low energy gamma ray source made of a sphere of nickel which emits 9 MeV gamma rays isotropically upon capturing the neutrons emitted from a  $^{252}\text{Cf}$  neutron source which is placed at the centre. The source is placed at the centre of the ID and produces on average 0.004 p.e./event at each PMT, and more than 99% of the produced hits will therefore be single p.e. hits.

After correcting for the relative gain variation for each PMT as described in Section 3.1, the observed charge distribution for the single p.e. hits produced by the nickel source is obtained by accumulating the hits from all

### 3.3. PMT Quantum Efficiency

---

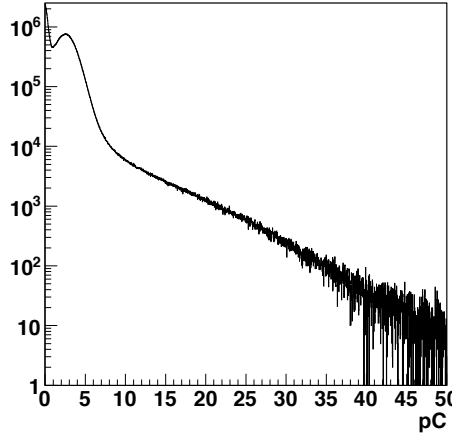


Figure 3.1: The observed charge distribution for single p.e. hits obtained from the nickel source calibration data. Figure taken from [42].

PMTs as is shown in Figure 3.1. From the average of this distribution, the conversion factor between the observed charge and the number of p.e.'s is determined to be 2.658 pC/p.e. The obtained single p.e. charge distribution is also used in the detector simulation which is discussed in Section 4.3.

### 3.3 PMT Quantum Efficiency

In addition to the gain, the quantum efficiency(Q.E.) also varies between different PMTs and the efficiency for each PMT needs to be measured. The measurement is done using the same nickel source as described in Section 3.2.

When the intensity of light reaching a PMT is small enough that the expected number of produced p.e. is significantly smaller than one as in the nickel source data, the average number of hits at a PMT, i.e. the hit probability, is proportional to the quantum efficiency as well as the intensity of the light as described by Equation 3.2. Therefore, the hit probabilities measured by the nickel source data can be used to calibrate the Q.E. for each PMT. Since it is not possible to express the light acceptance  $a(i)$  in Equation 3.2 in closed form and accurately correct for it to extract the Q.E.  $\epsilon(i)$  directly from the measured hit probability, the nickel source events are simulated assuming no individual variations for the Q.E. so that it can be compared to the observed data. The hit probability obtained from the simulated events, which accounts for the factor  $a(i)$  via simulation but does not include the variations in  $\epsilon(i)$ , is compared to the hit probability calculated

### 3.4. Relative Timing Calibration

---

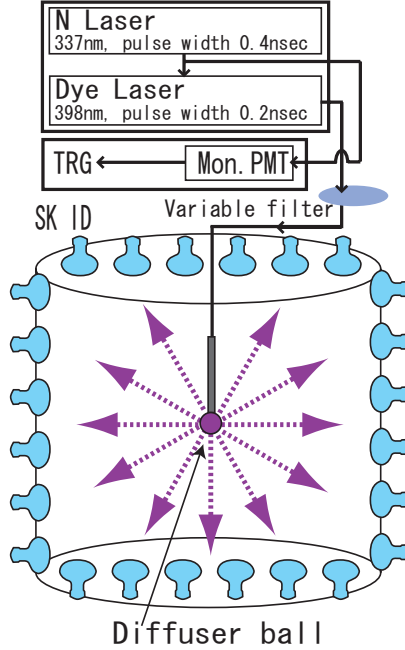


Figure 3.2: A schematic view of the timing calibration system. Figure taken from [42].

for each PMT using the real nickel source data and the Q.E. for each PMT  $\epsilon(i)$  is obtained. The resulting Q.E. for each individual PMT is used in the detector simulation.

## 3.4 Relative Timing Calibration

The time interval between the time a photoelectron is initially produced at a PMT and the time the signal from the PMT is registered as a hit by the electronics varies between the PMTs due to many factors including the difference in the length of the cables connecting the PMTs to the electronics. Also, since the time it takes for an analog signal from a PMT to cross the hit discriminator threshold depends on the pulse height, the time response depends on the observed charge.

In order to calibrate such variations in the time response, a fast pulsed laser light is injected isotropically at the centre of the ID as schematically shown in Figure 3.2. The time of the laser injection is monitored directly from the light source by a fast 2-inch monitoring PMT, and using that

### 3.4. Relative Timing Calibration

---

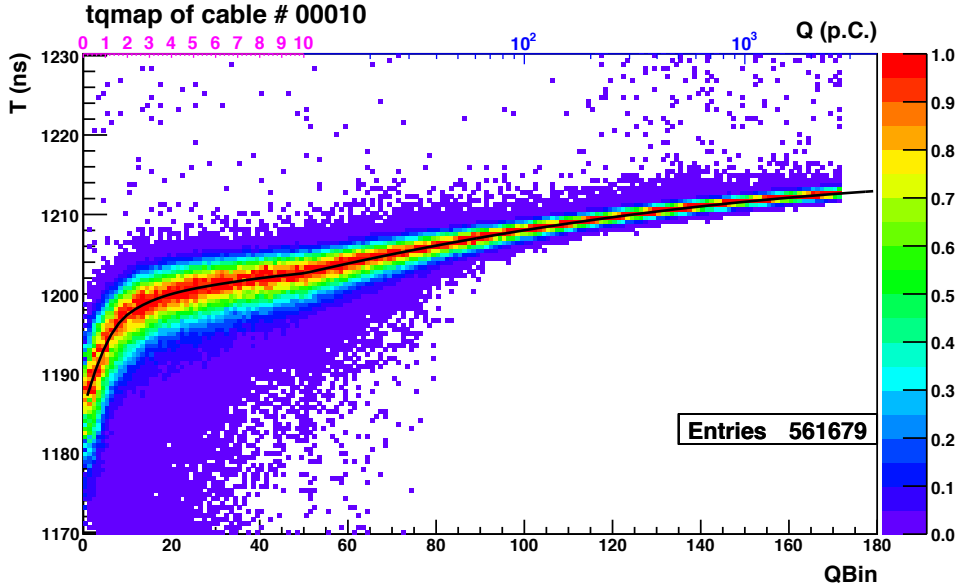


Figure 3.3: The TQ distribution for an ID PMT. The horizontal axis represents the charge where the scale in pC is shown at the top: the scale is linear up to 10pC and then goes to log scale. The vertical axis represents the TOF-corrected hit time where a larger value corresponds to earlier hits. Figure taken from [42].

injection time as a reference the relative offsets between the hit time of the ID PMTs are obtained from the time-of-flight(TOF) corrected hit time which is defined as the hit time subtracted by the time required for a photon to travel from the light source to the PMT. Since the timing also depends on the charge as stated before, calibration data is taken at various laser intensity and for each PMT the 2D distribution of the observed TOF-corrected time and charge is produced which is referred to as the “TQ distribution”.

Figure 3.3 shows an example of the TQ distribution for a PMT. In the figure, the horizontal axis represents the charge and the vertical axis represents the TOF-corrected hit time. Once the TQ distribution is obtained for each PMT, the distribution is fitted by an asymmetric Gaussian in each charge bin, and the peak position of the Gaussians is then fitted by a polynomial as a function of charge. The fitted peak position of the TQ distribution, named the TQ map, is saved into a database for each PMT and is then used to correct the hit timing as a function of charge on an individual PMT basis. This ensures that the time response of the PMTs in the entire detector is synchronized.

### 3.5. Water Property Measurement

---

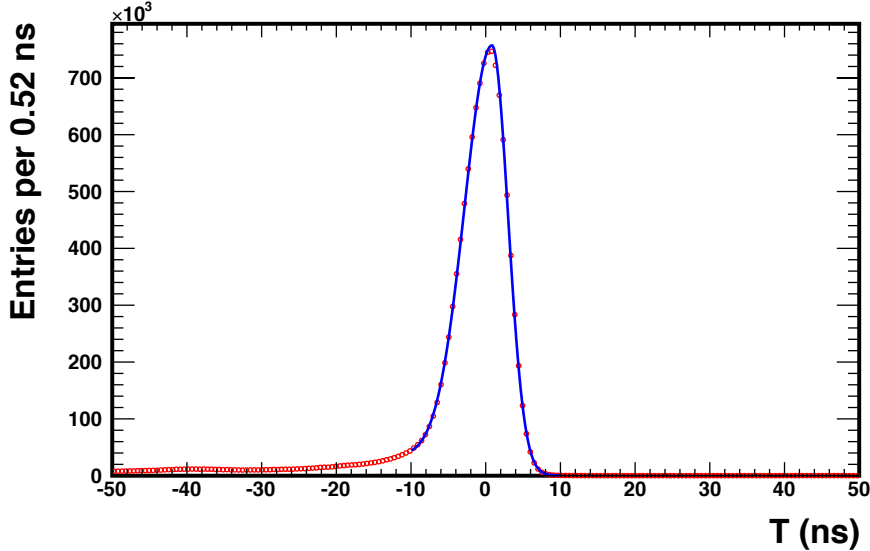


Figure 3.4: The timing distribution of ID PMTs at a charge bin  $\sim 1$  p.e., produced using hits from all PMTs. The horizontal axis represents the timing after TQ map correction, where a larger value corresponds to earlier hits. The red data points represent the data obtained from calibration, and the blue curve is the fitted asymmetric Gaussian. Figure taken from [42].

The same dataset is also used to obtain the PMT timing resolution which is put in to the detector simulation. At each charge bin, a timing distribution is produced by accumulating the hits from all PMTs after TQ map correction, and the distribution is fitted by an asymmetric Gaussian as shown in Figure 3.4. The detector simulation then simulates the PMT time response by an asymmetric Gaussian using the widths as a function of charge which is obtained from the calibration.

## 3.5 Water Property Measurement

In order to accurately model the Cherenkov photon propagation in water, an empirical model for light scattering and absorption in the detector simulation is tuned based on a calibration measurement using a laser injector.

In the detector simulation, the attenuation of light in water is characterized as  $\exp(-l/L(\lambda))$ , where  $l$  is the distance the light traveled and  $L(\lambda)$  is

### 3.5. Water Property Measurement

---

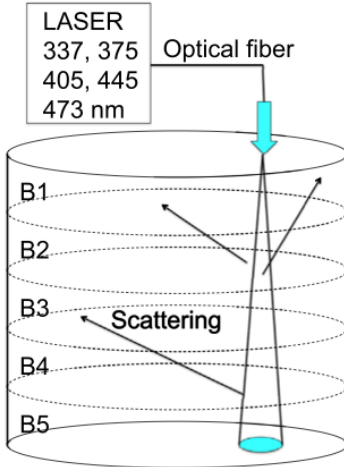


Figure 3.5: A schematic view of the laser injector system for measuring the water property and the reflectivity of the PMTs. Figure taken from [42].

a wavelength-dependent attenuation length defined as:

$$L(\lambda) = (\alpha_{\text{sym}}(\lambda) + \alpha_{\text{asy}}(\lambda) + \alpha_{\text{abs}}(\lambda))^{-1}. \quad (3.4)$$

The coefficient  $\alpha_{\text{sym}}(\lambda)$  represents the amplitude of the “symmetric scattering” which takes into account the effects from Rayleigh scattering and symmetric Mie scattering, and it has the angular distribution of the form  $1 + \cos^2 \theta$  where  $\theta$  is the photon scattering angle.  $\alpha_{\text{asy}}(\lambda)$  represents the “asymmetric scattering” which accounts for forward Mie scattering, and it has the angular dependence of  $\cos \theta$  in the forward direction while there is no backward scattering. Finally,  $\alpha_{\text{abs}}(\lambda)$  is for absorption. These coefficients are empirical functions of the wavelength  $\lambda$  which are determined based on the calibration data from a laser injector system as shown in Figure 3.5.

In the setup, a collimated laser beam is injected at the top of SK vertically down toward the bottom, and the light scattered in water and reflected from the bottom is detected by the PMTs on the barrel and the top wall of the detector. The TOF-subtracted hit time distribution, i.e. the PMT hit timing distribution after subtracting the time required for photons to travel from the beam spot at the bottom to each PMT, for the PMTs in each detector region as indicated in Figure 3.5 is shown in Figure 3.6. The sharp peaks on the right between 1830-1900 ns are due to the photons reflected at the beam spot from the bottom of the detector, whereas the hits at earlier times are caused by photons which scattered in water before reaching the bottom and arrived at the barrel or the top wall. The scattering

### 3.5. Water Property Measurement

---

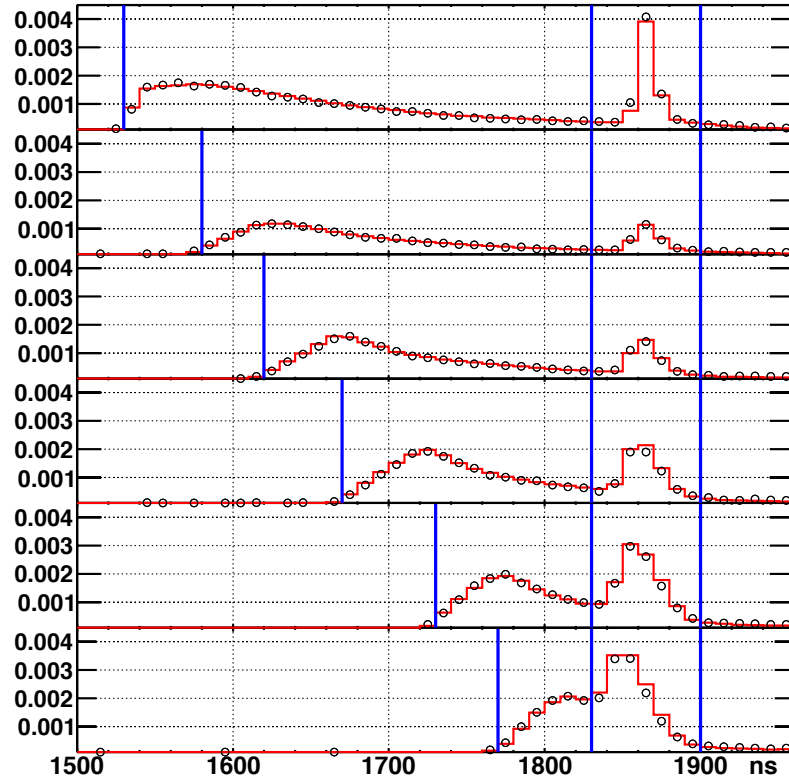


Figure 3.6: The TOF-subtracted hit time distributions for the laser injector data taken at 405 nm. The top plot is for the PMTs on the top wall, and the following five plots correspond to the the five regions on the barrel as indicated in Figure 3.5. The black circles represent the measured data and the red histograms are the result from the laser injector simulation after tuning the water properties and PMT reflectivity to data. The data before 1830 ns and between the two vertical blue lines on the left is used for the water measurement, and the data in the range 1830-1900 ns is used for tuning the PMT reflectivity. Figure taken from [42].

### 3.5. Water Property Measurement

---

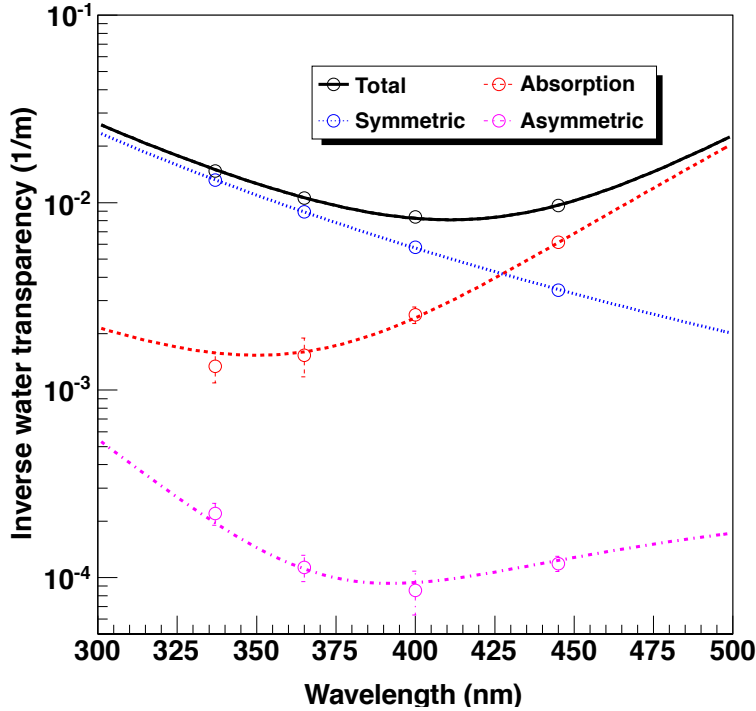


Figure 3.7: Light absorption and scattering coefficients as a function of wavelength. The data points are the data taken in April 2009, and the red, blue and magenta lines represent the tuned  $\alpha_{\text{abs}}(\lambda)$ ,  $\alpha_{\text{sym}}(\lambda)$  and  $\alpha_{\text{asy}}(\lambda)$  respectively. The black line represents the sum of the three, which is the inverse of the attenuation length  $L(\lambda)$ . Figure taken from [42].

and absorption coefficients  $\alpha_{\text{sym}}(\lambda)$ ,  $\alpha_{\text{asy}}(\lambda)$  and  $\alpha_{\text{abs}}(\lambda)$  are tuned using the latter, the data before 1830 ns, such that the tuned simulation best agrees within the model parameter space with the measured data taken at various wavelengths. Figure 3.7 shows the scattering and the absorption coefficients as functions of wavelength which are tuned using the data taken in April 2009, and the red histograms in Figure 3.6 are the timing distributions for the best-tuned laser injector simulation. The measurement leads to an overall attenuation length of  $\sim 120$  m at 400 nm wavelength. The apparatus is situated permanently in the detector and constantly takes data during the SK operation so that the water parameters can be constantly monitored. Figure 3.8 shows the time variation of the measured coefficients at various wavelengths.

### 3.6. PMT and Black Sheet Reflectivity

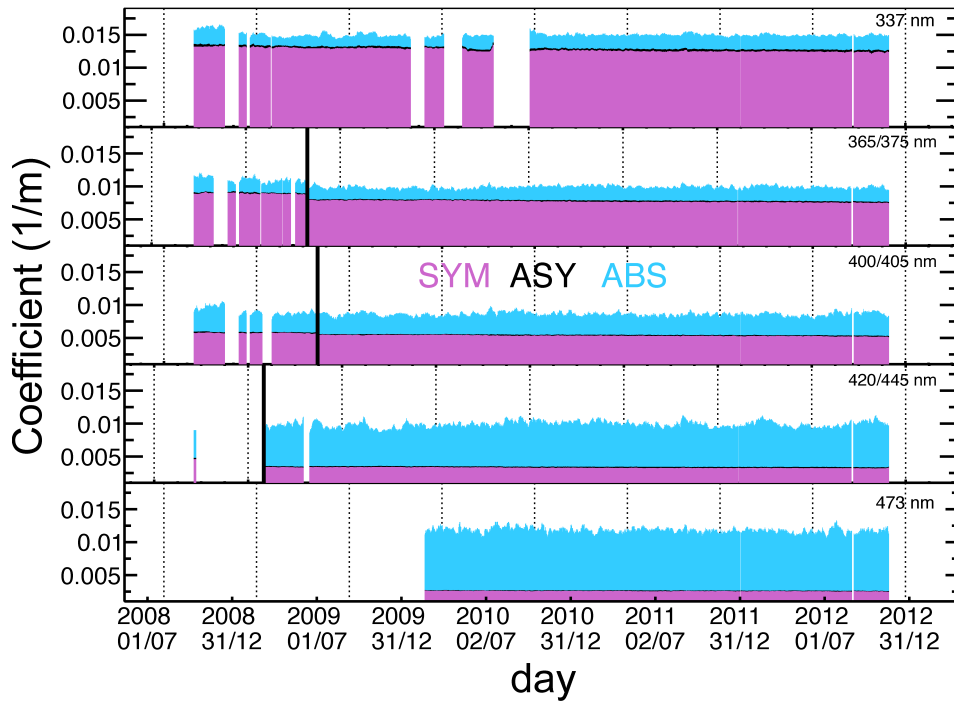


Figure 3.8: Time variation of the light absorption and scattering coefficients measured at various wavelengths. The coefficients  $\alpha_{\text{sym}}$ ,  $\alpha_{\text{asy}}$  and  $\alpha_{\text{abs}}$  are shown in purple, black and blue respectively. Some of the laser units were replaced in 2009 with some changes in the wavelength, and the vertical black lines indicate when the replacement took place. Figure taken from [42].

## 3.6 PMT and Black Sheet Reflectivity

The laser injector data used in Section 3.5 for water measurement is also used to tune the reflectivity of the PMTs in the detector simulation. Ignoring the reflections at the PMT internal structure, the detector simulation models light reflections at the PMT surface by considering the interface of four different layers: the water, the PMT glass, the photocathode and the vacuum inside the PMT. Each layer is characterized by a wavelength-dependent refractive index, and since the photocathode layer absorbs light a complex refractive index is assigned to the photocathode which is treated as an effective tuning parameter for PMT reflectivity. Using the laser injector data in the time range 1830-1900 ns which contains the peaks from the light reflected at the tank bottom as shown in Figure 3.6, the complex refractive index of the photocathode is tuned such that the laser injector simulation

### 3.7. Photosensor Test Facility

---

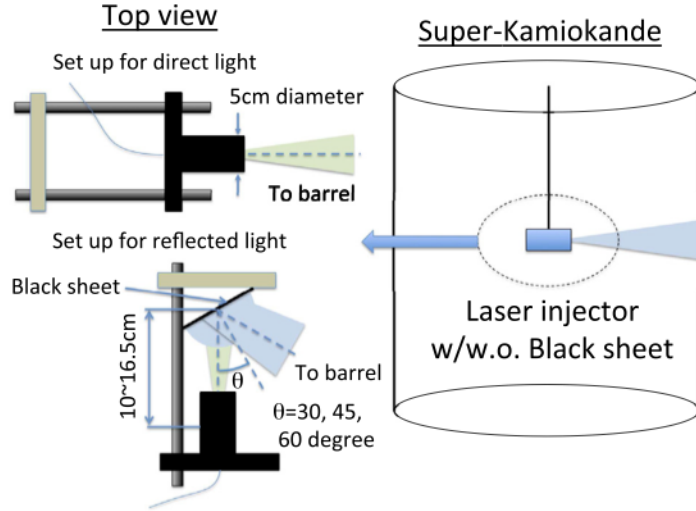


Figure 3.9: A schematic view of the apparatus for black sheet reflectivity measurement. Figure taken from [42].

best agrees with the measured data in this region. The tuning is performed at the wavelengths 337, 365, 400 and 420 nm, and the result is used when simulating physics events such as neutrinos.

The reflectivity of the black sheet is measured in the SK detector using a dedicated apparatus. As shown in Figure 3.9, a laser injector unit to which a specimen of the black sheet is attached is placed at the centre of SK, and the reflected laser from the black sheet is projected horizontally to the barrel of the ID. The intensity and the profile of the reflected light is then measured for each of the incident angles  $30^\circ$ ,  $45^\circ$  and  $60^\circ$  and for the wavelengths 377, 400 and 420 nm. The intensity of the injected light directly projected onto the wall without reflection is also measured for normalizing the reflected light data, and the reflectivity calculated from the measured result is used in the detector simulation.

## 3.7 Photosensor Test Facility

Properties of the SK PMTs have been measured over the years through various in-situ calibration measurements in SK as described above. While such methods have served well in calibrating the overall characteristics of the PMTs so far, the increasing physics data statistics and the growing complexities of physics analyses require more detailed understanding of the

### 3.7. Photosensor Test Facility

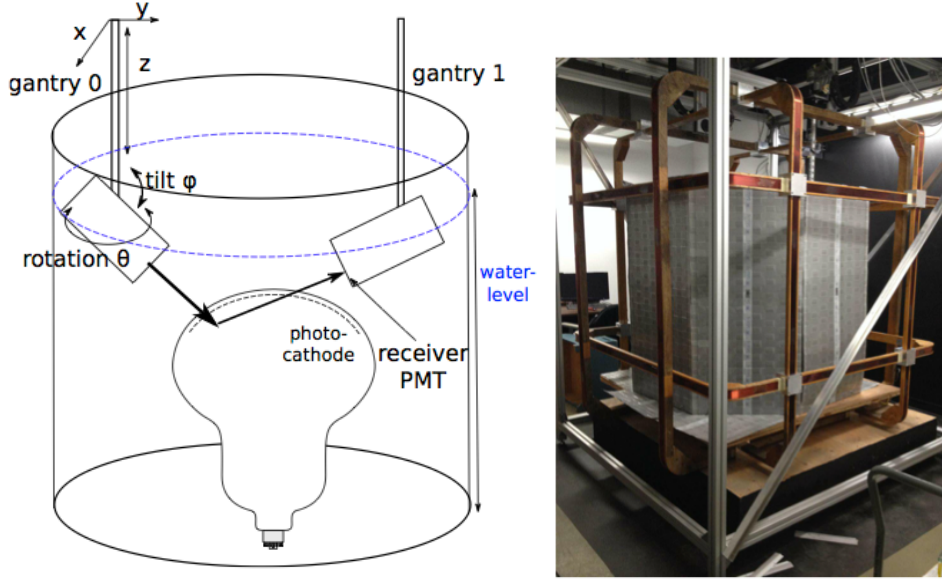


Figure 3.10: Left: A schematic drawing of the PTF, showing the water tank, mechanical arms, optical heads and the PMT which is being measured. Right: External view of the PTF magnetic field compensation system.

detector, so that we can improve the detector simulation for better data-MC agreement and also reduce the systematic uncertainties in the detector.

The Photosensor Test Facility (PTF) at TRIUMF (Vancouver, Canada) is a facility which was constructed to perform detailed ex-situ measurements of the responses and the passive optical properties of large photosensors in water. The left of Figure 3.10 shows the schematic drawing of the facility. The facility consists of a large water tank in which a 20-inch SK PMT can be placed upright and fully submerged in filtered water provided by a water purification system. An optical head unit equipped with a collimated light source is mounted on each of the two automated mechanical arms which move the optical heads with three translation and two rotation degrees of freedom with a position and direction accuracy of 1 mm and 1°. This allows the detailed measurement of the PMT response for light incident at various positions on the PMT. Each optical head is also equipped with a small receiver PMT which is used to detect reflected light, and by using both mechanical arms at the same time and receiving the light emitted by the other optical head, PMT reflectivity measurements can also be performed. Figure 3.11 shows the interior of the tank with a SK PMT submerged in

### 3.7. Photosensor Test Facility

---



Figure 3.11: A SK PMT submerged in the tank filled with water. The two black boxes are the water-tight optical head units mounted on the mechanical arms.

water, along with the optical heads.

The optical head unit is a water-tight box. Light from a pulsed laser or a Xe lamp is delivered via an optical fibre which is connected in the box to a light source unit, which collimates and linearly polarizes the light as shown in Figure 3.12. The collimated beam is then split in two by a beam splitter, one of which is projected onto the target PMT outside of the box while the other is detected by a small monitoring PMT in the box which monitors the intensity variation of the incident light. Another 18 mm square receiver PMT is placed next to the light source unit, which views out of the box and is used for reflectivity measurements.

The response of large photosensors are greatly affected by magnetic fields. In order to compensate the geomagnetic field and the field from the cyclotron at TRIUMF, active field cancellation using three-axis Helmholtz coils and passive magnetic shielding are employed as shown on the right of Figure 3.10. During a measurement, local magnetic fields are constantly monitored by a magnetometer placed in the optical head unit. Studies are ongoing to automatically tune the coil current based on real time field measurements so that the magnetic field can be reduced to  $\sim 10$  mG level, which is lower than the  $\sim 50$  mG field in SK.

### 3.7. Photosensor Test Facility

---

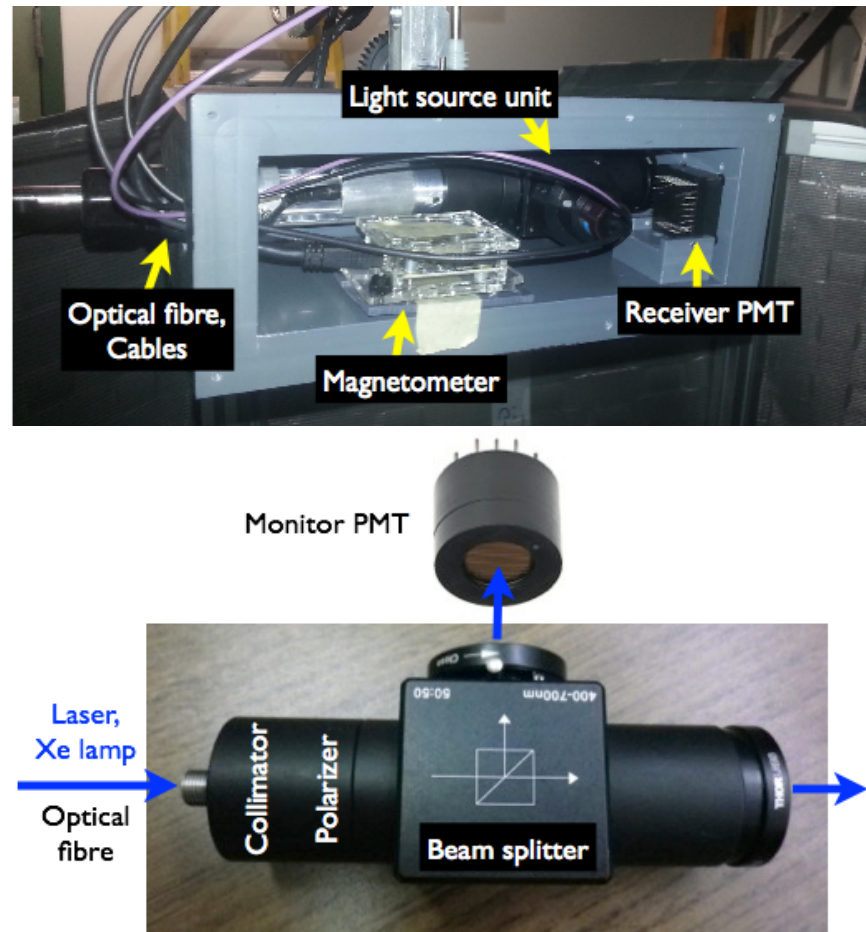


Figure 3.12: Top: The interior of the water-tight optical head box. Light is delivered via an optical fibre which is connected to the light source unit. A receiver PMT is placed next to the light source and receives the light from outside. Bottom: The light source unit, which consists of a collimator, a polarizer, a beam splitter and a monitoring PMT.

### 3.7. Photosensor Test Facility

---

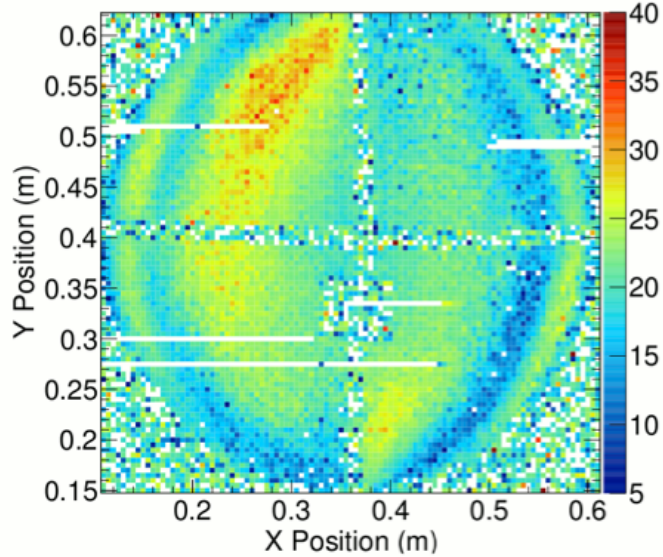


Figure 3.13: Local variations of the gain of a SK PMT. The plot shows the map of the gain variation viewing the PMT vertically down. This is a relative gain variation measurement and the colour scale is in arbitrary units. Note that the horizontal and vertical band structure crossing near the centre is produced by bands which are placed on the surface of the PMT for calibrating the position and directions of incident beam and is not the result of the characteristics of the PMT itself.

Finally, the entire apparatus is surrounded by two layers of dark curtains which produce a dark environment adequate for measuring PMT responses.

The facility has been making various measurements of different photosensors including the SK PMT, such as the measurement of local variations in the photon detection efficiencies and the gain. Figure 3.13 shows an example result of a relative gain variation measurement for a SK PMT performed in air, in which the peak position of the 1 p.e. distributions are measured by shining laser at different positions on the SK PMT. Although the results have not been incorporated into SK analyses yet, it is expected that the results from the PTF measurements will be used to improve the PMT models in the SK detector simulation and also to better understand the systematics related to detector response in near future.

## Chapter 4

# Atmospheric Neutrino Simulation

Physics analyses at Super-K are done by comparing the observed data to the predictions obtained from the Monte Carlo(MC) simulations. This chapter describes the atmospheric neutrino MC simulation which is used in the oscillation analysis. Producing the MC involves simulating the following three major components: the atmospheric neutrino flux reaching the detector, the interaction of the neutrinos with water and the response of the detector to the particles produced by the neutrino interaction.

### 4.1 Atmospheric Neutrino Flux

As the analysis of atmospheric neutrino oscillations is essentially done by investigating the change in the observed atmospheric neutrino flux at the detector due to oscillations, it is essential to have an accurate model for the production of neutrinos in the atmosphere. Super-K adopts the flux model by Honda *et al.*[43] for various analyses concerning atmospheric neutrinos, and the model is briefly described below.

The primary cosmic ray flux, which consists mostly of hydrogen nuclei, is modeled based on the measurements by AMS[44] and BESS[45][46]. The primary flux is affected by the solar wind and depending on whether the solar activity is at maximum or minimum the primary flux at  $\sim 1$  GeV varies by nearly a factor of two. The effect of the geomagnetic field manifests in the up-down and east-west asymmetry of the neutrino flux at Super-K as well as the low-energy cutoff in the flux due to the deflection of low energy primary cosmic rays out to space.

The US-standard atmosphere '76[47] is adopted as the model for the density structure of the atmosphere, and for the production of secondary cosmic ray particles in the atmosphere, DPMJET-III[48] is used for hadronic interactions above 32 GeV while for energy below 32 GeV JAM[49] is used for better agreement with low energy cosmic ray muon data. The hadron

#### 4.1. Atmospheric Neutrino Flux

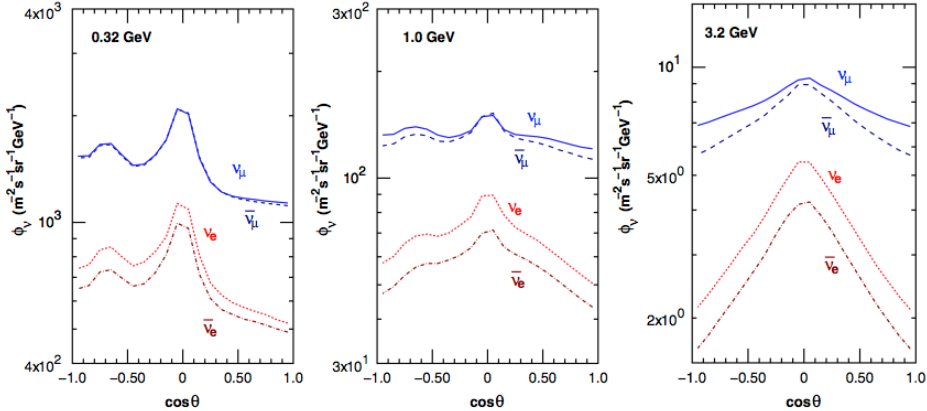


Figure 4.1: Zenith angle distributions of the atmospheric neutrino flux at Super-K averaged over the azimuth at 0.32 GeV(left), 1.0 GeV(middle) and 3.2 GeV(right).  $\cos\theta=1$  represents vertically downward going and  $\cos\theta=-1$  represents vertically upward going neutrinos. Figure taken from [43].

production models are further tuned based on the cosmic ray muon measurements at various altitudes such as [46], [50] and [51]. During the flux calculation the trajectories of the cosmic ray particles in the atmosphere are fully simulated in three-dimensions.

Figure 4.1 shows the zenith angle distributions of the atmospheric neutrino flux at Super-K calculated by the Honda model. The flux is peaked at the horizon largely since the cosmic ray particles can travel longer distances in the atmosphere horizontally rather than vertically, allowing more time for decay. The large up-down asymmetry as seen in the left plot is due to the geomagnetic field, and the effect gets smaller at higher energies since higher energy cosmic rays are affected less by the geomagnetic field.

Figure 4.2 shows the direction-averaged neutrino flux at Super-K as a function of energy. The plots compare the predictions from the Honda model with other flux models such as the Fluka model[52] and the Bartol model[53], which have differences in hadronic interaction simulations and particle trajectory calculations as well as the cosmic ray dataset the models are tuned to. The differences in the flux predictions between the models are used to estimate the systematic uncertainties related to the atmospheric neutrino flux.

The MC events are generated using the predicted flux at Super-K without considering any neutrino oscillations, i.e., assuming that all neutrinos

## 4.2. Neutrino Interaction

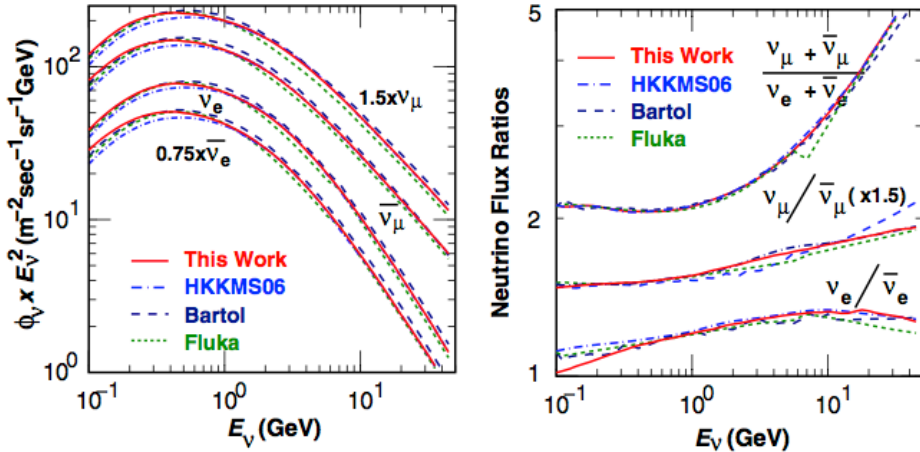


Figure 4.2: The direction-averaged atmospheric neutrino flux at Super-K as a function of energy. The left plot is the absolute flux and the right plot is the various flux ratios. Red represents the Honda flux model which is used in the Super-K MC, and predictions from other models are used for estimating the systematic uncertainties for the flux. Figure taken from [43].

reach the detector in their original flavour at the production in the atmosphere. Oscillations are applied at the time of performing an analysis by reweighting each MC event according to its oscillation probability based on the neutrino energy and direction, and the procedure is discussed in more detail in Section 8.3.1.

## 4.2 Neutrino Interaction

As stated in Section 2.2, neutrinos are detected at Super-K when they interact with the water in the detector. Neutrino interactions at Super-K are simulated by the neutrino event generator NEUT[54]. The software simulates the interaction of neutrinos with oxygen and hydrogen nuclei in water, while the interactions with electrons are neglected in atmospheric neutrino simulations due to the three orders of magnitude smaller cross sections relative to that for nuclei.

Neutrino interactions can be categorized into Charged Current (CC) and Neutral Current (NC) interactions. A CC interaction happens when a neutrino interacts with a target by exchanging a  $W^\pm$  boson producing a charged lepton whose flavour corresponds to that of the neutrino. Since the

flavour of the charged lepton, i.e. electron or muon, can be identified in Super-K as it will be discussed in Chapter 6, one can identify the flavour of the incoming neutrino in a CC event, which is important in observing the effects from neutrino flavour change in an oscillation analysis. On the other hand, a NC interaction is mediated by a  $Z^0$  boson in which case the outgoing lepton is also a neutrino and does not leave any clear signal in the detector concerning the flavour. The NC events are therefore in general considered as backgrounds in atmospheric neutrino oscillation analyses.

Although the original neutrino flux produced in the atmosphere only contains electron and muon neutrinos, tau neutrinos are also detected at Super-K because of oscillations. Due to the large  $1.78 \text{ GeV}/c^2$  rest mass of the tau lepton  $\nu_\tau$  CC interactions only occur at energies above several GeV, resulting in a significantly smaller number of produced events compared to  $\nu_e$  and  $\nu_\mu$ . Nevertheless,  $\nu_\tau$  interactions are simulated in the same manner as  $\nu_e$  and  $\nu_\mu$  CC interactions by NEUT. The produced tau leptons undergo complex decays into multiple mesons and leptons which are simulated by TAUOLA[55].

The neutrino interaction modes which are simulated by NEUT are summarized in the following, and the cross sections as functions of energy for the dominant interaction modes are shown in Figure 4.3. Except for meson exchange currents, each interaction mode is modeled for both CC and NC. In addition to the initial interaction of the incident neutrino with the target nucleus, NEUT also simulates the subsequent interaction of the produced particles within the nucleus, which is described in Section 4.2.5.

### 4.2.1 Elastic and Quasi-Elastic Scattering

NC elastic scattering is a process in which a neutrino simply scatters off a nucleon target by transferring some momentum without producing any new particles. Quasi-elastic (QE) scattering is an equivalent process for a CC interaction in which case the incident neutrino is converted into a corresponding charged lepton while the target nucleon also converts in order to preserve the total electric charge. For example, a  $\nu_\mu$  CCQE interaction is the following process:

$$\nu_\mu + n \rightarrow \mu^- + p. \quad (4.1)$$

In NEUT, such interactions on a free nucleon target are simulated by the Llewellyn-Smith model[58], and for a nucleon bound in an oxygen nucleus the relativistic Fermi gas model by Smith and Moniz[59] is used in order to take into account the Fermi motion and the Pauli blocking of the nucleon. The model contains a form factor which is characterized by the axial vector

## 4.2. Neutrino Interaction

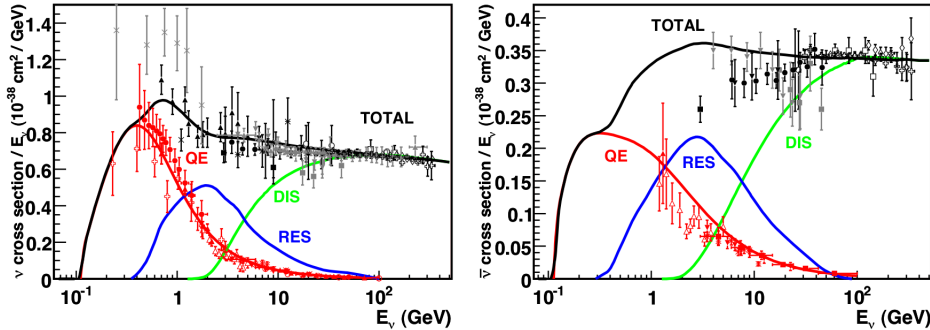


Figure 4.3:  $\nu_\mu$ (left) and  $\bar{\nu}_\mu$ (right) CC cross sections per nucleon divided by neutrino energy, plotted as a function of energy. Experimental data summarized in [56] is compared to the predictions from NEUT, and the contributions from quasi-elastic scattering(QE), resonance production(RES) and deep inelastic scattering(DIS) are shown separately in different colours. Figure taken from [57].

mass parameter  $M_A^{QE}$ , and the shape of the differential cross section as a function of  $Q^2$ (square of the four-momentum transfer) as well as the total cross section depend on the parameter.  $M_A^{QE}$  is set to 1.21 GeV/ $c^2$  based on the results from K2K[60] and MiniBooNE[61].

### 4.2.2 Meson Exchange Current

In the CCQE interaction on a bound nucleon described above, an approximation is made such that a neutrino interacts with a single nucleon only while neglecting any direct correlations between the nucleons in the nucleus. However, in reality the interactions among the nucleons must introduce some direct correlations such that an incident neutrino interacts simultaneously with multiple nucleons. The tension observed between the existing CCQE model and the data from experiments such as MiniBooNE[61] also suggests the existence of such process, and multi-nucleon correlations have been a growing interest in the field of neutrino research in the past several years.

The Meson Exchange Current(MEC) model by Nieves *et al.*[62] is one of the prominent models which attempt to go beyond the preexisting simplistic model of CCQE, and their model has been recently introduced to NEUT. In the simulated process, the incident neutrino interacts with a pair of two nucleons as opposed to a single nucleon target as:

$$\nu_\alpha + NN' \rightarrow l_\alpha + N''N''', \quad (4.2)$$

## 4.2. Neutrino Interaction

---

where  $NN'$  and  $N''N'''$  are the nucleon pair before and after the interaction.

Although multi-nucleon correlations should in principle be present in any neutrino interactions on a bound nucleon, the CC MEC interaction mentioned above is the only such process which is considered in NEUT at the present moment.

### 4.2.3 Single Meson Production

Production of a single meson in a neutrino interaction is modeled in NEUT primarily as a resonance production, in which a baryon resonance excitation produces a single meson in the final state as in:

$$\nu_\alpha + N \rightarrow l_\alpha + N^* \rightarrow l_\alpha + N' + m, \quad (4.3)$$

where  $N$  and  $N'$  are the nucleon in the initial and the final state,  $N^*$  is the intermediate baryon resonance and  $m$  is a meson such as  $\pi$ ,  $K$  and  $\eta$ .  $l_\alpha$  is the outgoing lepton which is a charged lepton for CC interaction while it is a neutrino for NC. Such interaction is considered in NEUT for  $W < 2 \text{ GeV}/c^2$ , where  $W$  is the invariant mass of the hadronic final state. The simulation is done adopting the Rein-Sehgal model[63] with the revised form factor by Graczyk and Sobczyk[64], and the parameters characterizing the form factor were determined using bubble chamber data[65][66].

Coherent pion production is also considered, in which the incident neutrino interacts with the entire oxygen nucleus producing a pion:

$$\nu_\alpha + {}^{16}\text{O} \rightarrow l_\alpha + {}^{16}\text{O} + \pi. \quad (4.4)$$

Due to the low momentum transfer in this process the outgoing lepton and pion produced through this mechanism are peaked in the forward direction. The interaction is simulated according to the model by Rein and Sehgal[67].

### 4.2.4 Deep Inelastic Scattering

In deep inelastic scattering (DIS), the incident neutrino interacts with a constituent quark in the target nucleon and often produce multiple hadrons. In NEUT the process is considered for the cases with hadronic invariant mass  $W > 1.3 \text{ GeV}/c^2$  and becomes increasingly dominant in multi-GeV energies. The nucleon structure functions used in the model are based on the GRV98 parton distribution functions[68], and the corrections by Bodek and Yang[69] are applied in order to use the model in the low  $Q^2$  region.

## 4.2. Neutrino Interaction

---

For  $W < 2 \text{ GeV}/c^2$ , only pions are considered as outgoing hadrons, and pion multiplicity in this region is estimated from bubble chamber experiments [70][71]. Since there is an overlap with the resonance pion production in this region, only the cases of producing two or more pions are considered in the DIS channel for  $W < 2 \text{ GeV}/c^2$ . For  $W > 2 \text{ GeV}/c^2$ , production of heavier mesons such as  $K$  and  $\eta$  are also considered and the hadronic final states are determined by PYTHIA/JETSET[72].

### 4.2.5 Final State Interaction

When a neutrino interaction happens in a nucleus, the hadrons which are produced at the initial interaction must propagate through the nuclear medium before getting detected outside of the nucleus, and during such time the hadrons often interact hadronically with the nuclear medium. Such interactions are referred to as final state interactions (FSI) and it is an important effect for neutrino analyses at Super-K since it directly alters the observable particle final state from what is initially produced at the neutrino interaction. NEUT considers the FSI for mesons and nucleons, and for nucleons[73] and heavy mesons such as  $K$ [74][75][76] and  $\eta$ [77] the FSI is simulated based on the cascade models and external data.

The hadrons which are most frequently seen at Super-K are, by far, the pions, and it is therefore important to accurately model the FSI for pions. Pion FSI is simulated by the NEUT pion cascade model[78] in which pions are propagated classically in finite steps through a nuclear medium described by the Woods-Saxon nuclear density profile[79]. At each step, a pion may undergo the following processes according to the interaction probabilities given in the model: quasi-elastic scattering in which a single pion of the same charge remains after the interaction, charge exchange in which a charged pion is converted into a  $\pi^0$  and vice versa, pion absorption in which no pions remain after the interaction and pion production in which multiple pions are produced. The model has been tuned based on various pion-nucleon and pion-nucleus scattering data, and Figure 4.4 shows the tuned  $\pi^+ - {}^{12}\text{C}$  scattering cross section simulated in NEUT compared with experimental data. The uncertainty in the model is evaluated by comparing the model variations against pion scattering data. As shown in Figure 4.5, by simultaneously varying the FSI model parameters and comparing the resulting cross sections against various pion scattering data, representative parameter sets are chosen which span a “ $1\sigma$  error surface” on the multi-dimensional FSI model parameter space. There are in total six model parameters which characterize the interaction probabilities for quasi-elastic scattering, charge

### 4.3. Detector Simulation

---

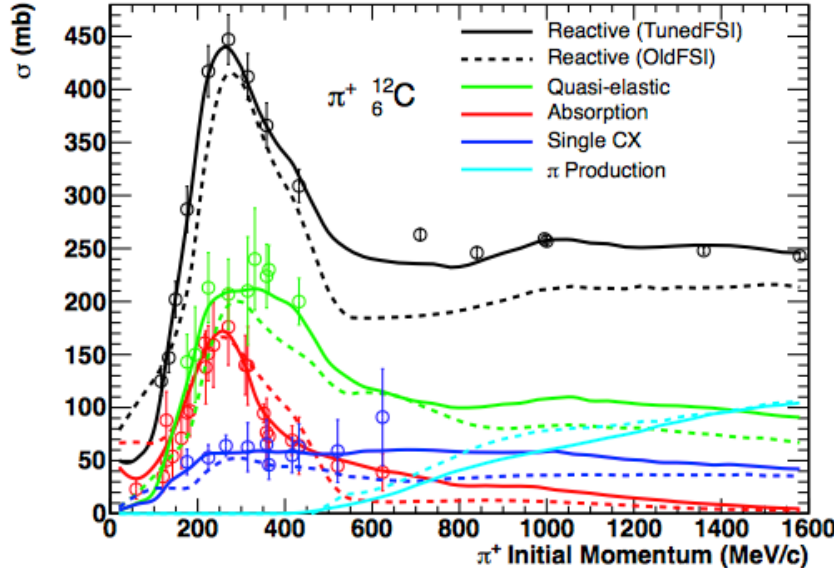


Figure 4.4:  $\pi^+ - {}^{12}\text{C}$  scattering cross sections, where the cross section for each interaction process is shown separately in the colour described in the legend. The data points are the measured results from  $\pi^+ - {}^{12}\text{C}$  scattering experiments and the solid lines are the cross sections calculated by the tuned NEUT pion cascade model. The dashed lines are for the previous NEUT pion FSI model. Figure taken from [78].

exchange, absorption and pion production in two energy ranges(pion momentum of below or above 500 MeV/ $c$ ), and 16 representative parameter sets are obtained as the  $1\sigma$  variations[80].

### 4.3 Detector Simulation

The particles which are produced by NEUT are then propagated in the detector by a GEANT3[81]-based detector simulation called SKDETSIM. GEANT simulates the interaction of the particles with water, particle decays as well as the production of Cherenkov photons. Hadronic interactions are simulated by GCALOR[82] except for the pions below 500 MeV/ $c$  for which the NEUT pion cascade model described in Section 4.2.5 is used.

The Cherenkov photons produced by the particles are then propagated in the detector using a custom code which models the scattering and absorption

### 4.3. Detector Simulation

---

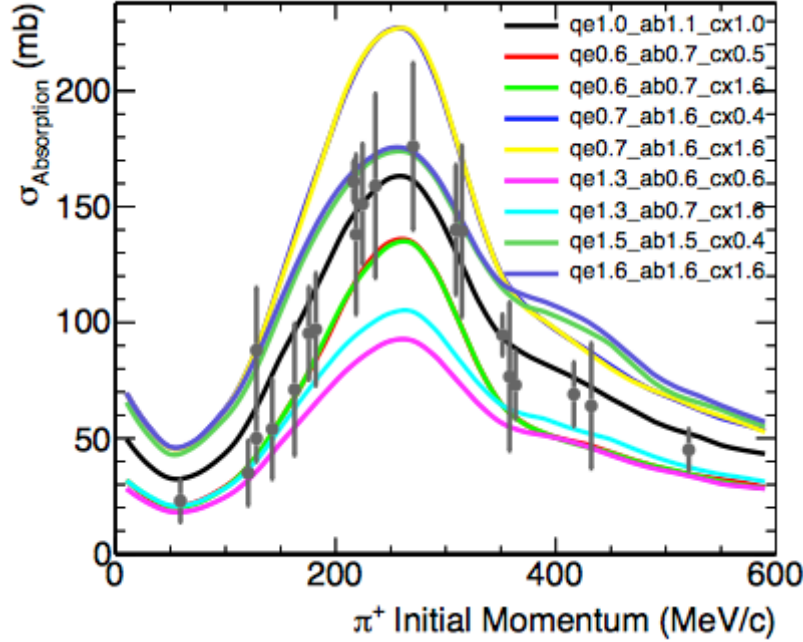


Figure 4.5: Low momentum  $\pi^+$  absorption cross sections compared between experimental data and the variations of the NEUT pion cascade model. In the figure, the interaction probabilities for quasi-elastic(qe), absorption(ab) and charge exchange(cx) for pions  $< 500$  MeV/ $c$  are simultaneously varied in NEUT, and the resulting cross sections for eight representative variations of the parameter set are shown in different colours. Figure taken from [78].

of light in water based on the calibration results in Section 3.5. Reflectivity of the PMT and the black sheet are also modeled using the results obtained in Section 3.6.

The charge and time response of the PMTs and the electronics are also simulated based on the calibration measurements, and the detector simulation at the end provides the same data structure as the observed data so that the two can be analyzed in the same manner.

# Chapter 5

## Data Reduction

While SK detects roughly 10 atmospheric neutrino events each day, the high-energy event trigger is fired  $\mathcal{O}(10^6)$  times per day, most of which are due to background events caused by cosmic ray muons, radioactivity and noise from the electronics. In order to remove such backgrounds and select the neutrino events for physics analyses, a series of reduction cuts are applied to the observed data.

The events which are targeted in the neutrino oscillation analysis presented in Chapter 8 are the atmospheric neutrinos which interact with the water in the ID, whose daughter particles are then detected as Cherenkov rings by the ID PMTs with high resolution. Such neutrino events can be classified into two categories based on the activity in the OD: an event is categorized as Fully-Contained(FC) if all produced particles stop within the ID and leave no signals in the OD, whereas it is categorized as Partially-Contained(PC) if any of the daughter particles exit to the OD and leave signals there. The FC event sample has large statistics and since all the Cherenkov photons are deposited in the ID the events can be precisely reconstructed and used in physics analyses. The oscillation analysis in Chapter 8 therefore uses the FC atmospheric neutrino data, and the procedures to select the FC events are described in the following. The selection process consists of a series of five data reduction stages which gradually eliminate the backgrounds in data.

### 5.1 First and Second Reduction

The first two stages of the reduction process are designed to quickly filter out the obvious backgrounds from cosmic ray muons, electrical noise and low energy backgrounds such as those caused by radioactivity.

In the first reduction, events whose total charge from the ID PMTs is less than 200 p.e. are rejected as low energy backgrounds. This threshold roughly corresponds to the charge deposited by a 22 MeV/ $c$  electron. As will be mentioned later, only the events with energy greater than that of a 30 MeV/ $c$  electron are used in the oscillation analysis, and this cut removes

### 5.2. Third Reduction

---

the majority of low energy backgrounds while keeping the targeted neutrino events. In addition, in order to reject cosmic ray muons which usually leave signals in the OD, events with more than 50 OD hits within a 800 ns time window around the event trigger are rejected.

In the second reduction, the threshold for the above OD activity cut is lowered to 30 OD hits for events with the total ID charge less than 100,000 p.e. so that lower energy muons can be further reduced. Furthermore, an event is rejected if more than half of the total ID charge originates from a single PMT. This cut is intended to reject low energy events which are caused by electrical noise such as a discharge in a PMT.

After the first and the second reduction the number events reduces to  $\sim$ 200 events/day, which is already more than three orders of magnitude reduction from the initial dataset defined by the high-energy triggers.

## 5.2 Third Reduction

The third reduction targets several specific background sources which cannot be removed by the first two reduction stages.

One of the major remaining backgrounds are the cosmic ray muons which enter from outside of the detector but leave low activity in the OD. In order to remove through-going muons which enter and exit the detector, the remaining events are processed by the through-going muon fitter which is a fast algorithm to reconstruct the entering and the exiting point on the ID wall assuming a muon. Once the events are reconstructed, a goodness of fit is evaluated based on the deviation of the observed PMT hit timings from the predictions assuming a through-going muon, and events which agree well with the muon hypothesis get rejected. In addition to the cut based the goodness of fit, events which have more than 9 OD hits within 8m from the estimated entrance or exit points are also rejected. Similar rejection methods are also applied assuming a stopping muon which is a muon entering the detector but stopping within the ID.

Another type of a muon background is the cable hole muons. At the top of the SK detector there are twelve holes where the bundles of signal and high voltage cables for the PMTs go through, and cosmic ray muons can enter the detector through the holes without leaving any signals in the OD. Such muons are rejected based on the signals from the plastic scintillation counters installed on top of the holes and whether the estimated entering point is within 4 m from a cable hole.

In order to reduce the remaining low energy backgrounds, events are

### 5.3. Fourth Reduction

---

rejected if they have less than 50 hits within a 50 ns time window in the the time-of-flight corrected hit time distribution. The time-of-flight correction is done using a vertex roughly estimated using the hit time information. The cut threshold corresponds to the energy equivalent to a 9 MeV/c electron.

A flasher PMT event is an event caused by an electrical discharge in a PMT. To reduce such background, an event is rejected if the minimum number of ID hits in a 100 ns time window sliding from 300 ns to 800 ns after the event trigger is greater than 19. Since flasher PMT events typically have broader hit timing distributions compared to real particle events, events having a long tail in the hit timing distribution are rejected by this cut.

After the third reduction the number events reduces to  $\sim$ 45 events/day.

## 5.3 Fourth Reduction

The fourth reduction employs a pattern matching algorithm to remove the remaining flasher PMT events. As flasher PMT events tend to repeat with similar PMT hit patterns, correlations of the charge pattern is calculated between different events. For a given event the charge correlation is calculated between the 10,000 events neighboring in time, and events with high correlations are rejected.

The event rate after the fourth reduction is  $\sim$ 18 events/day.

## 5.4 Fifth Reduction

The fifth reduction is designed to reject the remaining cosmic ray muon and flasher PMT events.

A cosmic ray muon whose momentum is near the Cherenkov threshold may not issue an event trigger by itself, but instead its decay electron can be detected as an event. Such events are rejected if there are more than 9 OD hits per 200 ns during any time between 8800 ns and 100 ns before the event trigger.

Further reduction of flasher PMT events are done by requiring tighter criteria for the tails in the hit timing distribution compared to the cut in the third reduction. This is done by using the time-of-flight corrected hit time based on the reconstructed vertex rather than the raw hit times.

Approximately 16 events/day remain after the fifth reduction.

## 5.5 Final FC Selection

After the five reduction stages are applied, the final FC event sample for physics analyses are selected by requiring the following:

- Number of hit PMTs in the largest OD hit cluster is less than 16.
- Visible energy is greater than 30 MeV.
- Reconstructed vertex position is more than 2 m away from the ID wall.

The first cut ensures that the OD activity is low enough that it can be classified as an FC event rather than PC. Atmospheric neutrino analyses only use the events with energy greater than that of a 30 MeV/ $c$  electron as the atmospheric neutrino flux falls off at such low energy, and the second cut is applied to reject any potential low energy events which are not relevant. The third cut is the fiducial volume(FV) cut which defines a 22.5 kt fiducial volume of the SK detector. The visible energy and the vertex is obtained using the event reconstruction algorithm described in Chapter 6 and more details can be found there as well as in Section 8.1.1.

The remaining backgrounds after the five reduction stages are mostly cosmic ray muons and flasher events, both of which are then largely rejected by the FV cut since they both originate on the ID wall. The background contamination in the final selected FC sample is estimated to be  $\sim 0.1\%$  based on the eye-scan of the selected events.

The overall efficiency of the FC sample selections for the true neutrino events which happen in the FV is estimated to be greater than 98% based on the simulation, and the average observation rate of the final FC sample is  $\sim 8$  events/day.

# Chapter 6

## Event Reconstruction

In order to use the observed events in physics analyses, one needs to reconstruct the type of the particles within an event as well as their kinematics. This chapter describes the event reconstruction algorithm which is used as an input for the oscillation analysis. The algorithm, named fiTQun, employs a maximum likelihood method using the charge and time information that is observed by the PMTs to reconstruct particle types and kinematics in the detector. The algorithm is based on the methods which are developed for the MiniBooNE experiment[83], but is developed from scratch for Super-K with additional features such as the advanced multi-ring reconstruction.

In the following, Sections 6.1 to 6.4 describe the core algorithm of the fiTQun maximum likelihood event reconstruction, and the subsequent sections detail the practical procedures of reconstructing Super-K events.

### 6.1 Likelihood Function

The basis of the fiTQun reconstruction algorithm is the likelihood function. Let  $\mathbf{x}$  denote a particle event hypothesis, which specifies the type of the particles in the event as well as their vertices and kinematics. An event in Super-K contains the information on which PMTs registered a hit, and for PMTs that were hit the integrated charge as well as the time of the first photon arrival are also provided. Using such observed information, one can construct the following likelihood function given the hypothesis  $\mathbf{x}$ :

$$L(\mathbf{x}) = \prod_j^{\text{unhit}} P_j(\text{unhit}|\mathbf{x}) \prod_i^{\text{hit}} \{1 - P_i(\text{unhit}|\mathbf{x})\} f_q(q_i|\mathbf{x}) f_t(t_i|\mathbf{x}). \quad (6.1)$$

In this equation, the index  $j$  runs over all PMTs which did not register a hit, and for each such PMT the unhit probability  $P_j(\text{unhit}|\mathbf{x})$  which is the probability the PMT does not register a hit given hypothesis  $\mathbf{x}$  is multiplied. For the PMTs which did register a hit, the hit probability as well as the charge likelihood and the time likelihood are multiplied, where  $q_i$  and  $t_i$  represent the observed charge and time respectively. The charge likelihood

## 6.2. Predicted Charge

---

$f_q(q_i|\mathbf{x})$  is a conditional probability density function of observing charge  $q_i$  at the  $i$ -th PMT given hypothesis  $\mathbf{x}$  provided that the PMT registered a hit. Similarly, the time likelihood  $f_t(t_i|\mathbf{x})$  is the probability density for a hit being produced at time  $t_i$ , given  $\mathbf{x}$ . Once the likelihood function is defined, one can look for the hypothesis  $\mathbf{x}$  which maximizes  $L(\mathbf{x})$  and use that in physics analyses as the estimate for the particle configuration in the event.

## 6.2 Predicted Charge

In practice, when calculating the likelihood, the process of particle and optical photon propagation are decoupled from the response of the PMTs and the electronics by introducing the predicted charge  $\mu_i$ , which is the mean number of photoelectrons that are produced at the  $i$ -th PMT given a hypothesis.  $\mu_i$  explicitly depends on the hypothesis  $\mathbf{x}$ , and Equation 6.1 is then rewritten using  $\mu_i$  as

$$L(\mathbf{x}) = \prod_j^{\text{unhit}} P_j(\text{unhit}|\mu_j) \prod_i^{\text{hit}} \{1 - P_i(\text{unhit}|\mu_i)\} f_q(q_i|\mu_i) f_t(t_i|\mathbf{x}), \quad (6.2)$$

where the unhit probability and the charge likelihood now depend on  $\mathbf{x}$  only through the predicted charge.  $P_i(\text{unhit}|\mu_i)$  and  $f_q(q_i|\mu_i)$  are purely the properties of the PMTs and the electronics and do not explicitly depend on the processes of Cherenkov photon emission and propagation.

Likelihood evaluation is then performed in two steps: for a given hypothesis  $\mathbf{x}$  the predicted charge  $\mu_i$  for each PMT is first calculated, and using the calculated  $\mu_i$  and the observed information the likelihood function Equation 6.2 is evaluated. For a given single particle hypothesis the predicted charge contribution from direct and indirect light are calculated separately, and the sum of the two is used in likelihood calculation. For a multi-particle hypothesis, predicted charge is first calculated separately for each particle in the hypothesis, and then the sum of the predicted charge from all the particles are used in evaluating Equation 6.2. The method for predicted charge calculation for a single particle is described in the following.

### 6.2.1 Predicted Charge from Direct Light

The predicted charge from direct light produced by a single particle is expressed as an integral along the particle track:

$$\mu^{\text{dir}} = \Phi(p) \int ds g(p, s, \cos \theta) \Omega(R) T(R) \epsilon(\eta), \quad (6.3)$$

## 6.2. Predicted Charge

---

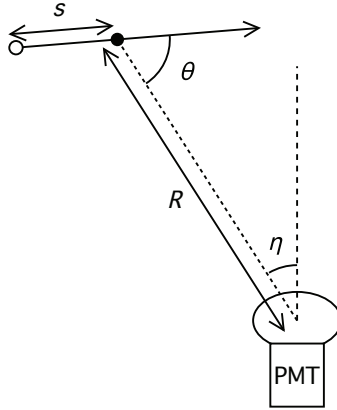


Figure 6.1: Schematic diagram describing the variables relevant to predicted charge calculation. The white dot is the initial position of the particle.

where  $s$  is the distance the particle traveled along the track from its initial position.  $p$  is the initial momentum of the particle, and variables  $R, \theta, \eta$  characterize the relative orientation of the particle and the PMT in concern which are all functions of  $s$ , as described in Figure 6.1. The following sections describe each of the following factors which appear in the above equation:  $\Phi$  which represents the photon yield, the Cherenkov emission profile  $g$ , the PMT solid angle factor  $\Omega$ , the light transmission factor  $T$  and the PMT angular acceptance  $\epsilon$ .

### 6.2.2 Cherenkov Emission Profile

The Cherenkov emission profile  $g(p, s, \cos \theta)$  describes the number of photons emitted per unit track length per unit solid angle at angle  $\theta$  with respect to the particle direction, at the instance when the particle with initial momentum  $p$  has traveled a distance  $s$  along the particle track.  $g(p, s, \cos \theta)$  is normalized such that

$$\int g(p, s, \cos \theta) ds d\Omega = 1. \quad (6.4)$$

For each particle type, the profiles are generated at a range of discrete initial momentum values using particle gun MC, which is produced by injecting a single particle in the GEANT3-based detector simulation(SKDETSIM) mentioned in Section 4.3. Representative distributions of the Cherenkov profile for electrons and muons are shown in Figures 6.2 and 6.3. When producing the profile, event-by-event randomness due to multiple scattering

## 6.2. Predicted Charge

---

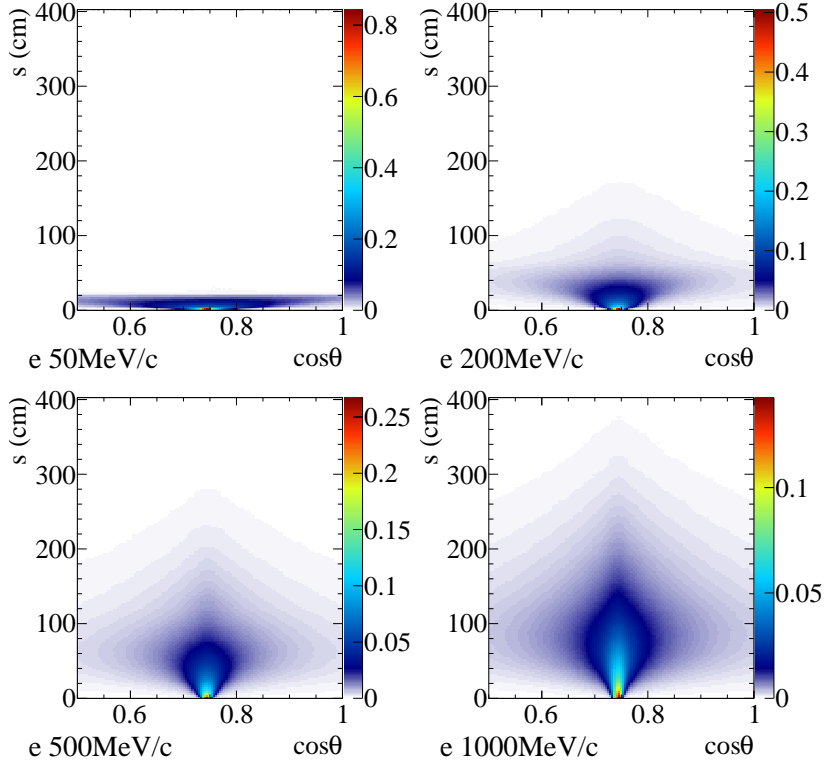


Figure 6.2: Cherenkov emission profile  $g(p, s, \cos\theta)$  for electrons at different initial momentum. Horizontal axes represent the cosine of the angle from the particle direction, and vertical axes are the distance traveled from the initial position of the particle.

etc. is averaged over. It can be seen in the figure that photon emission for electrons are peaked at  $\cos\theta \approx 0.75$  which corresponds to the opening angle of the Cherenkov cone from a particle travelling at the velocity  $\beta = 1$  in water, regardless of the momentum. Also, electromagnetic showers caused by electrons produce rather broad angular distributions. For muons on the other hand, the angular distribution of photon emission is much sharper and depends much stronger on momentum compared to electrons, and we see the collapse of the Cherenkov cone as the particle travels and loses its momentum. Such differences in the emission profile between different particle types provide particle identification capability, which will be discussed in more detail in later sections.

The factor  $\Phi(p)$  is a normalization factor which is proportional to the

## 6.2. Predicted Charge

---

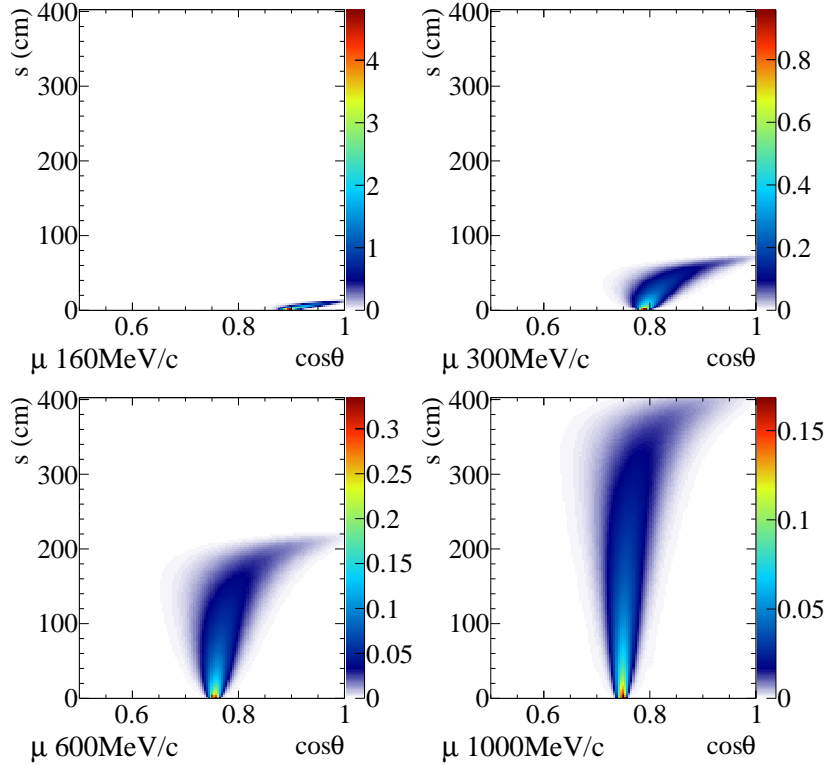


Figure 6.3: Cherenkov emission profile  $g(p, s, \cos \theta)$  for muons at different initial momentum. Horizontal axes represent the cosine of the angle from the particle direction, and vertical axes are the distance traveled from the initial position of the particle.

average total number of photons that are emitted by a particle with initial momentum  $p$ .  $\Phi(p)$  also absorbs the constant factors that are not accounted for by other factors in Equation 6.3 such as the quantum efficiencies of the PMTs, and enforces proper normalization to the predicted charge.

### 6.2.3 Solid Angle Factor

$\Omega(R)$  represents the solid angle subtended by a PMT viewed from its normal direction at distance  $R$ . In order to reduce computation time, the factor is simply approximated as the area of a circle normalized by the distance:

$$\Omega(R) = \frac{\pi a^2}{R^2 + a^2}, \quad (6.5)$$

## 6.2. Predicted Charge

---

where  $a = 25.4$  cm is the radius of the PMT. The approximation holds sufficiently well at distance  $R > 1$  m.

### 6.2.4 Light Transmission Factor

$T(R)$  is the attenuation factor of direct light due to absorption and scattering in water, and it is written as

$$T(R) = \exp(-R/L^{\text{att}}), \quad (6.6)$$

where  $L^{\text{att}}$  is the wavelength-averaged attenuation length for Cherenkov radiation. The attenuation length is obtained from the detector simulation and its value for SK-IV is 7496.46 cm.

### 6.2.5 PMT Angular Acceptance

$\epsilon(\eta)$  is the PMT angular acceptance, which is a function of the angle  $\eta$  between the PMT normal and the direction of the particle position viewed from the PMT. Figure 6.4 is the acceptance curve obtained from the detector simulation, which also includes the effect of the shadowing by neighboring PMTs at high incident angle. The distribution is fitted with a joint polynomial as indicated by the solid line in the figure, and the fit function is used as  $\epsilon(\eta)$  in event reconstruction. We adopt a normalization condition  $\epsilon(\eta = 0) = 1$ .

### 6.2.6 Predicted Charge from Indirect Light

In addition to direct light which was just discussed, indirect light must also be taken into account in order to properly predict the amount of charge deposited at each PMT. This includes the light scattered in water as well as the reflected light coming from detector components such as the black sheet and PMTs themselves. Similar to Equation 6.3 for direct light, the predicted charge from indirect light is written as

$$\mu^{\text{sct}} = \Phi(p) \int ds \frac{1}{4\pi} \rho(p, s) \Omega(R) T(R) \epsilon(\eta) A(s), \quad (6.7)$$

where

$$\rho(p, s) \equiv \int g(p, s, \cos \theta) d\Omega \quad (6.8)$$

is the fraction of photons emitted per unit track length, at position  $s$  along the particle trajectory. When the factor  $A(s)$  is removed from Equation 6.7,

## 6.2. Predicted Charge

---

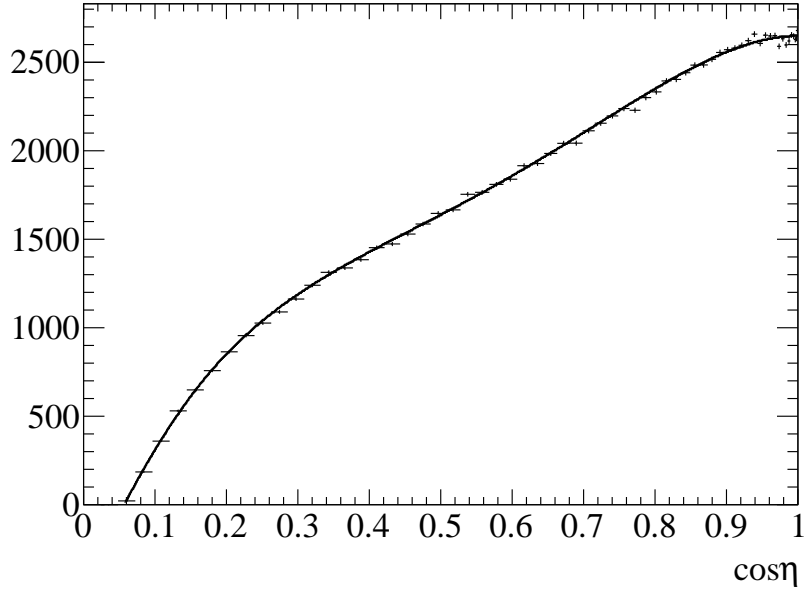


Figure 6.4: Angular acceptance of the PMT plotted as a function of  $\cos \eta$  which is obtained from detector simulation, with a fitted curve overlaid as a solid line. Note that the vertical axis in the figure is in arbitrary unit; after the shape of the curve is extracted, the fitted function is renormalized so that its value is 1 at  $\eta = 0$ .

the integral represents the amount of direct light deposited from an imaginary isotropic light source whose trajectory and the total light intensity are the same as the charged particle described by Equation 6.3. In other words, photon emission described in Equation 6.3 is averaged over all directions at each point on the particle track. The object

$$A(s) = A(x_{\text{PMT}}, z_{\text{vtx}}, R_{\text{vtx}}, \varphi, \theta, \phi) \equiv \frac{d\mu^{\text{sct}}}{d\mu^{\text{iso,dir}}}, \quad (6.9)$$

which is referred to as the scattering table, is the ratio of the differential predicted charges deposited from point  $s$  along the track, by the indirect Cherenkov light from the concerned charged particle and the direct light from the imaginary isotropic source which was discussed above. Assuming that the Cherenkov opening angle does not change as a function of momentum, the momentum dependence is factored out from the scattering table by taking the ratio. The scattering table then depends only on the positional and directional alignment of the particle and the PMT, and a common table

## 6.2. Predicted Charge

---

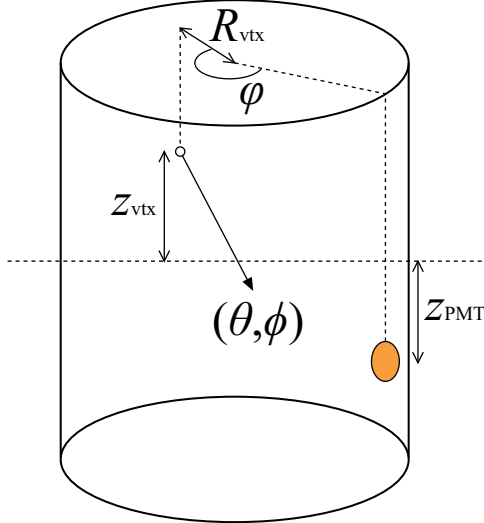


Figure 6.5: A schematic diagram describing the variables relevant to the scattering table. For PMTs on the top or the bottom wall, the distance  $R_{\text{PMT}}$  of the PMT position from the vertical axis at the tank center is used, instead of  $z_{\text{PMT}}$ .

can be used for particles at any momentum. Note, again, that this is an approximation which assumes the Cherenkov opening angle to be independent of momentum and is fixed at the opening angle for particles at  $\beta = 1$ , when calculating the distribution of the indirect light.

Assuming the azimuthal symmetry of the detector, the scattering table is sufficiently expressed as a function of six variables which describe the orientations of the PMT and the particle in the detector, as schematically shown in Figure 6.5. Note that the figure is for the PMTs on the side wall, in which case the variable  $x_{\text{PMT}}$  in Equation 6.9 corresponds to the PMT z position  $z_{\text{PMT}}$ . For the PMTs on the top or the bottom wall, the PMT's distance  $R_{\text{PMT}}$  from the vertical axis at the tank center is used, instead of  $z_{\text{PMT}}$ .

The scattering table is produced by generating a particle gun MC where 3 MeV/c electrons are placed randomly within the detector while multiple scattering is turned off. Such electrons can be considered as point Cherenkov sources with  $\beta = 1$ . During the simulation, the number of reflection and scattering of each photon which arrives at a PMT is recorded, and direct and indirect photons arriving at the PMTs are counted and filled separately into six-dimensional histograms, each axis corresponding to one of the six

## 6.2. Predicted Charge

---

variables in Equation 6.9. Then, at each bin in the six-dimensional parameter space, the numerator  $d\mu^{\text{sct}}$  in Equation 6.9 is obtained from the histogram for indirect photons, while the denominator  $d\mu^{\text{iso,dir}}$  is calculated by averaging the histogram for direct photons over the particle direction. The scattering table is thus obtained as a six-dimensional histogram, and it is linearly interpolated in terms of the six variables at the time of evaluating the predicted charge.

### 6.2.7 Parabolic Approximation

As in Equations 6.3 and 6.7, evaluation of the predicted charge involves integrals along the particle trajectory, and it is not computationally feasible to perform the integrals at the time of reconstructing an event. The following approximation is therefore made in order to avoid the need of evaluating the integral at the time event reconstruction.

Let  $J(s)$  denote the last three factors in Equation 6.3, which describes how the photons are received by the PMT:

$$J(s) \equiv \Omega(R)T(R)\epsilon(\eta) \approx j_0 + j_1 s + j_2 s^2. \quad (6.10)$$

This factor varies slowly as a function of  $s$ , and it is therefore reasonably approximated by a parabola, an example of which is shown in Figure 6.6. The coefficients  $j_n$  are obtained by evaluating  $J(s)$  at three points along the particle trajectory, namely, the particle's initial position, the point at which 90% of Cherenkov light is emitted, and their midpoint.

Once  $J(s)$  is approximated as a parabola, Equation 6.3 reduces to

$$\mu^{\text{dir}} = \Phi(p) \int ds g(s) J(s) \approx \Phi(p)(I_0 j_0 + I_1 j_1 + I_2 j_2), \quad (6.11)$$

where

$$I_n \equiv \int ds g(s)s^n. \quad (6.12)$$

The integral in Equation 6.12 is performed in advance, and  $I_n$  is tabulated as a function of three parameters which specify the initial condition of the particle and its relative orientation to the PMT; namely, the initial values of the momentum  $p$ , the distance  $R$  from the particle to the PMT, and the angle  $\theta$  between the particle direction and the line connecting the particle and the PMT positions. Once the integral Equation 6.12 is performed at discrete bins in  $R$ ,  $\theta$  and  $p$ ,  $I_n$  is fitted as a function of  $p$  at each  $R, \theta$  bin in order to smooth the likelihood surface. When reconstructing an event,  $I_n$  is

## 6.2. Predicted Charge

---

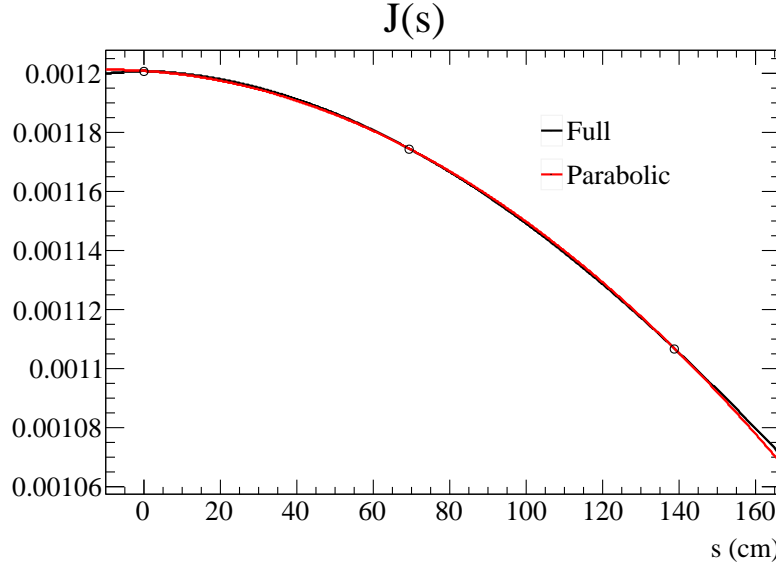


Figure 6.6: The photon acceptance factor  $J(s)$  (black) overlaid with an approximating parabola (red). The coefficients for the parabola are obtained by evaluating  $J(s)$  at the three points indicated by the hollow circles. The plot is for the initial conditions  $R = 500$  cm,  $\theta = 90^\circ$ ,  $\eta = 0^\circ$ .

linearly interpolated in terms of  $R$  and  $\theta$ , after the fit function is evaluated at momentum  $p$  at the relevant neighboring  $R, \theta$  bins.

Since the scattering table  $A(s)$  also tends to vary slowly as a function of  $s$ , for indirect light the approximation

$$J(s)A(s) \approx k_0 + k_1s + k_2s^2 \quad (6.13)$$

is made, which reduces Equation 6.7 to

$$\mu^{\text{sct}} = \Phi(p) \int ds \frac{1}{4\pi} \rho(s) J(s) A(s) = \Phi(p) \frac{1}{4\pi} (k_0 + K_1 k_1 + K_2 k_2), \quad (6.14)$$

where

$$K_n \equiv \int ds \rho(s) s^n. \quad (6.15)$$

$K_n$  is a function of  $p$  only, and it is therefore fitted as a function of  $p$ . The coefficients  $k_n$  are obtained in the same way as  $j_n$  in the direct light case.

### 6.3 Unhit Probability and Charge Likelihood

Once the direct and indirect predicted charge is evaluated for all the particles involved in the event hypothesis, the predicted charge is summed up and the unhit probability  $P_i(\text{unhit}|\mu_i)$  and the charge likelihood  $f_q(q_i|\mu_i)$  in Equation 6.2 are evaluated for each PMT.

Since the predicted charge  $\mu$  is the mean number of photoelectrons produced at a PMT, the actual number of the produced photoelectrons should obey a Poisson distribution with mean  $\mu$ . Therefore, the probability of no photoelectron being produced given the predicted charge  $\mu$  is  $e^{-\mu}$ . However, there are cases in which the signal from a photoelectron does not cross the PMT hit threshold such that it does not produce a hit, and in order to take into account such PMT threshold effects, a correction up to the third order is applied in the expression of the unhit probability:

$$P(\text{unhit}|\mu) \approx (1 + a_1\mu + a_2\mu^2 + a_3\mu^3)e^{-\mu}. \quad (6.16)$$

The coefficients  $a_n$  are obtained from the detector simulation, and Figure 6.7 shows the unhit probability with and without the correction, compared with the actual values obtained from the simulation.

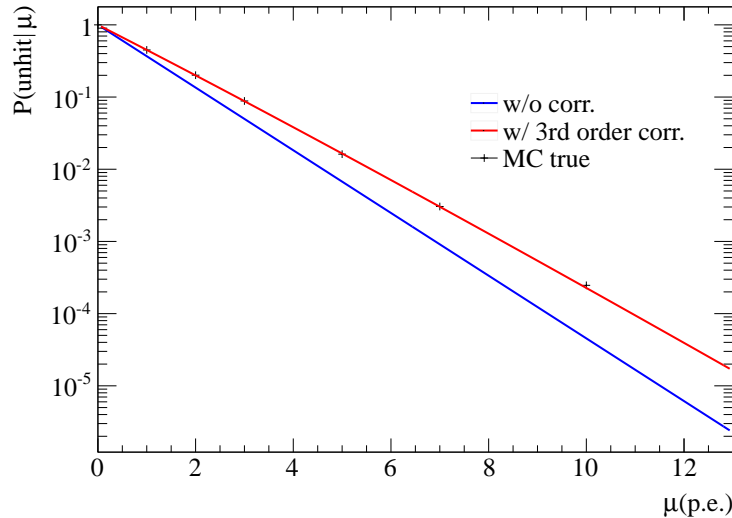


Figure 6.7: The unhit probability  $P(\text{unhit}|\mu)$  with(red) and without(blue) the correction for the PMT threshold effect. The data points show the values obtained from detector simulation.

## 6.4. Time Likelihood

---

The charge likelihood  $f_q(q|\mu)$  is obtained by directly generating photoelectrons following Poisson statistics with mean  $\mu$  at the PMTs in the detector simulation, and taking the distribution of the measured charge for the hit PMTs. Figure 6.8 shows the obtained normalized charge likelihood distribution at a range of predicted charge values. In order to smooth the likelihood surface, the normalized charge distributions are then fitted by a polynomial as a function of  $\mu$  at each fixed value of  $q$ . When evaluating the likelihood, the fit parameters are linearly interpolated in terms of the observed charge  $q$ , and the resulting polynomial is evaluated at  $\mu$ .

## 6.4 Time Likelihood

The time likelihood  $f_t(t_i|\mathbf{x})$  in Equation 6.2 depends on the event hypothesis  $\mathbf{x}$  as well as the position of the PMT in a complex way. Since it is impractical to accurately account for all such dependencies, the following approximations are made for the time likelihood calculation.

The approximation starts by expressing the time likelihood in terms of the residual hit time  $t_i^{\text{res}}$  which is defined based on the raw hit time  $t_i$  as

$$t_i^{\text{res}} := t_i - t - s_{\text{mid}}/c - |\mathbf{R}_{\text{PMT}}^i - \mathbf{x} - s_{\text{mid}}\mathbf{d}|/c_n, \quad (6.17)$$

where  $\mathbf{x}, t$  are the particle vertex position and time,  $\mathbf{d}$  is the particle direction,  $\mathbf{R}_{\text{PMT}}^i$  is the position of the  $i$ -th PMT and  $s_{\text{mid}}$  represents half of the particle track length.

$$c_n := c/n, \quad n = 1.38 \quad (6.18)$$

is the group velocity of Cherenkov light in water.  $t_i^{\text{res}}$  is therefore the residual hit time after subtracting the expected direct photon arrival time from the raw hit time, assuming all the photons are emitted when the particle is at the track midpoint.

As described below, time likelihoods for direct photon hits and indirect photon hits are calculated separately using  $t_i^{\text{res}}$ , and the two likelihoods are merged based on the relative intensities of the direct and indirect light to obtain the final time likelihood that is used in Equation 6.2. The direct and indirect light time likelihoods for a single particle is calculated as the following.

### 6.4.1 Direct Light Time Likelihood

In order to calculate the direct light time likelihood, an approximation is made so that the time likelihood depends only on  $t_i^{\text{res}}$ , the predicted charge

#### 6.4. Time Likelihood

---

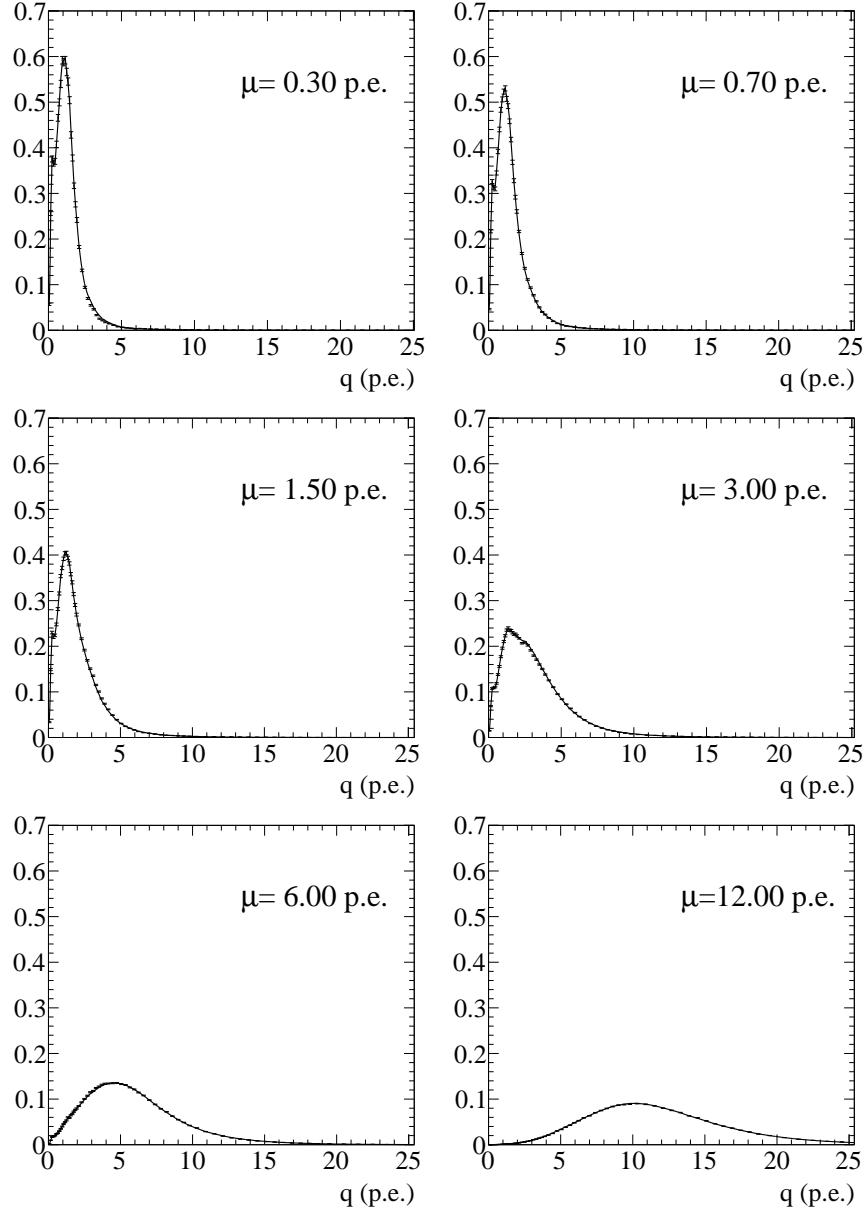


Figure 6.8: The normalized charge likelihood  $f_q(q|\mu)$  at a range of predicted charge  $\mu$ . The data points are obtained from the detector simulation, and the solid lines indicate the fitted function, which is used when evaluating the likelihood.

## 6.4. Time Likelihood

---

from direct light  $\mu^{\text{dir}}$  and the particle's momentum  $p$ . Since a hit is produced by the first photon arriving at a PMT, the width of the residual time distribution decreases as photon statistics increases, and such effect is characterized well by the predicted charge. The momentum also translates to the width of the residual time distribution since the photon time-of-flight correction in Equation 6.17 becomes less accurate as the particle track becomes longer, resulting in a wider distribution. All other dependencies on the configurations of the particle and the PMT are averaged out in this approximation, and part of such information is embedded in the predicted charge.

The residual time likelihood distribution for direct light  $f_t^{\text{dir}}(t^{\text{res}})$  is assumed to be a Gaussian, whose peak position and  $\sigma$  depending on  $\mu^{\text{dir}}$  and momentum  $p$ . In order to produce the residual time distribution, particle gun MC samples are generated at various fixed momentum, and at each momentum a 2D histogram of  $t^{\text{res}}\text{-}\log \mu^{\text{dir}}$  is filled for every hit caused by a direct photon. The  $t^{\text{res}}$  distribution is then fitted by a Gaussian at each  $\log \mu^{\text{dir}}$  bin, and its mean and  $\sigma$  are fitted by a sixth-order polynomial in  $\log \mu^{\text{dir}}$ . Finally, each of the polynomial fit parameters is fitted as a function of momentum. The direct light residual time likelihood  $f_t^{\text{dir}}(t^{\text{res}})$  is thus parameterized as a smooth function of  $\mu^{\text{dir}}$  and  $p$ . The resulting likelihood as well as the original distribution obtained from the MC are shown for electrons and muons in Figures 6.9 to 6.12.

### 6.4.2 Indirect Light Time Likelihood

The residual time PDF for indirect light is currently modeled in `fitQun` as:

$$f_t^{\text{sct}}(t^{\text{res}}) = 1/\left(\sqrt{\frac{\pi}{2}}\sigma + 2\gamma\right) \times \begin{cases} \exp(-\tau^2/2\sigma^2) & (\tau < 0) \\ (\tau/\gamma + 1)\exp(-\tau/\gamma) & (\tau > 0) \end{cases}, \quad (6.19)$$

where  $\tau = t^{\text{res}} - 5$  ns,  $\sigma = 8$  ns and  $\gamma = 25$  ns. This is an empirical function which was determined so that it reproduces a typical shape of the indirect light residual time distribution, and it has a characteristic long right side tail due to reflected light. No  $\mu^{\text{sct}}$  or momentum dependence is considered at the present moment.

### 6.4.3 Merging Direct and Indirect Light Time Likelihoods

The direct and indirect light time likelihoods obtained above are then merged to produce the final overall time likelihood function which appears in Equation 6.2. A further assumption is made here that all indirect photons arrive

#### 6.4. Time Likelihood

---

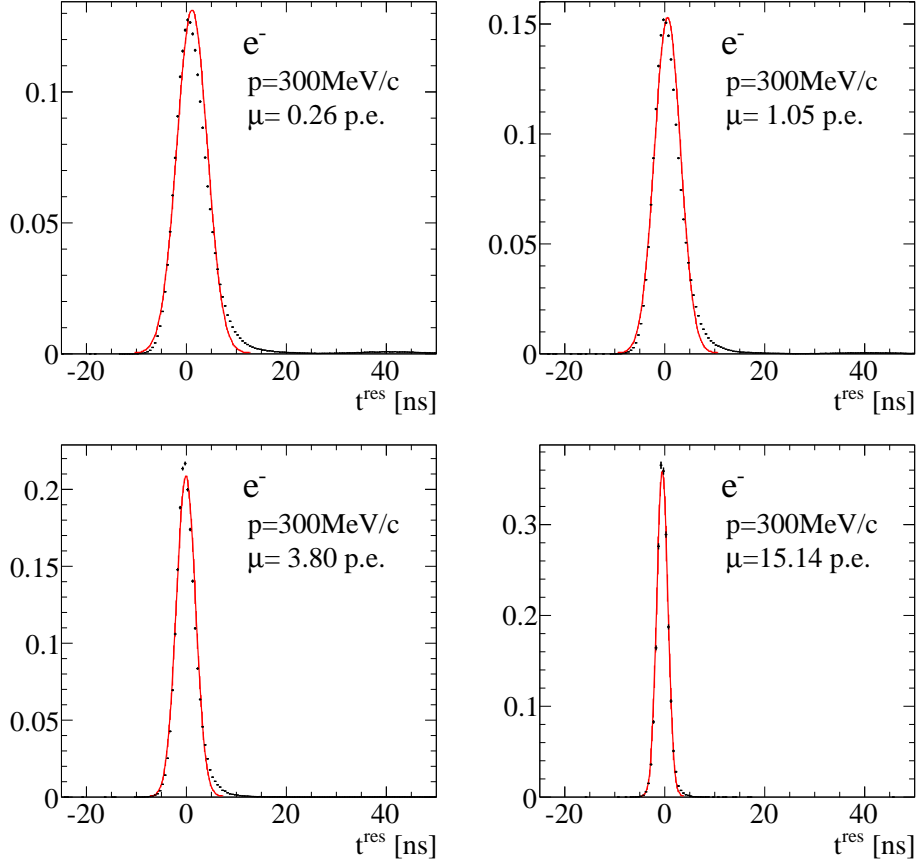


Figure 6.9: The direct light residual time likelihood  $f_t^{\text{dir}}(t^{\text{res}})$  for 300 MeV/c electrons, at a range of predicted charge  $\mu^{\text{dir}}$ . The data points indicate the original distributions obtained from the MC simulation, and the red curves are the Gaussian likelihood function which is parameterized as a function of  $\mu^{\text{dir}}$  and  $p$ .

#### 6.4. Time Likelihood

---

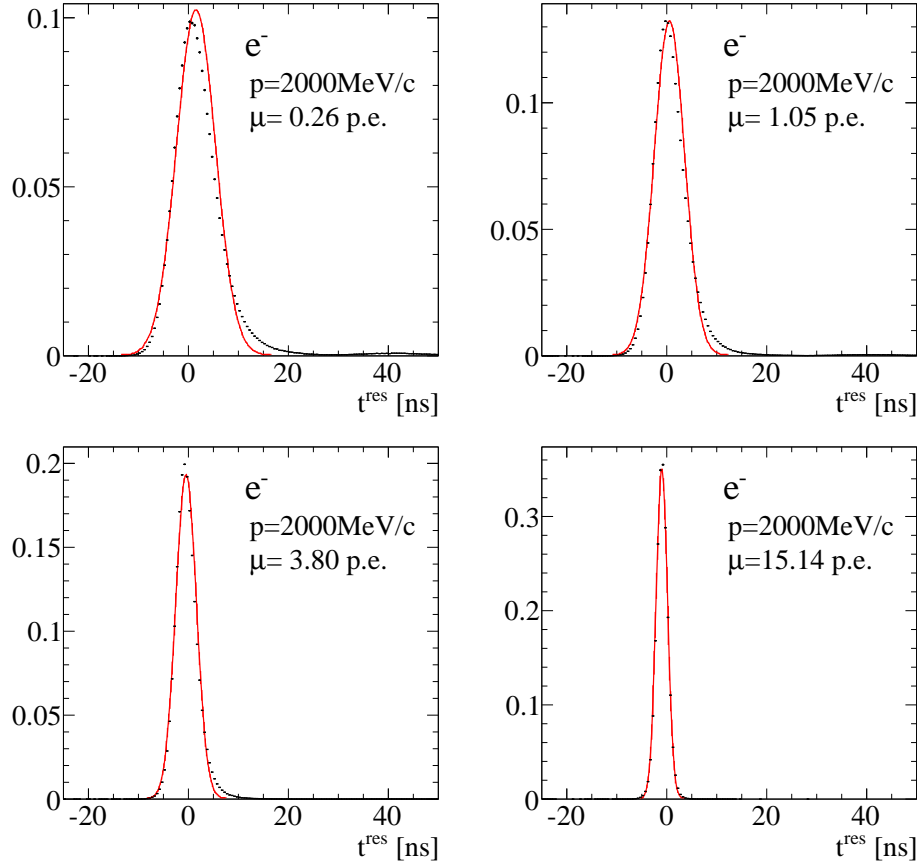


Figure 6.10: The direct light residual time likelihood  $f_t^{\text{dir}}(t^{\text{res}})$  for 2000 MeV/c electrons, at a range of predicted charge  $\mu^{\text{dir}}$ . The data points indicate the original distributions obtained from the MC simulation, and the red curves are the Gaussian likelihood function which is parameterized as a function of  $\mu^{\text{dir}}$  and  $p$ .

#### 6.4. Time Likelihood

---

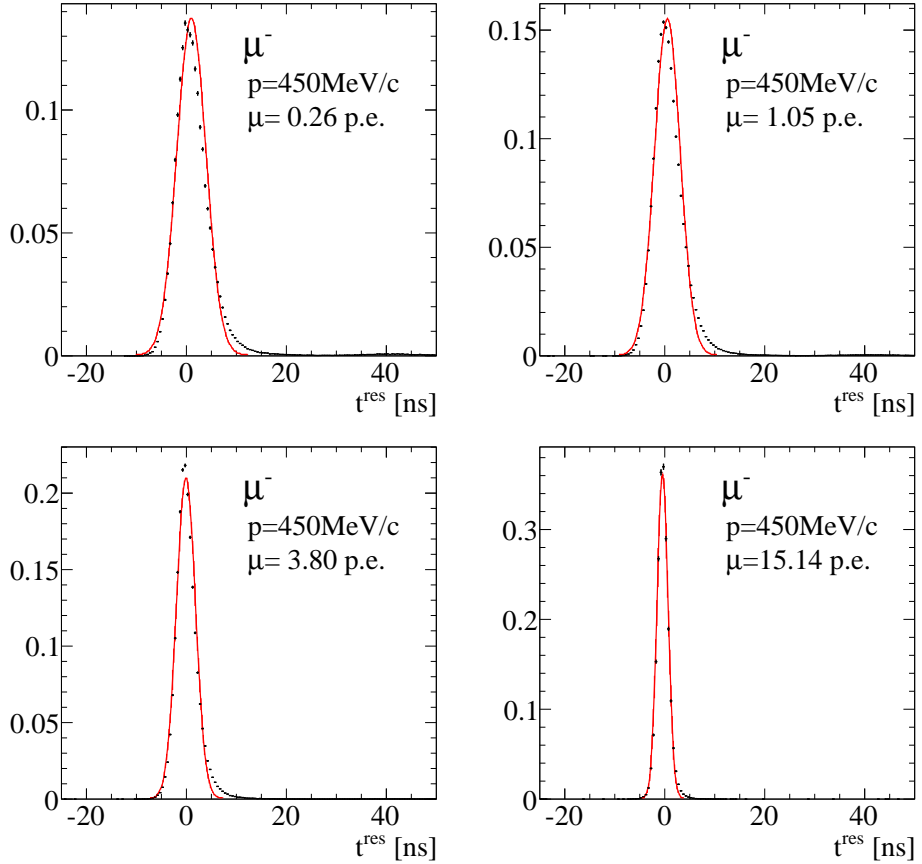


Figure 6.11: The direct light residual time likelihood  $f_t^{\text{dir}}(t^{\text{res}})$  for 450 MeV/c muons, at a range of predicted charge  $\mu^{\text{dir}}$ . The data points indicate the original distributions obtained from the MC simulation, and the red curves are the Gaussian likelihood function which is parameterized as a function of  $\mu^{\text{dir}}$  and  $p$ .

#### 6.4. Time Likelihood

---

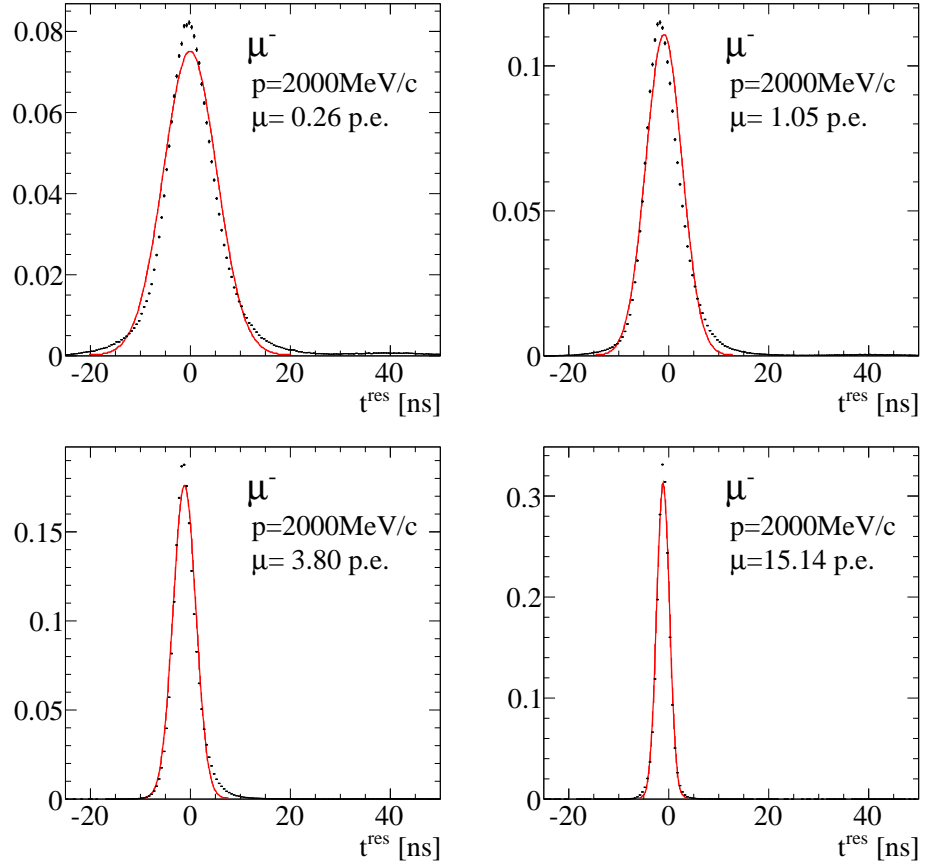


Figure 6.12: The direct light residual time likelihood  $f_t^{\text{dir}}(t^{\text{res}})$  for  $2000 \text{ MeV}/c$  muons, at a range of predicted charge  $\mu^{\text{dir}}$ . The data points indicate the original distributions obtained from the MC simulation, and the red curves are the Gaussian likelihood function which is parameterized as a function of  $\mu^{\text{dir}}$  and  $p$ .

### 6.5. Vertex Pre-fit

---

after any of the direct photons; i.e., an indirect photon can produce a hit only if there were no direct photons observed at the PMT. The time likelihood can then be written as:

$$f_t(t_i^{\text{res}}) = w f_t^{\text{dir}}(t_i^{\text{res}}) + (1 - w) f_t^{\text{sct}}(t_i^{\text{res}}), \quad (6.20)$$

where

$$w \equiv \frac{1 - e^{-\mu^{\text{dir}}}}{1 - e^{-\mu^{\text{dir}}} e^{-\mu^{\text{sct}}}}, \quad (6.21)$$

and  $f_t^{\text{dir}}(t_i^{\text{res}})$ ,  $f_t^{\text{sct}}(t_i^{\text{res}})$  are the normalized residual time likelihoods for direct light and indirect light respectively, at the given predicted charge and momentum values. The time likelihood is thus constructed on-the-fly by combining the time likelihoods for direct and indirect light based on their predicted charge values.

This method is extended to a multi-particle hypothesis by ordering the involving particles by the calculated residual time at each PMT, and then assuming that all the direct photons from a particle with smaller  $t^{\text{res}}$  always arrive earlier than any of the direct photons from a particle with larger  $t^{\text{res}}$ .

## 6.5 Vertex Pre-fit

As it was mentioned at the beginning of this chapter, fitQun is a maximum likelihood event reconstruction which searches for a particle event hypothesis  $\mathbf{x}$  which maximizes the likelihood function defined in Equation 6.1. In practice, this is done by minimizing the negative log likelihood  $-\ln L(\mathbf{x})$  with respect to  $\mathbf{x}$ , using the minimization package MINUIT[84]. In order to ensure the minimizer properly locates and converges at the global minimum rather than being stuck at a local minimum, it is important to seed the minimizer with reasonably accurate parameter values before execution.

The vertex pre-fitter is a fast algorithm which uses only the hit time information from the PMTs to roughly estimate the vertex position and time which can then be used as the parameter seed for  $-\ln L$  minimization, and it is run at the beginning of processing an event before the minimization is run. The estimation is done by searching for the vertex position  $\mathbf{x}$  and time  $t$  which maximizes the vertex goodness which is defined as:

$$G(\mathbf{x}, t) := \sum_i^{\text{hit}} \exp(-(T_{\text{res}}^i/\sigma)^2/2), \quad (6.22)$$

where

$$T_{\text{res}}^i := t_i - t - |\mathbf{R}_{\text{PMT}}^i - \mathbf{x}|/c_n. \quad (6.23)$$

## 6.6. Subevent Algorithm

---

$T_{\text{res}}^i$  is the residual hit time which is similar to Equation 6.17, however, a point light source is assumed to be located at the initial particle vertex in this case. When the vertex position and time get close to their true values,  $T_{\text{res}}^i$  distribute near zero, which results in a large value of the goodness. The pre-fitter first maximizes the goodness by performing an iterative coarse grid-search in space and time, gradually shrinking the grid size and  $\sigma$ . After the grid search is done, a MINUIT minimization of  $-G(\mathbf{x}, t)$  is performed with  $\sigma = 4$  ns, which provides the final seed values for vertex and time.

## 6.6 Subevent Algorithm

The term “subevent” refers to particle activities in the detector which happen closely in time. An event in Super-K, which is defined as detector activities in a  $\mathcal{O}(10 \mu\text{s})$  time window around an event trigger, may contain multiple subevents; for example, in case there is a neutrino interaction which produces a decay electron, the initial particles produced at the neutrino interaction and the subsequent decay electron are counted as separate subevents since they are well separated in time due to the relatively long muon lifetime of  $\sim 2 \mu\text{s}$ . A subevent algorithm is a mechanism to search for such subevent activities around the event trigger and associate the PMT hits produced by each of them so that precise maximum likelihood reconstruction can be applied to each subevent. The procedures are applied at the very beginning of processing an event by fitQun, prior to any of the likelihood reconstruction.

### 6.6.1 Peak Finder

The subevent algorithm starts by searching and locating in time the subevent activities around the event trigger, which is done by the peak finder.

As stated in Section 6.5, the vertex goodness Equation 6.22 takes a large value when it is evaluated at the vertex position  $\mathbf{x}$  and time  $t$  which are close to where the actual particle vertex is located, since in such case the residual hit time distributes near zero for hits that are produced by direct light emitted by the particle. Using this fact, the peak finder searches for subevents by fixing the vertex position  $\mathbf{x}$  at the value provided by the vertex pre-fitter, and scanning the goodness while varying the time  $t$ . Assuming that all the vertex positions of the primary particles and the decay electrons lie close to the pre-fit vertex, subevents appear as large peaks in the distribution of the goodness scanned as a function of  $t$ .

## 6.6. Subevent Algorithm

---

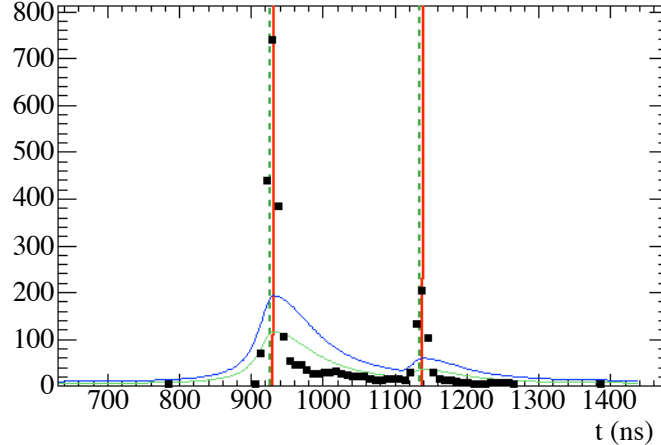


Figure 6.13: Distribution of the scanned goodness  $G(\mathbf{x}, t)$  as a function of time  $t$ , for an example event with a muon primary and a decay electron. The vertical dashed lines indicate true particle time, the black dots are the goodness scan points, and the blue and green curves represent the threshold curves which are used for subevent peak selection. The red vertical lines indicate the time of the subevent peaks which is found by the algorithm.

First, a rough interaction vertex search is done by running the vertex pre-fitter described in Section 6.5 using the PMT hits that are in the  $[-100 \text{ ns}, +400 \text{ ns}]$  time window around the event trigger. Then, the peak finder scans and evaluates the goodness every 8 ns step in  $t$  while  $\mathbf{x}$  is fixed at the pre-fit vertex, starting at  $\sim 300 \text{ ns}$  before the event trigger. For this scan, all the hits within the time window of  $[-200 \text{ ns}, 15000 \text{ ns}]$  around the event trigger is used. The parameter  $\sigma$  in Equation 6.22 is set to 6.3 ns, which was optimized for the step size. Figure 6.13 is an example of the distribution of the goodness for an event with a single muon and a decay electron, where the vertical dashed lines indicate true simulated particle time and black dots show the scan points.

In order to select subevent peaks in this distribution, a goodness threshold curve  $F(t)$  is defined as:

$$F(t) := 0.25 \max_{i \in M} \{G(\mathbf{x}, t_i) f(t - t_i)\} + \eta, \quad (6.24)$$

where

$$f(\tau) := \frac{1}{1 + (\tau/\gamma)^2}, \quad \gamma = \begin{cases} 25 \text{ ns} & (\tau < 0) \\ 70 \text{ ns} & (\tau > 0). \end{cases} \quad (6.25)$$

## 6.6. Subevent Algorithm

---

$M$  represents all local maxima of goodness scan points, i.e. a scan point which is higher than the neighboring two points, which has a goodness value larger than the constant threshold  $\eta = 9$ . The blue curve in the figure represents  $F(t)$ , and the green curve is  $0.6F(t)$ . The first subevent peak is defined as the first local maximum scan point which lies above the blue curve. The scan then continues onto later time searching for another peak, and a local maximum is ignored even if it is above the blue curve if there is no scan point after the previous found peak lying below the green curve. This double-threshold criterion is employed in order not to double count a subevent which produces multiple peaks, which often occurs since the photon time-of-flight subtraction assuming a point light source in Equation 6.23 does not work perfectly and a single subevent may produce multiple peaks.

### 6.6.2 Defining Time Windows and Final Subevents

Once the subevent candidates are found by the peak finder, a time window is defined around each of the peaks which contains the hits associated with the peak, in which likelihood reconstruction can be performed. Within a time window a PMT can produce a hit at most once, and only the hits that lie within the time window will be used for likelihood reconstruction; i.e., the PMT hits that lie outside of the time window are considered as unhit in Equation 6.2.

In order to define the time window for a given peak, hit times are first converted to residual time with respect to the peak using Equation 6.23, and the earliest and the latest hits in raw hit time  $t_i$  which satisfy  $-180 \text{ ns} < T_{\text{res}}^i < 800 \text{ ns}$  define the start and the end time of the time window respectively. The procedure is repeated for all the peaks identified by the peak finder, and time windows that overlap are merged into a single time window.

After the time windows are defined, the vertex pre-fitter and the peak finder are run once again in each time window, this time, by only using the hits that are contained within the respective time window. This procedure is necessary especially for the cases where the distance between the primary and the decay electron vertices is large, since in such case the original pre-fit vertex is far from the actual decay electron vertex and the photon time-of-flight correction in Equation 6.23 works poorly, which results in the peak finder finding fake subevent peaks around the true decay electron subevent.

The remaining peaks after re-running the peak finder are considered as the final subevents found in fitQun, and precise likelihood reconstruction is applied to each of them as discussed in the following sections. The number of decay electrons, which is a variable that is often used in various physics

## 6.7. Single-Ring Fit

---

analyses, is calculated as the number of the found subevents minus one.

### 6.6.3 Performance of the Subevent Algorithm

The performance of the subevent algorithm has been studied using the data and MC samples of stopping cosmic-ray muons, i.e., cosmic-ray muons that enter the detector and stop in the ID. Stopping muon events are clean single muon events which almost always leaves a single decay electron, and they are therefore an ideal source for studying the performance of the algorithm. Table 6.1 shows the detection efficiencies of decay electrons from stopping muons for data and MC in sub-GeV and multi-GeV energy range, where the energy range is defined by whether the muon momentum is below or above 1.33 GeV/ $c$ . The efficiency here is defined as the number of stopping muon events in which multiple subevents are found divided by the total number of events. Note that the detection efficiency gets lower at higher energy, since the more PMTs are hit by the primary muon, the harder it becomes to detect decay electrons that are produced shortly after the parent muon. The difference in efficiencies between data and MC is taken as the systematic uncertainty on the decay electron detection efficiency.

Energy range	Data	MC
Sub-GeV	$88.41 \pm 0.08\%$	$87.81 \pm 0.15\%$
Multi-GeV	$67.77 \pm 0.05\%$	$68.02 \pm 0.09\%$

Table 6.1: Decay electron detection efficiencies for stopping cosmic-ray muons for data and MC. The energy range is defined by whether the muon momentum is below or above 1.33 GeV/ $c$ .

## 6.7 Single-Ring Fit

After the subevents are defined by the subevent algorithm, precise maximum likelihood event reconstruction as discussed in Sections 6.1 to 6.4 is applied to each of the subevents. The most basic reconstruction which is applied to every subevent is the single-ring fitter which is a fit to obtain the single-particle hypothesis that maximizes the likelihood, which is described in this section.

fiTQuN considers three types of single-ring hypotheses: electron, muon and  $\pi^+$ , and the three fits are applied to every subevent that was found by the subevent algorithm. The electron and muon hypotheses contain

## 6.7. Single-Ring Fit

---

seven parameters, which are the vertex position  $\mathbf{x}$ , time  $t$ , zenith angle and azimuth of the direction  $\theta, \phi$ , and momentum  $p$ . The  $\pi^+$  hypothesis has one additional parameter and it is therefore an eight parameter hypothesis, which is described separately in detail in Section 6.8.

### 6.7.1 Single-Ring Electron & Muon Fit

The single-ring electron fit starts by setting the vertex initially at the position determined by the vertex pre-fit which was run in the time window to which the subevent belongs, and the time to the peak time. In order to determine the initial value for the direction, a likelihood scan of the direction is performed by sampling the likelihood at 400 points that are equally spaced on the unit sphere. During the direction scan, momentum is fixed at the value which is roughly estimated using the total observed charge. After the direction is determined by the grid scan, the momentum seed value is set by performing another likelihood scan, this time, by only varying the momentum. Once all the seven track parameters are seeded, the parameters are then simultaneously fit by minimizing the  $-\ln L$  in Equation 6.2 using the SIMPLEX algorithm in the MINUIT package, which provides the final maximum likelihood estimation of the particle track parameters assuming a single electron.

Following the single-ring electron fit is the single-ring muon fit, which takes the vertex, time and direction from the electron fit result as their seed values. The momentum is then estimated by a likelihood scan as it was done in the electron fit, after which the full simultaneous minimization of the  $-\ln L$  is performed.

### 6.7.2 Performance of the Single-Ring e & $\mu$ Fitter

In this section, the performance of the single-ring electron and muon fits described above are compared to APFIT, an event reconstruction algorithm which preexisted at Super-K before fiTQun. The algorithm of APFIT is fundamentally different from fiTQun which is detailed in [85].

Figure 6.14 shows the distribution of the distance between the reconstructed and true vertices for single electron and muon events in the FC single-ring CCQE event sample in the atmospheric neutrino MC whose true interaction vertex lies within the fiducial volume(as opposed to the reconstructed vertex as in Section 5.5), compared between APFIT and fiTQun. The resolution is defined as the 68 percentile of the respective distributions. Figure 6.15 shows the resolution plotted as a function of true momentum.

## 6.7. Single-Ring Fit

---

The angle between the reconstructed and true directions as well as direction resolution are shown similarly in Figures 6.16 and 6.17.

Figure 6.18 shows the momentum resolution for the same set of events. For these plots, the distribution of the fractional difference between the reconstructed and true momenta are fitted by a Gaussian at each true momentum bin, and the width of the fitted Gaussian is plotted.

It can be seen in the figures that fiTQun has higher resolution compared to APFIT, especially for vertex and momentum reconstruction.

### 6.7.3 e/μ Particle Identification

As mentioned in Section 6.2.2, Cherenkov light emission happens differently between particle types, and the ring pattern they produce will therefore be different. As shown in Figure 6.19, electrons produce fuzzy rings due to electromagnetic shower while muons which do not shower produce clear rings with sharp edges, and the difference arises from the differences in the Cherenkov emission as seen in Figures 6.2 and 6.3.

In fiTQun, particle identification (PID) is done by comparing the best-fit likelihood values between different particle hypotheses. For example, electrons and muons are distinguished by making a cut on  $\ln(L_e/L_\mu)$ , the log likelihood ratio between the best-fit electron and muon hypotheses.

Figure 6.20 shows the likelihood separation of the single-ring electron and muon events in the FC true-fiducial CCQE event sample in the atmospheric neutrino MC. In order to properly evaluate the PID performance for low momentum muons, for a muon event it is also required that a decay electron is found by the subevent algorithm, in order to remove the low momentum muon events which was triggered on the decay electron. The vertical axes in the plots are  $\ln(L_e/L_\mu)$ , and the horizontal axes are the reconstructed single-ring electron fit momentum. As it can be seen in the figure, electron events are clearly identified and separated from muon events by making a cut:

$$\ln(L_e/L_\mu) > -10, \quad (6.26)$$

as indicated by the magenta line. The cut threshold was determined based on the MC considering the misidentification rate for both electrons and muons.

The misidentification rate of the same electron and muon events as above are shown as a function of true momentum in Figure 6.21. As shown in the figure, for both particle types the misidentification rate is well below 1% and is smaller for fiTQun than APFIT.

### 6.7. Single-Ring Fit

---

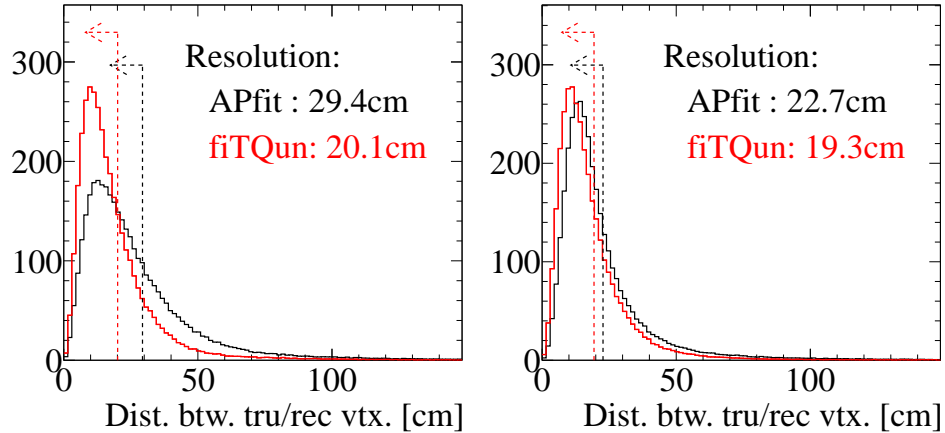


Figure 6.14: Single-ring electron(left) and muon(right) vertex resolution for FC true-fiducial CCQE events in atmospheric neutrino MC, compared between APFIT(black) and fiTQun(red). The resolution is defined as the 68 percentile of the respective distributions.

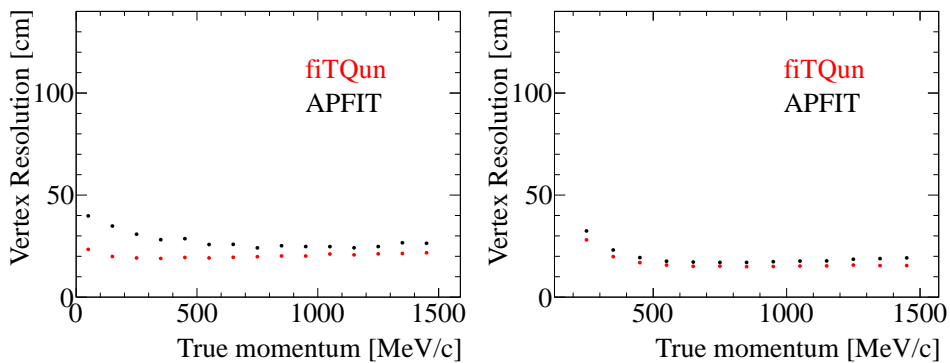


Figure 6.15: Single-ring electron(left) and muon(right) vertex resolution plotted as a function of true momentum, for FC true-fiducial CCQE events in atmospheric neutrino MC, compared between APFIT(black) and fiTQun(red).

### 6.7. Single-Ring Fit

---

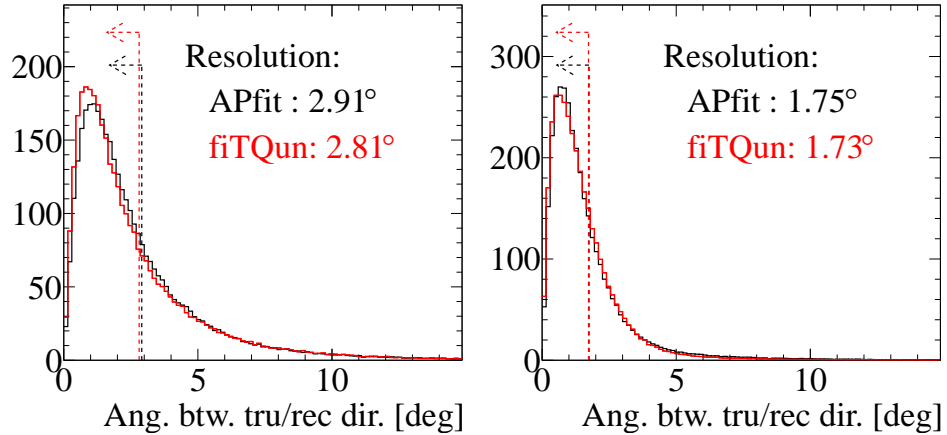


Figure 6.16: Single-ring electron(left) and muon(right) direction resolution for FC true-fiducial CCQE events in atmospheric neutrino MC, compared between APFIT(black) and fiTQun(red). The resolution is defined as the 68 percentile of the respective distributions.

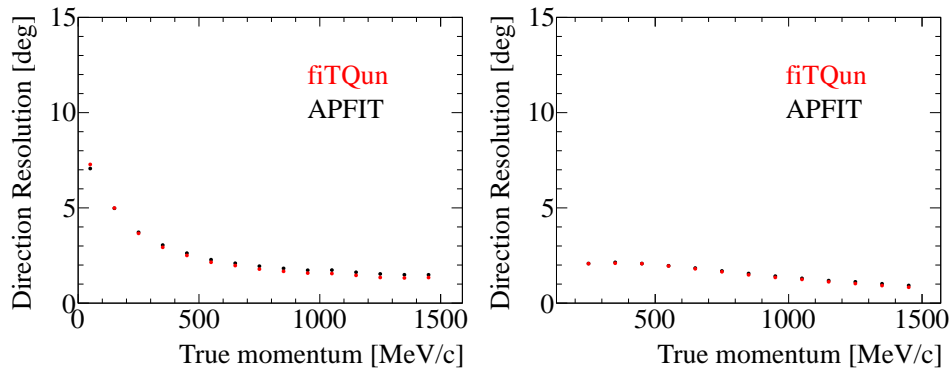


Figure 6.17: Single-ring electron(left) and muon(right) direction resolution plotted as a function of true momentum, for FC true-fiducial CCQE events in atmospheric neutrino MC, compared between APFIT(black) and fiTQun(red).

## 6.7. Single-Ring Fit

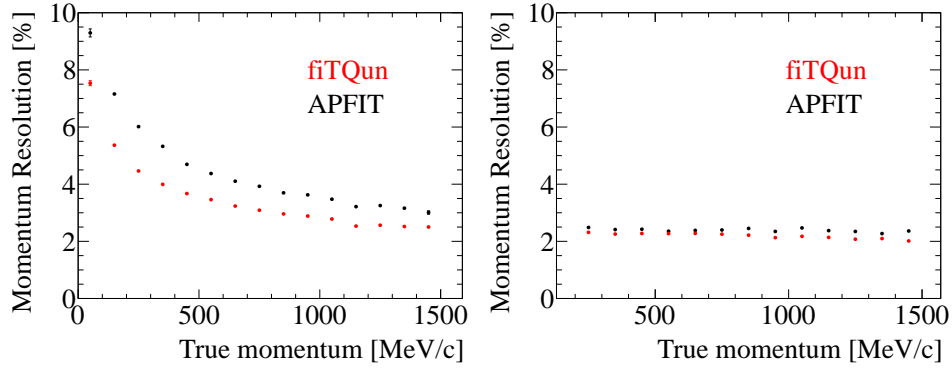


Figure 6.18: Single-ring electron(left) and muon(right) momentum resolution plotted as a function of true momentum, for FC true-fiducial CCQE events in atmospheric neutrino MC, compared between APFIT(black) and fiTQun(red).

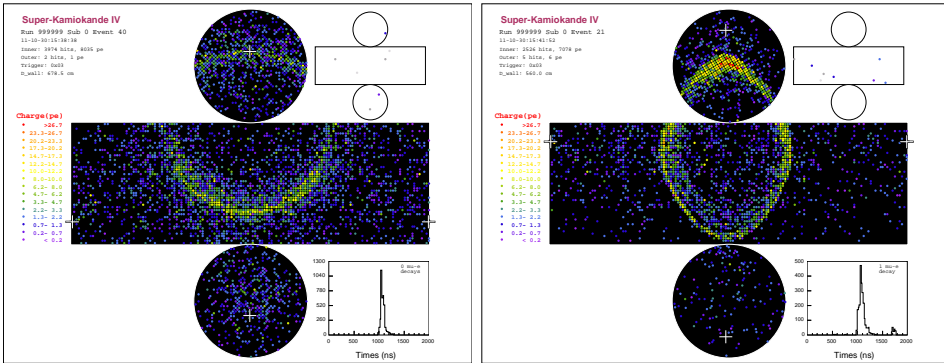


Figure 6.19: Event displays of simulated single electron(left) and muon(right) events. Electrons produce fuzzy rings due to electromagnetic shower, while muons, which do not shower, produce clear rings with sharp edges.

## 6.7. Single-Ring Fit

---

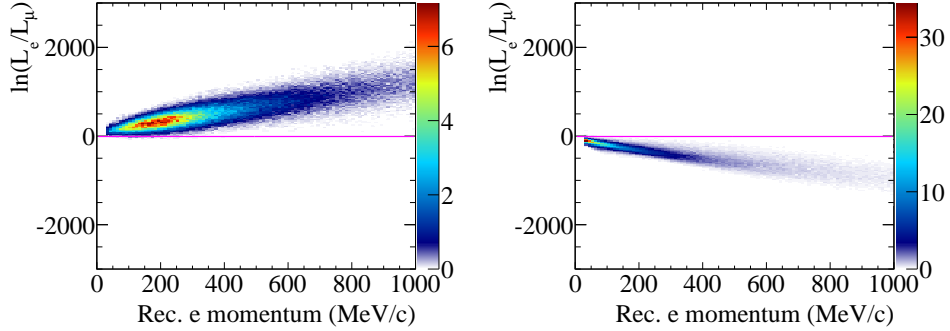


Figure 6.20: Likelihood separation of single-ring electron(left) and muon(right) events in the FC true-fiducial CCQE event sample in the atmospheric neutrino MC. The vertical axes are  $\ln(L_e/L_\mu)$ , and the horizontal axes are the reconstructed single-ring electron fit momentum. The magenta lines indicate the cut criteria for electron-muon separation.

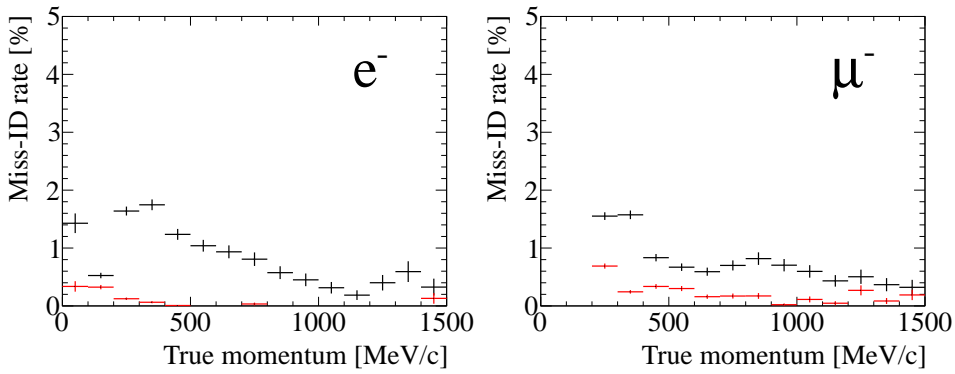


Figure 6.21: Misidentification rate of single-ring electron(left) and muon(right) events in the FC true-fiducial CCQE event sample in the atmospheric neutrino MC, plotted as a function of true momentum. The red markers indicate the performance of fitTQuN, and the black markers are for APfit.

#### 6.7.4 In-Gate Decay Electron Fit

As stated in Section 6.6.2, the initial time window which was defined around each subevent peak found by the peak finder can be merged with another time window in cases where two subevents happen closely in time, and in such case, the time window will contain multiple subevents. The decay electrons which are contained in the same time window as the parent primary particles are referred to as “in-gate” decay electrons, and fitting such events requires a special treatment since the hits that are contained in the time window have to be distributed among the subevents. By employing the hit separation scheme described below, the single-ring electron, muon and  $\pi^+$  fits are applied to all subevents including the in-gate ones.

For a given in-gate subevent, a PMT hit is considered to be associated with the subevent if the hit satisfies:

$$-30 \text{ ns} < T_{\text{res}}^i < 60 \text{ ns}, \quad (6.27)$$

where  $T_{\text{res}}^i$  is the residual time defined in Equation 6.23 calculated using the pre-fit vertex and the peak time of the subevent. In order to reconstruct the in-gate subevent, single-ring fits are performed by using the hits that satisfy Equation 6.27 only, while all the other hit PMTs are ignored. This procedure effectively masks the PMT hits that are caused by the particle activities that are not contained in the subevent in concern. This masking and fitting procedure is applied to each of the in-gate subevents in the time window except for the first, primary subevent.

The primary subevent is reconstructed by masking all the hits that are associated with the other in-gate subevents, i.e., a hit PMT is considered to be unhit if the hit satisfies Equation 6.27 for any of the in-gate subevents.

In order to see how the procedures described above work, event displays of an MC event which has an in-gate decay electron are shown in Figure 6.22. In this event, in addition to the rings from the primary particles, there is a ring from an in-gate decay electron in the upper half of the figures which was observed considerably later compared to the other rings, as it is clear from the hit time distribution on the right. The peak finder finds two in-gate subevents in this event, and after the hit allocation among the subevents is performed, the charge distributions for hits that are associated with each of the two subevents become as shown in Figure 6.23. As shown in the figures, hits from the primary particles and the in-gate decay electron are clearly separated. Single-ring fits are performed on each of the subevents using these allocated hits.

## 6.7. Single-Ring Fit

---

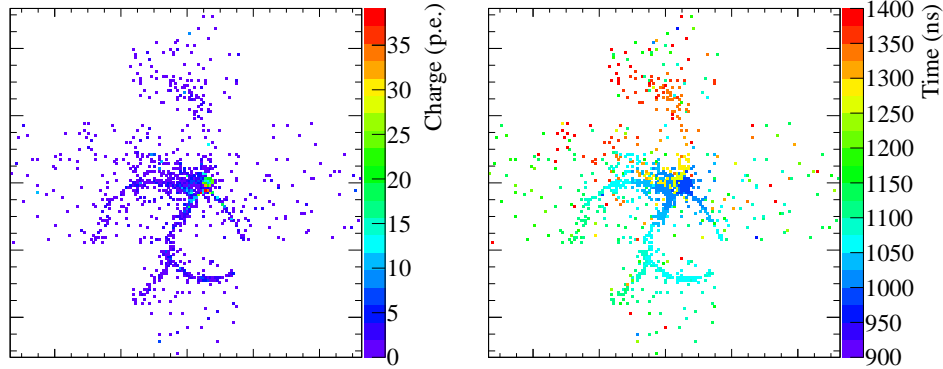


Figure 6.22: Event displays of an MC event which has an in-gate decay electron. The left plot shows the distribution of the charge of each hit in the time window, and the right plot shows the hit time. In addition to the rings due to the primary particles, a ring from an in-gate decay electron is visible in the upper half of the figures, and they are clearly separated in time as it is seen in the right figure.

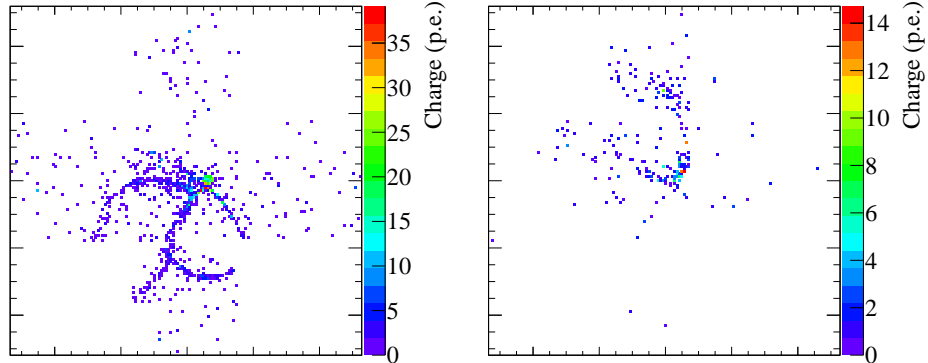


Figure 6.23: Charge distribution for hits that are associated with each in-gate subevent, for the same event which was shown in Figure 6.22. The left figure shows the hits allocated to the first subevent, and the right is for the in-gate second subevent. As it can be seen from the figures, rings from the primary particles and the in-gate decay electron are clearly separated.

## 6.8 Upstream-Track $\pi^+$ Fit

Another single-ring hypothesis which has not been discussed yet is the  $\pi^+$  hypothesis. As schematically shown on the left of Figure 6.24, when a charged pion propagates in water it often interacts hadronically with the nuclei in water, which results in an abrupt change in its direction due to hard scattering or even absorption. The “upstream” portion of the  $\pi^+$  trajectory, i.e., the part before the hadronic interaction happened, thus produces a thin and sharp ring pattern which is quite distinct from that of electrons or muons as seen in the event display on the right of Figure 6.24.

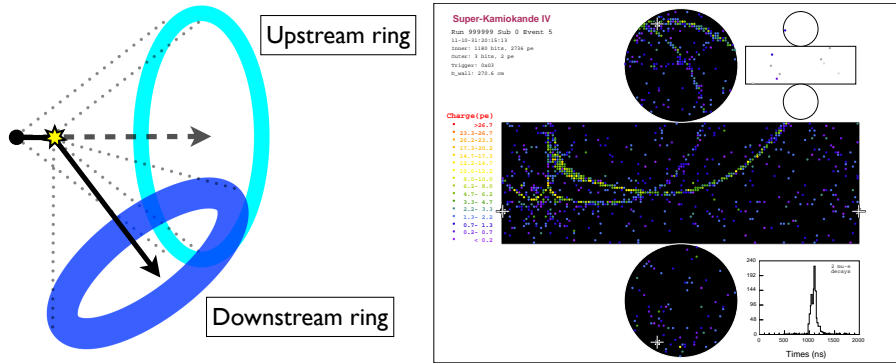


Figure 6.24: On the left is a schematic diagram of a charged pion which undergoes a hadronic scattering on a nucleus and the rings it produces. The thin cyan ring represents the “upstream” ring which is produced by the particle track before the scattering. On the right is an event display of a simulated single  $\pi^+$  event. The pion underwent multiple hadronic scattering and several upstream rings are seen as a result.

The “upstream-track”  $\pi^+$  hypothesis is designed to reconstruct such a thin upstream ring which is produced from a truncated charged pion track. Figure 6.25 schematically shows how an upstream-track hypothesis is constructed in `fitQun`. The “anti-track” starts at the assumed position of the hadronic interaction where the  $\pi^+$  track gets truncated, and the predicted charge deposited by the anti-track is subtracted from the predicted charge from the full track which originates at the initial  $\pi^+$  vertex. The remaining charge will then correspond to the predicted charge from the upstream track which is represented by the outer cyan ring in the figure. Predicted charges for both the full track and the anti-track are calculated using the same framework as in the regular single-ring hypothesis.

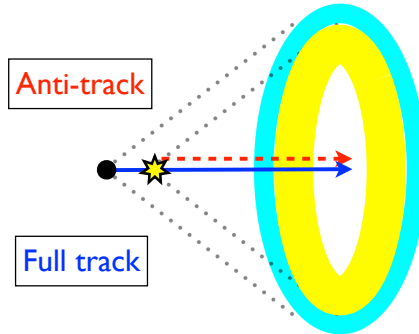


Figure 6.25: A schematic diagram describing how an upstream-track hypothesis is constructed in fitQun. The predicted charge from the anti-track (dashed red arrow) is subtracted from the predicted charge from the full track (solid blue arrow), in order to produce the predicted charge distribution for the upstream track which is represented by the outer cyan ring.

In practice, the upstream-track hypothesis has an additional parameter  $E_{\text{loss}}$  which represents the kinetic energy that was lost in the upstream-track, in addition to the seven parameters which the regular single-ring hypothesis has. The momentum of the anti-track is determined by the energy left after subtracting  $E_{\text{loss}}$  from the initial total energy. By assuming constant kinetic energy loss per unit track length, the vertex of the anti-track is calculated by converting  $E_{\text{loss}}$  to the distance using a constant conversion factor. Finally, for time likelihood, residual time as in Equation 6.17 is calculated using the midpoint of the upstream track, not the full track.

The upstream-track single-ring  $\pi^+$  fit is performed after the single-ring muon fit is done, taking the muon fit results as parameter seeds. This is an eight-parameter fit and all parameters are simultaneously fitted by MINUIT.

### 6.8.1 $\mu/\pi^+$ Identification

As muon and  $\pi^+$  have similar mass, in absence of any hadronic interaction the two produce similar ring pattern.  $\pi^+$ 's are therefore often hard to distinguish from muons, and they often become backgrounds to muon signals in Super-K. The upstream-track  $\pi^+$  fitter, however, provides means to separate the two particle types.

Figure 6.26 shows the likelihood separation of  $\nu_\mu$ CCQE and NC $\pi^+$  events in the T2K accelerator neutrino MC simulation, which has a narrow-band neutrino flux spectrum peaked at  $\sim 600$  MeV. The vertical axes are the

## 6.8. Upstream-Track $\pi^+$ Fit

---

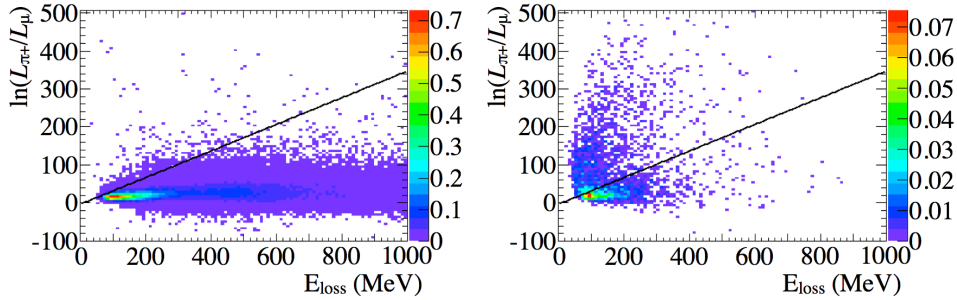


Figure 6.26: Likelihood separation of  $\nu_\mu$  CCQE(left) and NC $\pi^+$ (right) events, in the T2K accelerator neutrino MC simulation. The vertical axes are  $\ln(L_{\pi^+}/L_\mu)$  and the horizontal axes are  $E_{\text{loss}}$ .

log likelihood ratio  $\ln(L_{\pi^+}/L_\mu)$  between the best-fit upstream-track  $\pi^+$  fit and the muon fit, and the horizontal axes are the  $E_{\text{loss}}$  parameter from the  $\pi^+$  fit. It can be seen in the figures that, although there are some indistinguishable events, a significant fraction of  $\pi^+$  events can be clearly separated from muons. A study shows that introducing a cut as indicated by the black lines can reduce the NC $\pi^+$  background contamination in the T2K  $\nu_\mu$  signal sample by  $\sim 60\%$ . Although the  $\mu/\pi^+$  identification is not used in the atmospheric neutrino analysis at the present moment, it is expected that introducing such selection in future analyses will reduce the NC $\pi^+$  backgrounds in the signal single muon event samples.

It is interesting to note that the log likelihood ratio for muon events distribute near zero as in the left of Figure 6.26, which means that muons are fit almost equally well by the muon and the  $\pi^+$  hypotheses (although the reconstructed kinematics may be biased). As muons and  $\pi^+$ 's are both non-showering particles and have similar mass, the Cherenkov emission profile of the two are similar, and the  $\pi^+$  hypothesis can therefore reproduce muon rings well by increasing the  $E_{\text{loss}}$  parameter to the point where the momentum at the assumed upstream-track endpoint drops below the Cherenkov threshold. The fact that muon rings can be fit by the upstream-track  $\pi^+$  hypothesis is used in the multi-ring fitter, which will be described later in this chapter.

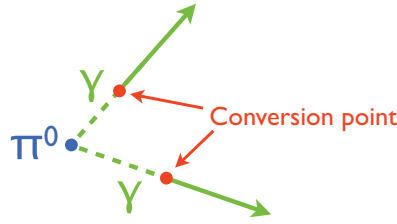


Figure 6.27: A schematic diagram showing how the  $\pi^0$  hypothesis is constructed. Rings from two electron tracks, as indicated by the green arrows, are combined in this hypothesis, and the two tracks point back to a single vertex while the actual origin of each track has some displacement along the track which corresponds to the photon conversion length.

## 6.9 $\pi^0$ Fit

A  $\pi^0$  in most cases decays into two gamma rays, and as a gamma ray produces a ring pattern which is almost indistinguishable to an electron in a water Cherenkov detector, a decayed  $\pi^0$  produces two electron-like rings which point back to a common single vertex. The  $\pi^0$  fitter in fiTQun is a dedicated two-ring fitter which is designed to fit such  $\pi^0$  events.

Figure 6.27 schematically shows how a  $\pi^0$  hypothesis is constructed in fiTQun. Two electron rings are combined in this hypothesis, and the rings are placed so that the two tracks point back to a single vertex which corresponds to the assumed  $\pi^0$  vertex. Since it takes some finite conversion length for a  $\gamma$  to convert into a  $e^+ + e^-$  pair and produce electromagnetic shower, the vertex of each electron ring is shifted along its track by a free parameter. The  $\pi^0$  hypothesis therefore has twelve parameters: the direction  $\theta_i, \phi_i$ , momentum  $p_i$  and the conversion length  $d_i^{\text{conv}}$  for each ring ( $i = 1, 2$ ), and the common vertex  $x, y, z, t$ .

The  $\pi^0$  fit starts by making a rough estimate for the twelve fit parameters using a dedicated seeding procedure. Taking the result of the single electron fit as the seed and fixing the parameters there for the first ring, the second ring is searched by placing the second ring and looking for the direction of the second ring which minimizes the  $-\ln L$  at 100 points uniformly distributed on the unit sphere surface. During this search, the momentum of the second ring is set arbitrarily to 50 MeV/c, and the conversion lengths of the two rings are set to 50 cm. After the second ring search is done, the momenta of the rings  $p_1, p_2$  are fit simultaneously while the other ten parameters are fixed at the seed values to improve the momentum estimation. Finally, all

## 6.9. $\pi^0$ Fit

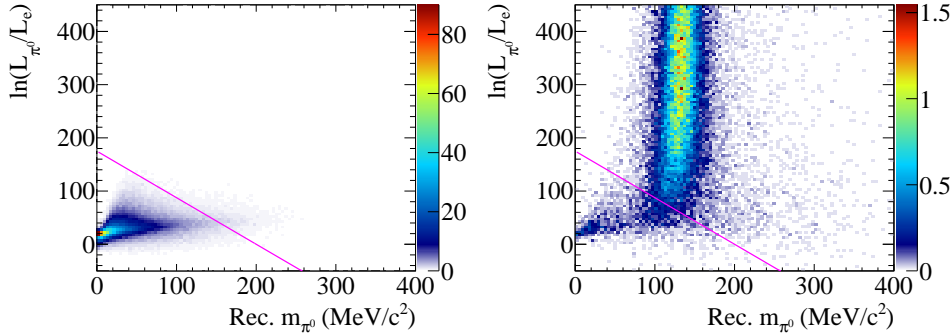


Figure 6.28: CC single electron(left) and NC single  $\pi^0$ (right) events in the FC true-fiducial atmospheric neutrino MC sample, separated using the  $\pi^0$  fit variables. The vertical axes are the log likelihood ratio  $\ln(L_{\pi^0}/L_e)$  and the horizontal axes are the reconstructed invariant mass of the  $\pi^0$  fit.

the twelve parameters are fit simultaneously to get the final best-fit values for the parameters. As in the single-ring fit case, the fit is done by minimizing the  $-\ln L$  using the SIMPLEX algorithm in MINUIT.

### 6.9.1 $e/\pi^0$ Identification

$\pi^0$ s were known as one of the main backgrounds to electron signals in water Cherenkov detectors as a  $\pi^0$  becomes indistinguishable to electrons if one of the two gamma rings are missed by event reconstruction, which happens often for high momentum  $\pi^0$ s which have significant Lorentz boost. One of the main applications of the  $\pi^0$  fitter is to efficiently separate  $\pi^0$ s from electrons and reduce the background contamination in electron signal event samples.

Figure 6.28 shows the CC single electron and NC single  $\pi^0$  events in the FC true-fiducial atmospheric neutrino MC sample, separated using the  $\pi^0$  fit variables. In the plots, the vertical axes are  $\ln(L_{\pi^0}/L_e)$ , the log likelihood ratio between the best-fit  $\pi^0$  and electron hypotheses, and the horizontal axes  $m_{\pi^0}$  are the reconstructed invariant mass calculated from the  $\pi^0$  fit result. As shown in the figures, the two particle types are separated well in the 2D distributions. By introducing a  $\pi^0$  rejection line cut:

$$\ln(L_{\pi^0}/L_e) < 175 - 0.875 \times m_{\pi^0}(\text{MeV}/c^2), \quad (6.28)$$

as indicated by the magenta lines in the plots, the two event categories can be separated by the misidentification rate shown in Figure 6.29.

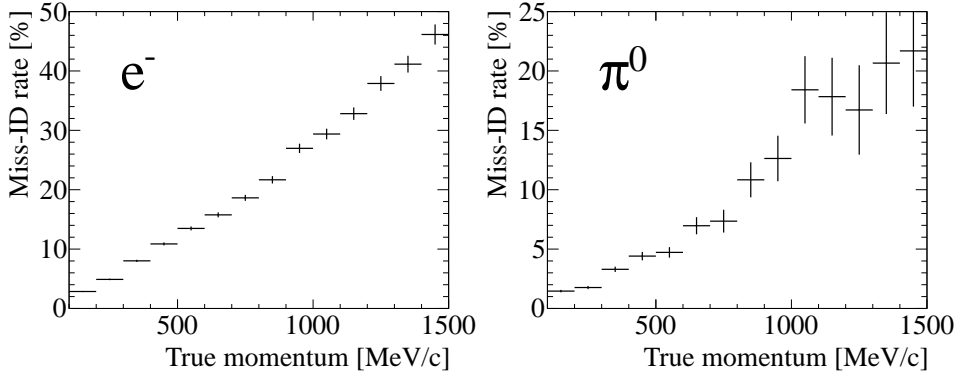


Figure 6.29: Misidentification rate for the  $\pi^0$  rejection cut Equation 6.28, for the CC single electron(left) and NC single  $\pi^0$ (right) events in the FC true-fiducial atmospheric neutrino MC sample, plotted as a function of the true particle momentum. For electrons the misidentification rate is calculated as the fraction of events above the cut line in Figure 6.28, while for  $\pi^0$ 's the fraction below the cut line is plotted.

## 6.10 Multi-Ring Fit

In atmospheric neutrino analyses, it is essential to reconstruct and use the events with multiple particles, since a large fraction of events in multi-GeV have multi-particle final states. This section describes the multi-ring fitter, which is designed to identify and reconstruct up to six rings in an event. The multi-ring fitter is applied only to the first subevent in an event; i.e., the detector activities caused by the particles which immediately follow the initial neutrino interaction, and not the subsequent decay electrons.

### 6.10.1 Initial Multi-Ring Fit

The process of reconstructing a multi-ring event starts by doing an exhaustive search for any possible ring candidates. This is done by doing an iterative search for an additional ring by increasing the number of rings one-by-one, considering electron and upstream-track  $\pi^+$  ring hypotheses. The electron rings are intended to fit the electron or gamma-ray rings, while the upstream-track  $\pi^+$  rings are expected to fit muon or  $\pi^+$  rings since they can both be fit by  $\pi^+$  rings as mentioned in Section 6.8.1.

The tree diagram in Figure 6.30 shows how the multi-ring hypotheses evolve as the number of rings is increased in this ring search procedure. Starting from the single-ring electron fit result, an additional electron ring

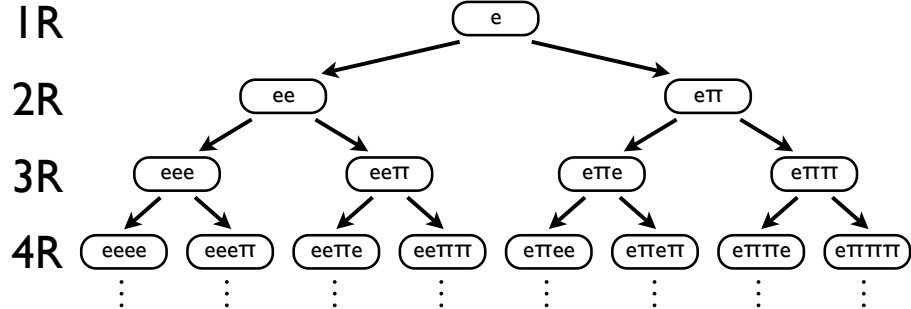


Figure 6.30: A tree diagram showing how the tree of the multi-ring hypotheses evolve as the number of rings is increased. The diagram is for the case assuming the first ring as electron, and equivalent procedure is done for the case of assuming  $\pi^+$  as the first ring.

is attached at the same vertex as the first electron ring, and the likelihood is evaluated at different directions for the second ring at 400 points which are uniformly distributed on the unit sphere surface. For this scan the second ring momentum is arbitrarily assumed to be  $50 \text{ MeV}/c$ . Then, the scan point with the minimum  $-\ln L$  is chosen and the momentum of the second ring is fitted while all the other parameters are fixed. After the momentum of the second ring is roughly estimated, the direction and the momentum of the second ring are simultaneously fitted, while the common vertex and the direction and the momentum of the first ring are fixed. The momenta of the two rings are then fit simultaneously while the vertex and the directions of the two rings are fixed in order to more properly distribute the observed visible energy among the rings, as the single-ring fit momentum tends to overestimate the momentum of the first ring due to the influence of the charge from the additional rings. Finally, the directions and momenta of the two rings as well as the rings' common vertex are all simultaneously fit to get the final best-fit two-ring result. After the two-ring fit assuming an electron second ring is done, the procedure above is repeated using a  $\pi^+$  ring as the second ring, this time, also fitting the  $E_{\text{loss}}$  parameter simultaneously with the other fitted parameters.

Once the two-ring fits are done, for each of the two particle hypotheses for the new ring, whether the fitted second ring is an actual true ring is checked by comparing the likelihoods between the hypotheses before and after adding the new ring. Figure 6.31 shows the square root of the log likelihood ratio between the best-fit single-ring electron hypothesis and the

## 6.10. Multi-Ring Fit

---

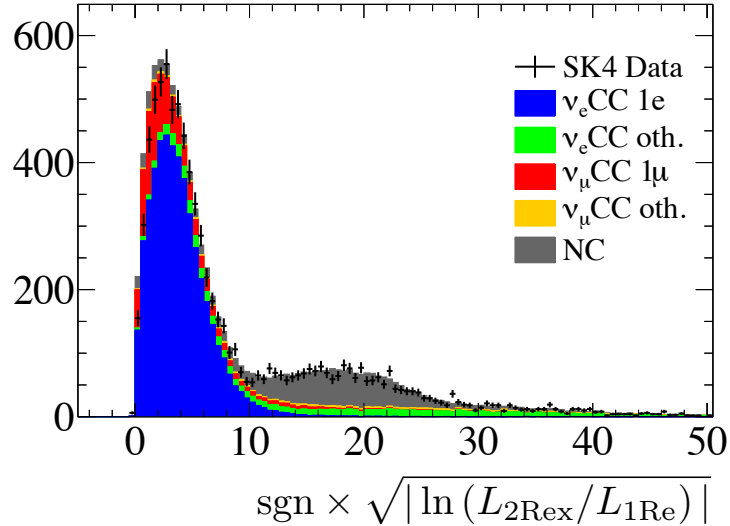


Figure 6.31: Distribution of the square root of the log likelihood ratio between the best-fit single-ring electron hypothesis and the 2R hypothesis assuming electron as the first ring, for FC sub-GeV atmospheric neutrino MC events with no decay electrons detected. MC distribution is subdivided by final state categories and shown in different colours. The data points overlaid are the SK-IV FC data.

better of the 2R hypotheses assuming electron as the first ring(for brevity, such variable will be called the “ring-counting likelihood” henceforth), for FC sub-GeV atmospheric neutrino MC events with no decay electrons detected. In the plot, MC events are categorized by the final states, based on whether there are any  $\pi^0$ 's or visible  $\pi^\pm$ 's or protons in the final state. As shown in the figure, true single-ring events such as the CC single electron events(blue) have relatively small value for the ring-counting likelihood, while the value is large for multi-ring events, for example for NC events(grey) which is dominated by single  $\pi^0$  events. A cut on the ring-counting likelihood is made at a constant threshold(9.35 in this case), and if the likelihood is below the threshold the new ring is assumed to be fake and no further action is done. If the likelihood exceeds the threshold, on the other hand, it is assumed that the new ring is a true ring, and another ring is searched based on the two-ring fit result and examined using the procedures described above.

As schematically shown in Figure 6.30, the above procedures of adding,

## 6.10. Multi-Ring Fit

---

fitting and examining the new ring is iterated until either the newly added ring fails the true ring criterion or reach six rings which is the maximum number of rings fitQun can handle. The simultaneous fit of all parameters including the direction of the rings and the common vertex is only done for the two-ring fit case, and for anything higher, only the simultaneous momentum fit of all rings is done. This is done mainly to save computation time, and it is assumed that once the simultaneous two-ring fit is done the fit vertex gives a reasonable estimate for the true interaction vertex. Also, for the fifth and the sixth ring, only electron hypothesis is considered to save computation time.

The entire procedure above is also repeated assuming  $\pi^+$  as the first ring, and once all the branches of the multi-ring hypothesis tree are terminated, the hypothesis with the smallest  $-\ln L$  is chosen as the “seeding multi-ring hypothesis” among the hypotheses that terminates a branch, i.e., the hypotheses which do not contain any fake rings. The chosen hypothesis will be the seed hypothesis for the next step of the multi-ring fit.

### 6.10.2 Sequential Multi-Ring Fit

The final multi-ring fit hypothesis obtained in Section 6.10.1 often contains fake rings as well misidentified rings due to the limitations of the seeding procedure. In order to improve the fit result, each ring is refitted sequentially and its particle type is reevaluated following the procedures below.

The rings in the final seeding multi-ring hypothesis obtained in Section 6.10.1 are first reordered in terms of the visible energy of the ring, i.e., the reconstructed kinetic energy above Cherenkov threshold. Then, for the most energetic ring, the angle between the directions of the ring and each lower energy ring is calculated, and if the angle for a given lower energy ring is smaller than  $20^\circ$ , the lower energy ring is merged to the highest energy ring by adding the visible energy. After that, the highest energy ring is re-fitted assuming three particle types: electron, muon and  $\pi^+$ , while all the other remaining rings which were not merged in the ring-merge procedure are fixed at their original configurations. This is essentially a single-ring fit in the presence of other fixed rings, and all the ring parameters are fit simultaneously including the vertex, which will in the end provide a multi-ring hypothesis with the vertex position of the rings not necessarily being at a single location. The type of the most energetic ring, whether it is a showering(such as electron and gamma) or a non-showering(such as muon and  $\pi^+$ ) ring, is then examined by comparing the best-fit likelihoods between the hypotheses assuming the most energetic ring as electron or  $\pi^+$ . The

## 6.10. Multi-Ring Fit

---

criterion for selecting it as a showering(electron) ring is:

$$\ln(L_e/L_{\pi^+}) > -10, \quad (6.29)$$

which is analogous to Equation 6.26, but instead of the muon the  $\pi^+$  ring hypothesis is used here since this way both muons and  $\pi^+$ 's can be distinguished from electrons. The ring type selected by this cut is accepted as the final type of the ring(showering or non-showering), and the ring in the original multi-ring hypothesis is replaced by the selected re-fitted hypothesis (the cases for muon and  $\pi^+$  is described below in more detail). After the most energetic ring is re-fitted, the above procedure is repeated for the subsequent lower energy rings which remained after ring merging, in the descending order of the ring energy until all the remaining rings are re-fitted.

At the present moment, the above  $e/\pi^+$  cut is the only particle identification cut that is applied in the sequential fit procedure, and the  $\mu/\pi^+$  identification as described in Section 6.8.1 is not applied. If the most energetic ring is determined to be non-showering( $\pi^+$ -like) as opposed to showering(electron-like), the ring is always assumed to be a muon, since such case usually happens only for  $\nu_\mu$ CC events with a true muon ring and rarely happens for NC events with a true  $\pi^+$  ring being most energetic. For other rings, a ring which is identified as  $\pi^+$ -like rather than electron-like is always assumed as a  $\pi^+$ .

The fit result obtained after the entire sequential fit procedure above is the final result which will be used as fiTQun's best estimate for the event's final state and is used in the atmospheric neutrino analysis.

### 6.10.3 Performance of the Multi-Ring Fitter

In this section, the ring-counting and particle identification performance of the fiTQun multi-ring fitter is compared to APFIT, the preexisting Super-K reconstruction which was mentioned in Section 6.7. The dataset used here is the FC atmospheric neutrino MC normalized to 2519.89 days exposure which is the same as the data exposure in SK-IV.

Figures 6.32 and 6.33 show the reconstructed event categories for the  $\nu_e$ CC single electron events and the NC single  $\pi^0$  events respectively, compared between fiTQun and APFIT. As shown in the figures, fiTQun has a higher fraction of NC1 $\pi^0$  events which are properly reconstructed as two electron ring events(shown in green), while the fraction of reconstructing CC single electron events properly as single electron ring event(shown in grey) is at a similar level between fiTQun and APFIT. Furthermore, Figure 6.34

### 6.10. Multi-Ring Fit

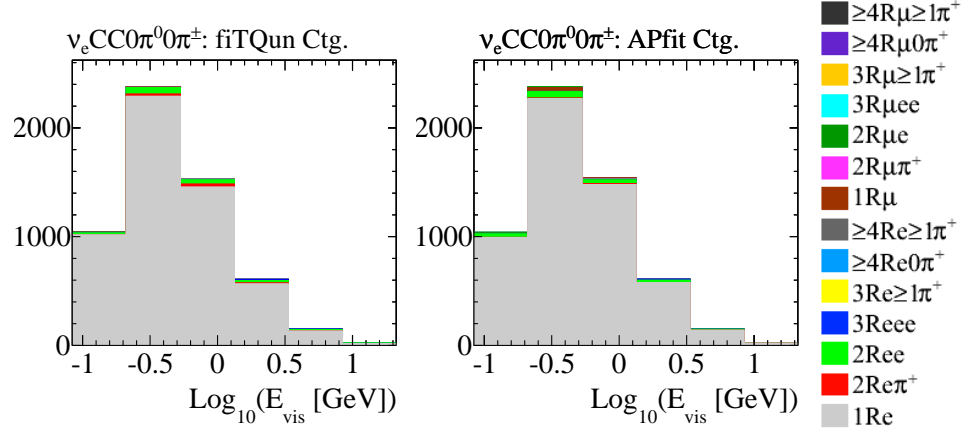


Figure 6.32: Reconstructed event categories of  $\nu_e$ CC events with no visible pions in final state in the FC atmospheric neutrino MC, for fiTQun(left) and APFIT(right). The horizontal axes are the log of the visible energy in GeV. Reconstructed single electron ring event category, which corresponds to the true category, is shown in grey.

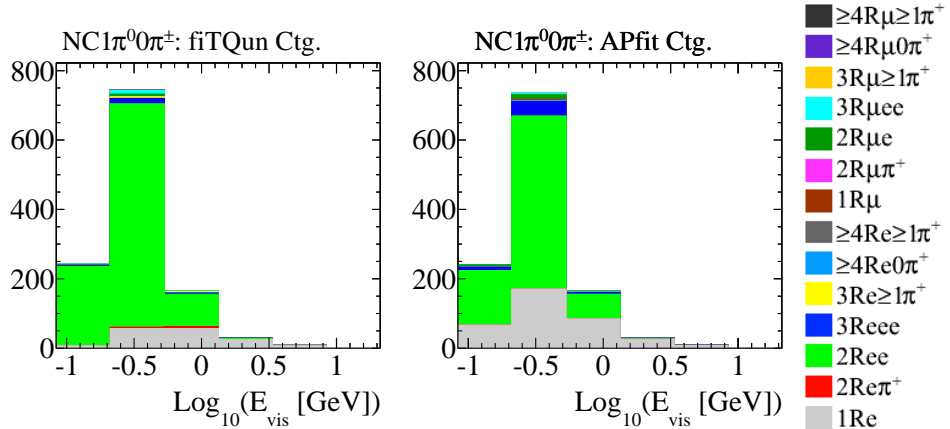


Figure 6.33: Reconstructed event categories of NC events with a single  $\pi^0$  and no visible  $\pi^\pm$  in final state in the FC atmospheric neutrino MC, for fiTQun(left) and APFIT(right). The horizontal axes are the log of the visible energy in GeV. Reconstructed two electron ring event category, which corresponds to the true category, is shown in green.

### 6.10. Multi-Ring Fit

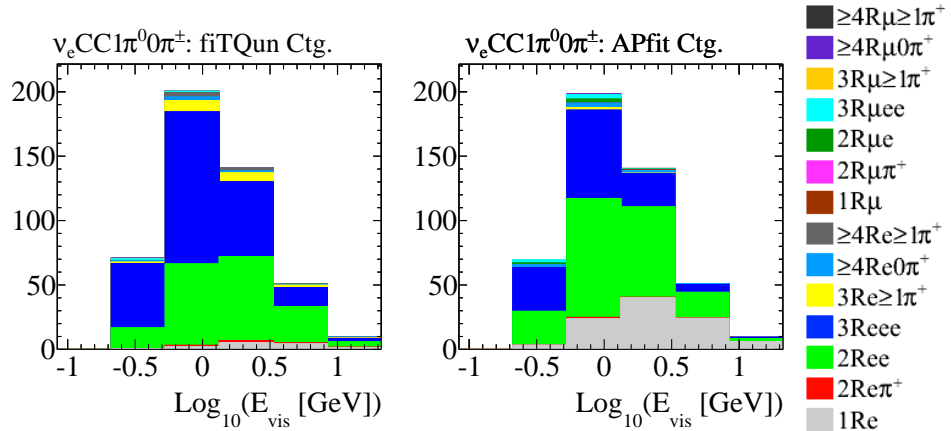


Figure 6.34: Reconstructed event categories of  $\nu_e$ CC events with a single  $\pi^0$  and no visible  $\pi^\pm$  in final state in the FC atmospheric neutrino MC, for fitQun(left) and APFIT(right). The horizontal axes are the log of the visible energy in GeV. Reconstructed three electron ring event category, which corresponds to the true category, is shown in blue.

shows that fitQun's efficiency for properly reconstructing  $\nu_e$ CC  $1\pi^0$  events as three electron ring events(shown in blue) is significantly higher compared to APFIT. Similarly, reconstructed event categories for  $\nu_\mu$ CC single muon and  $\nu_\mu$ CC  $1\pi^0$  events are shown in Figures 6.35 and 6.36, which lead to a similar conclusion.

In order to see how well the multi-ring kinematics are reconstructed, Figure 6.37 shows the reconstructed invariant mass calculated from the 2nd and the 3rd rings in the events categorized as  $3e$  ring events by fitQun and APFIT. The plots show that the true  $\nu_e$ CC  $1\pi^0$  events(shown in blue) which are targeted by the ring selection are selected with much higher efficiency and purity by fitQun than APFIT, and a clear  $\pi^0$  mass peak is seen. Figure 6.38 shows the equivalent plots for  $\nu_\mu$ CC  $1\pi^0$  events.

From these distributions, it is clearly seen that fitQun's multi-ring fitter has a significantly better performance in properly identifying and reconstructing the rings in multi-ring events compared to the preexisting APFIT reconstruction.

### 6.10. Multi-Ring Fit

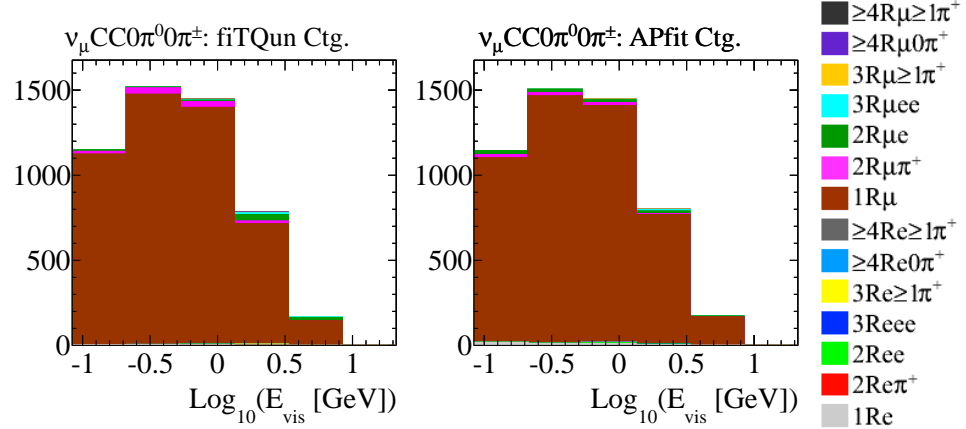


Figure 6.35: Reconstructed event categories of  $\nu_\mu \text{CC}$  events with no visible pions in final state in the FC atmospheric neutrino MC, for fiTQun(left) and APFIT(right). The horizontal axes are the log of the visible energy in GeV. Reconstructed single muon ring event category, which corresponds to the true category, is shown in brown.

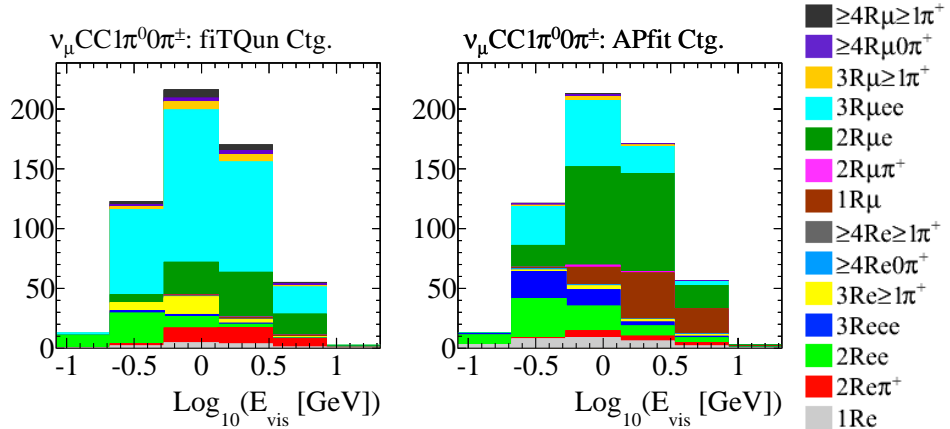


Figure 6.36: Reconstructed event categories of  $\nu_\mu \text{CC}$  events with a single  $\pi^0$  and no visible  $\pi^\pm$  in final state in the FC atmospheric neutrino MC, for fiTQun(left) and APFIT(right). The horizontal axes are the log of the visible energy in GeV. Reconstructed  $1\mu + 2e$  ring event category, which corresponds to the true category, is shown in cyan.

### 6.10. Multi-Ring Fit

---

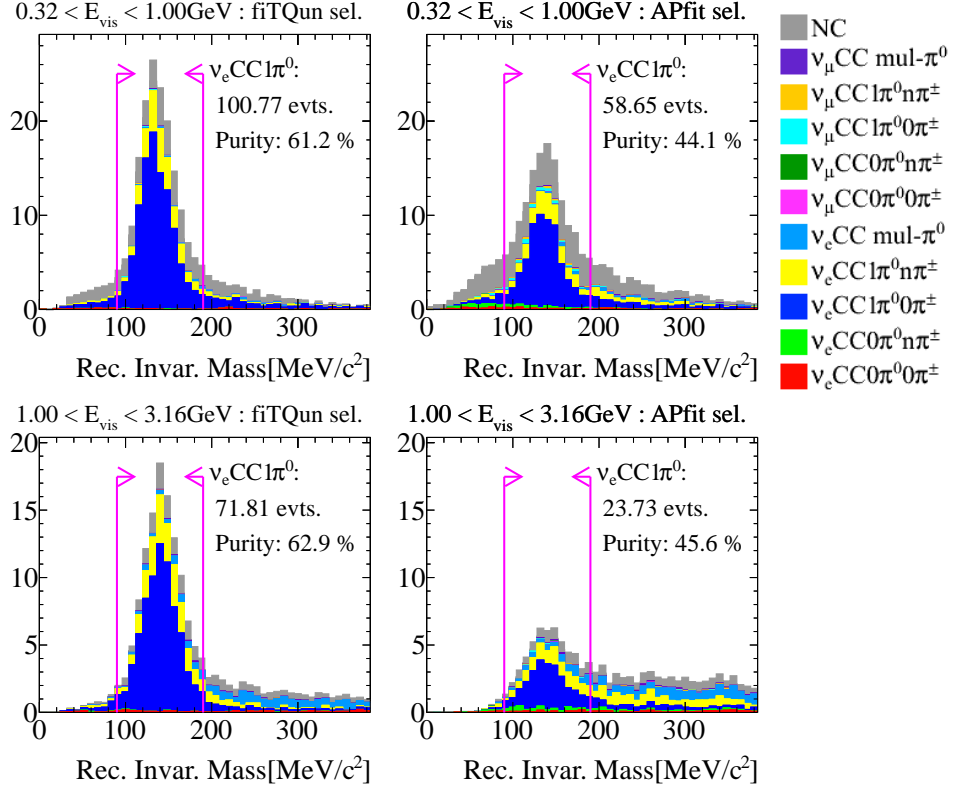


Figure 6.37: Reconstructed invariant mass calculated using the 2nd and the 3rd rings for events reconstructed as  $3e$  ring by fitTQun(left column) and APFIT(right column), in the FC atmospheric neutrino MC. The upper row is for visible energy in the range  $0.32 - 1.00 \text{ GeV}$ , and the lower row is for  $1.00 - 3.16 \text{ GeV}$ . Each true final state is shown in different colour in the plots, and the true  $\nu_e \text{CC } 1\pi^0$  events which are targeted by the ring selection is shown in blue. As shown in the plots, a clearer and larger peak is seen in the fitTQun plots near the  $\pi^0$  mass  $\sim 135 \text{ MeV}/c^2$ , which indicates that the  $\pi^0$  was reconstructed properly with higher efficiency. The event rate and the purity of the  $\nu_e \text{CC } 1\pi^0$  events which pass the invariant mass cut as indicated by the magenta arrows are also shown in the plots.

### 6.10. Multi-Ring Fit

---

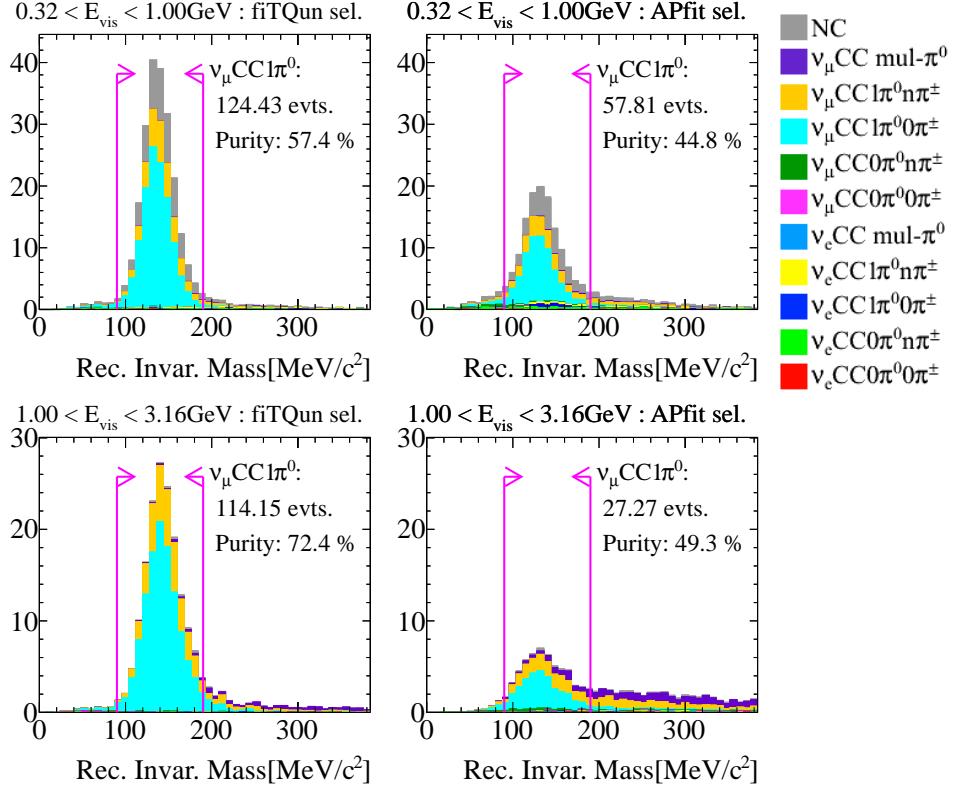


Figure 6.38: Reconstructed invariant mass calculated using the 2nd and the 3rd rings for events reconstructed as  $1\mu + 2e$  ring by fitQun(left column) and APFIT(right column), in the FC atmospheric neutrino MC. The upper row is for visible energy in the range  $0.32 - 1.00 \text{ GeV}$ , and the lower row is for  $1.00 - 3.16 \text{ GeV}$ . Each true final state is shown in different colour in the plots, and the true  $\nu_\mu \text{CC } 1\pi^0$  events which are targeted by the ring selection is shown in cyan. As shown in the plots, a clearer and larger peak is seen in the fitQun plots near the  $\pi^0$  mass  $\sim 135 \text{ MeV}/c^2$ , which indicates that the  $\pi^0$  was reconstructed properly with higher efficiency. The event rate and the purity of the  $\nu_\mu \text{CC } 1\pi^0$  events which pass the invariant mass cut as indicated by the magenta arrows are also shown in the plots.

## 6.11 fiTQun in SK-I to III

As mentioned in Section 2.3, there are four distinct detector phases in Super-K, and only the data from the latest SK-IV phase is used in the atmospheric neutrino oscillation analysis which is presented in Chapter 8. The data from the old SK-I to III phases is not used in the analysis at the present moment due to the large data-MC discrepancies observed in the reconstructed variable distributions from fiTQun, and usage of such data requires improvements in the detector simulation in those phases.

As an example of such data-MC discrepancy, Figure 6.39 shows the data-MC comparison of the distribution of the log likelihood ratio between the single-ring electron and muon fits  $\ln(L_e/L_\mu)$  discussed in Section 6.7.3, for the FC sub-GeV (i.e. visible energy below 1330 MeV) single-ring atmospheric neutrino events. It can be seen from the plots that while the distribution agrees well in SK-IV, there are rather large discrepancies between data and MC for SK-I and III, namely, the single electron events in data are shifted to the left such that the electron-muon separation appears to be worse in data compared to MC.

In general, SK-IV is the most stable of the four detector phases due to the various hardware improvements such as the electronics and the water system, and because of the sophisticated calibration methods described in Chapter 3 which have significantly improved over the years the detector simulation is also more detailed and better tuned in SK-IV. The data-MC agreement is therefore overall better in SK-IV compared to the other phases.

One of the potential improvements one can make in the detector simulation for SK-I to III is the time response of the PMTs. As discussed in Section 3.4, the time resolution of the ID PMTs is obtained from the timing calibration data using a laser system, and the time response is asymmetric having a longer tail in later time as Figure 3.4 shows. For SK-IV, such asymmetric time response is simulated by an asymmetric Gaussian based on the measured time resolution, however, for SK-I to III the response is simulated by a simple symmetric Gaussian. As the fiTQun likelihood uses the detailed time information, such differences in the time response between the reality and the simulation can directly manifest as the data-MC discrepancies in the fitted likelihoods. By reprocessing the old TQ calibration data, it is possible to improve the simulation for SK-I to III to incorporate the asymmetric time response.

Differences in the light attenuation length in water also cause differences in the fiTQun outputs. Figure 6.40 shows the variation of the measured light attenuation length over time, and as the figure shows the water quality

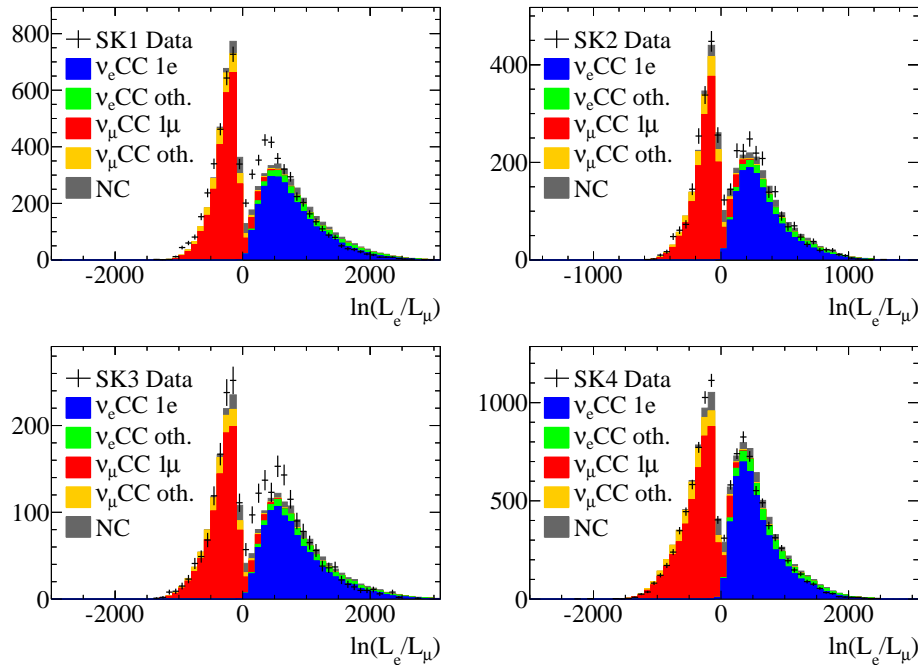


Figure 6.39: Distributions of the log likelihood ratio between the fitQun single-ring electron and muon fits  $\ln(L_e/L_\mu)$  for the FC sub-GeV single-ring atmospheric neutrino events in each SK phase. The plot on the top-left, top-right, bottom-left and bottom-right is for SK I, II, III and IV respectively. Points with error bars represent the data, and MC expectations are broken down by final state categories where 1e and 1 $\mu$  represent the events in which the only visible particle being an electron or a muon.

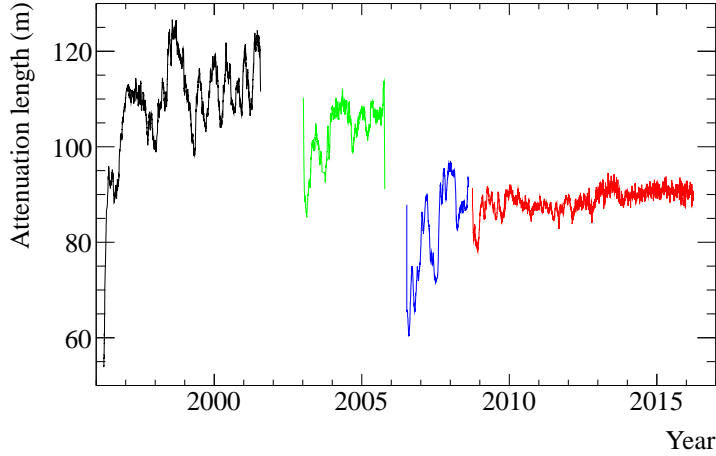


Figure 6.40: Time variation of the light attenuation length in water. The four detector phases are shown in different colours, where SK I, II, III and IV are shown in black, green, blue and red respectively.

in SK-IV is much more stable compared to the other phases. The variations in water quality such as the changes in absorption or scattering affects the charge pattern of the Cherenkov rings and hence affects the likelihood. Currently, atmospheric neutrino MC is produced without considering such variations in the detector properties over time, and the simulation is done using the calibration constants measured at a single point in time in each detector phase. For instance, the water in SK-IV is simulated based on the water calibration data taken in April 2009. When the property of the water significantly deviates in data compared to the simulation, the difference manifests as data-MC discrepancies in the fiTQun likelihoods. One potential solution to improve the data-MC agreement is to simulate the time variations in the MC based on the available calibration data.

It is thus expected that the detector simulation in SK-I to III can be improved in near future by using the available calibration data so that one can benefit from the advanced reconstruction performance of fiTQun when analyzing the data from the old SK phases.

# Chapter 7

## First Application of fiTQun: T2K $\nu_e$ Appearance

As an example application of fiTQun, this chapter briefly describes the T2K  $\nu_e$  appearance analysis which was the first application of fiTQun in a physics analysis. In the analysis, fiTQun is used to reduce the NC  $\pi^0$  background in the signal  $\nu_e$  event sample observed at Super-K, resulting in  $\sim 62\%$  reduction of the NC background compared to the previous  $\pi^0$  rejection method while the loss in the signal efficiency is only  $\sim 2\%$ . The analysis result has been published by the T2K collaboration in [29], which reports the discovery of the  $\nu_\mu \rightarrow \nu_e$  oscillation.

### 7.1 T2K Experiment

T2K is a long-baseline accelerator neutrino oscillation experiment located in Japan. A nearly pure  $\nu_\mu$  beam produced at the J-PARC accelerator facility in Tokai is detected at Super-K at the distance of 295 km, and the flavour change of the neutrinos are measured precisely.

As schematically shown in Figure 7.1, at the beam production site, protons accelerated to 30 GeV at the J-PARC main ring are collided with a graphite target producing mainly charged pions with some kaons, and the pions are subsequently focused by three magnetic horns. The focused pions

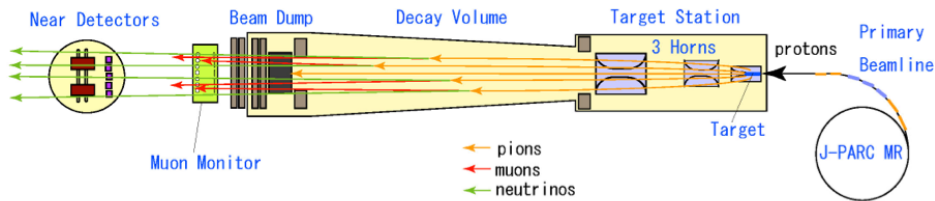


Figure 7.1: Schematic drawing of the T2K beam production site. Figure taken from [23].

### 7.1. T2K Experiment

---

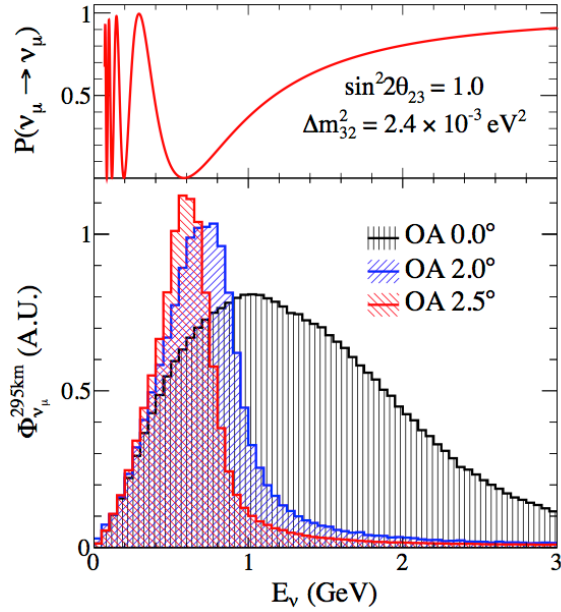


Figure 7.2: T2K  $\nu_\mu$  beam spectrum at different off-axis angles. The  $\nu_\mu$  survival probability at SK is also shown on the top. Figure taken from [86].

then undergo the decay  $\pi^+ \rightarrow \mu^+ + \nu_\mu$  in a decay volume, producing an intense  $\nu_\mu$  beam. The produced  $\mu^+$ 's are mostly stopped at the beam dump so that their decay  $\bar{\nu}_\mu$  and  $\nu_e$ , which become backgrounds to the oscillation measurements, are at very low energies and are not focused towards the beam direction. By reversing the current to the magnetic horns, one can either focus  $\pi^+$  and defocus  $\pi^-$  or vice versa and thus choose whether to produce a  $\nu_\mu$  or  $\bar{\nu}_\mu$  beam. SK is located  $2.5^\circ$  off-axis from the beam direction, which results in a narrow neutrino energy spectrum peaked at 0.6 GeV at SK as shown in Figure 7.2. The peak energy is where the  $\Delta m_{32}^2$ -induced oscillation effects become maximal given the known value for  $\Delta m_{32}^2$  and the 295 km baseline. The neutrino beam is pulsed, and a precise GPS timing system allows one to only select the T2K beam neutrino events at SK with beam-unrelated backgrounds being  $\sim 0.002\%$ . The neutrinos before oscillation are measured at a near detector complex located at 280 m from the target, which consists of an on-axis detector(INGRID) and an off-axis detector(ND280) at  $2.5^\circ$ . Figure 7.3 shows a schematic drawing of ND280 which is a suite of several sub-detectors enclosed in a magnet producing magnetic field of 0.2 T. The primary components of ND280 used in the oscillation analysis are the fine-grained detectors (FGDs) which are plastic scintillator

### 7.1. T2K Experiment

---

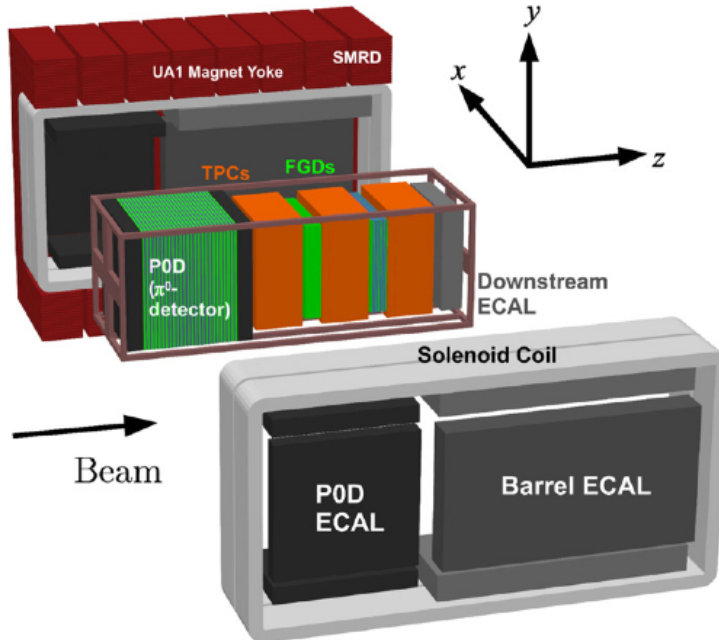


Figure 7.3: A schematic drawing of ND280. Figure taken from [87].

trackers and also serve as the target for neutrino interaction, and the time projection chambers (TPCs) which are placed next to the FGDs and are used to determine the type and the momentum of the particles produced in the FGDs. The near detectors are used to precisely measure the properties of the neutrino beam and neutrino cross sections in order to constrain the systematic uncertainties in oscillation analyses.

The initial goals of T2K are the discovery of  $\nu_\mu \rightarrow \nu_e$  oscillation induced by nonzero  $\theta_{13}$  and the precision measurement of  $\theta_{23}$  and  $\Delta m_{32}^2$  through  $\nu_\mu$  disappearance, i.e. the measurement of the survival probability  $\nu_\mu \rightarrow \nu_\mu$ . Given the value of  $\theta_{13}$  which is recently precisely measured by the reactor experiments, CP violation can also be probed by T2K through a CP-odd sub-leading term in the  $\nu_\mu \rightarrow \nu_e$  oscillation probability which depends on  $\sin \delta_{\text{CP}}$ :

$$\begin{aligned}
 P(\nu_\mu \rightarrow \nu_e) \approx & \sin^2 \theta_{23} \sin^2 2\theta_{13} \sin^2 \frac{\Delta m_{31}^2 L}{4E} \\
 & - \frac{\sin 2\theta_{12} \sin 2\theta_{23}}{2 \sin \theta_{13}} \sin \frac{\Delta m_{21}^2 L}{4E} \sin^2 2\theta_{13} \sin^2 \frac{\Delta m_{31}^2 L}{4E} \sin \delta_{\text{CP}} \\
 & + (\text{CP even, solar and matter effect terms}). \tag{7.1}
 \end{aligned}$$

## 7.2. $\nu_e$ Appearance Analysis

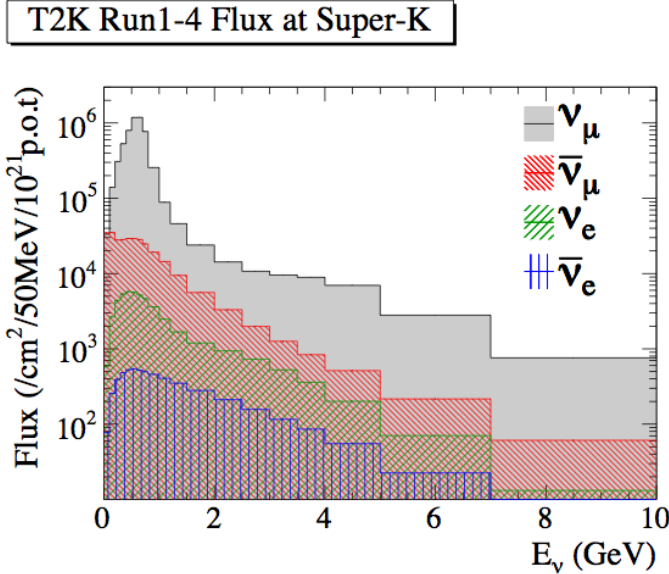


Figure 7.4: Predicted T2K neutrino flux at SK. Figure provided by the T2K beam working group.

## 7.2 $\nu_e$ Appearance Analysis

The initial goal of the T2K  $\nu_e$  appearance analysis is to discover the  $\nu_\mu \rightarrow \nu_e$  oscillation and precisely measure its oscillation probability, whose leading term depends on  $\sin^2 2\theta_{13}$  as shown in Equation 7.1. This is done by observing beam-induced  $\nu_e$  events appearing at SK in a beam which is originally produced consisting almost entirely of  $\nu_\mu$ . For a precise measurement, it is essential to accurately predict the neutrino flux at SK and also constrain the uncertainties related to neutrino interactions at SK, so that neutrino events can be simulated accurately and properly compared to the observed data for oscillation analyses.

For the neutrino flux prediction, hadron production at the graphite target is simulated using FLUKA[88] and the data from a dedicated hadron production experiment NA61/SHINE[89][90], and the propagation of the secondary particles are simulated by GEANT3[81] with GCALOR[82]. Figure 7.4 shows the predicted neutrino flux at SK based on the simulation. The flux consists mostly of  $\nu_\mu$ , however, there are some contaminations from  $\bar{\nu}_\mu$  and also  $\nu_e$  and  $\bar{\nu}_e$  which become irreducible backgrounds to  $\nu_e$  appearance analysis. The overall uncertainty on the absolute flux is estimated to be 10–15%, and it is dominated by the uncertainties in the hadron production.

## 7.2. $\nu_e$ Appearance Analysis

---

Other than the neutrino flux, T2K neutrino event simulation at SK is done following the same procedures as the atmospheric neutrino MC described in Chapter 4, using NEUT neutrino event generator and the GEANT3-based detector simulation SKDETSIM.

In order to constrain the systematic uncertainties related to the neutrino flux and cross sections, the data from ND280 is analyzed, namely, by performing a fit to the  $\nu_\mu$ CC interaction data in the FGDs. Taking the prior uncertainties on the flux simulation and the prior constraints on cross section model parameters estimated from external datasets such as [91][92][93], the neutrino energy spectrum and the NEUT interaction models are further constrained based on a simultaneous fit of the flux and cross section model parameters to the ND280 data. The resulting uncertainties on the model parameters after the fit are then propagated to the event predictions at SK and used in oscillation analysis. After the ND280 fit, the fractional total uncertainty on the expected number of  $\nu_e$  candidate events observed at SK reduces from 27.2% to 8.8% when assuming  $\sin^2 2\theta_{13} = 0.1$ .

The signal for  $\nu_e$  appearance at SK is observed as  $\nu_e$ CC events which are coincident with the beam. As CCQE is the dominant neutrino interaction mode at  $\sim 600$  MeV where the energy of the expected  $\nu_e$  appearance signal peaks at, single electron events are selected as candidate events for  $\nu_e$  appearance following the event selection criteria detailed in Section 7.3. According to the selection and assuming  $\sin^2 2\theta_{13} = 0.1$ , 21.6  $\nu_e$  candidate events are expected to be observed at the given beam exposure, out of which 4.3 events are backgrounds from beam-intrinsic  $\nu_e$  CC and NC events. Thus, the observation of a significant number of the selected  $\nu_e$  candidate events will be a clear evidence of  $\nu_e$  appearance.

Once  $\nu_e$  candidate events at SK are selected, an extended maximum likelihood fit is performed to obtain the neutrino oscillation parameters from the observed SK data. The likelihood is defined as:

$$L(N_{\text{obs}}, \vec{x} | \vec{\sigma}, \vec{f}) = L_{\text{norm}}(N_{\text{obs}} | \vec{\sigma}, \vec{f}) \times L_{\text{shape}}(\vec{x} | \vec{\sigma}, \vec{f}) \times L_{\text{syst}}(\vec{f}), \quad (7.2)$$

where  $N_{\text{obs}}$  is the number of observed  $\nu_e$  candidate events,  $\vec{x}$  represents the reconstructed kinematic variables for the candidate events,  $\vec{\sigma}$  is the oscillation parameters and  $\vec{f}$  represents the parameters for systematic uncertainties which include the parameters for the flux, neutrino interaction and the SK selection efficiencies.  $L_{\text{norm}}$  is the likelihood of observing  $N_{\text{obs}}$  events given the model parameters  $\vec{\sigma}$  and  $\vec{f}$ , and it is expressed as a Poisson distribution at the predicted event rate calculated with  $\vec{\sigma}$  and  $\vec{f}$ . For each observed event, its reconstructed momentum  $p_e$  and the angle  $\theta_e$  between

### 7.3. $\nu_e$ Event Selection

---

the directions of the neutrino beam and the observed electron are used as “shape” information in the likelihood term  $L_{\text{shape}}$  which is a 2D probability distribution for  $p_e - \theta_e$  given the model parameters. This is to improve the sensitivity to  $\nu_e$  appearance by taking advantage of the fact that the shape of the  $p_e - \theta_e$  distribution differs between the appearance signal and the background events. The predicted event rate for  $L_{\text{norm}}$  and  $p_e - \theta_e$  distribution for  $L_{\text{shape}}$  are both calculated using the T2K MC simulation.  $L_{\text{syst}}$  is the constraint on the parameters for systematic uncertainties, and the results from the ND280 fit mentioned above are used for the applicable parameters. During an oscillation fit, the parameters for systematic uncertainties are numerically integrated over at each point in the oscillation parameter space, and the resulting marginalized likelihood is then maximized with respect to the oscillation parameters of interest to obtain the best fit values.

## 7.3 $\nu_e$ Event Selection

Below summarizes the full event selection criteria for the  $\nu_e$  appearance analysis. In order to achieve high sensitivity to  $\nu_e$  appearance via  $\theta_{13}$ -induced oscillation, it is essential to keep the backgrounds unrelated to the oscillation signal as low as possible. The targeted event category for the signal is  $\nu_e$  CCQE which is a single electron event with no decay electrons. As discussed in Section 6.9.1, in SK,  $\pi^0$ 's are one of the major backgrounds to single electron events, and fiTQun is used in order to reduce the  $\pi^0$  background which contaminate the  $\nu_e$  candidate event sample. Other than the  $\pi^0$  rejection cut, the  $\nu_e$  event selection described below is done based on the information from APFIT[85], the preexisting reconstruction algorithm at SK before fiTQun was introduced as mentioned in Chapter 6.

T2K neutrino events at SK are first selected by a reduction process using a precise GPS timing system mentioned earlier, and then the FC selection as described in Section 5.5 using APFIT information is applied to select neutrino events whose interaction occur in the fiducial volume(FV) and are contained in the ID (T2K neutrino events passing such selection is referred to as FCFV). Then, single-ring events whose ring type is determined to be electron-like as opposed to muon-like are selected. In addition, in order to reject the events in which only a decay electron is seen, the reconstructed momentum of the electron ring is required to be  $> 100$  MeV/ $c$ . Since the targeted  $\nu_e$  CCQE events do not produce any decay electrons, it is also required that the number of detected decay electrons following the primary interaction is zero. Furthermore, only the events with the reconstructed

### 7.3. $\nu_e$ Event Selection

---

Parameter	Fixed value
$\sin^2 \theta_{12}$	0.306
$\sin^2 \theta_{23}$	0.50
$\Delta m_{21}^2$	$7.6 \times 10^{-5}$ eV $^2$
$ \Delta m_{32}^2 $	$2.4 \times 10^{-3}$ eV $^2$
$\delta_{\text{CP}}$	0

---

Table 7.1: Assumed values for the oscillation parameters.

neutrino energy  $E_\nu^{\text{rec}}$  being less than 1250 MeV are selected, since the events with larger  $E_\nu^{\text{rec}}$  are mostly beam-intrinsic  $\nu_e$  background events.  $E_\nu^{\text{rec}}$  is defined as:

$$E_\nu^{\text{rec}} = \frac{m_p^2 - (m_n - E_b)^2 - m_e^2 + 2(m_n - E_b)E_e}{2(m_n - E_b - E_e + p_e \cos \theta_e)}, \quad (7.3)$$

where  $m_p$  and  $m_n$  are the proton and the neutron mass respectively,  $E_b = 27$  MeV is the neutron binding energy in oxygen nucleus,  $m_e$  is the electron mass and  $E_e$  is the reconstructed total energy of the electron. Ignoring the Fermi momentum of the target neutron, the above equation gives the energy of the incident  $\nu_e$  based on the two body kinematics of  $\nu_e + n \rightarrow e + p$ , using the observed  $p_e$  and  $\theta_e$ .

After the above selection cuts based on APFIT are applied, the final cut to reduce the remaining NC  $\pi^0$  backgrounds are applied using fitQun, namely, the cut described by Equation 6.28. Table 7.2 shows the expected number of signal and background events after each stage of the selection cuts, assuming  $\sin^2 2\theta_{13} = 0.1$ , normal hierarchy and other oscillation parameters set to the values in Table 7.1. As in the table, the NC background remaining after the single-ring electron-like selections, which is dominated by NC  $\pi^0$  events, is drastically reduced after applying the fitQun  $\pi^0$  cut, while the loss in the  $\nu_\mu \rightarrow \nu_e$  CC appearance signal events by the cut is small. The final sample selected after all the cuts above has a  $\nu_\mu \rightarrow \nu_e$  CC signal purity of 80.2 %, while the background contamination from NC events is only 4.4 %. The remaining backgrounds are predominantly the irreducible backgrounds from CC interactions from the beam-intrinsic  $\nu_e$  and  $\bar{\nu}_e$ , i.e. the  $\nu_e$  and  $\bar{\nu}_e$  components at neutrino flux production as shown in Figure 7.4.

In the previous T2K  $\nu_e$  appearance analysis[28], a different method was employed for  $\pi^0$  rejection. Using a dedicated  $\pi^0$  reconstruction algorithm which assumes two electron-like rings and force-reconstructs an event as a  $\pi^0$  based on the light patterns[94], an invariant mass is calculated from the reconstructed momenta and the directions of the two rings, and  $\pi^0$

## 7.4. Results

Selection	Expected				Data	
	$\nu_\mu + \bar{\nu}_\mu$ CC	$\nu_e + \bar{\nu}_e$ CC	NC	BG total	$\nu_\mu \rightarrow \nu_e$ CC	
FCFV	247.75	15.36	83.02	346.13	26.22	377
Single-ring	142.44	9.82	23.46	175.72	22.72	193
Electron-like PID	5.63	9.74	16.35	31.72	22.45	60
$p_e > 100\text{MeV}/c$	3.66	9.68	13.99	27.32	22.04	57
No decay-e	0.69	7.87	11.84	20.40	19.63	44
$E_\nu^{\text{rec}} < 1250\text{MeV}$	0.21	3.73	8.99	12.94	18.82	39
Previous $\pi^0$ cut	0.13	3.41	2.55	6.08	17.69	31
fitQun $\pi^0$ cut	0.07	3.24	0.96	4.27	17.32	28
Fraction [%]	0.3	15.0	4.4	19.8	80.2	-
Efficiency [%]	0.0	21.1	1.2	1.2	66.0	-

Table 7.2: Expected numbers of signal and background events passing each selection stage with the assumption  $\sin^2 2\theta_{13} = 0.1$ , normal hierarchy and other oscillation parameters set to the values in Table 7.1. The fraction of each event category in the final selected sample is also shown, and the efficiency of the overall selection is calculated taking the FCFV event rates as the denominator. The shaded row also shows the event rates in the case of applying the previous  $\pi^0$  rejection method[28] as opposed to the fitQun  $\pi^0$  cut. Data taken from January 2010 to May 2013 which has the neutrino beam exposure of  $6.57 \times 10^{20}$  POT(protons on target) is also shown on the rightmost column, and the MC expectations are normalized to the same exposure.

rejection is done by selecting the events with the invariant mass being less than  $105\text{ MeV}/c^2$  as shown in Figure 7.5. The predicted event rates for the signal and backgrounds in the case of employing the previous  $\pi^0$  rejection method, instead of the fitQun  $\pi^0$  cut, are shown in the shaded row in Table 7.2. As in the table, the remaining NC background in the final selected sample is reduced by  $\sim 62\%$  by replacing the previous method with the fitQun cut, while the efficiency loss for the appearance signal is only  $\sim 2\%$ .

## 7.4 Results

The results of analyzing the data taken from January 2010 to May 2013 which has the neutrino beam exposure of  $6.57 \times 10^{20}$  POT(protons on target) is the following. As shown in Table 7.2, 28 events are observed as  $\nu_e$

## 7.4. Results

---

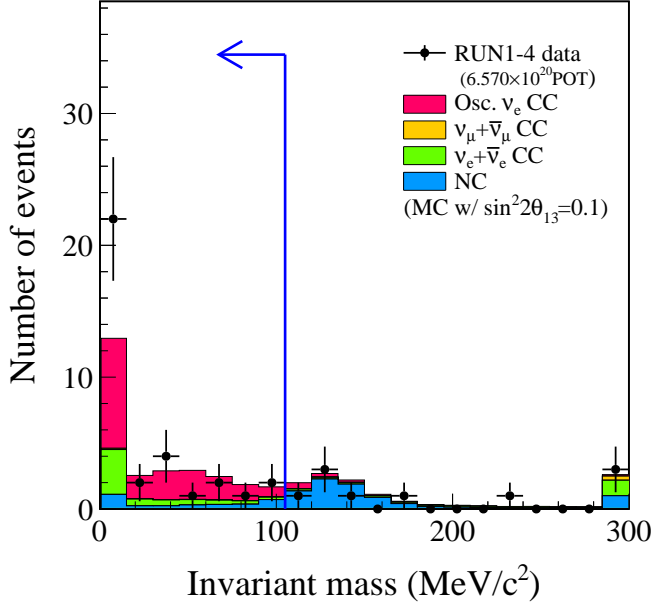


Figure 7.5:  $\pi^0$  rejection cut which was used in the previous  $\nu_e$  appearance analysis[28]. The reconstructed invariant mass calculated by a dedicated  $\pi^0$  reconstruction algorithm is required to be less than  $105 \text{ MeV}/c^2$  for an event to be selected as a  $\nu_e$  candidate. As in the plot, the NC backgrounds which are dominated by NC  $\pi^0$  events produce a peak near the  $\pi^0$  mass of  $\sim 135 \text{ MeV}/c^2$  and are largely rejected by the cut. The data and the expectations shown in the plot are for the dataset shown in Table 7.2.

candidates, and Figure 7.6 shows the 2D distribution of the fitQun  $\pi^0$  cut variables for the observed data after the  $E_\nu^{\text{rec}} < 1250 \text{ MeV}$  cut.

Using the observed data, a maximum likelihood fit as described in Section 7.2 is performed by fitting for  $\sin^2 2\theta_{13}$  only, while other oscillation parameters are fixed at the values in Table 7.1. The fit results in the best-fit value and the 68% confidence interval of  $\sin^2 2\theta_{13} = 0.140^{+0.038}_{-0.032}$  assuming normal hierarchy and  $\sin^2 2\theta_{13} = 0.170^{+0.045}_{-0.037}$  assuming inverted hierarchy, and the best-fit prediction of the  $p_e - \theta_e$  distribution overlaid with the observed data are shown in Figure 7.7.

The significance for nonzero  $\theta_{13}$  was calculated by generating a large number of toy experiments assuming  $\theta_{13} = 0$  and calculating a p-value. While generating the toy experiments, other oscillation parameters are fixed at the values on Table 7.1, and systematic uncertainties are randomly thrown

## 7.4. Results

---

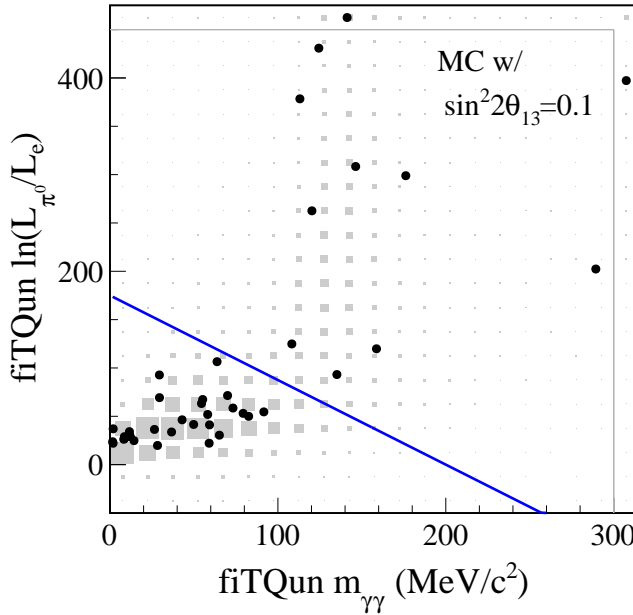


Figure 7.6: 2D distribution of the fitQun  $\pi^0$  cut variables after the  $E_\nu^{\text{rec}} < 1250\text{MeV}$  cut, for the dataset shown in Table 7.2. The horizontal axis is the reconstructed invariant mass from the  $\pi^0$  fit, and the vertical axis is the log likelihood ratio between the  $\pi^0$  and the single-ring electron fits. The black markers indicate the observed data and the gray box histograms are MC expectations. The events below the blue line are selected as the final  $\nu_e$  candidate events.

according to their prior uncertainties. Then, a test statistic defined as:

$$\Delta\chi^2 := -2 \times (\ln L'(\sin^2 2\theta_{13} = 0) - \ln L'(\sin^2 2\theta_{13}^{\text{best}})), \quad (7.4)$$

is calculated for each toy experiment, where  $L'$  is the likelihood marginalized over systematics and  $\sin^2 2\theta_{13}^{\text{best}}$  is the best-fit value obtained from data mentioned above. The p-value is then defined as the fraction of toy experiments which have  $\Delta\chi^2 > 53.64$ , where 53.64 is the  $\Delta\chi^2$  for the observed data. After producing  $10^{15}$  fake experiments the p-value is calculated to be  $1.0 \times 10^{-13}$ , which is equivalent to the exclusion of  $\theta_{13} = 0$  at  $7.3\sigma$  significance and shows a clear discovery  $\nu_e$  of appearance.

## 7.4. Results

---

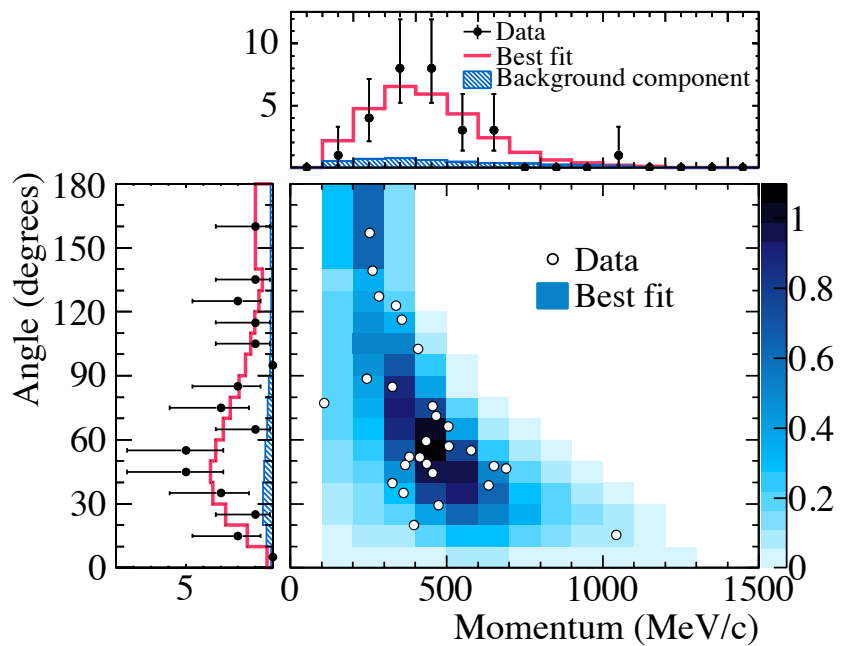


Figure 7.7: The best-fit (for normal hierarchy)  $p_e - \theta_e$  distribution plotted with the observed data. The 1D plots on the top and the left are the 1D  $p_e$  and  $\theta_e$  distributions respectively. Figure taken from [29].

## Chapter 8

# Atmospheric Neutrino Oscillation Analysis

In this chapter, a neutrino oscillation analysis using the SK atmospheric neutrino data is described in detail. As mentioned in Chapter 1, in atmospheric neutrino data, oscillation effects manifest in the energy and the zenith angle distributions of the observed neutrino events. In this analysis, the atmospheric neutrino data is first selected into several subsamples in order to separate the events in terms of neutrino type, and for each sample the events are binned in the 2D distribution of the observed momentum and the zenith angle of the direction. The oscillation parameters are then extracted by comparing the binned data to the expectation calculated from MC simulation at different oscillation parameters.

The dataset used in this analysis is the FC data in SK-IV, and reconstructed particle information from `fitQun` described in Chapter 6 is used for selecting and binning the data. For oscillation parameter estimation, a Markov Chain Monte Carlo technique is employed to make Bayesian predictions on the oscillation parameters based on the observed data. The following sections describe each of the analysis elements in detail.

### 8.1 Event Selection and Binning

This section describes the event selection and the binning which is used as an input for the oscillation analysis. FC data is categorized into subsamples based on the reconstructed particle information from `fitQun`, and then binned in reconstructed momentum and zenith angle. Since the oscillation effects manifest differently between the flavours of atmospheric neutrinos as described in Chapter 1, it is important to implement an event selection scheme which is capable of categorizing the observed neutrino events by neutrino flavour. In addition to separating the events by neutrino flavour(electron or muon) based on the reconstructed ring type, statistical separations of neutrinos and antineutrinos are done in order to improve the

### 8.1. Event Selection and Binning

---

sensitivity to the oscillation effects such as the ones from the mass hierarchy, which happen differently for neutrinos and antineutrinos.

#### 8.1.1 Selection Criteria

The events which are used in the analysis are the FC events as described in Chapter 5 which have the visible energy greater than 30 MeV. The visible energy,  $E_{\text{vis}}$ , is defined as the sum of the reconstructed kinetic energy above Cherenkov threshold for all rings, taking into account the assumed particle type (electron, muon or  $\pi^+$ ) of each ring. The fiducial volume cut is also applied, which requires that the distance from the reconstructed vertex of the most energetic ring to the nearest point on the wall to be greater than 200 cm. The events which pass these basic selections are further divided into 13 event categories based on the reconstructed information from fitQun as follows:

1. **Sub-GeV one-ring e-like 0 decay**

$E_{\text{vis}} < 1330 \text{ MeV}$ , one e-like ring with momentum  $> 100 \text{ MeV}/c$ ,  $n_{\text{dcy}} = 0$ .

2. **Sub-GeV one-ring e-like  $\geq 1$  decay**

$E_{\text{vis}} < 1330 \text{ MeV}$ , one e-like ring with momentum  $> 100 \text{ MeV}/c$ ,  $n_{\text{dcy}} \geq 1$ .

3. **Sub-GeV one-ring  $\mu$ -like 0 decay**

$E_{\text{vis}} < 1330 \text{ MeV}$ , one  $\mu$ -like ring with momentum  $> 200 \text{ MeV}/c$ ,  $n_{\text{dcy}} = 0$ .

4. **Sub-GeV one-ring  $\mu$ -like 1 decay**

$E_{\text{vis}} < 1330 \text{ MeV}$ , one  $\mu$ -like ring with momentum  $> 200 \text{ MeV}/c$ ,  $n_{\text{dcy}} = 1$ .

5. **Sub-GeV one-ring  $\mu$ -like  $\geq 2$  decay**

$E_{\text{vis}} < 1330 \text{ MeV}$ , one  $\mu$ -like ring with momentum  $> 200 \text{ MeV}/c$ ,  $n_{\text{dcy}} \geq 2$ .

6. **Sub-GeV two-ring  $\pi^0$**

$E_{\text{vis}} < 1330 \text{ MeV}$ , two e-like rings,  $n_{\text{dcy}} = 0$ , reconstructed invariant mass calculated from the two rings in the range  $85\text{-}215 \text{ MeV}/c^2$ .

7. **Multi-GeV one-ring e-like  $\nu_e$**

$E_{\text{vis}} > 1330 \text{ MeV}$ , one e-like ring,  $n_{\text{dcy}} \geq 1$

8. **Multi-GeV one-ring e-like  $\bar{\nu}_e$**

$E_{\text{vis}} > 1330 \text{ MeV}$ , one e-like ring,  $n_{\text{dcy}} = 0$

9. **Multi-GeV one-ring  $\mu$ -like**

$E_{\text{vis}} > 1330 \text{ MeV}$ , one  $\mu$ -like ring

### 8.1. Event Selection and Binning

---

#### 10. Multi-GeV multi-ring e-like $\nu_e$

$E_{\text{vis}} > 1330 \text{ MeV}$ , two or more rings, highest momentum ring is e-like, passes the MME selection cut, passes the multi-ring  $\nu_e$ -like cut.

#### 11. Multi-GeV multi-ring e-like $\bar{\nu}_e$

$E_{\text{vis}} > 1330 \text{ MeV}$ , two or more rings, highest momentum ring is e-like, passes the MME selection cut, fails the multi-ring  $\nu_e$ -like cut.

#### 12. Multi-GeV multi-ring $\mu$ -like

$E_{\text{vis}} > 600 \text{ MeV}$ , two or more rings, highest momentum ring is  $\mu$ -like, momentum of the  $\mu$ -like ring  $> 600 \text{ MeV}/c$ .

#### 13. Multi-GeV multi-ring e-like other

$E_{\text{vis}} > 1330 \text{ MeV}$ , two or more rings, highest momentum ring is e-like, fails the MME selection cut.

In the selection criteria above,  $n_{\text{dcy}}$  is the number of decay electrons, which is defined as the number of subevents minus 1 as described in Section 6.6.2. As discussed in Section 8.1.2, neutrinos and antineutrinos can be statistically separated using the decay electron information. In addition to the e-like and  $\mu$ -like samples which are the enriched samples of  $\nu_e$ CC and  $\nu_\mu$ CC events respectively, the two-ring  $\pi^0$  sample is included in the analysis in order to constrain the NC background in the e-like samples. The definitions of the MME selection cut and the multi-ring  $\nu_e$ -like cut which are applied to the multi-GeV multi-ring e-like samples are detailed in Section 8.1.3. In multi-GeV, while the e-like samples are statistically separated into  $\nu_e$  and  $\bar{\nu}_e$  enriched samples, no neutrino-antineutrino separation is done to the  $\mu$ -like samples, mainly due to the lack of statistics to give any noticeable improvement in the mass hierarchy sensitivity.

#### 8.1.2 $\nu/\bar{\nu}$ Separation for Single-Ring Events

A large fraction of the events selected as single-ring are CCQE events. In a CCQE event, the particles which are left after the neutrino interaction are the outgoing charged lepton and a nucleon, a proton or a neutron depending on whether it is a neutrino or antineutrino interaction. As the lepton charge is indistinguishable in a water Cherenkov detector and the emitted proton is usually below Cherenkov threshold, separating neutrinos and antineutrinos in the CCQE channel is therefore difficult.

The situation is, however, different for CC single charged pion events which are categorized as single-ring due to the pion momentum being below

### 8.1. Event Selection and Binning

---

Cherenkov threshold. Consider the CC1 $\pi^\pm$  interaction for a neutrino and an antineutrino:

$$\nu_\alpha + N \rightarrow l_\alpha^- + N + \pi^+, \quad (8.1)$$

$$\bar{\nu}_\alpha + N \rightarrow l_\alpha^+ + N + \pi^-. \quad (8.2)$$

For the case of neutrino, the produced  $\pi^+$  often decays into a  $\mu^+$ , which subsequently produces a decay positron which will be detected. For antineutrino, on the other hand, the emitted  $\pi^-$  in most cases gets absorbed by the nuclei in water, and the interaction therefore leaves no decay electron. Thus, a single-ring event with an extra decay electron being detected has a higher chance of being a neutrino event, rather than antineutrino. The event selection criteria in Section 8.1.1 thus subdivides the single-ring events further into neutrino-enriched and antineutrino-enriched samples by the number of decay electrons. For instance, the “Sub-GeV one-ring e-like  $\geq 1$  decay” sample has high concentration of  $\nu_e$  with significantly less  $\bar{\nu}_e$ , and the “Sub-GeV one-ring  $\mu$ -like  $\geq 2$  decay” sample, in which in most cases the decay electrons from the primary muon and a  $\pi^+$  are both detected, consists mostly of  $\nu_\mu$  with small  $\bar{\nu}_\mu$  content.

#### 8.1.3 Multi-Ring $\nu_e/\bar{\nu}_e$ Selection

As the fraction of multi-ring events increases at higher energy, multi-ring event samples are also included in the analysis in multi-GeV. Due to the complexity of multi-ring events, it is in general more difficult to achieve high purity of the targeted event types in a multi-ring event category compared to the single-ring case. The multi-ring e-like event sample, as selected by requiring the highest momentum ring to be e-like, has rather high contamination of  $\nu_\mu$ CC and NC events.

In order to reduce such backgrounds, a likelihood selection is applied to subdivide the Multi-GeV Multi-ring E-like(MME) sample into a  $\nu_e + \bar{\nu}_e$ CC enriched sample and a background enriched sample. Below are the descriptions of the four variables which are input to the likelihood selection, whose distributions are shown in Figure 8.1:

##### 1. Energy fraction of the Most Energetic Ring

The fraction of the visible energy of the Most Energetic Ring(MER) to the total visible energy. The definition of the visible energy is stated in Section 8.1.1. The variable tends to be large for  $\nu_e + \bar{\nu}_e$ CC events since the outgoing electron often carries a large fraction of the event’s energy, whereas the value is small for  $\nu_\mu + \bar{\nu}_\mu$ CC and NC events in

### 8.1. Event Selection and Binning

---

the same visible energy range since often in such events the MER is a gamma ring from a  $\pi^0$  and the hadronic system carrying large energy produces large number of rings and deposit larger energy outside of the MER.

#### 2. Energy fraction of the Most Energetic $\pi^+$ -like Ring

The fraction of the visible energy of the Most Energetic  $\pi^+$ -like(ME $\pi^+$ ) ring to the total visible energy. The value is set to zero if there is no  $\pi^+$ -like ring found. The  $\nu_\mu + \bar{\nu}_\mu$ CC events which are categorized as multi-ring e-like usually have a rather low momentum muon ring whose visible energy is lower than another ring such as the  $\gamma$  ring from a  $\pi^0$  decay. For such events the muon ring is often reconstructed as a  $\pi^+$ -like ring, and the ring tends to have higher energy than a true  $\pi^+$  ring which is produced in  $\nu_e + \bar{\nu}_e$  and NC events. The variable thus effectively discriminates  $\nu_\mu + \bar{\nu}_\mu$ CC events from the rest.

#### 3. Number of decay electrons

Number of decay electrons as defined in Section 8.1.1. The value tends to be larger for  $\nu_\mu + \bar{\nu}_\mu$ CC and NC events since the hadronic system carrying large energy produces large number of decay electrons for such events.

#### 4. Distance to the farthest decay electron

The distance between the vertices of the most energetic ring and the most distant decay electron, normalized by the visible energy of the most energetic ring. The variable is set to zero if there is no decay electron detected. The variable tends to be larger for  $\nu_\mu + \bar{\nu}_\mu$ CC events since the muon in such events travel longer distance than charged pions in  $\nu_e + \bar{\nu}_e$ CC events.

As shown in Figure 8.1, the variables provide power to discriminate between  $\nu_e + \bar{\nu}_e$ CC events and the backgrounds. For event selection, the normalized distributions for signal( $\nu_e + \bar{\nu}_e$ CC) and background( $\nu_\mu + \bar{\nu}_\mu$ CC and NC) for each variable are produced and used as likelihood functions. For a given event,  $\ln(L_{\text{sig}}/L_{\text{bkg}})$ , the log likelihood ratio of assuming the event as a signal and a background, is evaluated for each of the four variables using the likelihood functions, and the sum of the four log likelihood ratios is then used to make a selection cut. Figure 8.2 is the distribution of the cut variable for inclusive multi-GeV multi-ring e-like events where the signal and the background are shown separately, and the signal( $\nu_e + \bar{\nu}_e$ CC) enriched sample is selected by applying a cut as  $>-0.25$  which was determined based

### 8.1. Event Selection and Binning

---

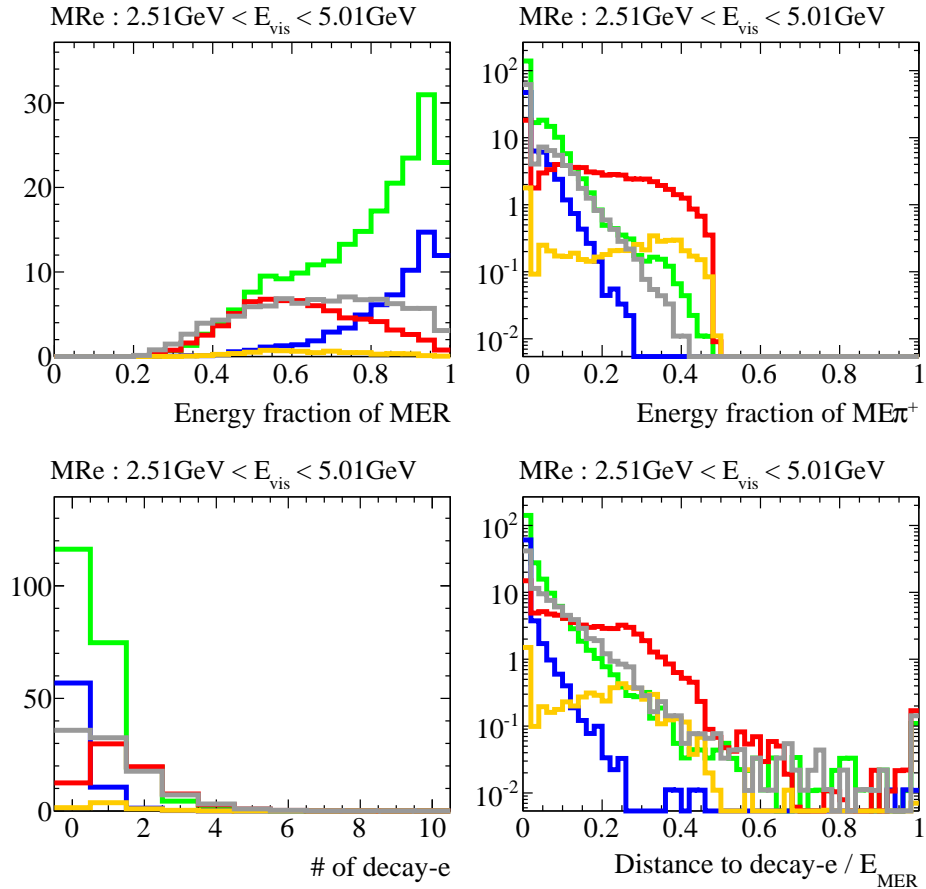


Figure 8.1: Distribution of the variables which are used for the Multi-GeV Multi-ring E-like(MME) likelihood selection, for the multi-ring e-like events with visible energy in the range 2.51-5.01 GeV. Distributions are shown separately for  $\nu_e\text{CC}$ (green),  $\bar{\nu}_e\text{CC}$ (blue),  $\nu_\mu\text{CC}$ (red),  $\bar{\nu}_\mu\text{CC}$ (yellow) and NC(gray).

### 8.1. Event Selection and Binning

---

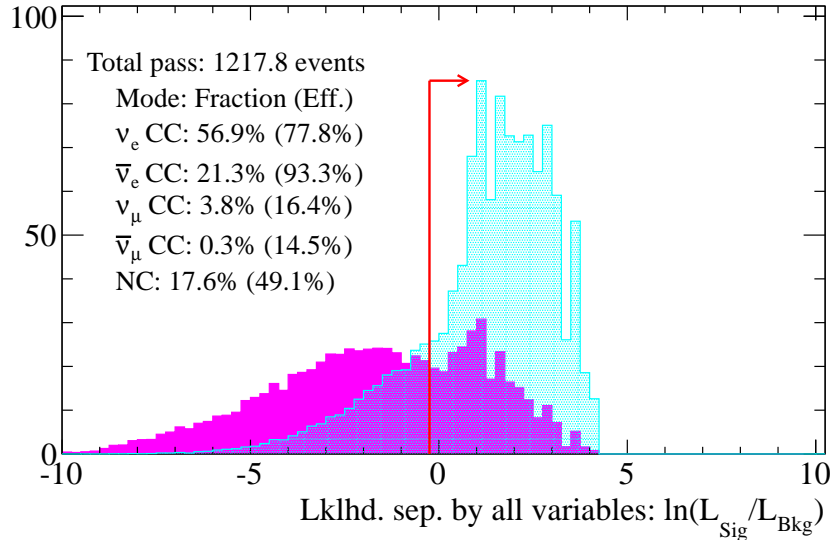


Figure 8.2: Distribution of the sum of  $\ln(L_{\text{sig}}/L_{\text{bkg}})$  for all four MME selection variables, for inclusive multi-GeV multi-ring e-like events. The distribution is shown separately for signal( $\nu_e + \bar{\nu}_e$  CC) and background( $\nu_\mu + \bar{\nu}_\mu$  CC and NC) in cyan and magenta respectively. The MME selection cut is applied at -0.25 as indicated by the red arrow, and the interaction mode breakdown of the selected sample is shown in the figure. The efficiency for passing the cut is shown in the parenthesis for each interaction mode. For comparison, the fraction of  $\nu_e$  CC and  $\bar{\nu}_e$  CC events before the selection cut is applied are 46.4% and 14.5% respectively.

on sensitivity. The events which are rejected by this cut are categorized as the “Multi-GeV multi-ring e-like other” sample.

Once the  $\nu_e + \bar{\nu}_e$  CC enriched sample is selected by the MME selection cut, another likelihood selection is applied, this time, to separate the  $\nu_e$  CC events from  $\bar{\nu}_e$  CC events. The selection is done in a similar manner as above using the following three variables:

1. **Number of rings**
2. **Number of decay electrons**
3. **Transverse momentum fraction**

## 8.1. Event Selection and Binning

---

Defined as:

$$p_{\text{tran}} := \sum_i E_{\text{vis}}^i \sin \theta_i / E_{\text{vis}}, \quad (8.3)$$

where  $\theta_i$  is the angle between each ring and the most energetic ring,  $E_{\text{vis}}^i$  is the visible energy of the ring and  $E_{\text{vis}}$  is the sum of the visible energies of all rings.

The variables are motivated by the fact that  $\nu_e$  scattering tends to be less forward peaked and have larger energy transferred to the hadronic system compared to  $\bar{\nu}_e$ , and as shown in Figure 8.3, the variables tend to be larger for  $\nu_e$  than  $\bar{\nu}_e$ . Similar to what was done for the MME selection, likelihood functions for  $\nu_e$ CC and  $\bar{\nu}_e$ CC are produced using the distributions, and then for a given event  $\ln(L_{\nu_e}/L_{\bar{\nu}_e})$ , the likelihood ratio between the  $\nu_e$  and  $\bar{\nu}_e$  hypotheses, is evaluated for each variable. The distribution of the sum of  $\ln(L_{\nu_e}/L_{\bar{\nu}_e})$  for all variables are shown in Figure 8.4, and the events passing the cut at  $>0$  are selected as the “Multi-GeV multi-ring e-like  $\nu_e$ ” sample, while the ones rejected are categorized as “Multi-GeV multi-ring e-like  $\bar{\nu}_e$ ”.

### 8.1.4 Sample Statistics and Purities

Table 8.1 shows the statistics and the interaction mode breakdown of each event sample selected by the selections in Section 8.1.1. Event rates for data and MC expectation are both shown in the table, and the expected event rates are calculated assuming two-flavour  $\nu_\mu \rightarrow \nu_\tau$  oscillations at  $\sin^2 2\theta = 1.0$  and  $\Delta m^2 = 2.5 \times 10^{-3}$  eV<sup>2</sup> and are normalized to 2519.89 days exposure which is the same as data. Note that the expectations for  $\nu_\tau + \bar{\nu}_\tau$ CC events are not shown on the table, however, they are properly considered in the actual oscillation analysis. It can be seen from the table that the event selection achieves the intended separation of observed events by neutrino type, namely, the  $\nu_e$ -enriched samples as selected in Sections 8.1.2 and 8.1.3 have high purity of  $\nu_e$  with low  $\bar{\nu}_e$  contamination.

As demonstrated in Section 6.10.3, fiTQun achieves a significantly better performance in reconstructing multi-ring events compared to the preexisting APFIT algorithm. In order to see the improvement in the atmospheric neutrino selection made by fiTQun, the event sample breakdown for an equivalent event selection using APFIT is shown in Appendix B.

### 8.1.5 Binning

Figure 8.5 shows the binning scheme for each event sample. The events in each sample are binned in the observed momentum and zenith angle in order

### 8.1. Event Selection and Binning

---

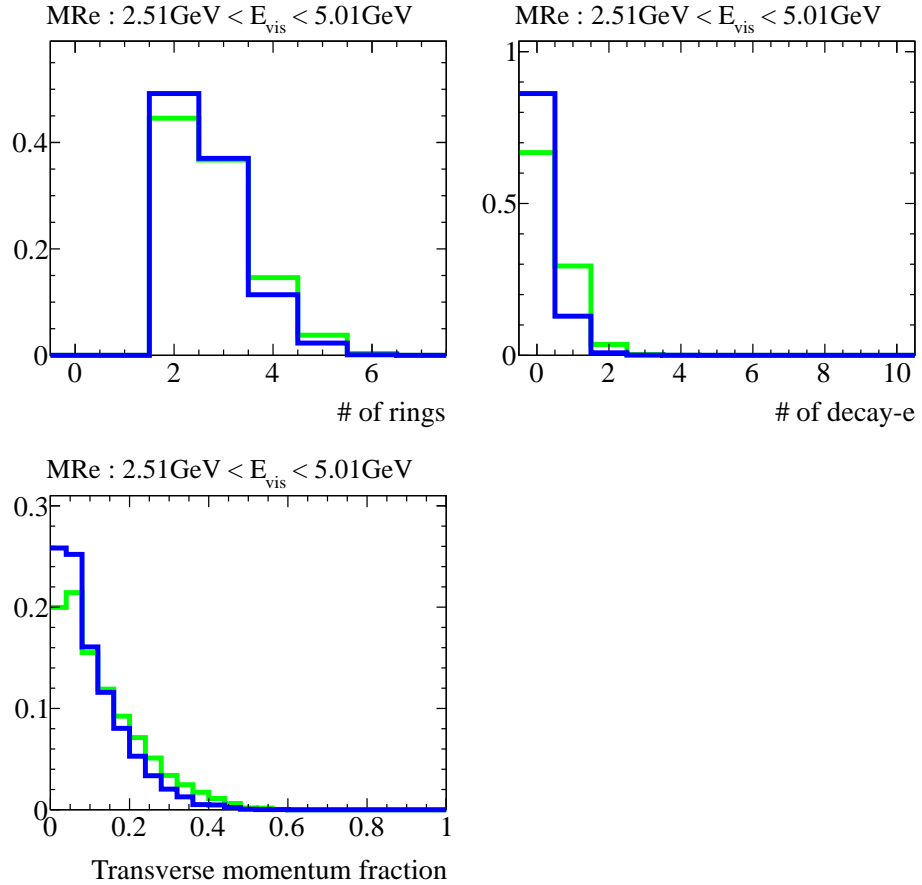


Figure 8.3: Distribution of the variables which are used for the multi-ring  $\nu_e/\bar{\nu}_e$  likelihood separation, for the multi-ring e-like events passing the MME selection cut with visible energy in the range 2.51-5.01 GeV. Distributions are shown separately for  $\nu_e\text{CC}$ (green) and  $\bar{\nu}_e\text{CC}$ (blue). Each distribution is area normalized for easier comparison of the shape.

### 8.1. Event Selection and Binning

---

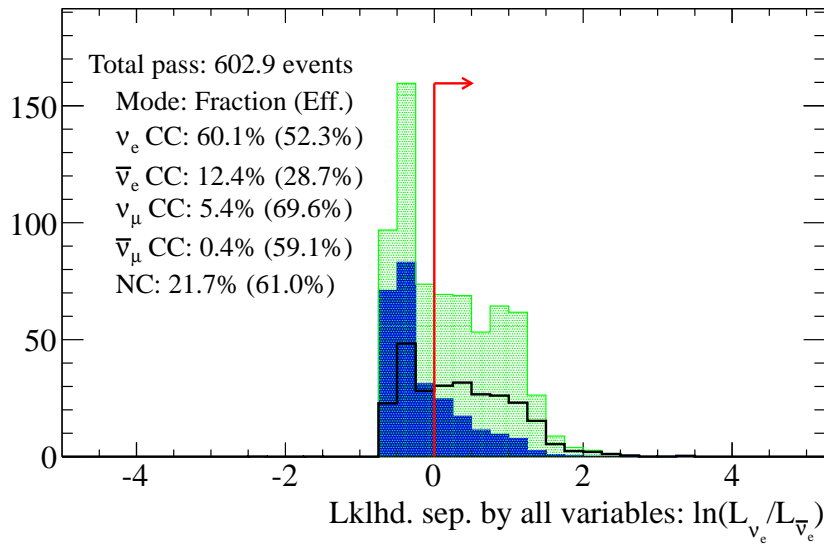


Figure 8.4: Distribution of the sum of  $\ln(L_{\nu_e}/L_{\bar{\nu}_e})$  for all three  $\nu_e/\bar{\nu}_e$  separation variables, for multi-GeV multi-ring e-like events passing the MME selection. The distribution is shown separately for  $\nu_e$ CC,  $\bar{\nu}_e$ CC and background( $\nu_\mu + \bar{\nu}_\mu$ CC and NC) in green, blue and black respectively. The  $\nu_e$ -like selection cut is applied at 0 as indicated by the red arrow, and the interaction mode breakdown of the selected sample is shown in the figure. The efficiency for passing the cut is shown in the parenthesis for each interaction mode. For comparison, the fraction of  $\nu_e$ CC and  $\bar{\nu}_e$ CC events before the selection cut is shown are 56.9% and 21.3% respectively.

### 8.1. Event Selection and Binning

---

%	1Re $0_{\text{dcy}}$	1Re $\geq 1_{\text{dcy}}$	1R $\mu$ $0_{\text{dcy}}$	1R $\mu$ $1_{\text{dcy}}$	1R $\mu$ $\geq 2_{\text{dcy}}$	2R $\pi^0$
$\nu_e$ CC	73.22	91.30	0.92	0.02	0.00	5.00
$\bar{\nu}_e$ CC	23.96	2.14	0.35	0.00	0.00	1.49
$\nu_\mu$ CC	0.10	2.46	69.82	68.15	94.86	0.81
$\bar{\nu}_\mu$ CC	0.02	0.60	10.08	29.38	3.57	0.08
NC	2.70	3.50	18.83	2.45	1.57	92.61
Total event rate						
MC	4876.2	450.7	851.7	4378.1	356.5	1130.5
Data	4677	450	814	4412	378	1095
%	1Re $\nu_e$	1Re $\bar{\nu}_e$	1R $\mu$	MRe $\nu_e$	MRe $\bar{\nu}_e$	MRe oth.
$\nu_e$ CC	75.39	56.11	0.02	60.15	53.70	0.92
$\bar{\nu}_e$ CC	8.26	38.35	0.02	12.38	30.14	0.11
$\nu_\mu$ CC	4.55	0.22	59.71	5.36	2.30	72.56
$\bar{\nu}_\mu$ CC	0.93	0.05	40.20	0.38	0.26	24.07
NC	10.87	5.27	0.05	21.73	13.61	2.34
Total event rate						
MC	161.2	839.1	763.0	602.9	614.9	1627.0
Data	174	773	721	585	536	1562
						807

Table 8.1: Interaction mode breakdown and the total event rates for each event sample, where the upper and the lower table is for sub-GeV and multi-GeV samples respectively. Event rates for MC and data are both shown in the tables. MC expectations are calculated with two-flavour oscillations at  $\sin^2 2\theta=1.0$  and  $\Delta m^2=2.5 \times 10^{-3}$  eV $^2$  and is normalized to the same 2519.89 days exposure as data.

### 8.1. Event Selection and Binning

---

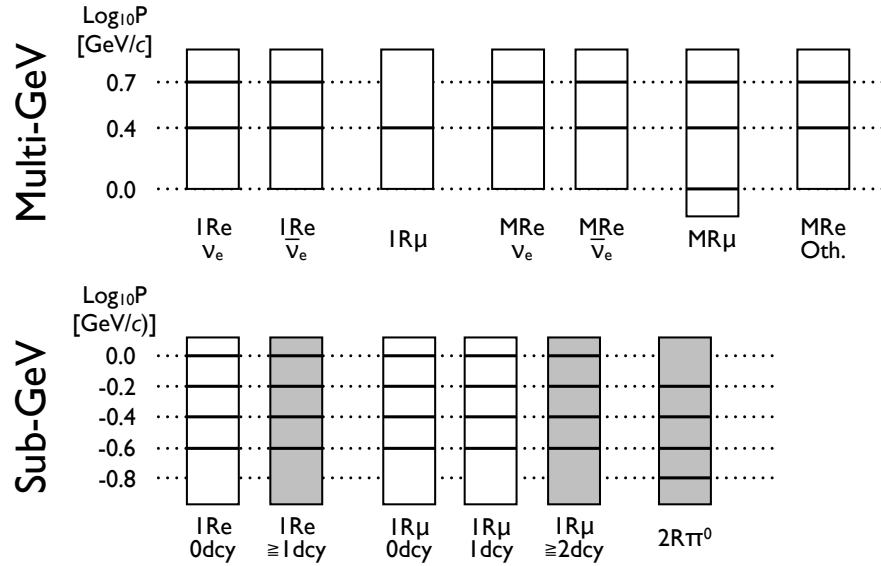


Figure 8.5: Binning for each event sample. In the figure, the momentum bin edges are shown in the  $\log_{10}$  of the momentum in  $\text{GeV}/c$ , and the highest and the lowest momentum bins in each sample are overflow and underflow bins respectively. The unshaded samples are further subdivided into 10 bins in the cosine of the zenith angle equally spaced in  $[-1, +1]$ , while there is no zenith angle subdivision for the shaded samples.

to extract the oscillation pattern as mentioned before, and for single-ring events the momentum and the zenith angle of the direction of the observed ring are used. For multi-ring events, the total visible energy  $E_{\text{vis}}$  is used as the “generalized momentum”, and the direction of the reconstructed total 3-momentum vector is used for the zenith angle. The zenith angle is binned in 10 bins equally spaced in the cosine of the zenith angle, except for some samples whose statistics are too low such that the statistical fluctuation of MC expectation becomes problematic, or have no directional sensitivity.

#### 8.1.6 Observing the Oscillation Effects

Once the events are selected and binned, the binned data is compared against the expectations and the oscillation parameters are estimated. In order to see how the oscillation effects are observed in each sample, the effects of varying each oscillation parameter on the predicted zenith distributions are

### 8.1. Event Selection and Binning

---

Parameter	Default Value
$\sin^2 \theta_{12}$	0.304
$\sin^2 \theta_{13}$	0.0219
$\sin^2 \theta_{23}$	0.50
$\Delta m_{21}^2$	$7.53 \times 10^{-5} \text{ eV}^2$
$\Delta m_{32}^2$	$+2.39 \times 10^{-3} \text{ eV}^2$ (NH)
$\delta_{\text{CP}}$	0

Table 8.2: Default values for the oscillation parameters which are used for event rate calculation.

shown below. Full three-flavour oscillations including the matter effect are considered, with the base values for the oscillation parameters set to what are shown in Table 8.2. The event rates are normalized to the data-equivalent 2519.89 days exposure. In the zenith distributions,  $\cos \theta_Z < 0$  is for upward-going events and  $\cos \theta_Z > 0$  is for downward-going. The discussions below follow the discussions of atmospheric neutrino oscillations in Section 1.5.

Figure 8.6 shows the zenith distributions for the sub-GeV e-like and  $\mu$ -like samples when  $\sin^2 \theta_{23}$  is varied as 0.4, 0.5 and 0.6. Since the  $\mu$ -like sample mainly observes  $\nu_\mu$  disappearance which depends on  $\sin^2 2\theta_{23}$ , the observed event rate is minimized when  $\theta_{23}=45^\circ$ , i.e.  $\sin^2 \theta_{23}=0.5$ , and any deviation from that will increase the event rates. For the e-like sample on the other hand, the  $\Delta m_{21}^2$ -induced oscillation which depends on  $\cos^2 \theta_{23}$  is important in sub-GeV, and thus an excess of event rate is seen when  $\theta_{23} < 45^\circ$  while a deficit is seen when  $\theta_{23} > 45^\circ$ . Thus, the sub-GeV e-like sample is sensitive to the  $\theta_{23}$  octant.

Figure 8.7 shows the effect of  $\sin^2 \theta_{23}$  on the multi-GeV e-like samples. These samples observe the enhanced  $\nu_e$  appearance by the MSW resonance effect which is proportional to  $\sin^2 \theta_{23}$ . Therefore, we see a corresponding excess or deficit of the upward-going e-like events depending on whether  $\sin^2 \theta_{23}$  is greater or smaller than 0.5.

The most noticeable effect from  $\delta_{\text{CP}}$  is the enhancement of sub-GeV  $\nu_e$  events when  $-\pi < \delta_{\text{CP}} < 0$ , as seen in Figure 8.8. Since this effect somewhat competes with the effect from  $\sin^2 \theta_{23}$  shown in Figure 8.6, the correlations between the two parameters will be seen in the oscillation analysis discussed in Section 8.6.

Finally, Figure 8.9 compares the zenith distributions for the multi-GeV e-like samples for normal and inverted hierarchy. The MSW resonance enhancement of electron type neutrino appearance only happens for neutrinos when it is normal hierarchy, while for inverted hierarchy it only happens for

### 8.1. Event Selection and Binning

---

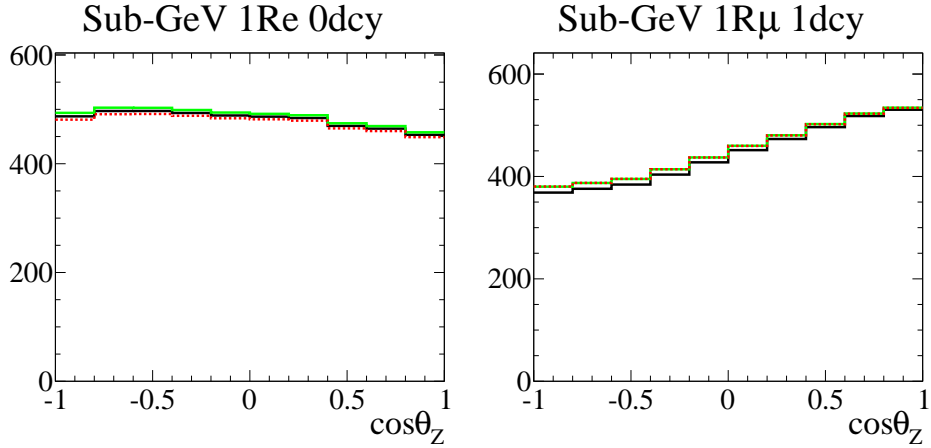


Figure 8.6: The effect of  $\sin^2\theta_{23}$  variations on the distributions of the cosine of the zenith angle for sub-GeV samples. The left is for one-ring e-like 0decay and the right is for one-ring  $\mu$ -like 1decay. The plots show the expectations at  $\sin^2\theta_{23}$  set to 0.4(solid green), 0.5(solid black) and 0.6(dashed red).

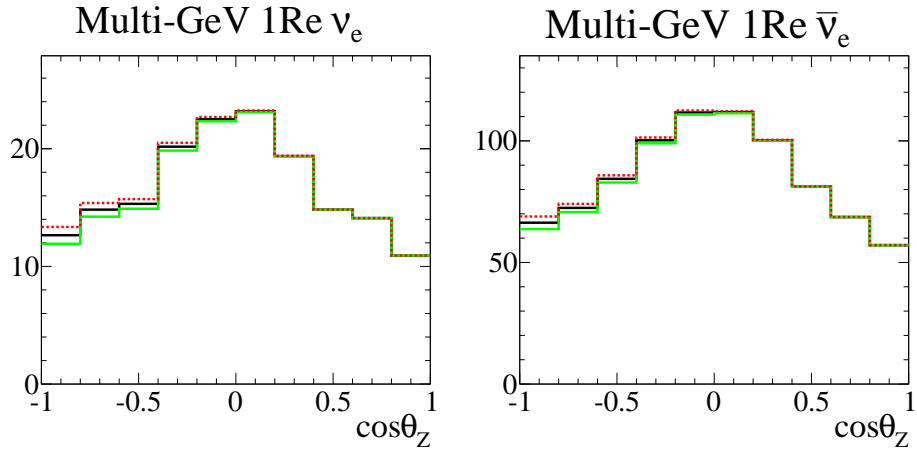


Figure 8.7: The effect of  $\sin^2\theta_{23}$  variations on the distributions of the cosine of the zenith angle for Multi-GeV samples. The left is for one-ring e-like  $\nu_e$  and the right is for one-ring e-like  $\bar{\nu}_e$ . The plots show the expectations at  $\sin^2\theta_{23}$  set to 0.4(solid green), 0.5(solid black) and 0.6(dashed red).

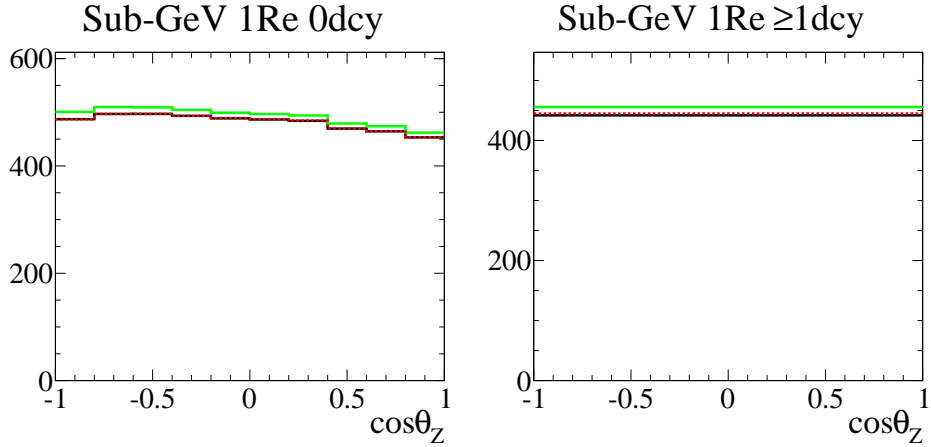


Figure 8.8: The effect of  $\delta_{\text{CP}}$  variations on the distributions of the cosine of the zenith angle for Sub-GeV samples. The left is for one-ring e-like 0decay and the right is for one-ring e-like  $\geq 1$  decay. The plots show the expectations at  $\delta_{\text{CP}}$  set to  $-\pi/2$ (solid green), 0(solid black) and  $+\pi/2$ (dashed red).

antineutrinos. As in the left plots, the multi-GeV  $\nu_e$ -enriched event samples, selected by the  $\nu_e/\bar{\nu}_e$  separation scheme as described in Sections 8.1.2 and 8.1.3, therefore observe an excess of upward-going events in the case of normal hierarchy compared to inverted hierarchy. On the other hand, the  $\bar{\nu}_e$ -enriched samples on the right, which have much closer to equal mixture of  $\nu_e$  and  $\bar{\nu}_e$  as in Table 8.1, show almost no sensitivity to the mass hierarchy, since the effect of flipping the hierarchy almost cancels between neutrinos and antineutrinos. Employing the  $\nu_e/\bar{\nu}_e$  separation and having the  $\nu_e$ -enriched samples thus makes the effect from the mass hierarchy more prominent and improves the sensitivity.

### 8.1. Event Selection and Binning

---

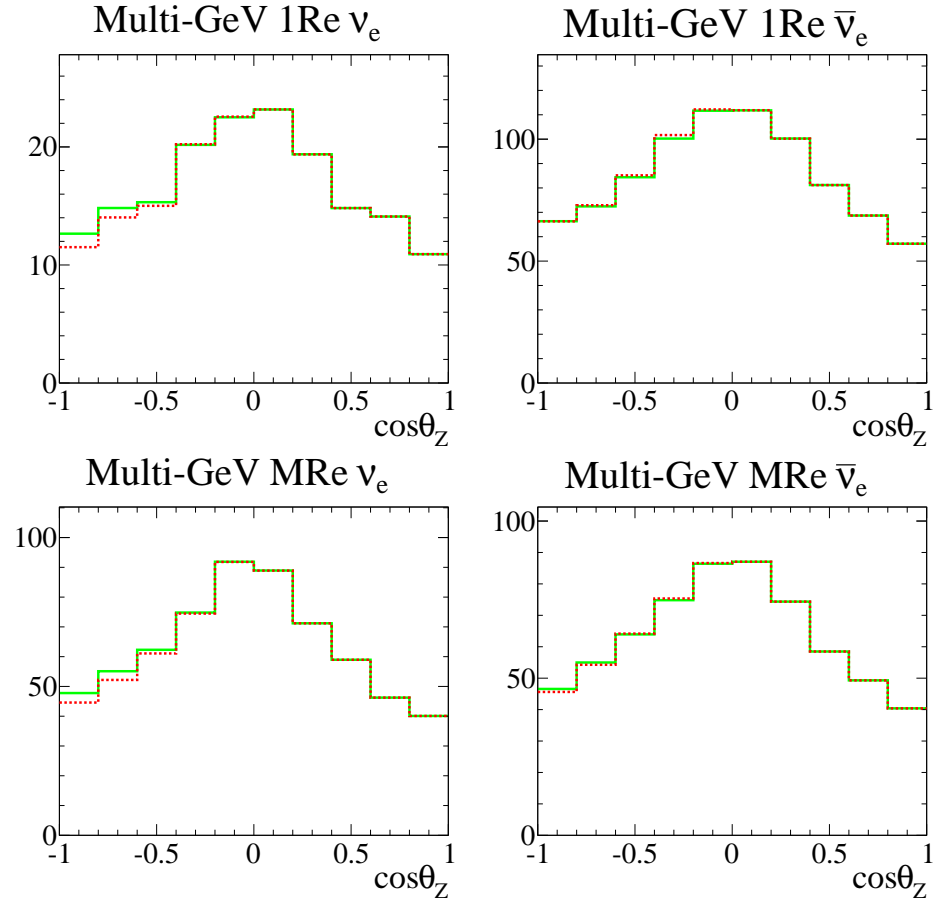


Figure 8.9: The effect of the mass hierarchy on the distributions of the cosine of the zenith angle for Multi-GeV e-like samples. The left side is for the  $\nu_e$ -enriched samples and the right side is for the  $\bar{\nu}_e$ -enriched samples. The solid green lines are the expectations for normal hierarchy while the dashed red lines are for inverted hierarchy.

## 8.2 Systematic Uncertainties

This section describes the sources of systematic uncertainties which are considered in the oscillation analysis. While comparing the observed data to prediction in order to extract the oscillation parameters, the parameter for each systematic is also varied and its effect is propagated to the predicted event rate for each bin. In total there are 82 model parameters considered in the analysis, six of which are the oscillation parameters. Out of the remaining 76 parameters for systematics, 18 are for the atmospheric neutrino flux, 19 are for neutrino interaction, 27 are for FSI and 12 are for the detector response and reconstruction, and the full list of the systematic parameters can be found in Appendix A. The prior uncertainties on the systematic parameters are all treated as Gaussians where the  $1\sigma$  widths are given below, and apart from the FSI parameters they are assumed to be uncorrelated.

### 8.2.1 Atmospheric Neutrino Flux

#### Absolute Normalization

The uncertainty on the absolute flux normalization is given by Honda *et al.*[95] as an energy-dependent error as in Figure 8.10. Scaling parameters for below and above 1 GeV independently scale the flux according to the function shown. In order to account for the additional differences between the base Honda flux model[95] and other flux models such as FLUKA[52] and Bartol[53] above 10 GeV, an additional 5% normalization error on multi-GeV events is considered as an independent parameter.

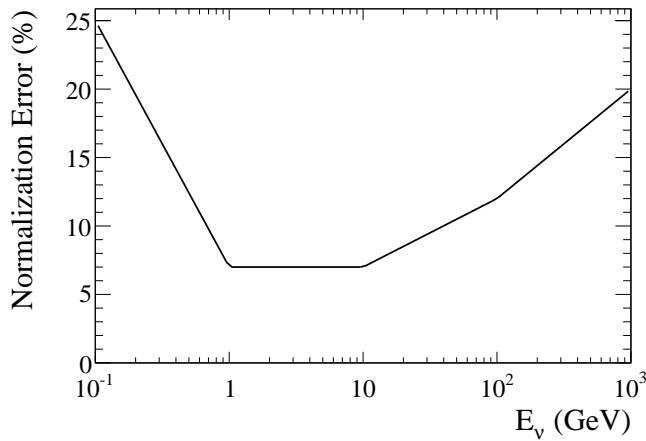


Figure 8.10: Uncertainty on the flux normalization as a function of energy.

### Flux Ratios

The uncertainties on the various flux ratios are estimated by the comparison of the Honda flux[95] to the FLUKA[52] and the Bartol[53] flux models. For the flavour ratio  $(\nu_\mu + \bar{\nu}_\mu)/(\nu_e + \bar{\nu}_e)$ , the uncertainty is 2% for  $E_\nu < 1$  GeV, 3% for  $1 \text{ GeV} < E_\nu < 10$  GeV, 5% for  $10 \text{ GeV} < E_\nu < 30$  GeV and then linearly increases in  $\log_{10} E_\nu$  to 30% at 1 TeV. For  $\bar{\nu}_e/\nu_e$  ratio the uncertainty is 5% for  $E_\nu < 10$  GeV, 8% for  $10 \text{ GeV} < E_\nu < 100$  GeV and then linearly increases in  $\log_{10} E_\nu$  to 30% at 1 TeV. Finally, the uncertainty on  $\bar{\nu}_\mu/\nu_\mu$  ratio is 2% for  $E_\nu < 1$  GeV, 6% for  $1 \text{ GeV} < E_\nu < 50$  GeV and then linearly increases in  $\log_{10} E_\nu$  to 60% at 1 TeV. For these ratio uncertainties, the flux in the following three energy regions are varied independently according to a scaling parameter in each region:  $E_\nu < 1$  GeV,  $1 \text{ GeV} < E_\nu < 10$  GeV and  $E_\nu > 10$  GeV. The uncertainty on the up/down ratio and the horizontal/vertical ratio of the flux is also estimated by comparing the three flux models, and the differences in the zenith distributions between the flux models are taken as the uncertainty.

### $K/\pi$ Ratio

While the atmospheric neutrino flux below 10 GeV is mainly from pion decays, contributions from kaons become increasingly dominant as the energy increases. Based on the  $K/\pi$  production ratio measurement by the SPY experiment[96], the uncertainty on the ratio of the flux induced by kaons and pions is estimated to be 5% for  $E_\nu < 100$  GeV and then linearly increases with energy to 20% at 1 TeV.

### Solar Activity

The activity of the sun cycles with 11 year period, and the resulting variations in the magnetic field affects the cosmic-ray flux. The variation in the neutrino flux caused by a  $\pm 1$  year variation in the solar cycle is taken as the uncertainty on the flux.

### Neutrino Path Length

The production height of atmospheric neutrinos depends on the density structure of the atmosphere, and the uncertainty on that needs to be propagated to the oscillation probability which depends on the path length of neutrinos. The uncertainty in the density of the atmosphere is estimated to be 10% based on the comparison between the US-standard 76 and the MSISE-90 models for the atmosphere[97], and the resulting variations in the production height of atmospheric neutrinos are propagated to the oscillation

probability calculation.

### **Matter Effect**

Although the matter density structure of the earth is rather well known[35], there is an uncertainty on the electron density which depends on the exact chemical composition of the core, and such uncertainty needs to be taken into account when calculating the matter-induced oscillation probabilities through the Earth. As the core is assumed to consist of heavy elements such as iron whose electron density is about 6.8% less than that of light elements, the uncertainty on the electron density in the core is estimated to be 6.8% and is considered during oscillation probability calculation.

### **8.2.2 Neutrino Interaction**

#### **CCQE**

For CCQE interaction the uncertainties on the absolute total cross section as well as the cross section ratios  $\bar{\nu}/\nu$  and  $(\nu_\mu + \bar{\nu}_\mu)/(\nu_e + \bar{\nu}_e)$  are assigned according to the differences between the base model of relativistic Fermi gas and the model by Nieves *et al.*[98]. In addition, 20% uncertainty is assigned on the axial vector mass  $M_A^{QE}$ .

#### **MEC**

As there are still large uncertainties on the MEC model and the cross section has not been explicitly measured at the present moment, 100% uncertainty is assigned to the total cross section of the MEC process.

#### **Single Meson Production**

The uncertainties on the parameters which characterize the Graczyk-Sobczyk form factor[64] were obtained from the data from bubble chamber experiments [65][66]. Additional uncertainties in the total cross sections are assigned based on the differences between the base model in NEUT to the model by Hernandez *et al.*[99].

#### **DIS**

For DIS interaction, 10% uncertainty is assigned to the total cross section, and in order to account for the larger uncertainties in the energy below 10 GeV the differences between the base model of GRV98 with the Bodek-Yang correction and the CKMT model[100] are considered as an additional uncertainty. Also, the uncertainty on the  $Q^2$  distributions of the DIS interaction is assigned by the differences between the GRV98 model with and without

## 8.2. Systematic Uncertainties

---

the Bodek-Yang correction. Separate parameters for  $W < 1.3 \text{ GeV}/c^2$  and  $W > 1.3 \text{ GeV}/c^2$  vary the  $Q^2$  distributions in the two regions independently.

### Coherent Pion Production

As there was no evidence for  $\nu_\mu$ CC coherent pion production observed by the SciBooNE experiment[101], 100% uncertainty is assigned to the total cross section of coherent pion production.

### NC/CC Ratio

20% uncertainty is assigned to the ratio of the inclusive NC and CC cross sections.

### $\nu_\tau$ CC Cross Section

25% uncertainty is assigned to the inclusive  $\nu_\tau$ CC total cross section.

### 8.2.3 Final State Interaction

As final state interactions(FSI) change the observable final state of particles which exit the nucleus, information such as the number of rings and decay electrons which the event selection is based on is directly affected by the FSI. It is therefore important to consider the uncertainties in the FSI model in the oscillation analysis.

As described in Section 4.2.5, based on the external pion scattering data the uncertainties on the NEUT pion cascade model parameters are given as representative sets of the FSI model parameters which span the  $1\sigma$  error surface in the multi-dimensional FSI parameter space. In order to incorporate this uncertainty in the analysis, a covariance matrix is formed among the event rates of the selected event samples based on the allowed FSI variations. Figure 8.11 shows the error matrix for the fractional event rate variations for the sub-GeV samples by the simultaneous variations of the FSI parameters on the  $1\sigma$  surface. In addition to the FSI which happens within the initial target nucleus, secondary interactions(SI) of pions outside the target nucleus are also varied simultaneously since they are simulated in the detector simulation using the same NEUT pion cascade model. In the oscillation analysis, instead of directly manipulating the underlying FSI model parameters, a systematic parameter to scale the event rate is introduced for each sample, and the prior uncertainty on the scaling parameters are treated as a multivariate Gaussian with the errors and the correlations given in Figure 8.11. For the sub-GeV event samples, each selected sample is further subdivided into two momentum bins and there are thus 12 scaling

## 8.2. Systematic Uncertainties

---

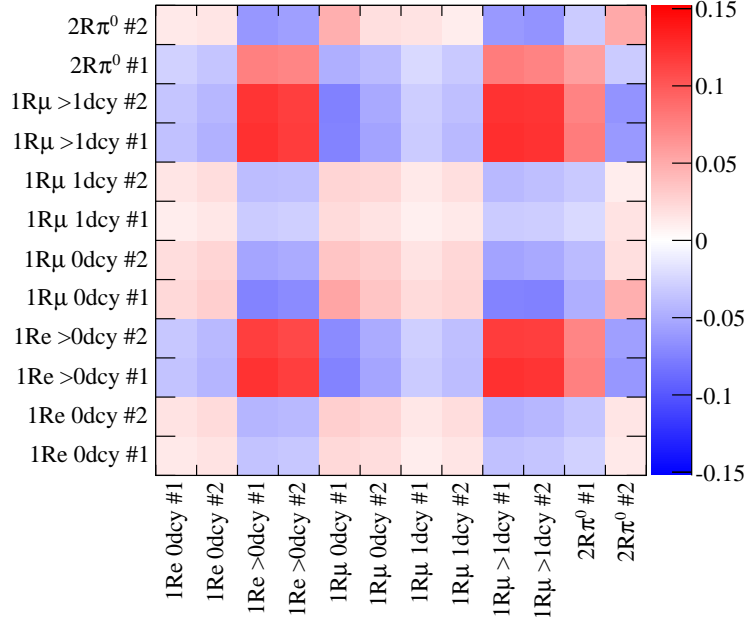


Figure 8.11: The fractional error matrix  $\text{sgn}(V_{ij}) \times \sqrt{|V_{ij}|}$  for the sub-GeV samples, where  $V_{ij}$  is the covariance for the fractional variations in the event rate of each sample by FSI and SI parameter variations. Each sample is further subdivided into two momentum bins, for below(#1) and above(#2) 400 MeV/ $c$  momentum. The diagonal elements represent the fractional error on the event rate of each sample which can be up to 13% depending on the sample.

parameters in total.

For multi-GeV, while there is no subdivision of the samples by momentum, the e-like samples are subdivided into  $\nu_e\text{CC}$ ,  $\bar{\nu}_e\text{CC}$  and background ( $\nu_\mu + \bar{\nu}_\mu\text{CC}$  and NC) based on the true interaction mode. Since the multi-GeV samples are not as pure as the sub-GeV samples, the composition of each sample is also allowed to change this way as well as the total event rate during the oscillation analysis. When forming the covariance matrix for multi-GeV samples, in addition to the parameters for FSI and SI, pion multiplicity is also varied based on the differences between NEUT and the result from the CHORUS experiment[102] in order to account for the uncertainties which may not be covered by the FSI/SI variations. Figure 8.12 is the resulting error matrix for the multi-GeV samples. There are thus 15 scaling parameters for multi-GeV samples which are introduced to the anal-

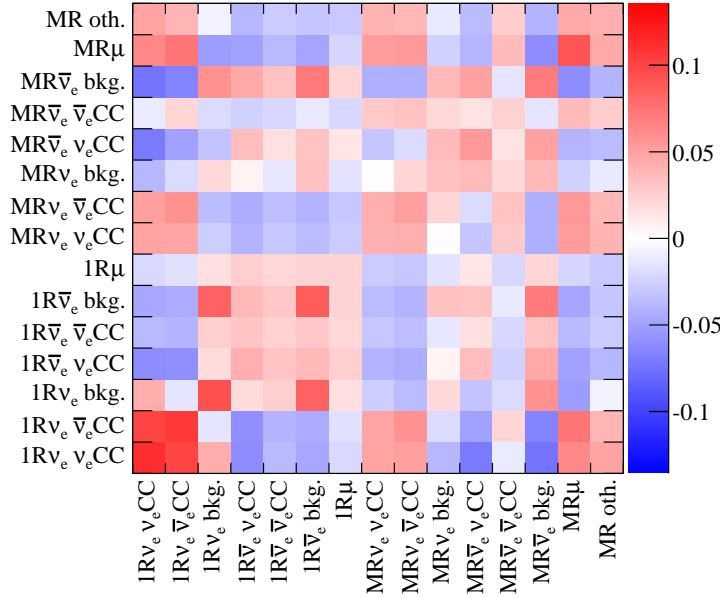


Figure 8.12: The fractional error matrix  $\text{sgn}(V_{ij}) \times \sqrt{|V_{ij}|}$  for the multi-GeV samples, where  $V_{ij}$  is the covariance for the fractional variations in the event rate of each sample by FSI, SI and pion multiplicity variations. The diagonal elements represent the fractional error on the event rate of each sample which can be up to 11% depending on the sample.

ysis whose prior correlations are given by the figure. No prior correlation is introduced between the sub-GeV and the multi-GeV parameters.

### 8.2.4 Detector Response and Reconstruction

#### FC Reduction

The uncertainty on the FC reduction efficiency is estimated to be 1.3% based on the comparison of the relevant cut variables between data and MC. The uncertainty on the efficiency of the FC/PC separation cut is estimated to be 0.2%. Contaminations from non-neutrino backgrounds such as the flasher PMT events and cosmic-ray muon events are estimated by eye-scanning to be within 0.1%.

#### Fiducial Volume

The fiducial volume uncertainty is estimated to be 2%, which corresponds

## 8.2. Systematic Uncertainties

---

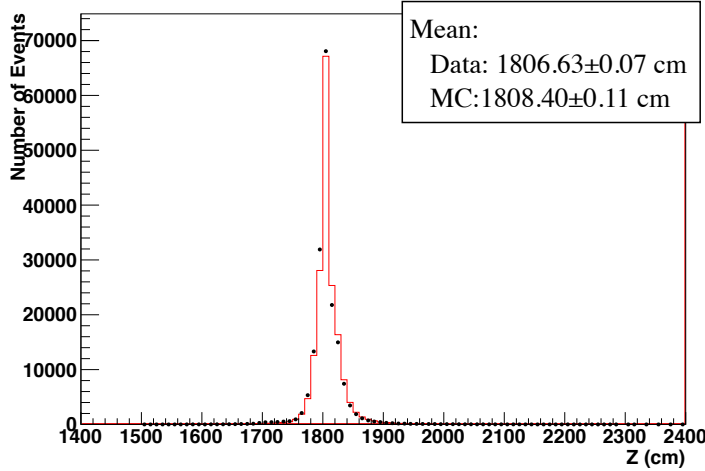


Figure 8.13: Reconstructed vertex  $Z$  position of stopping cosmic-ray muons entering from the top of the detector. The red histogram is for MC and the black data points are for data, and the mean of each distribution is shown on the top-right of the plot. The top wall of the ID is located at  $Z = 1810$  cm.

to a systematic inward/outward shift of the vertex position by  $\sim 10$  cm near the fiducial boundary. The reconstructed vertex distributions of stopping cosmic-ray muons for data and MC agree well within this uncertainty as shown in Figure 8.13.

### Ring Counting

The uncertainty on the ring-finding efficiency is evaluated by comparing the distributions of ring-counting likelihood as described in Section 6.10.1 between the FC data and MC. The uncertainty ranges from 0.3% to 2.8% depending on the event category, and it is in general larger in multi-GeV.

### Particle Identification

Particle identification uncertainties are estimated by comparing the distributions of  $e/\pi^+$  likelihood ratio as discussed in Section 6.10.2 between the FC data and MC. The errors are estimated separately for single-ring and multi-ring events and vary from 0.1% to 0.4% depending on the event category.

### Energy Calibration

### 8.3. Event Rate Prediction

---

The uncertainty on the absolute energy scale is estimated by the data-MC comparison of the energy scales in three control samples: stopping cosmic-ray muons, decay electrons and the mass peak of NC $\pi^0$ . The largest difference between data and MC across all samples is taken as the uncertainty on the absolute energy scale and is estimated to be 2.1%. The up/down asymmetry of the energy scale is also estimated from the momentum of decay electrons with different directions and is estimated to be 0.3%.

#### Decay Electron Tagging

As in Section 6.6.3, the uncertainty on decay electron detection efficiency is estimated by the data-MC comparison of the detection efficiency in stopping cosmic-ray muon samples. The uncertainty is estimated to be 0.8% across all energies.

## 8.3 Event Rate Prediction

This section describes the procedures to calculate the predicted event rates in the analysis bins for a given set of oscillation and systematic parameters. The calculation is done by manipulating the base atmospheric neutrino MC which was described in Chapter 4, and the method to reflect the variations of each parameter depends on the type of the parameter.

### 8.3.1 Oscillation Weighting

The predicted the event rates at a given oscillation parameter set and nominal systematic parameters are calculated as the following.

The atmospheric neutrino MC is produced assuming no oscillations. The oscillation is reflected to the event rate predictions by reweighting the MC from unoscillated flux to oscillated flux on event-by-event basis. For each MC event, the ratio of the calculated oscillated flux over the original unoscillated flux is taken as a weight factor, and the event is filled into a reconstructed momentum and zenith bin as is done for the observed data but with the calculated weight. When reweighting a MC event of neutrino type  $\alpha (=e, \mu, \tau)$ , the following weight factor is applied:

$$\omega = \frac{T_{\text{Data}}}{T_{\text{MC}}} \frac{1}{\Phi_\alpha^0} \{ \Phi_e P(\nu_e \rightarrow \nu_\alpha) + \Phi_\mu P(\nu_\mu \rightarrow \nu_\alpha) \}. \quad (8.4)$$

The first factor in the equation adjusts the exposure of the original MC to the data exposure where  $T_{\text{Data}}$  and  $T_{\text{MC}}$  are the exposure for the data and the MC respectively.  $T_{\text{MC}}$  is 500 years for the MC which is used in

### 8.3. Event Rate Prediction

---

this analysis.  $\Phi_\alpha^0$  is the atmospheric neutrino flux from which the MC was generated, evaluated at the energy and the direction of the neutrino in the event, and the Honda flux at middle solar activity before oscillations was used for each neutrino type. For  $\nu_\tau$  and  $\bar{\nu}_\tau$  event generation the flux for  $\nu_\mu$  and  $\bar{\nu}_\mu$  respectively was used, since tau neutrinos are not produced in the atmosphere via pion and kaon decays and only appear after oscillations. The terms in the middle parentheses represent the total flux of neutrino type  $\alpha$  after oscillations where  $\Phi_e$  and  $\Phi_\mu$  are the electron and muon neutrino flux respectively before oscillations, and as the original atmospheric neutrino flux consists of electron and muon neutrinos there are contributions from both once the oscillation is considered. The flux used here is the Honda flux as described in Section 4.1 weighted according to the solar activity corresponding to the data period as:

$$\Phi_\beta = (1 - \eta)\Phi_\beta^{\min} + \eta\Phi_\beta^{\max}, \quad (8.5)$$

where  $\Phi_\beta^{\min}$  and  $\Phi_\beta^{\max}$  are the flux at the minimum and maximum solar activity respectively.  $\Phi_\beta$  is thus linearly interpolated between the two with a weight factor  $\eta$ , and for this analysis the weight is set to 0.35 which represents the average solar activity during the data period. Finally, the object  $P(\nu_\beta \rightarrow \nu_\alpha)$  is the transition probability from a neutrino of type  $\beta$  to type  $\alpha$  calculated at the energy and the direction of the neutrino in the event.

The oscillation probability is calculated using the Prob3++ software package developed by the Super-Kamiokande collaboration[103] which is publicly available and has been widely used in various neutrino oscillation analyses. Following the methods given by Barger *et al.*[34] the software algebraically calculates the full three-flavour oscillation probabilities for atmospheric neutrinos including the matter effect in the earth based on the radial density structure of the earth given by the PREM model[35].

#### 8.3.2 Propagating Variations of Systematics

Variations in the atmospheric neutrino flux parameters are applied on event-by-event basis at the time of filling the MC events into analysis bins, by manipulating the weight for each MC event according to the variations in the flux systematics. For example, if the absolute flux at the energy for a given event is supposed to be increased by 5%, the weight for the event is increased by 5%. The weights from all flux parameters are multiplied together to get the overall weight for the flux systematic variations for each event. The solar activity systematic is propagated by accordingly changing

### 8.3. Event Rate Prediction

---

the mixture of the fluxes at minimum and maximum solar activity when linearly combining them as described in Section 8.3.1. For the neutrino path length and matter effect systematics, the variations are reflected to the oscillation probabilities by directly manipulating the path length and the matter density which are used in Prob3++ for probability calculation.

Unlike the flux uncertainties which can be parameterized rather simply based on the neutrino type, energy and direction, the cross section uncertainties have complex dependencies on the event configurations and it is therefore not computationally feasible to do an event-by-event reweighting. The cross section systematic variations are propagated instead by directly manipulating the predicted event rate at each analysis bin, after the MC events are reweighted by flux and oscillation parameters and binned. Assuming a linear response of the bin contents to each cross section systematic parameter, the cross section parameter variations are applied to each bin as:

$$\lambda_i \rightarrow \lambda_i \prod_j \left(1 + f_i^j \epsilon_j\right), \quad (8.6)$$

where  $\lambda_i$  is the predicted event rate in the  $i$ -th bin(before the systematic variations are applied),  $\epsilon_j$  is the variation of the  $j$ -th systematic from its nominal value in the unit of  $\sigma$ : the magnitude of the uncertainty as described in Section 8.2. The object  $f_i^j$  is a linear response coefficient which gives the fractional change in the content of the  $i$ -th bin by the variation of the  $j$ -th systematic by  $1\sigma$ , and it is calculated for each systematic and analysis bin by reweighting the MC events event-by-event using the detailed MC truth information, prior to executing the software for oscillation parameter estimation. Figure 8.14 shows an example of such pre-calculated response coefficients. In order to allow the interaction mode composition of each bin to change, the MC events are first binned separately for  $\nu_e$ CC,  $\bar{\nu}_e$ CC,  $\nu_\mu$ CC,  $\bar{\nu}_\mu$ CC,  $\nu_\tau + \bar{\nu}_\tau$ CC and NC, and after the response is applied as in Equation 8.6 separately for the event rates from each interaction mode, the total predicted event rate in each bin is obtained by combining the contributions from all interaction modes.

Most of the detector response and reconstruction systematic parameters are treated in the same way as the cross section systematics, by applying the response linearly according to Equation 8.6. The exceptions are the energy scale parameters, which are applied event-by-event by manipulating the reconstructed momentum before the MC events are binned, in order to more properly treat the migration of events between the momentum bins due to energy scale change.

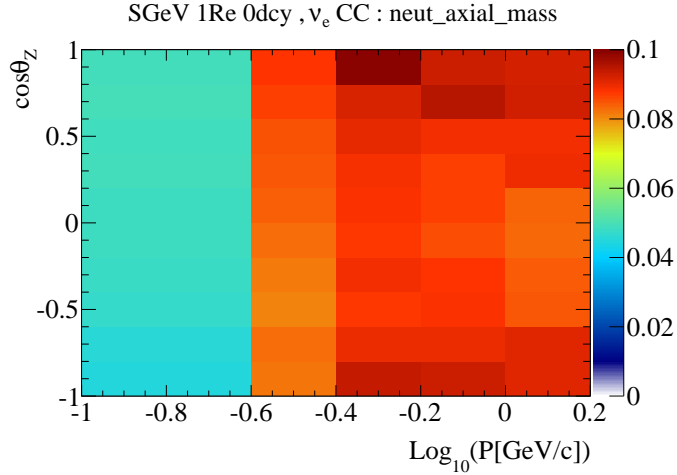


Figure 8.14: The response coefficient  $f_i^j$  for the  $M_A^{\text{QE}}$  systematic for the  $\nu_e$ CC events in each bin in the sub-GeV one-ring e-like 0decay sample. The entries represent the fractional variations in the expected event rate at each bin caused by a  $+1\sigma$  variation in the systematic parameter.

Finally, for the FSI parameters, the predicted rate at each bin is simply scaled according to the scaling parameter for the event sample in concern. The correlations between the scaling parameters for different samples are then enforced using the covariance which was discussed in Section 8.2.3, and the details will be discussed again later in Section 8.4.2.

## 8.4 Bayesian Analysis using Markov Chain Monte Carlo

Once the events in the observed data are binned and the predicted event rate at each bin is ready to be calculated, the oscillation parameters can be obtained by searching for the set of the parameters for which the prediction best matches with the observed data. This analysis employs a Markov Chain Monte Carlo method to make Bayesian predictions on the oscillation parameters based on the observed data, and the procedures are detailed in the following.

### 8.4.1 Likelihood Function

In order to compare the observed binned data to MC expectations, this analysis defines the following likelihood function which is based on the observed data and the model parameters in the MC simulation:

$$L(D|\vec{o}, \vec{f}) := \prod_{i=1}^n \frac{\lambda_i^{N_i}}{N_i!} \exp(-\lambda_i), \quad (8.7)$$

where  $D$  represents the observed data,  $\vec{o}$  is the vector of model parameters which we are interested in such as the oscillation parameters and  $\vec{f}$  is the vector of nuisance parameters: the model parameters which we are not interested in such as the parameters for systematic uncertainties.  $N_i$  is the observed number of events in the  $i$ -th bin where there are  $n$  bins in total, and  $\lambda_i = \lambda_i(\vec{o}, \vec{f})$  is the expected event rate in the  $i$ -th bin given the model parameters  $\vec{o}, \vec{f}$  which is calculated as described in Section 8.3. A likelihood function is the probability for obtaining the observed data given an assumed model, and as the data is binned in this analysis, the likelihood is defined as the product of the probability at each bin of observing  $N_i$  events given the mean event rate  $\lambda_i$  based on the assumed model, which is given by the Poisson distribution with mean  $\lambda_i$ .

### 8.4.2 Bayesian Posterior Probability

The Bayes' theorem states that the probability of a hypothesis being true given data is given by:

$$P(H|D, I) = \frac{P(D|H, I)P(H|I)}{P(D|I)}, \quad (8.8)$$

where  $H$  represents the hypothesis,  $I$  is the prior knowledge on the hypothesis and  $D$  represents the observed data.  $P(H|I)$  is the prior probability for the hypothesis  $H$ , and the object  $P(D|H, I)$  is the likelihood, which is the probability for observing the data given the hypothesis and the prior knowledge. The denominator  $P(D|I)$  can simply be considered as a normalization term:

$$P(D|I) = \sum_{\{H\}} P(D|H, I)P(H|I), \quad (8.9)$$

where the sum runs over all possible hypotheses in the given model space, as is clear from the normalization condition of applying the model sum to each side of Equation 8.8.

The discussions above is directly applicable to the problem of estimating the oscillation parameters from the atmospheric neutrino data in this analysis. The probability distribution for the model parameters  $\vec{\sigma}, \vec{f}$  given the observed data  $D$ , i.e. the posterior probability given data, is written as:

$$P(\vec{\sigma}, \vec{f}|D) = \frac{L(D|\vec{\sigma}, \vec{f})p(\vec{\sigma}, \vec{f})}{\int L(D|\vec{\sigma}, \vec{f})p(\vec{\sigma}, \vec{f}) d\vec{\sigma} d\vec{f}}, \quad (8.10)$$

where  $L(D|\vec{\sigma}, \vec{f})$  is the likelihood function defined in Equation 8.7.  $p(\vec{\sigma}, \vec{f})$  is the prior probability distribution for the model parameters  $\vec{\sigma}, \vec{f}$ , and in this analysis, except for some oscillation parameters for which flat priors are used, it is assumed that the prior is described as a multivariate Gaussian:

$$p(\vec{\sigma}, \vec{f}) = p(\vec{\sigma})p(\vec{f}), \quad (8.11)$$

$$p(\vec{\sigma}) \propto \exp(-\frac{1}{2}\vec{d}_o^T V_o^{-1} \vec{d}_o), \quad (8.12)$$

$$p(\vec{f}) \propto \exp(-\frac{1}{2}\vec{d}_f^T V_f^{-1} \vec{d}_f), \quad (8.13)$$

where  $\vec{d}_o$  and  $\vec{d}_f$  are the deviations from the nominal values for  $\vec{\sigma}$  and  $\vec{f}$  respectively.  $V_o$  and  $V_f$  are the covariance matrices for the prior constraints on the parameters  $\vec{\sigma}$  and  $\vec{f}$ , and apart from the systematic parameters related to the FSI uncertainties which are correlated as described in Section 8.2.3, the parameter priors are assumed to be uncorrelated, i.e., only the diagonal elements in the matrices are nonzero for the majority of the parameters.

Once the Bayesian posterior probability Equation 8.10 is defined, one can obtain the joint probability distribution for the model parameter sets  $\vec{\sigma}, \vec{f}$  given the observed data in two steps: by calculating the expected event rate  $\lambda_i$  at each bin for the assumed values of  $\vec{\sigma}$  and  $\vec{f}$ , and then evaluating Equation 8.10.

#### 8.4.3 Marginalization and Parameter Estimation

In the oscillation analysis, we are only interested in certain oscillation parameters while not caring about the rest of the model parameters. Therefore, rather than the joint probability  $P(\vec{\sigma}, \vec{f}|D)$ , we want the probability for the interesting parameters  $\vec{\sigma}$  only, disregarding the values of the nuisance parameters  $\vec{f}$ . This is done by marginalization, i.e., by integrating out the nuisance parameters from the posterior probability  $P(\vec{\sigma}, \vec{f}|D)$ :

$$P(\vec{\sigma}|D) = \int P(\vec{\sigma}, \vec{f}|D) d\vec{f}. \quad (8.14)$$

The probability  $P(\vec{\sigma}|D)$  is now simply the probability for the interesting parameters  $\vec{\sigma}$  given the observed data, taking into consideration all the possibilities for the values for the nuisance parameters based on their prior uncertainties and data. Obtaining such marginalized posterior probabilities for the oscillation parameters based on the SK data is the goal of this oscillation analysis.

#### 8.4.4 Markov Chain Monte Carlo

In this analysis there are 82 model parameters in total, and performing the integration in Equation 8.14 in such high dimensionality numerically can be challenging. Markov Chain Monte Carlo provides means to perform such high dimensional integrals efficiently.

Markov Chain Monte(MCMC) is essentially a directed random walk in a multi-dimensional parameter space which is used to sample from a multi-dimensional probability distribution. After randomly sampling large number of points from the multi-dimensional parameter space following this procedure, the density distribution of the sampled points will eventually approximate the multi-dimensional probability distribution in concern.

Metropolis-Hastings algorithm[104] is the method which is used in this analysis to produce a Markov chain, and the procedures to produce sampled points  $\{X_t\}$  from a probability distribution  $P(X)$  for a multi-dimensional parameter set  $X$  follow as below:

1. Randomly chose the initial state  $X_0$  for the parameters.
2. Define a proposal function  $Q(X \rightarrow Y)$  which gives the probability distribution for proposing the next state  $Y$  given the current state  $X$ .
3. After  $t$  steps when the chain is currently at the state  $X_t$ , propose a new state  $Y$  using  $Q(X_t \rightarrow Y)$ .
4. Accept the proposed state  $Y$  with the acceptance probability:

$$\alpha(X_t \rightarrow Y) := \min \left( 1, \frac{P(Y)}{P(X_t)} \frac{Q(X_t \rightarrow Y)}{Q(Y \rightarrow X_t)} \right), \quad (8.15)$$

i.e., move to the proposed new state( $X_{t+1} = Y$ ) with the probability  $\alpha(X_t \rightarrow Y)$ , discard the proposed state and remain in the current state( $X_{t+1} = X_t$ ) with the probability  $1 - \alpha(X_t \rightarrow Y)$ .

5. Repeat the procedures from 3.

In the case when the proposal function is symmetric, i.e.,

$$Q(X \rightarrow Y) = Q(Y \rightarrow X), \quad (8.16)$$

Equation 8.15 reduces to:

$$\alpha(X_t \rightarrow Y) = \min\left(1, \frac{P(Y)}{P(X_t)}\right). \quad (8.17)$$

It is interesting to note that although the number of steps required for the chain to reasonably converge to the sampled distribution depends on the choice for the proposal function  $Q(X \rightarrow Y)$ , given sufficient number of sampled points the chain will eventually approximate the distribution regardless of the choice of the functional form of  $Q(X \rightarrow Y)$ , as long as the transition probability to any point where  $P(Y) \neq 0$  is nonzero.

For the oscillation analysis, the distribution which is sampled using the above algorithm is the posterior probability distribution  $P(\vec{o}, \vec{f}|D)$  in Equation 8.10, and a Gaussian proposal function is chosen which draws a Gaussian-distributed random number centered at the current parameter value. Since this is a symmetric proposal function, proposed steps are accepted with the probability:

$$\alpha(\vec{o}, \vec{f} \rightarrow \vec{o}', \vec{f}') = \min\left(1, \frac{P(\vec{o}', \vec{f}'|D)}{P(\vec{o}, \vec{f}|D)}\right). \quad (8.18)$$

Note that since the denominator in Equation 8.10 is a constant which does not depend on  $\vec{o}$  and  $\vec{f}$ , the above equation further reduces to:

$$\alpha(\vec{o}, \vec{f} \rightarrow \vec{o}', \vec{f}') = \min\left(1, \frac{L(D|\vec{o}', \vec{f}')p(\vec{o}', \vec{f}')}{{L(D|\vec{o}, \vec{f})p(\vec{o}, \vec{f})}}\right), \quad (8.19)$$

which eliminates the need of evaluating the integral in Equation 8.10.

Once a large number of points are sampled from the probability distribution, marginalization as in Equation 8.14 is readily done: one can simply project the sampled points onto the axes of interesting parameters and bin them in a histogram. In this oscillation analysis, the posterior probability density distribution for the model parameters Equation 8.10 is sampled using MCMC, and the sampled points are then binned into histograms of oscillation parameters which, after normalizing, gives the marginalized posterior probability distributions for the oscillation parameters which is presented as the final result.

## 8.5 Sensitivity Studies

In order to test the oscillation analysis framework and understand its behaviour before analyzing the real data, a sensitivity study was performed by running the analysis on an Asimov dataset, i.e., taking the expected event rates without any statistical fluctuations as a dataset. The expectations are calculated at the oscillation parameters in Table 8.3, and all the systematic parameters are set to the nominal values. The exposure is taken to be 2519.89 days which is the same as the real data.

Parameter	True value
$\sin^2 \theta_{12}$	0.304
$\sin^2 \theta_{13}$	0.0219
$\sin^2 \theta_{23}$	0.50
$\Delta m_{21}^2$	$7.53 \times 10^{-5} \text{ eV}^2$
$\Delta m_{32}^2$	$+2.39 \times 10^{-3} \text{ eV}^2$ (NH)
$\delta_{\text{CP}}$	$-\pi/2$

Table 8.3: True oscillation parameters for the Asimov dataset production.

The MCMC oscillation analysis as described in Section 8.4 is performed on the above dataset, which in the end provides Bayesian predictions on the oscillation parameters estimated from the Asimov data. During the analysis the priors for the oscillation parameters are taken as shown in Table 8.4, while the priors for the systematic parameters are all Gaussian with the uncertainties assigned as in Section 8.2. Prior constraints on  $\sin^2 \theta_{12}$ ,  $\Delta m_{21}^2$  and  $\sin^2 \theta_{13}$  are based on the PDG2015 average values[15]. Flat priors are assumed for  $\sin^2 \theta_{23}$ ,  $\Delta m_{32}^2$  and  $\delta_{\text{CP}}$  to which the atmospheric neutrino data is sensitive, and the results on the three parameter will therefore be purely driven by sensitivity of the Super-K data. Since we expect a large gap between the normal and inverted hierarchy peaks in the  $\Delta m_{32}^2$  posterior, a special treatment is made for the proposal function for  $\Delta m_{32}^2$  so that the sign of the proposed  $\Delta m_{32}^2$  flips by 50% probability at each step, in addition to the Gaussian proposal for its absolute value. This ensures that the Markov Chain properly samples the posterior probability in both hierarchies within the limited number of MCMC steps. The resulting posterior can be used to predict the mass hierarchy as well as the value for  $\Delta m_{32}^2$ .

For this sensitivity study, 50 MCMC chains were produced, each having 120,000 steps. Figure 8.15 shows the evolution of  $\Delta m_{32}^2$  and  $-\ln P(\vec{o}, \vec{f}|D)$ , the negative-log of the posterior probability, as the MCMC processes progress, where the horizontal axes are the number of steps taken within each chain.

### 8.5. Sensitivity Studies

---

Parameter	Prior
$\sin^2 \theta_{12}$	Gaussian, $0.304 \pm 0.014$
$\sin^2 \theta_{13}$	Gaussian, $0.0219 \pm 0.0012$
$\sin^2 \theta_{23}$	Flat in $[0, 1]$
$\Delta m_{21}^2$	Gaussian, $7.53 \pm 0.18 \times 10^{-5}$ eV $^2$
$\Delta m_{32}^2$	Flat, P(NH)=P(IH)=0.5
$\delta_{\text{CP}}$	Flat in $[-\pi, +\pi]$

Table 8.4: Priors for the oscillation parameters which are used in the analysis. Constraints on  $\sin^2 \theta_{12}$ ,  $\Delta m_{21}^2$  and  $\sin^2 \theta_{13}$  are based on the global fit and averaged results listed in [15].

It can be seen especially from the  $-\ln P(\vec{\sigma}, \vec{f}|D)$  plot that for the first  $\sim 5000$  steps the distribution of the variable depends on the number of steps taken, which indicates that the random walk has not reached an equilibrium during this period. Such period is referred to as the “burn-in” period, and since the steps taken during this time do not properly represent the posterior distribution, certain number of steps at the beginning of the chains need to be discarded. In this analysis, the initial 20,000 steps in each chain are discarded as burn-in, and as it can be seen from the plots the MCMC process reaches an equilibrium after 20,000 steps and is evenly sampling the posterior distribution. Thus, there are  $5 \times 10^6$  post-burn-in steps used for this sensitivity study.

Once the posterior probability is sampled by MCMC, the marginalized posterior distributions for the oscillation parameters are readily obtained simply by projecting the sampled points into histograms for the oscillation parameters. Figure 8.16 shows the marginalized 2D posterior distribution for  $\Delta m_{32}^2$  and  $\sin^2 \theta_{23}$  where all the other oscillation and systematic parameters have been marginalized over. The blue cross indicates the mode of this 2D posterior, i.e. the point with the highest posterior probability density which is analogous to the “best fit” point in a more-common frequentist analysis, and the cyan star is the true point where the Asimov dataset was produced. The dashed and solid contours indicate the 68% and 90% Highest Posterior Density(HPD) credible regions respectively. A  $\alpha\%$  HPD credible region is defined such that the integrated probability within the region is  $\alpha\%$  while the posterior density in any point within the region is higher than any point outside. Thus, the point estimate and the allowed regions for the oscillation parameters can be obtained from the Bayesian posterior probability distributions produced using MCMC.

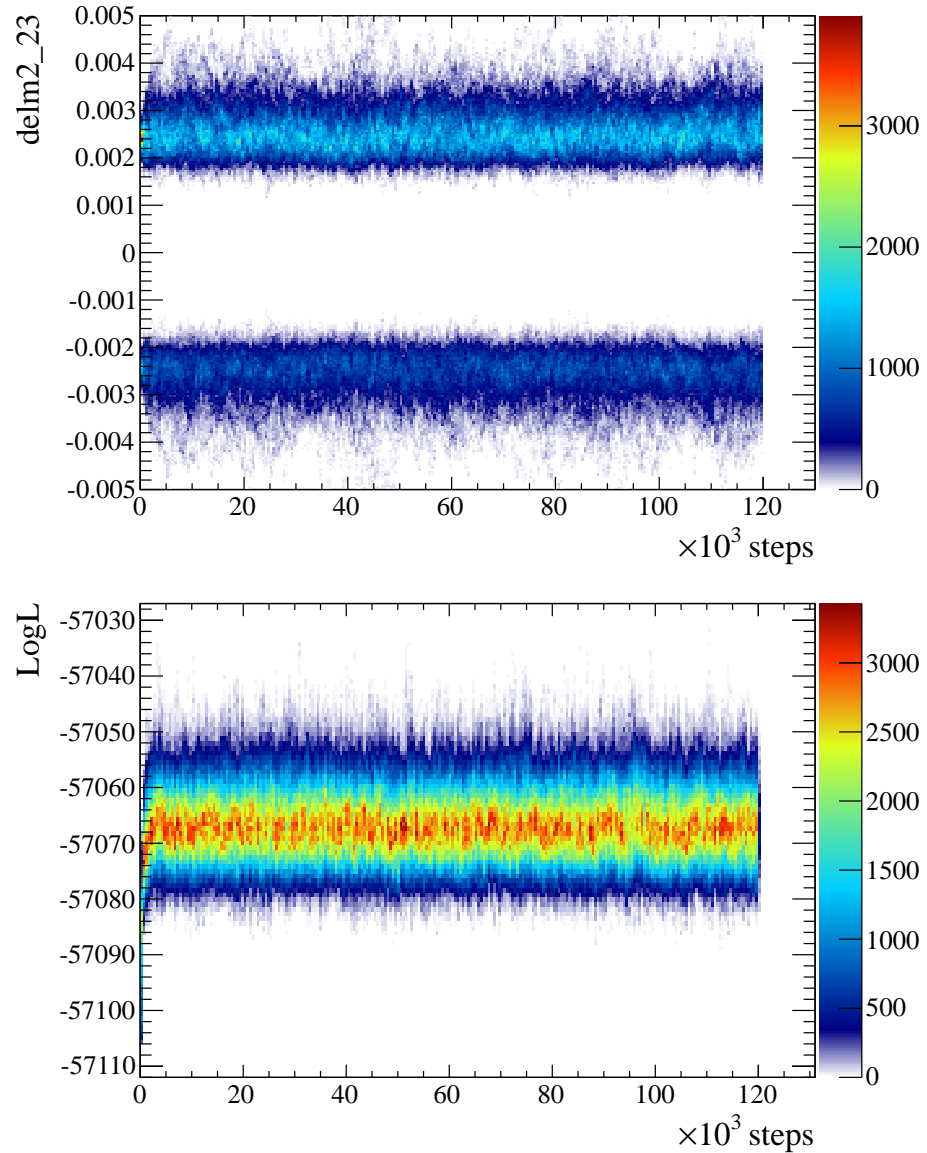


Figure 8.15:  $\Delta m_{32}^2$  (upper plot) and  $-\ln P(\vec{o}, \vec{f}|D)$  (lower plot), the negative-log of the posterior probability, plotted against the number of steps taken in each chain. Steps from all the produced MCMC chains are combined in the plots.

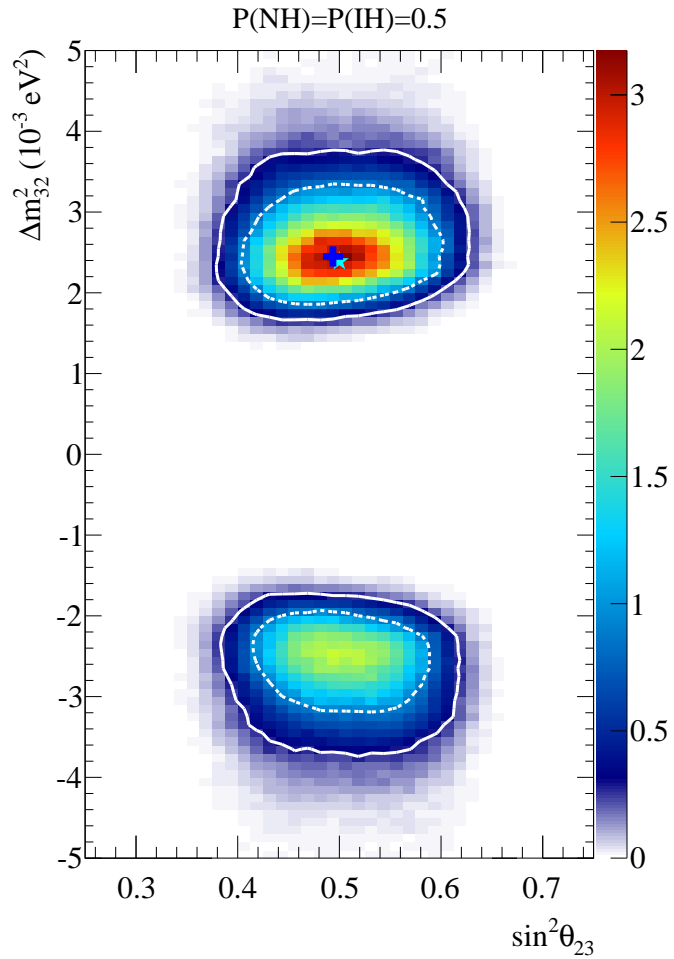


Figure 8.16: The marginalized 2D posterior distribution for  $\Delta m_{32}^2$  and  $\sin^2 \theta_{23}$  given the Asimov dataset, where the blue cross indicates the mode of this 2D posterior and the cyan star is the true point where the Asimov dataset was produced. The dashed and solid contours indicate the 68% and 90% HPD credible regions respectively.

## 8.5. Sensitivity Studies

---

As in Figure 8.16, the posterior is distributed for both positive and negative signs for  $\Delta m_{32}^2$ , and one can obtain the posterior probabilities for the mass hierarchy by marginalizing over all other information, i.e., by simply integrating the  $\Delta m_{32}^2$  posterior for above and below zero which is equivalent to counting the number of steps taken in the normal and inverted hierarchies. For this Asimov dataset the ratio of the number of steps taken in each hierarchy is NH:IH=2901738:2098262, which yields the posterior probability for normal hierarchy to be 58.0%.

By selecting the steps in either one of the hierarchies only, one can also obtain the posteriors in the case of assuming one of the hierarchy to be true. For example, Figure 8.17 shows the 2D posteriors for  $\sin^2 \theta_{23}$  and  $\delta_{\text{CP}}$  in the case of fixed mass hierarchy. Figure 8.18 is the 1D posteriors for the three parameters for each hierarchy where the 68% and 90% HPD credible regions are indicated by the dark gray and light gray regions respectively.

It is interesting to note that, although the mode of the 2D posterior is located near the true point as in the upper plot of Figure 8.17, once the distribution is further marginalized over  $\sin^2 \theta_{23}$  the mode of the 1D posterior for  $\delta_{\text{CP}}$  drifts away from the true value. This is due to the correlations between the two variables as seen in Figure 8.17, namely, although the local density is higher near the true point at  $\delta_{\text{CP}} = -0.5\pi$  and  $\sin^2 \theta_{23} = 0.5$ , the distribution is wider in  $\sin^2 \theta_{23}$  at  $\delta_{\text{CP}} \approx -0.7\pi$ . Being able to fully marginalize over the nuisance parameters with complex correlations in such way without having to assume the Gaussian-ness of the posterior is one of the distinct features of a Bayesian analysis such as this analysis, as opposed to the more common frequentist analysis by  $\chi^2$  minimization.

Figure 8.19 shows the mean and the standard deviation ( $\sigma$ ) of the 1D marginalized posterior for each systematic parameter in the case of assuming normal hierarchy. The enumeration of the systematic parameters can be found in Appendix A. In the plot the markers and the error bars represent the mean and the  $\sigma$  of the posterior respectively, where the nominal value of each systematic parameter is taken to be zero and the deviation from nominal is normalized by the prior uncertainty. Although it is a small effect, the posterior mean for some of the parameters deviate from zero due to the correlations with other parameters. This plot essentially shows how each systematic parameter can be constrained by the atmospheric neutrino data itself, and for the parameters whose posterior is significantly narrower than the prior, i.e. the parameters whose width of the error bar is significantly smaller than one, the constraint from the data is strong. For instance, the flux normalization below 1 GeV (parameter #1) which has  $\sim 10\%$  prior uncertainty is strongly constrained by the large statistics of sub-GeV samples.

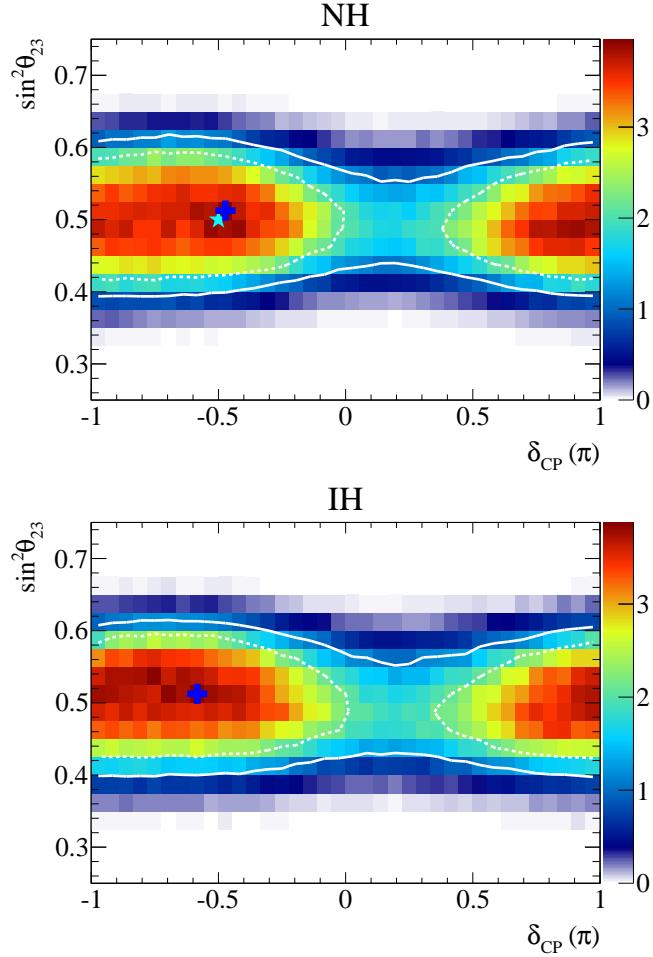


Figure 8.17: The 2D marginalized posterior distributions for  $\sin^2 \theta_{23}$  and  $\delta_{CP}$  given the Asimov dataset, where the upper plot is for assuming normal hierarchy to be true while the lower plot is for inverted hierarchy. The blue cross indicates the mode of this 2D posterior and the cyan star is the true point where the Asimov dataset was produced. The dashed and solid contours indicate the 68% and 90% HPD credible regions respectively.

### 8.5. Sensitivity Studies

---

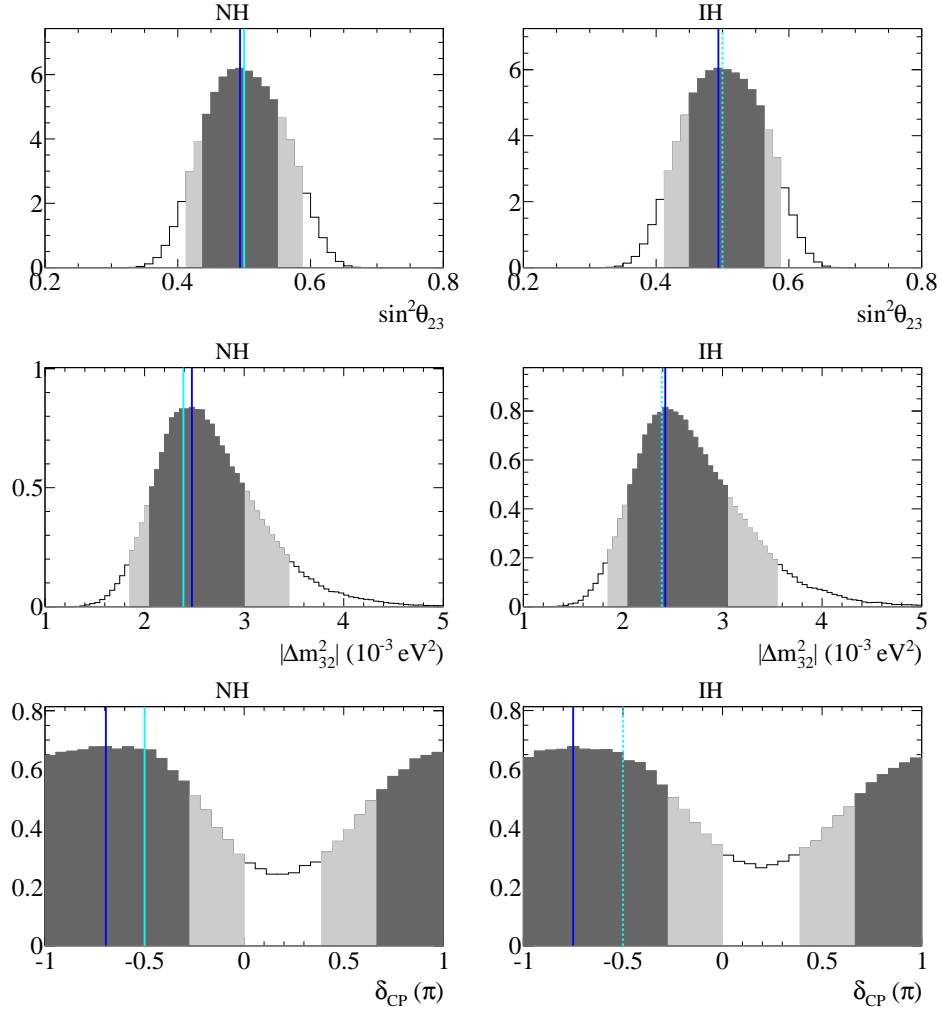


Figure 8.18: The marginalized 1D posterior distributions for  $\sin^2 \theta_{23}$  (top),  $|\Delta m_{32}^2|$  (middle) and  $\delta_{\text{CP}}$  (bottom) for the cases of assuming normal (left) and inverted (right) hierarchy, given the Asimov dataset. The vertical blue lines indicate the mode of the 1D posteriors while the cyan lines indicate the true point where the Asimov dataset was produced. The dark gray and light gray regions indicate the 68% and 90% HPD credible regions respectively.

## 8.6. Data Analysis Results

---

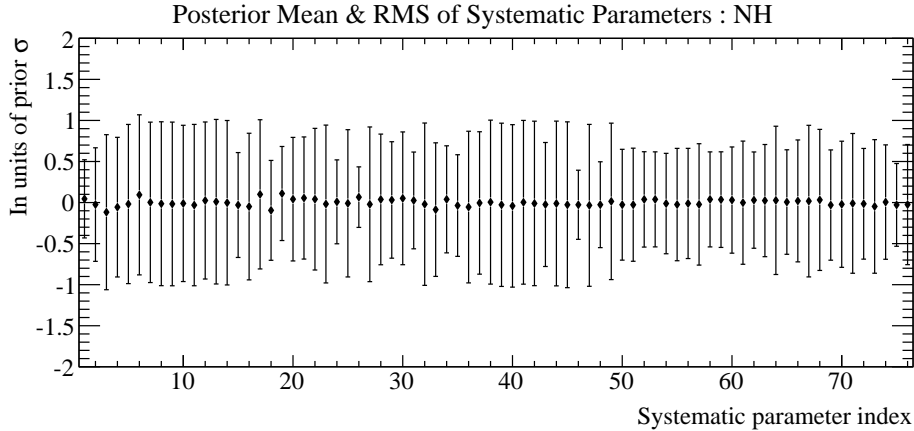


Figure 8.19: The mean and the  $\sigma$  of the marginalized 1D posterior for each systematic parameter in the case of assuming normal hierarchy, for the Asimov dataset. The enumeration of the systematic parameters can be found in Appendix A. The markers and the error bars represent the mean and the  $\sigma$  of the posterior respectively, where the nominal value of each systematic parameter is taken to be zero and the deviation from nominal is normalized by the prior uncertainty.

A similar sensitivity study was performed using APFIT for event selection instead of fitQun, and the comparison of the sensitivity between the two cases can be found in Appendix B.

## 8.6 Data Analysis Results

The result of analyzing the Super-K data is presented in this section. The dataset which is used in this analysis is the FC data from SK-IV with 2519.89 days exposure. The observed number of events in each selected event category has been summarized in Table 8.1.

The analysis is performed in the same manner as in the sensitivity study in Section 8.5, taking the priors for the oscillation parameters as described in Table 8.4. 200 MCMC chains of 120,000 steps were produced where the initial 20,000 steps in each chain are discarded as burn-in, which leaves in total  $2 \times 10^7$  post-burn-in steps for this analysis.

### 8.6.1 Posterior Distributions

Figure 8.20 shows the marginalized 2D posterior distribution for  $\Delta m_{32}^2$  and  $\sin^2 \theta_{23}$ . It can be seen in the figure that the posterior is distributed more in the upper half which indicates that there is a larger preference for normal hierarchy, which is due to the observed overall excess in the upward-going multi-GeV  $\nu_e$  events as shown in Figure 8.27. The posteriors for the case of assuming one of the hierarchy to be true are also shown in Figure 8.21. The mode of the posteriors are located at  $\sin^2 \theta_{23} = 0.606$  and  $\Delta m_{32}^2 = +2.15 \times 10^{-3} \text{ eV}^2$  for normal hierarchy, and at  $\sin^2 \theta_{23} = 0.406$  and  $\Delta m_{32}^2 = -1.85 \times 10^{-3} \text{ eV}^2$  for inverted hierarchy.

Figure 8.22 shows the 2D posteriors for  $\sin^2 \theta_{23}$  and  $\delta_{\text{CP}}$  for each of the hierarchy assumption. As was discussed in Section 8.1.6, since decreasing  $\sin^2 \theta_{23}$  from 0.5 and decreasing  $\delta_{\text{CP}}$  from 0 both have the effect of increasing the sub-GeV e-like events, the competing effects introduce high correlations in the posterior for the two parameters and the preference for  $\delta_{\text{CP}}$  is different depending on the  $\theta_{23}$  octant.

Figure 8.23 shows the marginalized 1D posteriors for the three oscillation parameters plotted separately for normal and inverted hierarchy, and the mode and the 68% HPD credible region for each 1D posterior are summarized in Table 8.5. The 1D posteriors in the case mass hierarchy is marginalized are also shown in Figure 8.24.

Parameter	Normal Hierarchy	Inverted Hierarchy
$\sin^2 \theta_{23}$	0.606 [0.488,0.650]	0.406 [0.375,0.475] $\cup$ [0.538,0.625]
$ \Delta m_{32}^2  (10^{-3} \text{ eV}^2)$	2.13 [1.75,2.30]	1.88 [1.7,2.3]
$\delta_{\text{CP}}(\pi)$	-0.92 [-1.00,-0.17] $\cup$ [0.72,1.00]	0.92 [-1.00,-0.17] $\cup$ [0.61,1.00]

Table 8.5: The 1D posterior mode and the 68% HPD credible intervals.

From the posterior in Figure 8.20, the posterior probabilities for normal ( $\Delta m_{32}^2 > 0$ ) and inverted ( $\Delta m_{32}^2 < 0$ ) hierarchy as well as the first ( $\sin^2 \theta_{23} < 0.5$ ) and the second ( $\sin^2 \theta_{23} > 0.5$ )  $\theta_{23}$  octant are calculated by integrating the 2D posterior in each of the four quadrants. The results are summarized in Table 8.6, and the data shows mild preferences for the normal hierarchy and the second  $\theta_{23}$  octant.

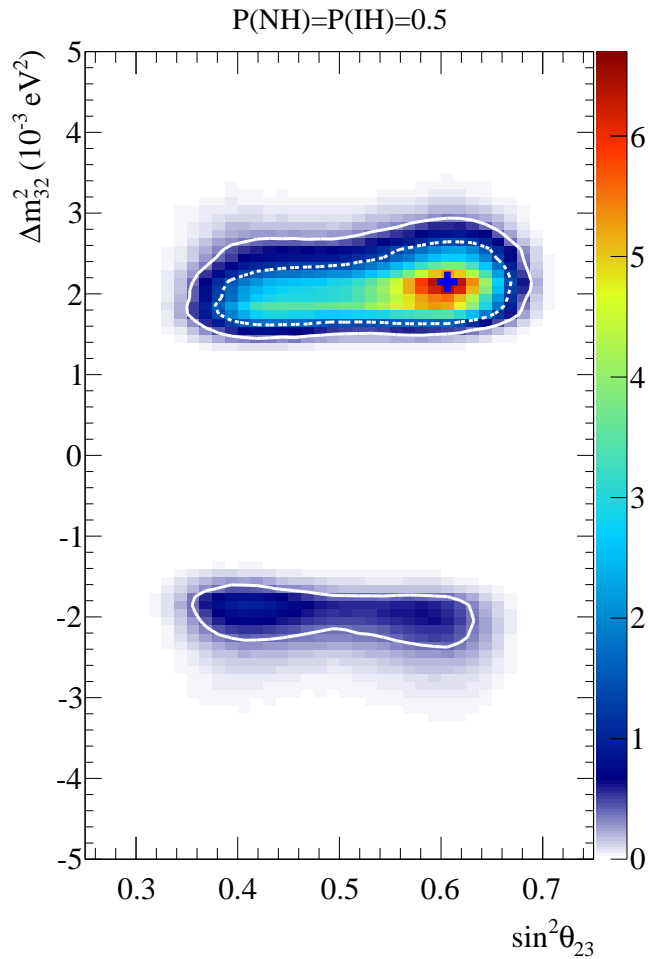


Figure 8.20: The marginalized 2D posterior distribution for  $\Delta m_{32}^2$  and  $\sin^2 \theta_{23}$  given the SK-IV FC data, where the blue cross indicates the mode of this 2D posterior. The dashed and solid contours indicate the 68% and 90% HPD credible regions respectively.

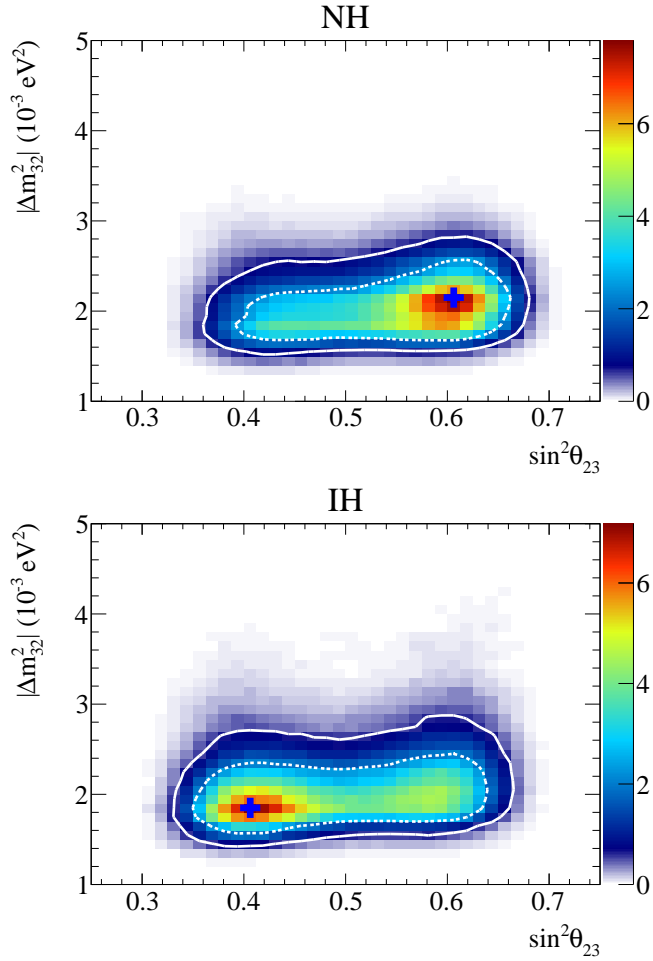


Figure 8.21: The marginalized 2D posterior distributions for  $|\Delta m_{32}^2|$  and  $\sin^2 \theta_{23}$  for the cases of assuming normal (top) and inverted (bottom) hierarchy, given the SK-IV FC data. The blue cross indicates the mode of each posterior. The dashed and solid contours indicate the 68% and 90% HPD credible regions respectively.

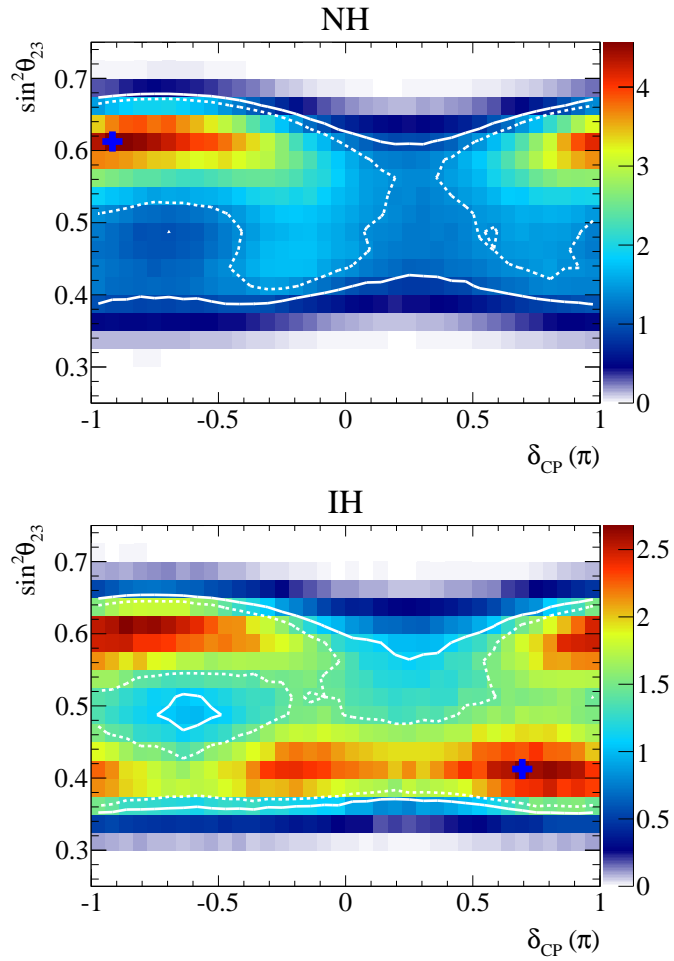


Figure 8.22: The marginalized 2D posterior distributions for  $\sin^2\theta_{23}$  and  $\delta_{CP}$  for the cases of assuming normal (top) and inverted (bottom) hierarchy, given the SK-IV FC data. The blue cross indicates the mode of each 2D posterior. The dashed and solid contours indicate the 68% and 90% HPD credible regions respectively.

## 8.6. Data Analysis Results

---

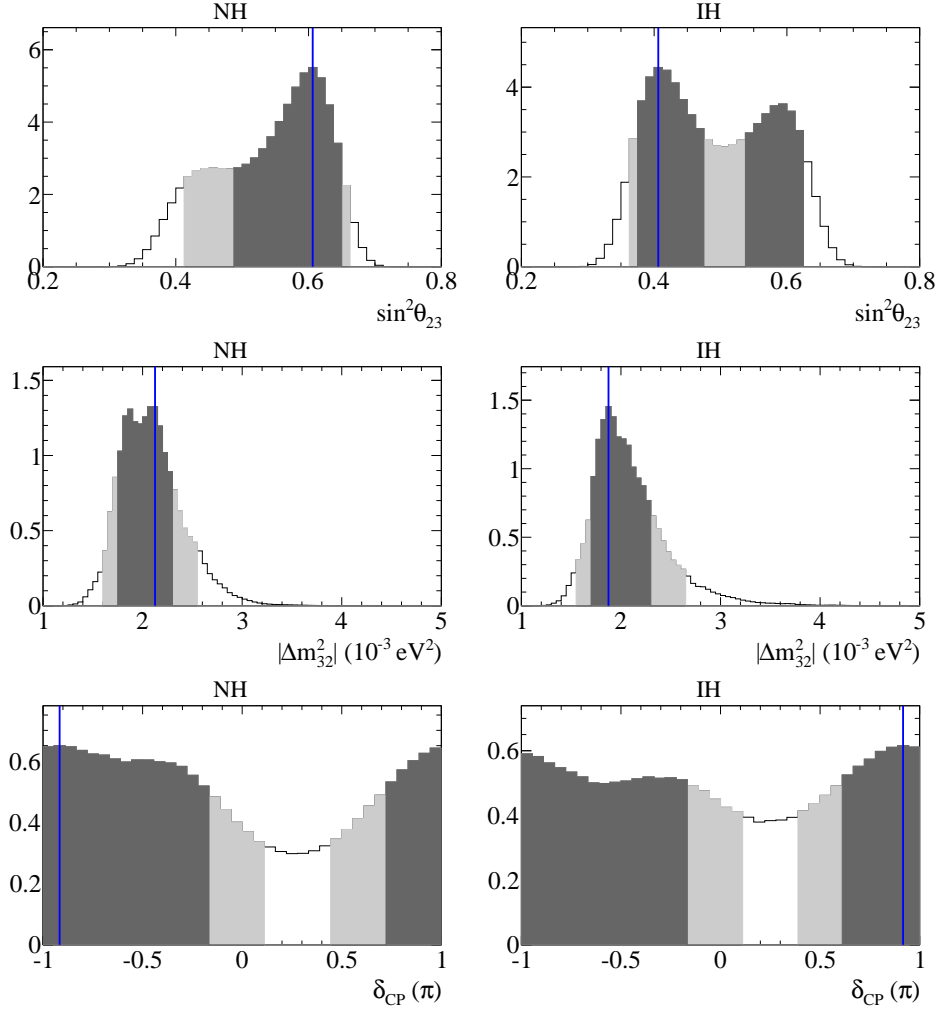


Figure 8.23: The marginalized 1D posterior distributions for  $\sin^2 \theta_{23}$  (top),  $|\Delta m_{32}^2|$  (middle) and  $\delta_{\text{CP}}$  (bottom) for the cases of assuming normal (left) and inverted (right) hierarchy, given the SK-IV FC data. The vertical blue lines indicate the mode of the 1D posteriors. The dark gray and light gray regions indicate the 68% and 90% HPD credible regions respectively.

## 8.6. Data Analysis Results

---

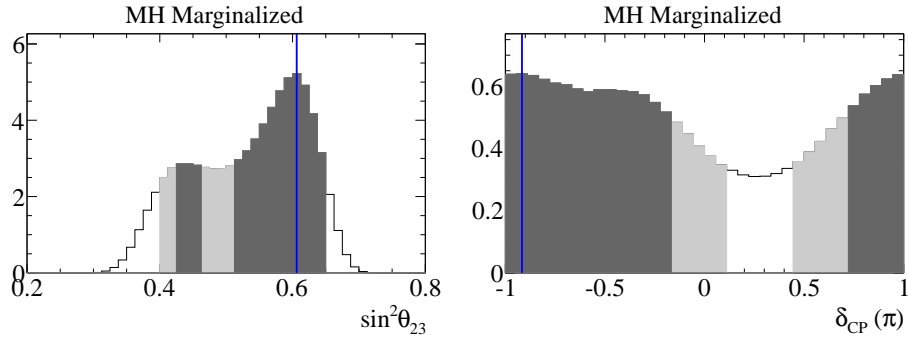


Figure 8.24: The marginalized 1D posterior distributions for  $\sin^2 \theta_{23}$  and  $\delta_{CP}$  after marginalizing over the mass hierarchy, given the SK-IV FC data. The vertical blue lines indicate the mode of the 1D posteriors. The dark gray and light gray regions indicate the 68% and 90% HPD credible regions respectively.

	1st Oct.	2nd Oct.	Sum
Normal	0.275	0.584	0.859
Inverted	0.076	0.065	0.141
Sum	0.351	0.649	1.000

Table 8.6: Posterior probabilities for the mass hierarchy and the  $\theta_{23}$  octant.

The 1D posterior distributions for the other oscillation parameters have the mean and the  $\sigma$  of the following:  $\sin^2 \theta_{12} = 0.304 \pm 0.014$ ,  $\sin^2 \theta_{13} = 0.0219 \pm 0.0012$  and  $\Delta m_{21}^2 = 7.53 \pm 0.18 \times 10^{-5}$  eV $^2$ . These values are nearly identical to the prior constraints listed in Table 8.4 due to the lack of sensitivity of atmospheric neutrino data to these parameters.

Figure 8.25 shows the mean and the  $\sigma$  of the marginalized 1D posterior for each systematic parameter where the posteriors for normal and inverted hierarchy are shown separately. The enumeration of the systematic parameters can be found in Appendix A.

### 8.6.2 Zenith Angle Distributions

Figures 8.26 to 8.28 show the zenith angle distributions for each event sample comparing the data with the expectations calculated with normal and inverted hierarchy. For each hierarchy, the expectations are calculated by setting each oscillation and systematic parameter to the value at the mode of the parameter's 1D posterior for the given choice of mass hierarchy. For

## 8.6. Data Analysis Results

---

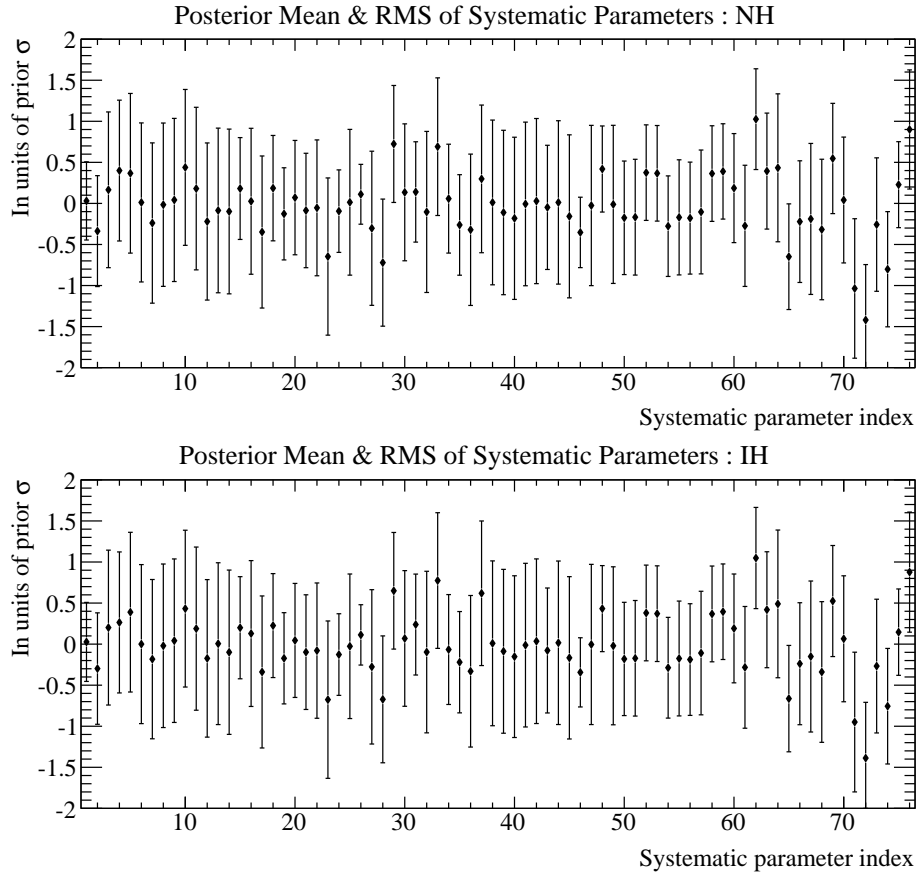


Figure 8.25: The mean and the  $\sigma$  of the marginalized 1D posterior for each systematic parameter in the cases of assuming normal (top) and inverted (bottom) hierarchy, for the SK-IV FC data. The enumeration of the systematic parameters can be found in Appendix A. The markers and the error bars represent the mean and the  $\sigma$  of the posterior respectively, where the nominal value of each systematic parameter is taken to be zero and the deviation from nominal is normalized by the prior uncertainty.

## 8.6. Data Analysis Results

---

the oscillation parameters  $\sin^2 \theta_{23}$ ,  $\Delta m_{32}^2$  and  $\delta_{\text{CP}}$  only, since there are large complex correlations between the parameters, their values are set to what are shown in Table 8.7 which are close to the mode of the 2D posteriors. The observed overall excess in the upward-going multi-GeV  $\nu_e$  events contributes to the preference for the normal hierarchy.

Parameter	Normal Hierarchy	Inverted Hierarchy
$\sin^2 \theta_{23}$	0.61	0.41
$\Delta m_{32}^2 (10^{-3} \text{eV}^2)$	+2.15	-1.85
$\delta_{\text{CP}}(\pi)$	-0.9	+0.7

Table 8.7: Oscillation parameters which are used to calculate the event rate predictions shown in Figures 8.26 to 8.28.

### 8.6.3 Goodness of Fit

In order to test whether or not the models assumed in this analysis disagree with the observed data, a goodness of fit test is performed according to the prescriptions described in [105]. First, 2000 points are randomly sampled from the MCMC chains which were used in the data analysis, which produces a reduced set of sample points which represents the posterior distribution. For each sampled point, a fake dataset is thrown using the predictions at that point, and the likelihood Equation 8.7 is compared between the fake data and the real data. Figure 8.29 shows the distribution of the log likelihood ratio between the real and the fake data for all points. A p-value is then calculated as the fraction of points at which the real data having a larger likelihood value than the fake data. The calculated p-value, which the authors of [105] refer to as the posterior predictive p-value, is essentially the classical p-value as used in the standard goodness of fit test in frequentist analyses averaged over the entire posterior. This test is therefore assessing the fitness of the entire Bayesian posterior model to the observed data, rather than at a single best-fit point. The posterior predictive p-value for this analysis is calculated to be 10.3%, which is large enough that the assumed models are not excluded by the data according to this test.

### 8.6.4 Result Comparison to Other Experiments

Figure 8.30 compares the results of this analysis for  $\Delta m_{32}^2$  and  $\sin^2 \theta_{23}$  with the latest results from other experiments. In the plots, 90% HPD credible regions are shown for Bayesian analyses, whereas for frequentist

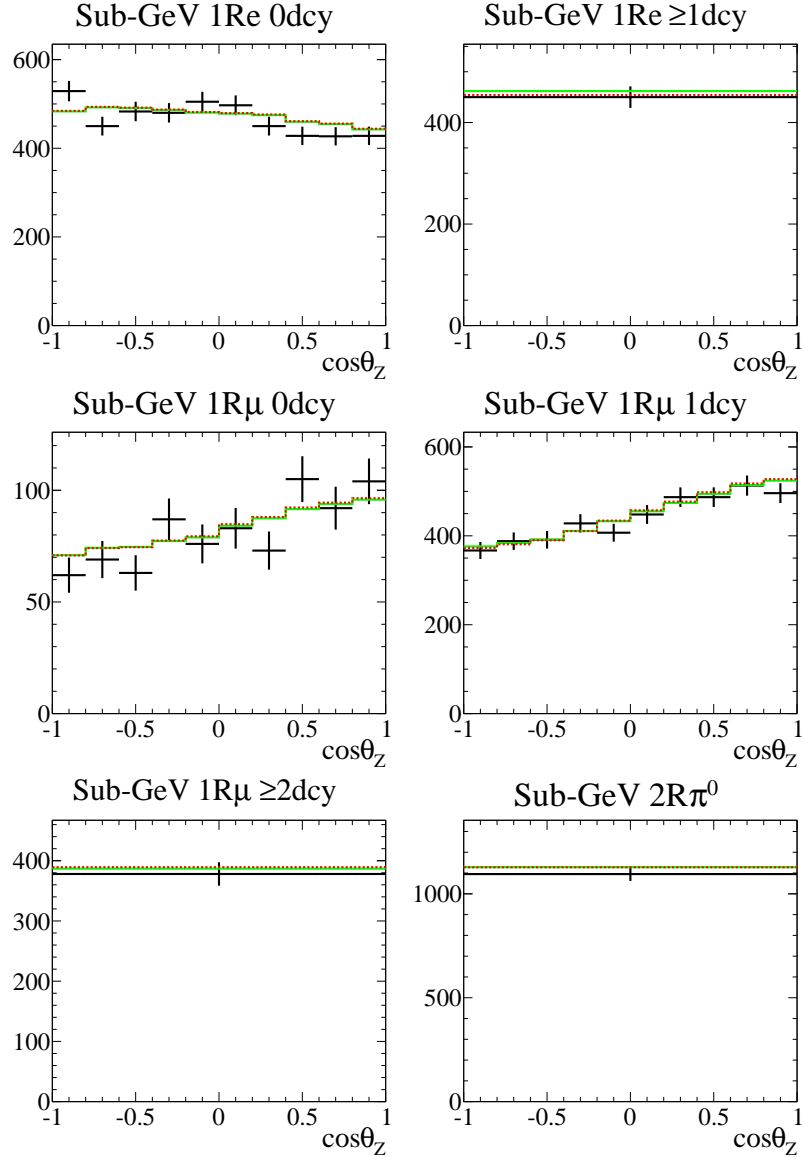


Figure 8.26: Distributions of the cosine of the zenith angle for the sub-GeV event samples. The black markers indicate the data, and the solid green and the dashed red lines represent the expectations calculated with normal hierarchy and inverted hierarchy respectively. For each hierarchy, the expectation is calculated by setting the oscillation and systematic parameters at the mode of the posteriors for the respective hierarchy.

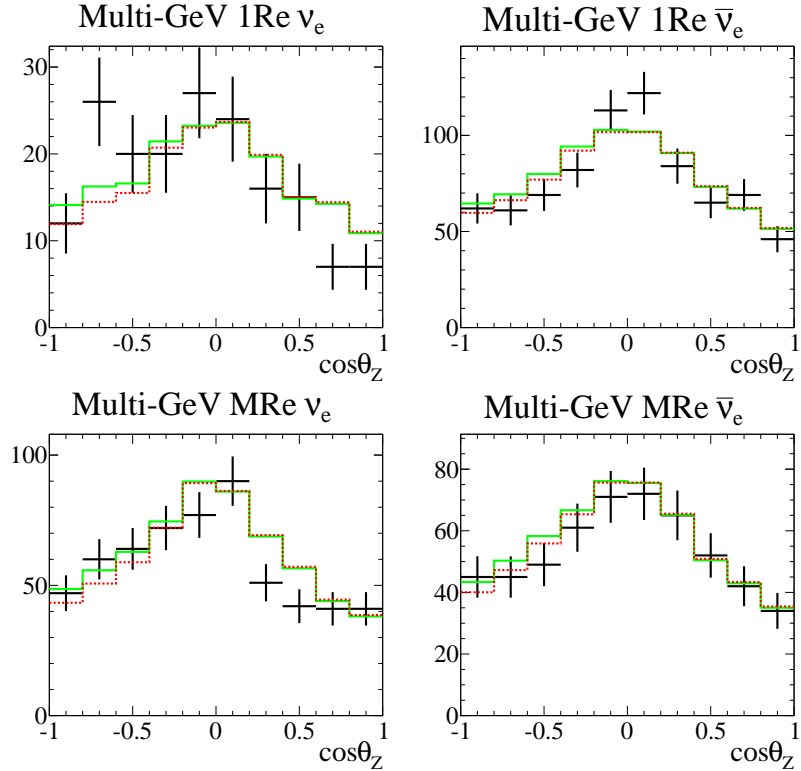


Figure 8.27: Distributions of the cosine of the zenith angle for the multi-GeV e-like event samples. The black markers indicate the data, and the solid green and the dashed red lines represent the expectations calculated with normal hierarchy and inverted hierarchy respectively. For each hierarchy, the expectation is calculated by setting the oscillation and systematic parameters at the mode of the posteriors for the respective hierarchy.

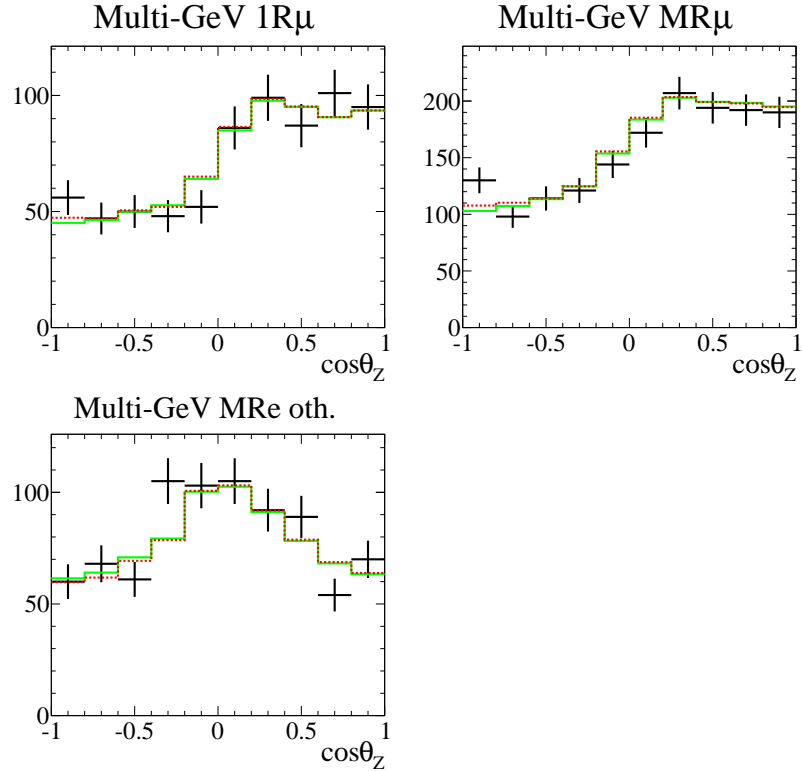


Figure 8.28: Distributions of the cosine of the zenith angle for the multi-GeV  $\mu$ -like and other event samples. The black markers indicate the data, and the solid green and the dashed red lines represent the expectations calculated with normal hierarchy and inverted hierarchy respectively. For each hierarchy, the expectation is calculated by setting the oscillation and systematic parameters at the mode of the posteriors for the respective hierarchy.

## 8.6. Data Analysis Results

---

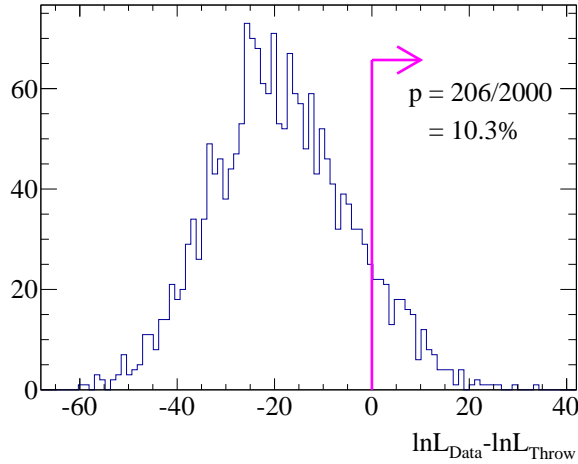


Figure 8.29: Distribution of the log likelihood ratio between the observed data and fake data which is used for the goodness of fit test. The posterior predictive p-value is calculated to be 10.3%.

analyses 90% confidence regions are shown instead. The plots show the latest preliminary results from the conventional SK atmospheric neutrino analysis[106][107](labeled as “SK1-4 Freq.” in the plots) which employs a frequentist analysis technique by  $\chi^2$  minimization and event selection based on APFIT, the preexisting event reconstruction which was mentioned in Chapter 6. The analysis uses the full SK-I to IV data of 5326 days exposure which is more than double the data statistics compared to the SK-IV-only data which is used in the Bayesian analysis with fitQun event selection presented in this chapter, and the difference in sensitivity between the two analyses is dominantly due to the additional data in the APFIT-based analysis. The data from the old SK-I to III phases is not included in the fitQun-based analysis due to the observed large data-MC discrepancies as discussed in Section 6.11, and inclusion of such data requires improvements in the detector simulation which is expected to be achievable in near future. The T2K result[108] is from a Bayesian analysis which uses a similar MCMC technique described in Section 8.4 and produces Bayesian credible regions. The results from MINOS[109] and NO $\nu$ A[110] are both from frequentist analyses which report their results as confidence regions. One should note that the Bayesian credible regions and frequentist confidence regions are different and are not comparable in a strict sense, although such comparison is interesting as a rough measure.

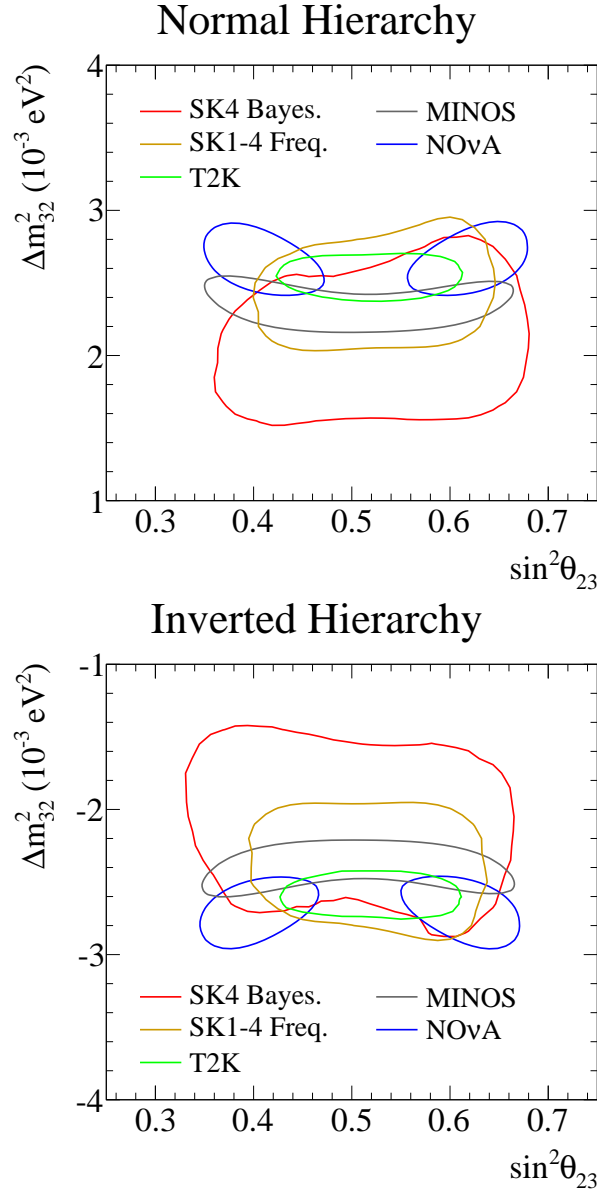


Figure 8.30: 90% credible and confidence regions for  $\Delta m_{32}^2$  and  $\sin^2 \theta_{23}$  for the results from various experiments. The red contours labeled as “SK4 Bayes.” are the results from the analysis presented in this chapter which is a Bayesian analysis using SK-IV atmospheric neutrino data selected by fitQun event reconstruction. The upper and the lower plots are the cases of assuming normal and inverted hierarchy respectively.

## Chapter 9

# Conclusions and Outlook

An oscillation analysis of the Super-Kamiokande atmospheric neutrino data was presented. The analysis employed a new maximum likelihood event reconstruction algorithm to reconstruct and select atmospheric neutrino events, and oscillation parameters were estimated using a Markov chain Monte Carlo technique which produces marginalized Bayesian posterior probability distributions for neutrino oscillation parameters based on the observed data.

Analyzing the data of 2520 days exposure from SK-IV, the result prefers normal hierarchy with the posterior probability of 85.9%, and the mode and the 68% highest posterior density credible interval of each oscillation parameter’s 1D posterior probability distribution for normal hierarchy are  $\sin^2 \theta_{23} = 0.606^{+0.044}_{-0.118}$  and  $\Delta m_{32}^2 = 2.13^{+0.17}_{-0.38} \times 10^{-3}$  eV<sup>2</sup>. The analysis also has small sensitivity to  $\delta_{\text{CP}}$ , however, nothing conclusive can be said regarding whether CP violation is observed.

The Bayesian analysis method using MCMC allows one to fully marginalize over nuisance parameters and report the result on the parameters of interest as marginalized Bayesian posterior probabilities. When parameters have highly non-Gaussian behaviours, which is the case for the oscillation parameters in this analysis, being able to actually marginalize over nuisance parameters is advantageous compared to the more common frequentist technique of profiling the likelihood, i.e. to minimize the negative-log-likelihood or the  $\chi^2$  over nuisance parameters, which becomes equal to marginalization only when the parameters have Gaussian behaviours.

The new event reconstruction algorithm “fITQun” significantly improves particle identification and vertex and kinematic reconstruction performances compared to the preexisting event reconstruction at SK. The new algorithm was first used in the T2K  $\nu_e$  appearance analysis for  $\pi^0$  rejection, which resulted in more than 60% reduction of the NC background in the signal  $\nu_e$  event sample compared to the previous  $\pi^0$  rejection method. However, the application of fITQun in T2K has been limited to the  $\pi^0$  rejection only, and the SK atmospheric neutrino analysis presented in this thesis is the first physics analysis which makes an extensive use of the new algorithm

by employing an entirely fitQun-based event selection. There are currently ongoing efforts to extend the usage of fitQun in various other studies such as the nucleon decay analyses at SK[111], T2K oscillation analyses[112] and studies for future water Cherenkov detectors[113].

Only the data from SK-IV was used in the analysis presented in this thesis due to the large data-MC discrepancy observed in SK-I to III as mentioned in Section 6.11. However, by improving the detector simulation, it is expected that the data from SK-I to III can also be included in the oscillation analysis using fitQun in near future. Table 9.1 shows the expected sensitivity to the mass hierarchy at each of the following SK exposure: 2520 days which is the current SK-IV exposure used in the presented data analysis, 5300 days which is roughly the current total exposure from SK-I to IV, and 8500 days which is the expected accumulated exposure in 10 years when the next generation neutrino oscillation experiments such as Hyper-Kamiokande[114] and DUNE[115] are expected to start. As in the table, sensitivity to the mass hierarchy continues to improve significantly as the data statistics increase.

Exposure	2520 days	5300 days	8500 days
True NH	67.2%	81.6%	91.0%
True IH	61.8%	71.4%	80.9%

Table 9.1: Expected posterior probabilities for favouring the correct mass hierarchy for different SK exposure, based on the Asimov dataset produced at either normal or inverted hierarchy,  $\sin^2 \theta_{23} = 0.6$  and other oscillation parameters set to the values in Table 8.3. The middle row shows the posterior probabilities for favouring NH for the dataset produced with NH, and the bottom row are the probabilities for favouring IH for the datasets produced with IH.

Long baseline accelerator neutrino experiments such as T2K and NO $\nu$ A are rapidly accumulating data, and the experiments have sensitivity to  $\delta_{CP}$  and mass hierarchy. However, the competing effects from the unknowns produce degeneracies in the oscillation probabilities which limit the experiments' sensitivities. By combining their results and the results from SK atmospheric neutrino analysis which strongly constrains the mass hierarchy, one can disentangle the different oscillation effects and improve the sensitivity to  $\delta_{CP}$  and the mass hierarchy compared to the analyses of individual experiments. It is expected that decisive measurements of the neutrino mass hierarchy and CP violation would require the next generation neu-

trino oscillation experiments such as Hyper-Kamiokande and DUNE which are planned to start their operation in the late 2020's. However, by combining the current global efforts we can further explore the remaining mysteries of neutrino oscillations in the interim.

# Bibliography

- [1] M. Goldhaber *et al.*. “Helicity of Neutrinos”. *Phys. Rev.*, 109:1015, 1958.
- [2] K.A. Olive *et al.*(Particle Data Group). “Neutrino Properties”. *Chin. Phys. C*, 38:090001, 2014 and 2015 update.
- [3] M. Kobayashi and T. Maskawa. “CP-Violation in the Renormalizable Theory of Weak Interaction”. *Prog. Theor. Phys.*, 49:652–657, 1973.
- [4] B. Pontecorvo. “Inverse beta processes and nonconservation of lepton charge”. *Sov. Phys. JETP*, 7:172–173, 1958.
- [5] Z. Maki *et al.*. “Remarks on the Unified Model of Elementary Particles”. *Prog. Theor. Phys.*, 28:870–880, 1962.
- [6] L. Wolfenstein. “Neutrino oscillations in matter”. *Phys. Rev. D*, 17:2369, 1978.
- [7] S.P. Mikheev and A.Y. Smirnov. “Resonance Amplification of Oscillations in Matter and Spectroscopy of Solar Neutrinos”. *Sov.J.Nucl.Phys.*, 42:913–917, 1985.
- [8] R. Davis Jr. *et al.*. “Search for Neutrinos from the Sun”. *Phys. Rev. Lett.*, 20:1205, 1968.
- [9] J.N. Bahcall. “Solar Neutrinos. I. Theoretical”. *Phys. Rev. Lett.*, 12:300302, 1964.
- [10] Q.R. Ahmad *et al.*. “Measurement of the Rate of  $\nu_e + d \rightarrow p + p + e^-$  Interactions Produced by  $^8\text{B}$  Solar Neutrinos at the Sudbury Neutrino Observatory”. *Phys. Rev. Lett.*, 87:071301, 2001.
- [11] Q.R. Ahmad *et al.*. “Direct Evidence for Neutrino Flavor Transformation from Neutral-Current Interactions in the Sudbury Neutrino Observatory”. *Phys. Rev. Lett.*, 89:011301, 2002.

## Bibliography

---

- [12] B. Aharmim *et al.*. “Electron energy spectra, fluxes, and day-night asymmetries of  ${}^8\text{B}$  solar neutrinos from measurements with NaCl dissolved in the heavy-water detector at the Sudbury Neutrino Observatory”. *Phys. Rev. C*, 72:055502, 2005.
- [13] S. Fukuda *et al.*. “Solar  ${}^8\text{B}$  and hep Neutrino Measurements from 1258 Days of Super-Kamiokande Data”. *Phys. Rev. Lett.*, 86:5651, 2001.
- [14] K. Eguchi *et al.*. “First Results from KamLAND: Evidence for Reactor Antineutrino Disappearance”. *Phys. Rev. Lett.*, 90:021802, 2003.
- [15] K.A. Olive *et al.*(Particle Data Group). “Neutrino Mixing”. *Chin. Phys. C*, 38:090001, 2014 and 2015 update.
- [16] K.S. Hirata *et al.*. “Experimental study of the atmospheric neutrino flux”. *Phys. Lett. B*, 205:416–420, 1988.
- [17] K.S. Hirata *et al.*. “Observation of a small atmospheric  $\nu_\mu/\nu_e$  ratio in Kamiokande”. *Phys. Lett. B*, 280:146–152, 1992.
- [18] D. Casper *et al.*. “Measurement of atmospheric neutrino composition with the IMB-3 detector”. *Phys. Rev. Lett.*, 66:2561, 1991.
- [19] R. Becker-Szendy. “Electron- and muon-neutrino content of the atmospheric flux”. *Phys. Rev. D*, 46:3720, 1992.
- [20] Y. Fukuda *et al.*. “Evidence for Oscillation of Atmospheric Neutrinos”. *Phys. Rev. Lett.*, 81:1562, 1998.
- [21] M.H. Ahn *et al.*. “Measurement of neutrino oscillation by the K2K experiment”. *Phys. Rev. D*, 74:072003, 2006.
- [22] D.G. Michael *et al.*. “Observation of Muon Neutrino Disappearance with the MINOS Detectors in the NuMI Neutrino Beam”. *Phys. Rev. Lett.*, 97:191801, 2006.
- [23] K. Iwamoto. “Recent Results from T2K and Future Prospects”. Slides from ICHEP 2016.  
<http://indico.cern.ch/event/432527/contributions/2143636/>. Accessed:2016/08/17.
- [24] M. Apollonio *et al.*. “Search for neutrino oscillations on a long base-line at the CHOOZ nuclear power station”. *Eur. Phys. J. C*, 27:331374, 2003.

## Bibliography

---

- [25] Y. Abe *et al.*. “Indication of Reactor  $\bar{\nu}_e$  Disappearance in the Double Chooz Experiment”. *Phys. Rev. Lett.*, 108:131801, 2012.
- [26] F.P. An *et al.*. “Observation of Electron-Antineutrino Disappearance at Daya Bay”. *Phys. Rev. Lett.*, 108:171803, 2012.
- [27] J.K. Ahn *et al.*. “Observation of Reactor Electron Antineutrinos Disappearance in the RENO Experiment”. *Phys. Rev. Lett.*, 108:191802, 2012.
- [28] K. Abe *et al.*. “Indication of Electron Neutrino Appearance from an Accelerator-Produced Off-Axis Muon Neutrino Beam”. *Phys. Rev. Lett.*, 107:041801, 2011.
- [29] K. Abe *et al.*. “Observation of Electron Neutrino Appearance in a Muon Neutrino Beam”. *Phys. Rev. Lett.*, 112:061802, 2014.
- [30] X. Qian and P. Vogel. “Neutrino mass hierarchy”. *Prog. Part. Nucl. Phys.*, 83:130, 2015.
- [31] M. Fukugita and T. Yanagida. “Baryogenesis without grand unification”. *Phys. Lett. B*, 174:45–47, 1986.
- [32] G.C. Branco *et al.*. “A bridge between CP violation at low energies and leptogenesis”. *Nucl. Phys. B*, 617:475492, 2001.
- [33] M.N. Rebelo. “Leptogenesis without CP violation at low energies”. *Phys. Rev. D*, 67:013008, 2003.
- [34] V. Barger *et al.*. “Matter effects on three-neutrino oscillations”. *Phys. Rev. D*, 22:2718, 1980.
- [35] A. M. Dziewonski and D. L. Anderson. “Preliminary Reference Earth Model”. *Phys. Earth Planet. Inter.*, 25:297–356, 1981.
- [36] C. Ishihara. “Full three flavor oscillation analysis of atmospheric neutrino data observed in Super-Kamiokande”. *PhD Thesis*, 2010.
- [37] C. Giunti *et al.*. “Atmospheric neutrino oscillations with three neutrinos and a mass hierarchy”. *Nucl. Phys. B*, 521:3–36, 1998.
- [38] O.L.G. Peres and A.Yu. Smirnov. “Testing the solar neutrino conversion with atmospheric neutrinos”. *Phys. Lett. B*, 456:204213, 1999.

## Bibliography

---

- [39] O.L.G. Peres and A.Yu. Smirnov. “Atmospheric neutrinos: LMA oscillations,  $U_{e3}$  induced interference and CP-violation”. *Nucl. Phys. B*, 680:479509, 2004.
- [40] S. Fukuda *et al.*. “The Super-Kamiokande detector”. *Nucl. Instrum. Meth.*, A501:418–462, 2003.
- [41] H. Nishino *et al.*. “High-speed charge-to-time converter ASIC for the Super-Kamiokande detector”. *Nucl. Instrum. Meth.*, A610:710717, 2009.
- [42] K. Abe *et al.*. “Calibration of the Super-Kamiokande detector”. *Nucl. Instrum. Meth.*, A737:253272, 2014.
- [43] M. Honda *et al.*. “Improvement of low energy atmospheric neutrino flux calculation using the JAM nuclear interaction model”. *Phys. Rev. D*, 83:123001, 2011.
- [44] J. Alcaraz *et al.*. “Cosmic protons”. *Phys. Lett. B*, 490:2735, 2000.
- [45] T. Sanuki *et al.*. “Precise Measurement of Cosmic-Ray Proton and Helium Spectra with the BESS Spectrometer”. *Astrophys. J.*, 545:1135–1142, 2000.
- [46] S. Haino *et al.*. “Measurements of primary and atmospheric cosmic-ray spectra with the BESS-TeV spectrometer”. *Phys. Lett. B*, 594:3546, 2004.
- [47] USCOESA. “U.S. Standard Atmosphere 1976”.  
[http://ccmc.gsfc.nasa.gov/modelweb/atmos/us\\_standard.html](http://ccmc.gsfc.nasa.gov/modelweb/atmos/us_standard.html). Accessed:2016/08/12.
- [48] S. Roesler *et al.*. “The Monte Carlo Event Generator DPMJET-III”. *arXiv:hep-ph/0012252*, 2000.
- [49] K. Niita *et al.*. “PHITS—a particle and heavy ion transport code system”. *Radiat. Meas.*, 41:10801090, 2006.
- [50] T. Sanuki. “Measurements of atmospheric muon spectra at mountain altitude”. *Phys. Lett. B*, 541:234242, 2002.
- [51] K. Abe *et al.*. “Measurements of proton, helium and muon spectra at small atmospheric depths with the BESS spectrometer”. *Phys. Lett. B*, 564:820, 2003.

## Bibliography

---

- [52] G. Battistoni *et al.*. “The FLUKA atmospheric neutrino flux calculation”. *Astropart. Phys.*, 19:269–290, 2003.
- [53] G. D. Barr *et al.*. “Three-dimensional calculation of atmospheric neutrinos”. *Phys. Rev. D*, 70:023006, 2004.
- [54] Y. Hayato. “NEUT”. *Nucl. Phys. B (Proc. Suppl.)*, 112:171–176, 2002.
- [55] S. Jadach *et al.*. “The  $\tau$  decay library TAUOLA, version 2.4”. *Comput. Phys. Commun.*, 76:361–380, 1993.
- [56] J.A. Formaggio and G.P. Zeller. “From eV to EeV: Neutrino cross sections across energy scales”. *Rev. Mod. Phys.*, 84:1307, 2012.
- [57] T.J. Irvine. “Development of Neutron-Tagging Techniques and Application to Atmospheric Neutrino Oscillation Analysis in Super-Kamiokande”. *PhD Thesis*, 2014.
- [58] C.H. Llewellyn Smith. “Neutrino Reactions at Accelerator Energies”. *Phys. Rept.* 3, 5:261–379, 1972.
- [59] R.A. Smith and E.J. Moniz. “Neutrino reactions on nuclear targets”. *Nucl. Phys. B*, 43:605–622, 1972.
- [60] R. Gran *et al.*. “Measurement of the quasielastic axial vector mass in neutrino interactions on oxygen”. *Phys. Rev. D*, 74:052002, 2006.
- [61] A.A. Aguilar-Arevalo. “First measurement of the muon neutrino charged current quasielastic double differential cross section”. *Phys. Rev. D*, 81:092005, 2010.
- [62] J. Nieves *et al.*. “Inclusive charged-current neutrino-nucleus reactions”. *Phys. Rev. C*, 83:045501, 2011.
- [63] L.M. Sehgal D. Rein. “Neutrino-excitation of baryon resonances and single pion production”. *Annals Phys.*, 133:79–153, 1981.
- [64] K.M. Graczyk and J.T. Sobczyk. “Form factors in the quark resonance model”. *Phys. Rev. D*, 77:053001, 2008.
- [65] C Wilkinson *et al.*. “Reanalysis of bubble chamber measurements of muon-neutrino induced single pion production”. *Phys. Rev. D*, 90:112017, 2014.

## Bibliography

---

- [66] P. Rodrigues. “Tuning the neut resonance model”. *T2K-TN-197(Internal)*, 2014.
- [67] L.M. Sehgal D. Rein. “Coherent  $\pi^0$  production in neutrino reactions”. *Nucl. Phys. B*, 223:29–44, 1983.
- [68] M. Gluck *et al.*. “Dynamical parton distributions revisited”. *Eur. Phys. J.*, C5:461470, 1998.
- [69] A. Bodek and U.K. Yang. “Modeling Neutrino and Electron Scattering Cross Sections in the Few GeV Region with Effective LO PDFs”. *AIP Conf. Proc.*, 670:110, 2003.
- [70] M. Derrick. “Properties of the hadronic system resulting from  $\bar{\nu}_\mu p$  interactions”. *Phys. Rev. D*, 17:1, 1978.
- [71] S. Barlag *et al.*. “Charged Hadron Multiplicities in High Energy  $\bar{\nu}_\mu n$  and  $\bar{\nu}_\mu p$  Interactions”. *Z. Phys. C*, 11:283–292, 1982.
- [72] T. Sjostrand. “PYTHIA 5.7 and JETSET 7.4 Physics and Manual”. *arXiv:hep-ph/9508391*, 1995.
- [73] H.W. Bertini. “Nonelastic Interactions of Nucleons and  $\pi$  Mesons with Complex Nuclei at Energies Below 3 GeV”. *Phys. Rev. C*, 6:631, 1972.
- [74] B.R. Martin and M.K. Pidcock. “KN interactions in the resonance region: (I). Analysis of data”. *Nucl. Phys. B*, 126:266–284, 1977.
- [75] B.R. Martin and M.K. Pidcock. “KN interactions in the resonance region: (II). Amplitudes”. *Nucl. Phys. B*, 126:285–297, 1977.
- [76] J.S. Hyslop *et al.*. “Partial-wave analysis of  $K^+$ -nucleon scattering”. *Phys. Rev. D*, 46:961, 1992.
- [77] D.A. Sparrow. “Effects of the nuclear medium on the observation of baryon number violation”. *AIP Conf. Proc.*, 123:1019, 1984.
- [78] P. de Perio. “NEUT Pion FSI”. *AIP Conf. Proc.*, 1405:223, 2011.
- [79] R.D. Woods and D.S. Saxon. “Diffuse Surface Optical Model for Nucleon-Nuclei Scattering”. *Phys. Rev.*, 95:577, 1954.
- [80] P. de Perio. “Joint Three-Flavour Oscillation Analysis of  $\nu_\mu$  Disappearance and  $\nu_e$  Appearance in the T2K Neutrino Beam”. *PhD Thesis*, 2014.

## Bibliography

---

- [81] R. Brun *et al.*. “Geant3”. *CERN-DD-EE-84-1*, 1987.
- [82] C. Zeitnitz and T.A. Gabriel. “The GEANT-CALOR interface and benchmark calculations of ZEUS test calorimeters”. *Nucl. Instrum. Meth.*, A349:106–111, 1994.
- [83] R. B. Patterson *et al.*. “The extended-track reconstruction for Mini-BooNE”. *Methods in Physics Research*, A608:206, 2009.
- [84] F. James. “MINUIT - Function Minimization and Error Analysis - Reference Manual Version 94.1”. *CERN-D-506*, 1994.
- [85] M. Shiozawa. “Reconstruction algorithms in the Super-Kamiokande large water Cherenkov detector”. *Nucl. Instrum. Meth.*, A433:240–246, 1999.
- [86] K. Abe *et al.*. “T2K neutrino flux prediction”. *Phys. Rev. D*, 87:012001, 2013.
- [87] K. Abe *et al.*. “The T2K experiment”. *Nucl. Instrum. Meth.*, A659:106135, 2011.
- [88] A. Ferrari *et al.*. “FLUKA : A multi-particle transport code”. *CERN-2005-010*, 2005.
- [89] N. Abgrall *et al.*. “Measurements of cross sections and charged pion spectra in proton-carbon interactions at 31 GeV/c”. *Phys. Rev. C*, 84:034604, 2011.
- [90] N. Abgrall *et al.*. “Measurement of production properties of positively charged kaons in proton-carbon interactions at 31 GeV/c”. *Phys. Rev. C*, 85:035210, 2012.
- [91] A.A. Aguilar-Arevalo. “Measurement of  $\nu_\mu$  and  $\bar{\nu}_\mu$  induced neutral current single  $\pi^0$  production cross sections on mineral oil at  $E_\nu \sim \mathcal{O}(1 \text{ GeV})$ ”. *Phys. Rev. D*, 81:013005, 2010.
- [92] A.A. Aguilar-Arevalo. “Measurement of neutrino-induced charged-current charged pion production cross sections on mineral oil at  $E_\nu \sim 1 \text{ GeV}$ ”. *Phys. Rev. D*, 83:052007, 2011.
- [93] A.A. Aguilar-Arevalo. “Measurement of  $\nu_\mu$ -induced charged-current neutral pion production cross sections on mineral oil at  $E_\nu \in 0.5 - 2.0 \text{ GeV}$ ”. *Phys. Rev. D*, 83:052009, 2011.

## Bibliography

---

- [94] T. Barszczak. “The Efficient Discrimination of Electron and Pi-Zero Events in a Water Cherenkov Detector and the Application to Neutrino Oscillation Experiments”. *PhD Thesis*, 2005.
- [95] M. Honda *et al.*. “Calculation of atmospheric neutrino flux using the interaction model calibrated with atmospheric muon data”. *Phys. Rev. D*, 75:043006, 2007.
- [96] G. Ambrosini *et al.*. “K / pi production ratios from 450-GeV/c protons on beryllium”. *Phys. Lett. B*, 420:225, 1998.
- [97] A. E. Hedin. “Extension of the MSIS Thermosphere Model into the middle and lower atmosphere”. *J. Geophys. Res.*, 96:11591172, 1991.
- [98] J. Nieves *et al.*. “Inclusive quasielastic charged-current neutrino-nucleus reactions”. *Phys. Rev. C*, 70:055503, 2004.
- [99] E. Hernandez *et al.*. “Weak pion production off the nucleon”. *Phys. Rev. D*, 76:033005, 2007.
- [100] A. Capella *et al.*. “Structure functions and low x physics”. *Phys. Lett. B*, 337:358–366, 1994.
- [101] K. Hiraide *et al.*. “Search for charged current coherent pion production on carbon in a few-GeV neutrino beam”. *Phys. Rev. D*, 78:112004, 2008.
- [102] A. Kayis-Topaksu *et al.*. “Charged Particle Multiplicities in Charged-Current Neutrino and Anti-Neutrino Nucleus Interactions”. *Eur. Phys. J.*, C51:775–785, 2007.
- [103] Super-Kamiokande collaboration. “Prob3++”.  
<http://www.phy.duke.edu/~raw22/public/Prob3++/>. Accessed:2016/08/12.
- [104] W. K. Hastings. “Monte Carlo Sampling Methods Using Markov Chains and Their Applications”. *Biometrika*, 57:97–109, 1970.
- [105] A. Gelman *et al.*. “Posterior predictive assessment of model fitness via realized discrepancies”. *Statistica Sinica*, 6:733–760, 1996.
- [106] K.P. Lee. “Study of the neutrino mass hierarchy with the atmospheric neutrino data observed in Super-Kamiokande”. *PhD Thesis*, 2012.

- [107] R. Wendell. “Overview of Atmospheric Oscillation Analyses”. *Slides from Super-K Collaboration Meeting(Internal)*, 2016.
- [108] K. Duffy *et al.*. “A Joint ND280-SK 1R <sub>$\mu$</sub> -SK 1R<sub>e</sub> fit of neutrino and antineutrino-mode data using MCMC”. *T2K-TN-269(Internal)*, 2016.
- [109] A.B. Sousa. “First MINOS+ data and new results from MINOS”. *AIP Conf. Proc.*, 1666,:110004, 2015.
- [110] K. Matera. “First measurement using NOvA detectors of neutrino oscillation parameters  $\sin^2 \theta_{23}$  and  $\Delta m_{32}^2$ ”. Slides from ICHEP 2016. <http://indico.cern.ch/event/432527/contributions/2194572/>. Accessed:2016/08/17.
- [111] Y. Suda. “Improvement of proton decay sensitivity in the Super-Kamiokande detector by using a new event reconstruction algorithm”. Presentation at the JPS Autumn 2015 meeting.
- [112] A. Missant. “Improving T2K oscillation analyses using fiTQun: A new maximum-likelihood event reconstruction for Super-Kamiokande”. Poster presentation at NEUTRINO 2016.
- [113] C. Vilela. “FiTQun: water Cherenkov event reconstruction for current and future experiments”. Poster presentation at NEUTRINO 2016.
- [114] K. Abe *et al.*. “Letter of Intent: The Hyper-Kamiokande Experiment — Detector Design and Physics Potential —”. *arXiv:1109.3262*, 2011.
- [115] R. Acciarri *et al.*. “Long-Baseline Neutrino Facility (LBNF) and Deep Underground Neutrino Experiment (DUNE) Conceptual Design Report Volume 1: The LBNF and DUNE Projects”. *arXiv:1601.05471*, 2016.

## Appendix A

# List of Systematic Parameters

1	Absolute flux E<1GeV	26	DIS model difference
2	Absolute flux E>1GeV	27	DIS xsec.
3	Flux $\nu_\mu/\nu_e$ ratio E<1GeV	28	DIS $Q^2$ shape low-W
4	Flux $\nu_\mu/\nu_e$ ratio 1<E<10GeV	29	DIS $Q^2$ shape high-W
5	Flux $\nu_\mu/\nu_e$ ratio E>10GeV	30	Coherent $\pi$ xsec.
6	Flux $\bar{\nu}_e/\nu_e$ ratio E<1GeV	31	NC/CC ratio
7	Flux $\bar{\nu}_e/\nu_e$ ratio 1<E<10GeV	32	$K/\pi$ ratio
8	Flux $\bar{\nu}_e/\nu_e$ ratio E>10GeV	33	Up/down ratio
9	Flux $\bar{\nu}_\mu/\nu_\mu$ ratio E<1GeV	34	Horizontal/vertical ratio
10	Flux $\bar{\nu}_\mu/\nu_\mu$ ratio 1<E<10GeV	35	Multi-GeV normalization
11	Flux $\bar{\nu}_\mu/\nu_\mu$ ratio E>10GeV	36	Hadron simulation
12	$\nu$ path length	37	CC $\nu_\tau$ xsec.
13	Matter effect	38	FC/PC separation
14	Solar activity	39	FC reduction
15	CCQE xsec.	40	Fiducial volume
16	CCQE $\nu/\bar{\nu}$ ratio	41	Non- $\nu$ bkg. e-like
17	CCQE $\nu_\mu/\nu_e$ ratio	42	Non- $\nu$ bkg. mu-like
18	$M_A^{QE}$	43	Ring separation
19	MEC xsec.	44	PID 1-ring
20	Single meson xsec.	45	PID multi-ring
21	Single meson $M_A$	46	Energy scale
22	Single meson $C_5^A(0)$	47	Up/down energy scale asym.
23	Single meson bkg.	48	Decay-e tagging eff.
24	Single meson $\pi^0/\pi^\pm$ ratio	49	$2R\pi^0$ eff.
25	Single meson $\bar{\nu}/\nu$ ratio	50	Sub-GeV FSI parameter #00

Table A.1: List of systematic parameters. Continues to Table A.2.

---

*Appendix A. List of Systematic Parameters*

---

51	Sub-GeV FSI parameter #01	64	Multi-GeV FSI parameter #02
52	Sub-GeV FSI parameter #02	65	Multi-GeV FSI parameter #03
53	Sub-GeV FSI parameter #03	66	Multi-GeV FSI parameter #04
54	Sub-GeV FSI parameter #04	67	Multi-GeV FSI parameter #05
55	Sub-GeV FSI parameter #05	68	Multi-GeV FSI parameter #06
56	Sub-GeV FSI parameter #06	69	Multi-GeV FSI parameter #07
57	Sub-GeV FSI parameter #07	70	Multi-GeV FSI parameter #08
58	Sub-GeV FSI parameter #08	71	Multi-GeV FSI parameter #09
59	Sub-GeV FSI parameter #09	72	Multi-GeV FSI parameter #10
60	Sub-GeV FSI parameter #10	73	Multi-GeV FSI parameter #11
61	Sub-GeV FSI parameter #11	74	Multi-GeV FSI parameter #12
62	Multi-GeV FSI parameter #00	75	Multi-GeV FSI parameter #13
63	Multi-GeV FSI parameter #01	76	Multi-GeV FSI parameter #14

Table A.2: List of systematic parameters. Continues from Table A.1.

## Appendix B

# Atmospheric Neutrino Selection Improvement by fiTQun

In the previously published Super-K atmospheric neutrino oscillation analyses, APFIT was used for event selection instead of fiTQun. The impact of employing fiTQun for event selection is discussed in this appendix.

The event selection criteria for APFIT-based analysis, as described in detail in [106], are very similar to the fiTQun-based event selection introduced in Section 8.1.1, with some differences in the sample definitions. In particular, the events selected as sub-GeV one-ring e-like with 0 decay electron by APFIT are further subdivided into two categories using the fiTQun  $\pi^0$  fit variables discussed in Section 6.9.1: out of the selected events, the ones which satisfy  $\ln(L_{\pi^0}/L_e) > 130$  and  $95 < m_{\pi^0}(\text{MeV}/c^2) < 185$  are categorized as “Sub-GeV one-ring  $\pi^0$ ” sample, and the rest are categorized as “Sub-GeV one-ring e-like 0 decay” sample. The additional cut using fiTQun was introduced to reduce the rather large  $\text{NC}\pi^0$  background contamination in the events selected as one-ring e-like by APFIT. Other than the  $\pi^0$  cut above, all selection cuts are done using APFIT information only in the APFIT-based analysis. Such additional  $\pi^0$  rejection cut is not employed for the fiTQun-only selection since the one-ring e-like selection by fiTQun reduces the  $\pi^0$  background to a sufficiently low level.

Table B.1 shows the expected event rates and the interaction mode breakdown of each event sample selected by the APFIT-based event selection. MC expectations are calculated using the same oscillation parameters and normalization as described in Section 8.1.4. Comparing this to Table 8.1 for fiTQun-only selection, it can be seen that fiTQun event selection achieves higher fraction of the targeted event category and lower fraction of backgrounds across all event samples. In particular,  $\nu_\mu$  contamination in the e-like samples in multi-GeV is significantly reduced by fiTQun.

In order to see the impact of the above improvement in event selection on

## Appendix B. Atmospheric Neutrino Selection Improvement by fiTQun

%	1Re $0_{\text{dcy}}$	1Re $\geq 1_{\text{dcy}}$	1R $\mu$ $0_{\text{dcy}}$	1R $\mu$ $1_{\text{dcy}}$	1R $\mu$ $\geq 2_{\text{dcy}}$	1R $\pi^0$	2R $\pi^0$
$\nu_e$ CC	72.77	81.20	4.36	0.11	0.05	9.97	7.04
$\bar{\nu}_e$ CC	23.92	1.80	1.32	0.00	0.00	3.25	2.44
$\nu_\mu$ CC	0.19	8.24	68.07	68.21	94.75	1.23	0.99
$\bar{\nu}_\mu$ CC	0.04	2.31	8.03	29.11	3.29	0.23	0.08
NC	3.08	6.44	18.23	2.57	1.91	85.32	89.44
Total	4899.5	563.0	909.0	4185.9	367.0	234.6	889.9

%	1Re $\nu_e$	1Re $\bar{\nu}_e$	1R $\mu$	MRe $\nu_e$	MRe $\bar{\nu}_e$	MR $\mu$	MRe oth.
$\nu_e$ CC	63.70	54.96	0.27	53.43	53.66	2.74	29.31
$\bar{\nu}_e$ CC	9.44	37.68	0.12	10.03	26.60	0.42	3.26
$\nu_\mu$ CC	8.98	0.72	62.19	14.70	4.73	70.50	31.72
$\bar{\nu}_\mu$ CC	1.55	0.20	37.26	1.98	0.58	21.25	3.54
NC	16.33	6.44	0.15	19.86	14.43	5.09	32.17
Total	345.8	1040.4	1358.7	431.9	427.7	1190.2	681.5

Table B.1: Interaction mode breakdown and the total MC event rates for each event sample categorized by the APFIT-based selection, where the upper and the lower table is for sub-GeV and multi-GeV samples respectively. MC expectations are calculated with two-flavour oscillations at  $\sin^2 2\theta=1.0$  and  $\Delta m^2=2.5 \times 10^{-3} \text{ eV}^2$  and is normalized to 2519.89 days exposure.

the sensitivity to oscillation parameters, a sensitivity study was performed following the same procedures described in Section 8.5. The Asimov datasets for this study were produced by taking  $\sin^2 \theta_{23} = 0.55$  and  $\Delta m_{32}^2 = +2.39 \times 10^{-3} \text{ eV}^2$  (normal hierarchy), and the rest of the oscillation parameters set to the values listed in Table 8.3. The exposure was taken to be 2519.89 days.

Figure B.1 compares resulting 90% HPD credible regions for  $\Delta m_{32}^2$  and  $\sin^2 \theta_{23}$  between the cases of using APFIT or fiTQun for event selection. The posterior probability for normal hierarchy is 61.5% for APFIT selection and 63.0% for fiTQun selection.

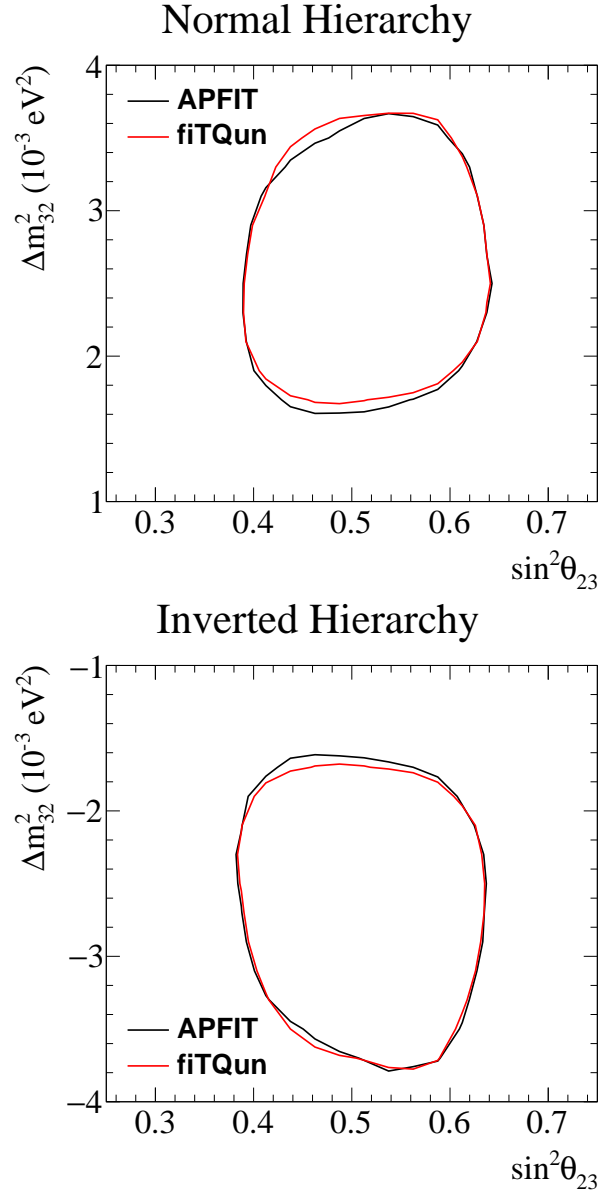


Figure B.1: 90% HPD credible regions for  $\Delta m_{32}^2$  and  $\sin^2 \theta_{23}$  compared between the cases of using APFIT or fiTQun for event selection, on Asimov datasets. The black contours are for APFIT selection and the red contours are for fiTQun. The upper and the lower plots are the cases of assuming normal and inverted hierarchy respectively.